AN ABSTRACT OF THE THESIS OF

Daniel P. Krebs for the degree of Master of Science in Mechanical Engineering presented on May 16, 2008.

Title: A Technique for Spatially Resolved Wall Temperature Measurements in Microchannel Heat Sinks Using Infrared Thermography

Abstract approved:

Vinod Narayanan

A non-intrusive measurement technique for direct quantitative thermal visualization of channel wall temperatures in two phase microchannel flows using infrared thermography (IRT) is presented. Specifically, the measurement of top channel wall temperatures in a fractal-like branching microchannel silicon heat sink during flow boiling is demonstrated and thoroughly documented. Obtaining quantitative local temperature measurements involving IRT poses significant challenges and requires careful consideration with regard to heat sink design, fabrication and calibration as well as data acquisition, reduction and analysis procedures -- all of which are addressed and discussed in detail. Also discussed and rigorously quantified are the potentially significant measurement uncertainties associated with obtaining non-intrusive, local data of this nature. Results indicate that temperature maps of the microchannel top wall during flow boiling can be obtained with a spatial resolution of 10 μm and an uncertainty varying from 0.82°C-1.67°C at 25 °C and 0.96°C-2.80°C.

A Technique for Spatially Resolved Wall Temperature Measurements in Microchannel Heat Sinks Using Infrared Thermography

by
Daniel P. Krebs

A THESIS

Submitted to

Oregon State University

in partial fulfillment of
the requirement for the
degree of

Master of Science

Presented May 16, 2008
Commencement June 2008

Master of Science thesis of Daniel P. Krebs presented on May 16, 2008.

APPROVED:

Major Professor, representing Mechanical Engineering

Head of the School of Mechanical, Industrial & Manufacturing Engineering

Dean of the Graduate School

I understand that my thesis will become part of the permanent collection of Oregon State University libraries. My signature below authorizes release of my thesis to any reader upon request.

Daniel P. Krebs, Author

ACKNOWLEDGMENTS

I would first and foremost like to acknowledge my wife Janine, without whose patience and constant, unwavering support I never would have made it this far. I would also like to thank my advisor Dr. Vinod Narayanan as well as Dr. Deb Pence, Dr. Jim Liburdy and the Office of Naval Research (contract number N0014-06-1-0017) for giving me the opportunity to contribute to their research. A special thanks to Mr. Douglas Heymann for his support in developing the image shifting cross correlation algorithm. Thank you also to Mr. Lee Edward and Mr. Younghoon Kwak for their friendship as well as their contributions to the development and troubleshooting of the experimental facility. Lastly, I would like to thank Mr. J.J. Jenks who as my officemate and friend provided a vital HONClBrF’n link to sanity.

TABLE OF CONTENTS

Page

TABLE OF CONTENTS (Continued)

LIST OF FIGURES

LIST OF FIGURES (Continued)

LIST OF FIGURES (Continued)

LIST OF FIGURES (Continued)

LIST OF TABLES

LIST OF APPENDICES

LIST OF APPENDIX FIGURES

LIST OF APPENDIX FIGURES (Continued)

Page

APPENDIX H

APPENDIX I

APPENDIX K

APPENDIX L

APPENDIX N

APPENDIX O

APPENDIX P

APPENDIX Q

LIST OF APPENDIX FIGURES (Continued)

Page

APPENDIX R

APPENDIX S

APPENDIX T

Page

APPENDIX T

LIST OF APPENDIX FIGURES (Continued)

Page

APPENDIX T

LIST OF APPENDIX TABLES

Page

APPENDIX A

APPENDIX B

APPENDIX C

APPENDIX D

APPENDIX E

APPENDIX F

APPENDIX G

APPENDIX I

LIST OF APPENDIX TABLES (Continued)

ABBREVIATIONS

DNE	Does not exist
FPA	Focal plane array
HMTS	Horizontal micro-traverse stage
IML	Image location
IR	Infrared
IRT	Infrared thermography
OLA	Overlapped average
PW	Piecewise
VMTS	Vertical micro-traverse stage
WTC	Washington Technology Center

NOMENCLATURE

Au	Gold
C	Correction factor defined in Eq. 5.8
E	Emitted radiant energy (W/m^2)
k	Branching level
L	Microchannel length
n	Refractive index
NiCr	Nichrome
Si	Silicon
Si_3N_4	Silicon nitride
SiO_2	Silicon dioxide
T	Temperature
t	Thickness
$\overline{T}$	Overall transmittance
w	Microchannel width

SYMBOLS

β	Width ratio
γ	Length ratio
ε	Emissivity
σ	Stefan-Boltzmann constant

SUBSCRIPTS

Au	Gold
det	Detector
r	Reflected
sens	Sensed
Si	Silicon

1 Introduction

Recent technological developments, in the areas of telecommunications, micro-fluidic devices, micro-electronics and overall circuit architecture have lead to an overall miniaturization of electronic components and a near exponential growth in required heat flux dissipation to ensure component reliability. Traditional forced air convection cooling systems for these applications have all but reached their limits and have forced the investigation into the applicability of alternate cooling systems [1-4]. Specifically, phase-change heat transfer such as microchannel flow boiling, which has been given significant attention in recent years [4-8].

Flow boiling in microchannels takes advantage of the latent heat of the coolant available during the phase change process and can significantly increase heat flux dissipation while at the same time decreasing coolant flow rates when compared to single phase coolant systems [5]. By taking advantage of the phase change process during flow boiling, heat transfer to or from the working fluid can occur without influencing the fluid temperature. This results in the potential for significant heat transfer rates through small temperature differences.

To capitalize on this idea, knowledge of the local boiling heat transfer coefficient (h_b) is desired and can be obtained through application of Newton's Law of Cooling and direct knowledge of the input heat flux (q"), the bulk fluid temperature (T_f) and the microchannel surface temperature (T_s).

$$q'' = h_b(T_s - T_f) \tag{1.1}$$

Considerable attention has been given to quantifying the flow and heat transfer characteristics in singular circular microchannels as well as parallel sets of circular, rectangular, trapezoidal, and triangular shaped microchannels [6,7]. These experiments typically incorporate evenly spaced thermocouples embedded below and along the entire length of the microchannel of interest. To quantify heat transfer characteristics from these experiments, channel wall surface temperatures are inferred from heat sink surface temperatures and not directly measured. Measuring wall surface temperature in this manner provides single point or spatially averaged data at best and is useful in determining area averaged heat transfer coefficients over the entire heat sink or heat transfer coefficients at specific areas within the heat sink.

Recent innovations that provide greater spatial resolution when measuring wall surface temperatures have been investigated by Lee and Garimella [5] and Zhang et.al. [8]. Lee and Garimella [5] utilized a 5 x 5 array of heat sources and temperature sensing diodes embedded in a test chip below a set of rectangular parallel microchannels. Each element in the 5 x 5 array measured 2.54 mm x 2.54 mm. Zhang et.al. [8]. utilized a 9 segment resistor constructed of a single crystal silicon substrate formed from ion implantation. Rectangular parallel microchannels were etched into the resistor which functioned as a heater and nine thermometers in series, evenly spaced along the microchannel length. Both of these experiments measured channel wall temperatures and ultimately provided heat transfer coefficients for the flow conditions observed. However, just as with embedded thermocouples, these integrated temperature sensors still only provided single point or spatially averaged temperature data.

Thermal imaging techniques, such as infrared thermography (IRT) provide the ability to acquire accurate temperature measurements even in the presence of large spatial temperature fluctuations. [9,10] with spatial resolutions of approximately 10 μm. IRT is a well established measurement technique for macroscale heat transfer research and is evident from the work done by Astarita [9,10], Montelpare [1], Mori [11], Sargent [12], Carlomagno [13] and Hestroni [14]. The non-intrusive nature of IRT and thermal imaging in general, is appealing to researchers and makes it a viable candidate for temperature measurements in microscale heat transfer research.

Several studies detailing non-intrusive, quantitative, thermal imaging of mini- and microchannel heat sink surface temperatures have been reported recently by Hestroni et.al. [15,16], Hollingworth [17], Hapke [18] and Patil [19]. Hestroni et.al. [15,16] performed visualization studies of flow boiling in triangular microchannel arrays. Hollingworth [17] measured the local channel wall temperature in single and two phase minichannel flows. Hapke [18] examined the outside wall temperature of rectangular microchannels during flow boiling. Patil [19] measured wall/near-wall fluid temperatures of single phase flows through a rectangular microchannel. These works illustrate the application and effective use of thermal imaging techniques such as, infrared (IR) radiometry, thermochromic liquid crystal imaging and IRT to accurately measure spatially resolved wall temperatures at the microscale. Despite this, experimental studies detailing spatially resolved temperature measurements of flow boiling through microchannels are quite limited in open literature. This thesis discusses the application of IRT to directly measure spatially resolved local wall temperatures in flow boiling through microchannels.

2 Objectives

This document demonstrates the use of infrared thermography to quantitatively determine wall surface temperatures during microchannel flow boiling. Specifically, the top wall temperature of a fractal-like branching microchannel network etched in a silicon heat sink. Microchannel top wall temperatures were determined from directly measured radiation intensities rather than being inferred from heat sink surface temperatures. This allows a local heat transfer coefficient to be determined, provided the local fluid temperature is known. Temperature maps for a 19.05 mm x 19.05 mm area of the heat sink were obtained with a spatial resolution of 10 μm and uncertainty estimates for this technique were rigorously quantified.

3 Background

This chapter provides supplemental as well as applicable information pertinent to IRT, IR detectors and microchannel heat sinks. A brief history of IRT is provided for completeness purposes. A brief overview of IR detectors is provided to qualitatively illustrate the differences between classes and types of detectors. A brief overview of microchannel heat sinks is provided to illustrate reasons for using a fractal-like branching microchannel network in this study.

3.1 Infrared Thermography-A Brief History

IRT is a non-intrusive technique by which detected radiation emitted from a body, in the IR range of the electromagnetic spectrum, is measured and converted to an electronic video signal displayable in visible light. When the radiation properties of the body are known, thermography can provide the temperature through a measure of this detected radiation. The idea for IRT originated in the early 1800's from the work of the English physicist William Herschel and his discovery of thermal radiation outside the boundaries of the visible spectrum [9]. Later work by German physicists Max Planck and Wilhelm Wien lead to the development of Wien's displacement law which mathematically describes the relationship between color and temperature. Wien's displacement law mathematically expresses the observation that colors vary from red to yellow as the temperature of a thermal radiator increases [9,10].

IRT was first utilized as a macroscale temperature measurement technique in the 1960's and was considered a major scientific breakthrough as it provided experimentalists with the ability to obtain accurate, spatially resolved, temperature measurements for the first time [9]. Prior to the introduction of IRT, spatially resolved temperature measurements were extremely difficult since typical temperature measurement devices such as thermocouples, RTD's, thermisters, thermopiles and pyrometers only provided single point or spatially averaged data at best. IRT allows for the acquisition of accurate surface temperature measurements even in the presence of large spatial temperature fluctuations [9,10].

3.2 Infrared Detectors-A Brief Overview

IRT is considered a radiometric measurement technique. Generally speaking, radiometry is defined as the measurement of any radiometric quantity such as irradiance and radiance. Consequently, a radiometer is defined as an apparatus used to measure the magnitudes of these radiometric quantities. Three essential components comprising all radiometers are 1) optics, 2) detectors and 3) electronics. The optics collect, disperse and/or filter radiation through an aperture. The detectors transduce the radiation into an electronic signal such as voltage or current. The electronics process, record and/or display the signal. These components are typically packaged together and are available commercially as thermal imaging or IR cameras [20].

The most important component of any IR camera is the detector. Physical operating principles dictate the existence of two main classes of IR detectors: 1) thermal detectors and 2) photon detectors. Thermal detectors consist of a material that absorbs incident radiation and takes advantage of a resultant change in a physical property of the material such as resistance, voltage or current. The change in the physical property is used to generate an electrical output signal. Lead Titanate (PT), Lead Zirconate Titanate (PZT) and Lead Lanthanum Titanate (PLT) are examples of materials used in the construction of thermal detectors. Photon detectors consist of a material that absorbs incident radiation and takes advantage of a resultant change in the electronic energy distribution of the material due to absorbed radiation interaction with the material electrons. The change in electronic energy distribution is used to generate an electrical output signal [21,22]. Germanium (Ge), Lead Sulfide (PbS) and Indium Antimonide (InSb) are examples of materials used in the construction of photon detectors.

The primary difference between thermal detectors and photon detectors is their operating temperature. Thermal detectors typically operate at room temperature while photon detectors are cryogenically cooled during operation. Qualitatively, this difference in operating temperature results in photon detectors exhibiting higher costs, increased response times and increased sensitivities relative to thermal detectors. In addition to this, photon detectors typically exhibit wavelength dependence while thermal detectors are generally wavelength independent [21,22]. Several photon detector materials and their approximate spectral operating ranges are documented on Table 3.1 below [23].

Table 3.1 Photon detector material and spectral operating ranges.

Material	**Abbreviation**	**Spectral Operating Range (μm)**
Indium Gallium Arsenide	InGaAs	0.7-2.6
Germanium	Ge	0.8-1.7
Lead Sulfide	PbS	1.0-3.2
Lead Selenide	PbSe	1.5-5.2
Indum Arsenide	InAs	1.0-3.8
Platinum Silicide	PtSi	1.0-5.0
Indium Antimonide	InSb	1.0-6.7
Mercury Cadmium Telluride	HgCdTe	1.0-25.0

The change in the resistance, voltage or current used to generate an electrical output signal in thermal detectors is driven primarily by the rate of change of the incident radiant power rather than by the spectral content. Qualitatively, thermal detectors are generally considered more rugged than photon detectors due to this wavelength independence [21,22].

Thermal and photon detectors are further classified into single sensor detectors and focal plane arrays (FPA) [24]. A single sensor detector consists of a single radiation sensor. With the aid of a mechanical scanning mechanism, such as a rotating prism or mirror, the entire field of view is scanned line by line at a given frequency and the emitted radiation of the object in question is recorded. This type of technology is commonly referred to as scanning technology. A focal plane array consists of a matrix of radiation sensors. A mechanical scanning mechanism is not necessary for a focal plane array since the entire field of view is captured at the same instant in time. This type of technology is commonly referred to as staring technology [21,24].

Single sensor detectors are typically less susceptible to thermal noise contributions from the surrounding environment than focal plane arrays. However, they are highly susceptible to internal frequency noise resulting from the operation of the mechanical scanning mechanism [24]. Focal plane arrays on the other hand, provide increased spatial resolution, decreased acquisition time and enhanced image quality and contrast relative to single sensor detectors [24].

The IR camera utilized in this study was a mid-range wavelength detector. In general, the IR spectral band of the electromagnetic spectrum encompasses wavelengths ranging from 0.7 μm to 1000 μm. The IR spectral band is further broken down into four sub-bands: 1) near-IR, 2) mid-IR, 3) far-IR and 4) extreme-IR [9]. The near-IR spectral band encompasses wavelengths ranging from 0.7 μm to 3.0 μm. The mid-IR spectral band encompasses wavelengths ranging from 3.0 μm to 6.0 μm. The far-IR spectral band encompasses wavelengths ranging from 6.0 μm to 15.0 μm. The extreme-IR spectral band encompasses wavelengths ranging from 15.0 μm to 1000.0 μm [9].

The IR camera detected radiation in two separate mid-range wavelength bands of 3.5-4.1 μm and 4.5-5.1 μm and consisted of a front illuminated, 256 x 256, Indium Antimonide (InSb) focal plane array of photovoltaic-type detectors that were cryogenically cooled to approximately 77 K to ensure high sensitivity and low noise measurement [19].

3.3 Microchannel Heat Sinks

The use of microchannel heat sinks to cool integrated circuits was first introduced by Tuckerman and Pease [25,26]. Since this introduction, investigations of microchannel heat sinks have primarily focused on straight single microchannels or straight parallel sets of microchannels with either circular, rectangular, trapezoidal, or triangular cross-sectional areas [6,7]. The motivation behind microchannel heat sinks for heat dissipation is illustrated by examining the classical correlations derived for macroscopic channels. Consider internal, fully developed, laminar, single phase, flow. The Nusselt number is constant for this flow condition and is defined as

$$\mathrm{Nu} = \frac{\mathrm{hd}}{\mathrm{k}} \qquad 3.1$$

For a constant Nu, the heat transfer coefficient (h) is inversely proportional to the channel diameter (d). A decrease in channel diameter results in an increase in the heat transfer coefficient and ultimately an increase in the heat transfer rate.

A decrease in channel diameter also results in an increase in pressure drop within the channel. Consider the relationship describing the pressure drop in a macroscale horizontal tube due to frictional interaction with the pipe wall.

$$\Delta P = f\frac{L}{d_h}\frac{\rho V^2}{2} \tag{3.2}$$

Where f is friction factor, L is the pipe length, d_h is the tube hydraulic diameter, ρ is the fluid density and V is the fluid velocity. For fully developed laminar flow in a square tube the friction factor is defined as

$$f = \frac{57}{Re} = \frac{57\mu}{\rho V d_h} = \frac{57\nu}{V d_h} \tag{3.3}$$

where Re is the Reynolds number, μ is the fluid dynamic viscosity and υ is the fluid kinematic viscosity. Substituting Equation 3.3 into Equation 3.2 and simplifying gives

$$\Delta P = 28.5\frac{\nu L \rho V}{d_h^2} \tag{3.4}$$

The velocity term in Equation 3.4 can be expressed as

$$V = \frac{Q}{A} = \frac{4Q}{W d_h} \tag{3.5}$$

where Q is the volumetric flow rate, A is the tube cross-sectional area and W is the tube wetted perimeter. Substituting Equation 3.5 into Equation 3.4 gives

$$\Delta P = 114 \frac{\nu L \rho Q}{W d_h^3} \qquad 3.6$$

Equation 3.6 illustrates that the pressure drop is inversely proportional to the tube hydraulic diameter to the power of 3. A small decrease in the channel diameter results in a rather significant pressure drop within the channel, which ultimately increases the pumping power required to overcome this resistance. Increased heat transfer rates at the expense of increased pressure drop and pumping power is a typical characteristic of flow through microchannels.

The microchannel heat sink used in this study was inspired by naturally occurring flow networks such as the mammalian circulatory system [27]. These naturally occurring flow networks consist of bifurcating channels that exhibit a fixed length and width ratio scaling [27]. Pence [28] proposed that the typically high pressure drop associated with flows through parallel microchannels could be reduced by using bifurcating channels or fractal-like branching microchannel networks in heat sinks. It was anticipated that the increased cross-sectional flow area across each branching level would result in a lower pressure drop and that the decrease in hydraulic diameter at each branching level would decrease the total cross-sectional thermal resistance [28]. Pence [26,29] developed 1-D and 3-D computational models and reported a significant reduction in pressure drop (~ 50%) as well as surface temperature variation (~ 75%) for fractal-like branching microchannel networks when compared to straight microchannel networks. Figure 3.1 illustrates a top view of the flow network developed by Pence and used in this study.

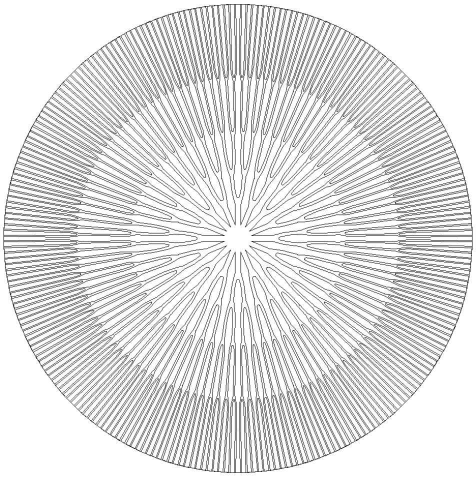

Figure 3.1 Fractal-like branching microchannel network.

The fractal-like branching microchannel network consisted of sixteen branching trees uniformly spaced around the periphery of an inlet plenum. Each branching tree started at the inlet plenum and bifurcated at four distinct radial locations resulting in five different branching levels. Figure 3.2 illustrates a single branching tree denoting each branching level and the radial locations used to define the microchannel lengths.

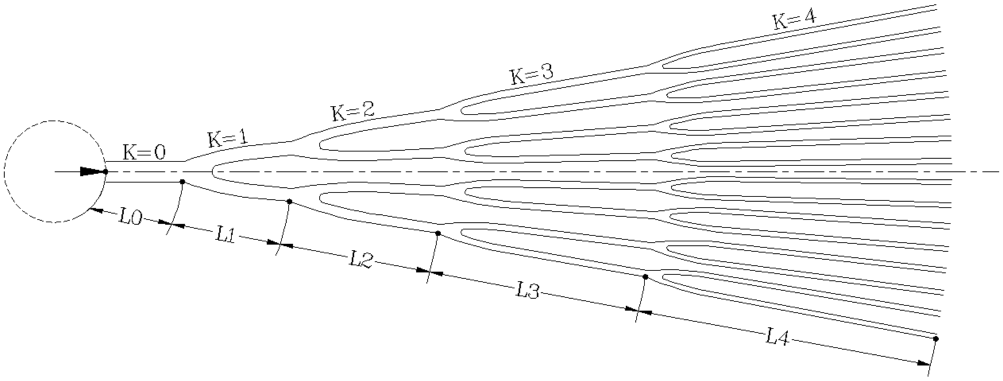

Figure 3.2 Single branching tree.

Each branching level was identified and referenced by the value of the index k. For example, the k=0 branching level consisted of the 16 microchannels exiting the inlet plenum upstream of the first bifurcation. The k=1 branching level consisted of the 32 microchannels downstream of the first bifurcation and upstream of the second bifurcation, etc. Microchannels upstream of a bifurcation were considered mother branches while microchannels downstream of a bifurcation were considered daughter branches. The physical dimensions of the microchannels in each branching level were characterized by a width and length scale ratio, β and γ respectively. The width and length scale ratios for this flow network were fixed at 0.70 and 1.41 and were defined mathematically as

$$\beta = \frac{w_{k+1}}{w_k} = 0.70 = \text{width scale ratio} \tag{3.7}$$

$$\gamma = \frac{L_{k+1}}{L_k} = 1.41 = \text{length scale ratio} \tag{3.8}$$

A width ratio less than one ($\beta < 1$) indicates that as a channel progress from inlet to outlet its width decreases. A length ratio greater than one ($\gamma > 1$) indicates that as a channel progress from inlet to outlet its length increases. Table 3.2 documents the physical dimensions of each branching level for the heat sink used in this study.

Table 3.2 Branching level physical dimensions.

Branching Level (k)	**Channel Quantity (--)**	**Channel Width (μm)**	**Channel Length (mm)**	**Channel Depth (μm)**	**Hydraulic Diameter (μm)**	**Width Ratio (β)**	**Length Ratio (γ)**
0	16	400	1.62	250	308	0.70	1.41
1	32	283	2.28	250	265		
2	64	200	3.22	250	222		
3	128	141	4.54	250	180		
4	256	100	6.40	250	143		

The channel lengths reported on Table 3.2 are based upon radial distances from the inlet plenum and are not actual channel lengths. The channel and bifurcation curvatures were neglected in determining the channel lengths.

4 Experimental Heat Sink

A composite, silicon heat sink incorporating a fractal-like branching microchannel network was used in this study. Twelve heat sinks total were fabricated by Washington Technology Center (WTC) in Seattle, WA and each heat sink received presented with visual blemishes as well as jagged protrusions of extra silicon (see Figs. 4.3 and 4.4). A series of tests were performed to determine heat sink quality and to identify the heat sink(s) suitable for data acquisition. Once identified, the heat sink(s) required modification to ensure proper functionality during calibration and experimental data acquisition. The fabrication details, inspection, testing and modifications undergone by each heat sink are summarized in this chapter.

4.1 Heat Sink Fabrication

The heat sinks consisted of six unique physical components: 1) a top silicon (Si) wafer, 2) a bottom silicon (Si) wafer, 3) a gold (Au) layer, 4) a silicon nitride (Si_3N_4) anti-reflective coating (ARC), 5) three nichrome (NiCr) heater rings and 6) two silicon dioxide (SiO_2) isolative coatings. The heat sinks measured 38.10 mm in diameter with an overall thickness of approximately 1.00 mm. Figure 4.1 illustrates an exploded view of the composite heat sink detailing the individual heat sink components. Table 4.1 documents the heat sink component nominal physical dimensions.

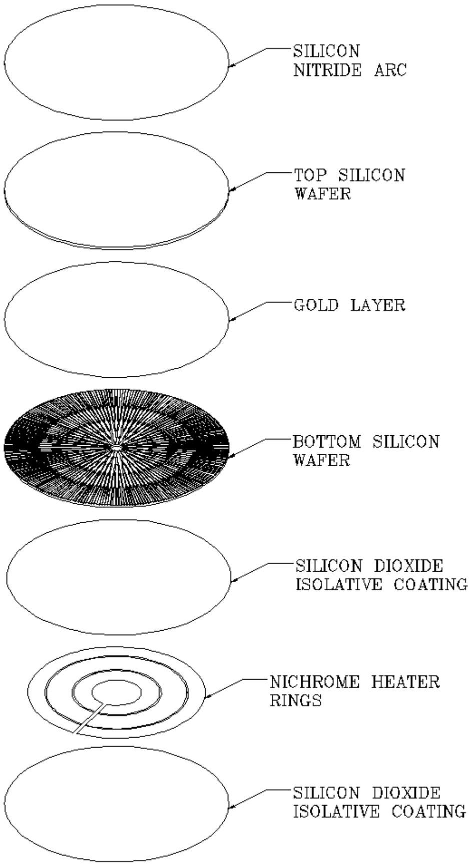

Figure 4.1 Composite heat sink components.

Table 4.1 Heat sink component overall physical dimensions.

Heat Sink Component	Diameter (mm)	Thickness (µm)
Top Si wafer	38.10	500
Bottom Si wafer	38.10	500
Gold layer	38.10	4.0-8.0
Si_3N_4 ARC	38.10	1.1
Nichrome heater rings	See Fig. 4.2/Table 4.2	0.5
SiO_2 isolative coatings	38.10	1.0

Three sides of the fractal-like branching microchannel network were Deep Reactive Ion Etched (DRIE) to a depth of 250 µm into the top surface of the bottom Si wafer. Three NiCr heater rings, 0.5 µm thick, were deposited on the non-channel side of the bottom silicon wafer to allow heat input to the heat sink. One SiO_2 isolative coating was applied to the non-channel side of the bottom Si wafer prior to deposition of the heater rings. The second SiO_2 isolative coating was applied after deposition of the heater rings. Therefore, the inner, middle and outer heater rings were sandwiched between two 1.0 μm thick layers of SiO_2 to electrically isolate them from each other and the heat sink. Electrically isolating the three heater rings allows for independent heater control making a uniform input heat flux to the heat sink achievable. During the application of the second SiO_2 isolative coating, six rectangular contact pads, two per heater ring, were left uncoated to allow electrical connections to DC power supplies. Figure 4.2 illustrates a top view of the three nichrome heater rings and contact pads. Table 4.2 documents the heater ring and contact pad physical dimensions.

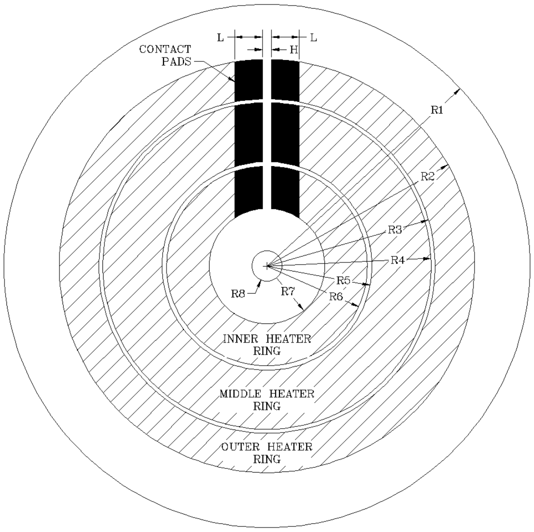

Figure 4.2 Heater rings and contact pads.

Table 4.2 Heater ring and contact pad physical dimensions.

Variable	Description	Value (mm)
R1	Heat sink outer radius	19.05
R2	Inner heater ring outer radius	15.04
R3	Inner heater ring inner radius	12.17
R4	Middle heater ring outer radius	11.89
R5	Middle heater ring inner radius	7.59
R6	Outer heater ring outer radius	7.26
R7	Outer heater ring inner radius	4.19
R8	Inlet plenum outer radius	1.00
H	Heater ring gap width	0.66
L	Contact pad width	2.00

A gold layer, 4.0-8.0 μm thick, was deposited on the bottom surface of the top Si wafer and used to bond the top and bottom Si wafers together. The wafers were gold-silicon eutectically bonded [30] such that the gold layer formed the top wall of the fractal-like branching microchannel network. A 1.1 μm thick Si_3N_4 anti-reflective coating was deposited on the top surface of the top Si wafer to minimize reflected radiation incident upon the heat sink from the focal plane array and the surroundings. Figures 4.3 and 4.4 are digital photographs of a heat sink as it arrived from the manufacturer.

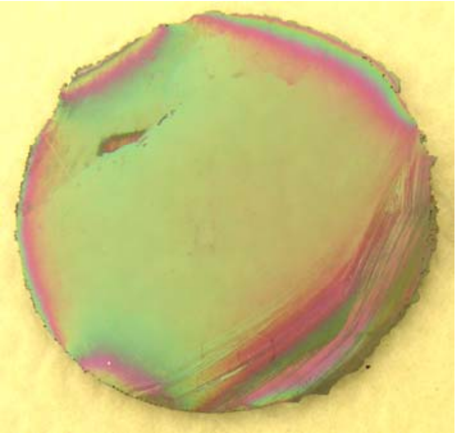

Figure 4.3 Heat sink top.

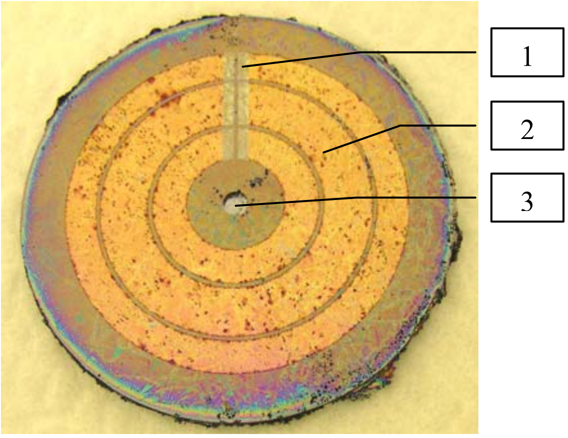

Figure 4.4 Heat sink bottom.
1 = Contact Pads
2 = Heater Ring
3 = Inlet Plenum

Notice the irregular shape of the heat sink resulting from the jagged protrusions of extra silicon sporadically spaced around its periphery as well as the pitted appearance of the heater rings and bottom Si wafer. The heat sink condition upon delivery from WTC led to questions regarding quality and functionality. Therefore, the heat sinks were thoroughly inspected and tested to determine their suitability for data acquisition.

4.2 Heat Sink Quality Inspection and Testing

Prior to quality inspection and testing, each heat sink was placed in a padded, plastic storage case for protection and numbered, 1 through 12 for identification purposes. The heat sinks were subjected to thorough visual inspections using the naked eye and a Leica Zoom 2000 desktop microscope with a magnification range of 10.5 to 45. The visual inspection was used to determine if the heater rings and the anti-reflective coatings existed on the provided heat sinks. When viewed at an angle, the anti-reflective coating had a green tint; therefore its existence could be determined visually. A magnified visual inspection of the heat sinks revealed pitting on both the top and bottom surfaces. In some instances the pitting actually penetrated the entire depth of the bottom silicon wafer providing a path for fluid to exit the heat sink at a location other than at its periphery. Fluid discharge through the bottom silicon wafer upstream of the designed microchannel exit presents an electrical hazard with regard to the vacuum chuck. To verify the potential for this hazard, an air flow test was conducted for each heat sink.

A rubber tipped syringe was utilized to force air into the heat sink submerged in deionized, distilled water. Air bubbles were visually observed exiting the heat sink. If the observed bubbles exited the heat sink through the microchannel exit, the heat sink was considered to have passed the air flow test. If the observed bubbles exited the heat sink upstream of the microchannel exit, the heat sink was considered to have failed the air flow test.

Finally, the resistance for each heater ring, as well as the resistance between adjacent heater rings was measured to verify proper application of the SiO_2 isolative coatings. Resistance measurements were obtained using a handheld Tektronix® DM 250 multimeter. The resistance values measured between adjacent heater rings approached infinity and indicated that the heater rings were in fact electrically isolated from each other and the heat sink.

A summary of the results from the visual inspection, air flow and the heater ring resistance tests is provided in Table 4.3. Note that several heat sinks did not posses heater rings therefore their resistances did not exist (DNE). Complete details and results of the visual inspection, air flow and heater ring resistance tests are provided in Appendix F.

Table 4.3 Summary of quality inspection and test results.

Heat Sink #	Heater Rings	ARC	Air Flow	Inner Heater Ring (Ω)	Middle Heater Ring (Ω)	Outer Heater Ring (Ω)	Inner to Middle Heater Ring (Ω)	Middle to Outer Heater Ring (Ω)	Inner to Outer Heater Ring (Ω)
1	Yes	Yes	Fail	15	28	28	∞	∞	∞
2	Yes	Yes	Pass	579	673	410	∞	∞	∞
3	Yes	Yes	Pass	1043	159	8628	∞	∞	∞
4	Yes	Yes	Pass	710	712	565	∞	∞	∞
5	Yes	Yes	Fail	1055	412	406	∞	∞	∞
6	Yes	Yes	Fail	12	14	38	∞	∞	∞
7	Yes	No	Pass	12	13	27	∞	∞	∞
8	Yes	No	Fail	12	13	28	∞	∞	∞
9	No	No	Fail	DNE	DNE	DNE	∞	∞	∞
10	No	No	Fail	DNE	DNE	DNE	∞	∞	∞
11	No	No	Fail	DNE	DNE	DNE	∞	∞	∞
12	No	No	Fail	DNE	DNE	DNE	∞	∞	∞

The quality inspection and testing revealed that out of twelve possible heat sinks only three proved to be viable candidates for use in data acquisition. During preliminary data acquisition, heat sinks number 2 and 3 proved to be inadequate. Suspected internal microchannel blockages created increased inlet pressures that resulted in an increase in power supplied to the pump for a desired flow rate. The increased power exceeded the acceptable limits of the pump and resulted in the inability to achieve the desired flow rates. In addition to this, the increased pumping power required resulted in inadequate inlet plenum sealing creating an electrical hazard with the vacuum chuck. Heat sink number 4 was ultimately selected (by default) and used for data acquisition.

4.3 Heat Sink Modifications and Preparation for Data Acquisition

Prior to use in data acquisition, heat sink number 4 required several modifications. These modifications included: 1) heat sink sanding, 2) contact pad painting and 3) the application of a reference point.

4.3.1 Heat Sink Sanding

To eliminate fluid interaction between the microchannel exit and the jagged protrusions, a sanding process utilizing 120, 320 and 380 grit sandpaper in succession was employed to excise the unwanted silicon. 120 grit sandpaper was used for bulk silicon removal until the protrusions measured approximately 0.031 in (0.80 mm). As the protrusions approached the edge of the heat sink, finer grits of sandpaper were employed to reduce the risk of heat sink surface damage. 320 grit sandpaper was used for initial smoothing and less aggressive silicon removal until the protrusions were nearly flush with the heat sink edge. 380 grit sandpaper was used for final smoothing and shaping of the heat sink.

Upon sanding completion, the heat sink was soaked in deionized, distilled water for approximately 30 minutes. A rubber tipped syringe was used to force air through the inlet plenum and out the microchannel exit to remove any silicon particulate that may have accumulated as a result of the sanding process. The heat sink was removed from the deionized, distilled water and allowed to air dry. Figures 4.5 and 4.6 show digital photographs of an actual heat sink after sanding completion.

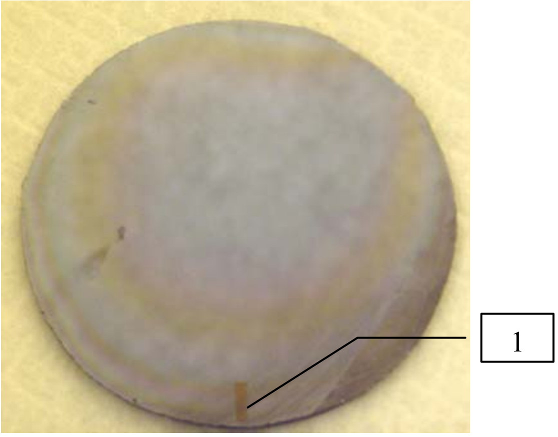

Figure 4.5 Heat sink top after sanding.
1 = Kapton® Tape

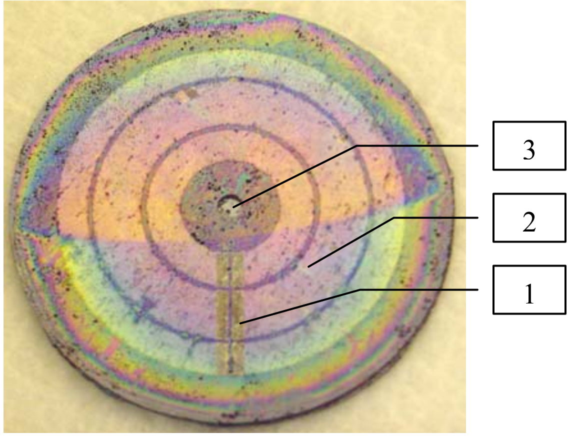

Figure 4.6 Heat sink bottom after sanding.
1 = Contact Pads
2 = Heater Ring
3 = Inlet Plenum

4.3.2 Contact Pad Painting

The heat sinks arrived from WTC with six rectangular areas, two per heater ring, designated as contact pads. Original heat sink design required the contact pads to be left uncoated with SiO_2 to allow electrical connection between the heat sink and the vacuum chuck pogo pins. Design calculations indicated that heater ring resistances were expected to be on the order of 25 Ω, 31 Ω and 65 Ω for the inner, middle and outer heater rings respectively. The calculated resistances were based upon the resistivity, thickness and length of the NiCr heater rings. Details of the heater ring resistance calculations are provided in Appendix G. Upon arrival from WTC, the heater ring resistances for heat sink number 4 were measured and found to be approximately 710 Ω, 712 Ω and 565 Ω for the inner, middle and outer heater rings respectively.

These measured resistance values exceeded the expected calculated resistance values by at least an order of magnitude. A magnified visual inspection revealed that the contact pad surface contained multiple, minute cracks and voids. It was discovered that significantly decreased heater ring resistance values could be measured depending upon the location of the multimeter measurement leads within the contact pad area.

The spatial dependence and variability of the measured resistance values led to the hypothesis that the contact pads were partially coated with SiO_2 during heat sink fabrication. It was further hypothesized that a conductive coating applied to the existing contact pad area would provide a path through the SiO_2 layer so the heater ring resistance value could be measured consistently over the entire contact pad area. Spatially dependent heater ring resistances were problematic due to the limited flexibility available for successful alignment of the contact pads with the pogo pins. To eliminate this spatial dependence, the periphery of the contact pad areas were masked off and a silver conductive paint was applied over the original contact pad areas. Figure 4.7 is a digital photograph of the heat sink after the application of silver conductive paint.

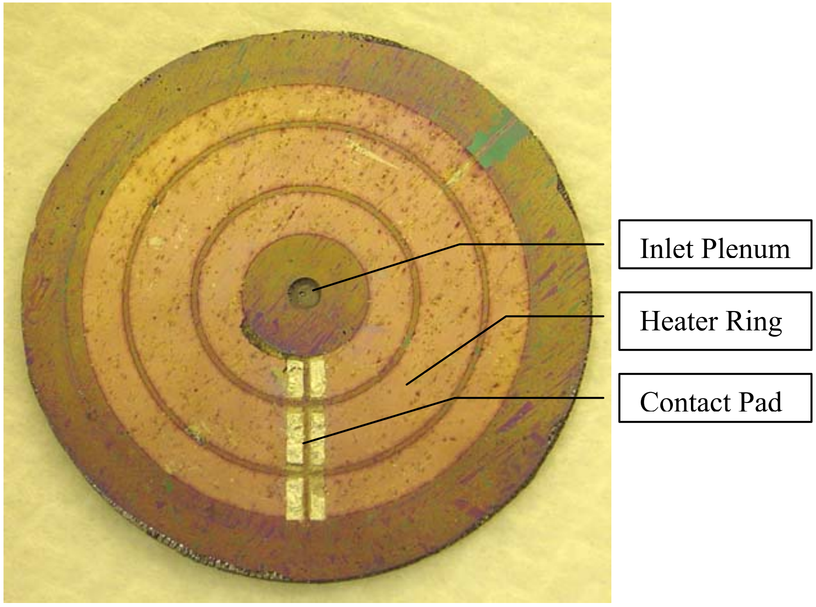

Figure 4.7 Heat sink after silver conductive paint application.

The silver conductive paint was allowed to dry for 24 hours and the heater ring resistances were measured to be 22 Ω, 25 Ω and 51 Ω for the inner, middle and outer heater rings respectively. These measured values were consistent, independent of spatial location and nearly matched the expected calculated resistances. The application of silver conductive paint over the original contact pad areas resulted in a decrease in the measured heater ring resistances and provided much needed flexibility with regard to alignment of the contact pads with the pogo pins. Complete details of the contact pad painting process are provided in Appendix H.

4.3.3 Reference Point Application

Successful data acquisition depended upon spatial accuracy and repeatability. To achieve this, a reference point on the heat sink was required to ensure data acquisition started and ended at the same spatial location repeatedly. Since no reference point was provided by the heat sink manufacturer, one was incorporated post fabrication. A rectangular piece of Kapton® tape measuring approximately 0.031 in x 0.188 in (0.79 mm x 4.76 mm) was adhered to the heat sink top surface opposite of the heat sink contact pads, see Fig. 4.8. Kapton® tape was selected for its high operating temperatures.

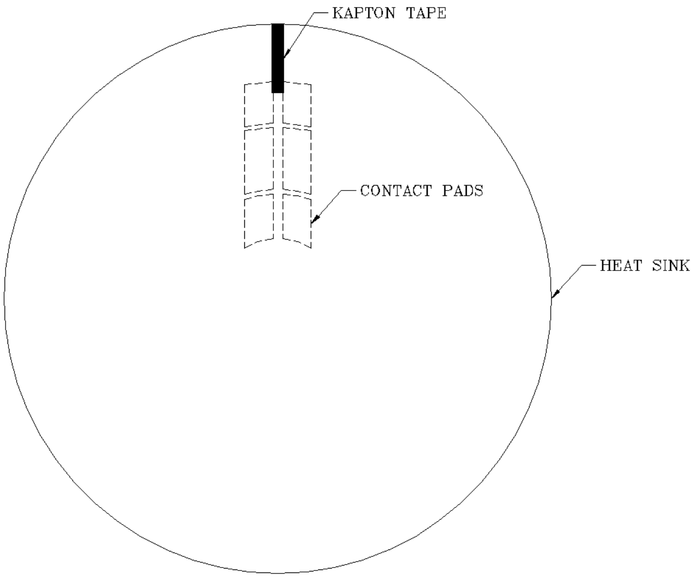

Figure 4.8 Kapton® tape placement.

With the sanding, contact pad painting and reference point application complete, heat sink number 4 was finally ready for data acquisition.

5 Radiation Analysis

The effective use of IRT to measure channel surface temperatures in a heat sink of this design requires isolation of the radiation emitted by the gold layer/microchannel top wall. The gold layer was the focal plane on which the IR camera was focused during data acquisition. Figure 5.1 illustrates a section view of the heat sink denoting the gold layer/focal plane where radiation intensity measurements were taken.

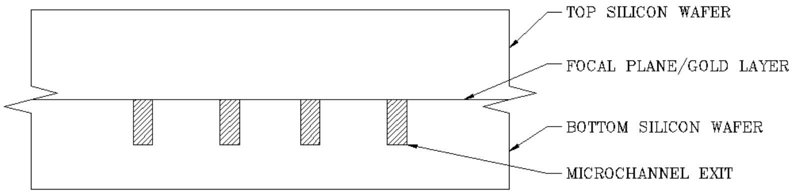

Figure 5.1 Heat sink gold layer/focal plane.

Classical radiation theory was used to identify the components contributing to 1) the total radiant flux emitted by the heat sink, 2) the total radiation sensed by the detector and 3) the effect of the anti-reflective coating. Figure 5.2 illustrates a schematic of the IR camera, microscope objective, the heat sink and various thermal energy contributions to the total intensity sensed by the detector array.

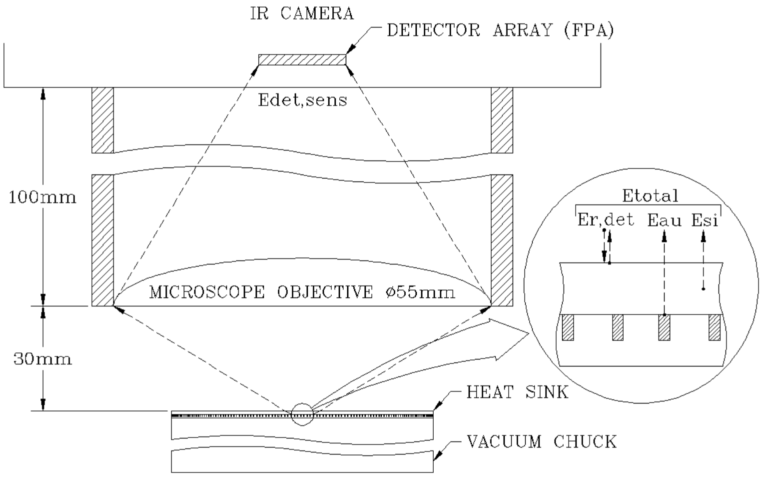

Figure 5.2 Total radiation sensed by the detector.

The IR camera consists of a 256 x 256 focal plane array that detects photons in the wavelength bands of 3.5-4.1 μm and 4.5-5.1 μm. The microscope objective with a 30 mm fixed focal distance provided a field of view (FOV) measuring 2.56 mm x 2.36 mm. The 2.56 mm x 2.36 mm FOV translated into a 256 pixel x 236 pixel FOV with a 10 μm/pixel resolution. This resulted in radiation intensity measurements at 60,416 locations within the camera field of view at an instant in time. The thermal energy contributions to the total intensity sensed by the detector array ($E_{r,det}$, E_{Au}, E_{Si}) are discussed in detail in Sections 5.1 and 5.2.

5.1 Radiant Flux Emitted by the Heat Sink

The total radiant energy flux emitted by the heat sink consisted of three main components: 1) the radiation emitted by the gold layer (E_{Au}) as a result of its elevated temperature, 2) the radiation emitted by the top silicon wafer (E_{Si}) as a result of its elevated temperature and 3) the reflected radiation incident upon the top silicon wafer from the detector itself ($E_{r,det}$). Mathematically the total emitted radiant energy flux was represented by Equation 5.1.

$$E_{total} = E_{Au} + E_{Si} + E_{r,det} \qquad 5.1$$

Using Stefan-Boltzmann's law for radiation emitted by a blackbody and the definition of the total hemispherical emissivity of a real surface, the total radiant flux emitted by the gold layer and the top silicon wafer, due to elevated temperatures were defined as

$$E_{Au} = \overline{T}_{Si} \varepsilon_{Au} \sigma T_{Au}^4 \qquad 5.2$$

$$E_{Si} = \varepsilon_{Si} \sigma T_{Si}^4 \qquad 5.3$$

where $\overline{T}_{Si}$ was the net transmittance of silicon to radiation emitted by the gold layer at the gold silicon interface, ε_{Au} and ε_{Si} were the total hemispherical emissivity of gold and silicon respectively, σ was the Stefan-Boltzmann constant and T_{Au} and T_{Si} were the temperature of the gold layer and top silicon wafer respectively. The total reflected radiation incident upon the top silicon wafer from the detector was defined as

$$E_{r,det} = R_{Si} G_{det} \tag{5.4}$$

where R_{Si} was the total reflectance of the top silicon wafer and G_{det} was the radiant flux incident upon the top silicon wafer from the detector. Substituting Equations 5.2, 5.3 and 5.4 into 5.1 gives the total radiant energy flux emitted by the heat sink as

$$E_{total} = \overline{T}_{Si} \varepsilon_{Au} \sigma T_{Au}^4 + \varepsilon_{Si} \sigma T_{Si}^4 + R_{Si} G_{det} \tag{5.5}$$

The total radiant flux emitted by the top silicon wafer (the second term on the right hand side of Equation 5.5) was eliminated by assuming the following; 1) the temperature variation along the depth of the top silicon wafer was negligible and 2) the absorption coefficient through the top silicon wafer was constant. The relatively high thermal conductivity of silicon, approximately 100-150 W/m K, [42] and the small thermal path length through the top silicon wafer, 500 μm, allowed the assumption that the temperature variation along the depth of the top silicon wafer could be considered negligible. A negligible temperature variation led to the assumption that the absorption coefficient through the top silicon wafer could be considered constant. In order to evaluate the total radiant flux emitted by the top silicon wafer, the transmittance of radiation through the top silicon wafer (τ_{Si}) was given by Siegel and Howell to be [44].

$$\tau_{Si} = e^{(-a_{Si} t_{Si} / \cos\varphi)} \tag{5.6}$$

where a_{Si} was the bulk absorption coefficient for silicon, t_{Si} was the thickness of the top silicon wafer and φ was the angle of incidence. The bulk absorption coefficient for silicon in the detector wavelength bands of 3.5-4.1 μm and 4.5-5.1 μm was 4.2×10^{-4} cm^{-1} [31]. The thickness of the top silicon wafer was 500 μm. Substituting these values into Equation 5.6 and assuming normal incidence ($\varphi = 0$) resulted in the transmittance of radiation through the top silicon wafer being equal to 1 ($\tau_{Si} = 1$). If $\tau_{Si} = 1$, then the absorbance and emittance of the top silicon wafer were all equal to 0. Ultimately, the radiation emitted by the top silicon wafer (the second term on the right hand side of Equation 5.5) was considered negligible.

The reflected radiation incident upon the top silicon wafer from the detector (the third term on the right hand side of Equation 5.5) was also eliminated. The actual detector or the focal plane array was cooled to 77 K during operation. With this operating temperature, the radiation emitted by the detector was negligible when compared to the operating temperature range of the heat sink, which corresponded to 298 K-398 K. In addition to this, a silicon nitride anti-reflective coating minimized reflected radiation from the top silicon wafer. Ultimately, the reflected radiation incident upon the top silicon wafer from the detector (the third term on the right hand side of Equation 5.5) was considered negligible. Ultimately, Equation 5.5 reduced to

$$E_{total} = E_{Au} = \overline{T}_{Si}\varepsilon_{Au}\sigma T_{Au}^4 \qquad 5.7$$

where the total radiant energy flux emitted by the heat sink was dominated solely by the radiation emitted by the gold layer (E_{Au}).

5.2 Radiant Flux Sensed by the Detector

The IR opaque, gold layer of the heat sink provided a non-transmissive microchannel surface upon which radiation intensity measurements could be taken. Therefore, unfocused background radiation from the heater rings or the fluid did not bias the desired intensity measurements. The actual radiation intensity detected by each individual sensor in the focal plane array varied from sensor to sensor due to: 1) variations in the configuration factor between the heat sink and the focal plane array, 2) variations in the type of radiation emitted by the gold layer, such as diffuse, normal or specular, 3) noise from the IR camera optics, 4) unfocused radiation incident upon the focal plane array from the IR camera and lens walls resulting from surrounding temperature variations, 5) reflected surrounding radiation incident upon the heat sink and 6) the participating medium between the IR camera and the heat sink [3,19].

The unfocused radiation incident upon the focal plane array from the IR camera and lens walls resulting from surrounding temperature variations was neglected based on the fact that both the IR camera and lens were calibrated by the manufacturer. It was also assumed that the manufacturer minimized this noise through careful design of the IR camera itself. The reflected surrounding radiation incident upon the heat sink was considered negligible since the configuration factor from the surroundings to the heat sink was on the order of 10^{-4}. Any variation in detected radiation intensity due to the participating medium between the IR camera and heat sink was considered negligible since the distance between the heat sink and the lens was small, 30 mm, and the IR camera optics incorporated filters to mitigate the effects of atmospheric CO_2 and H_2O vapor emissions. [3,19].

Ultimately, the variations in the detected radiation intensity by each individual sensor in the focal plane array only varied due to: 1) variations in the configuration factor between the heat sink and the focal plane array, 2) variations in the type of radiation emitted by the gold layer and 3) noise from the IR camera optics. Combining all these contributions into one correction factor (C), the radiation intensity actually sensed by the detector ($E_{det,sens}$) was expressed as

$$E_{det,sens} = CE_{total} = C\overline{T}_{Si}\varepsilon_{Au}\sigma T_{Au}^{4} \qquad 5.8$$

5.3 Anti-Reflective Coating.

To ensure accurate intensity measurements using IRT, the radiation incident upon the detector from the gold layer, needed to be maximized while reflections from the top silicon wafer needed to be minimized. The use of an anti-reflective coating reduced the overall reflectance of the top Si wafer and resulted in thermal noise minimization, overall transmittance enhancement and ultimately, increased the desired signal intensity.

Calculations of silicon overall reflectance with a single and double layer thin film anti-reflective coating were performed for varying film thicknesses of SiO_2 and Si_3N_4. SiO_2 and Si_3N_4 were the only materials available to WTC for use as anti-reflective coatings. The general equations necessary to describe the theory of multilayer thin films were based on the transfer matrix approach described in Pedrotti [45]. Complete detailed calculations of the overall reflectance of silicon for both a single layer ARC and a double layer ARC are provided in Appendix A. Consider the reflection of a non-normal, incident, radiation beam upon both a single and double layer thin film anti-reflective coating as illustrated in Figs. 5.3 and 5.4.

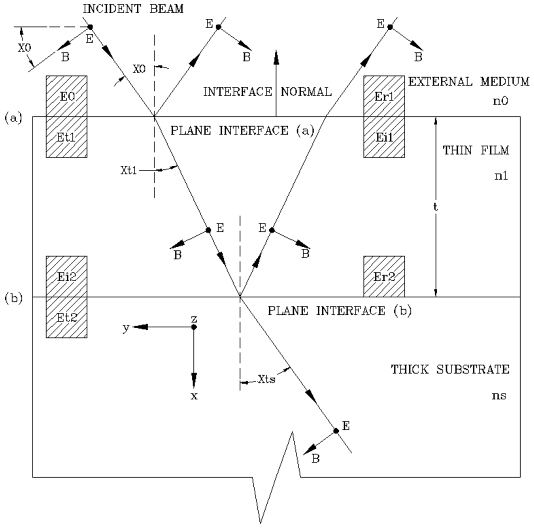

Figure 5.3 Single layer ARC schematic.

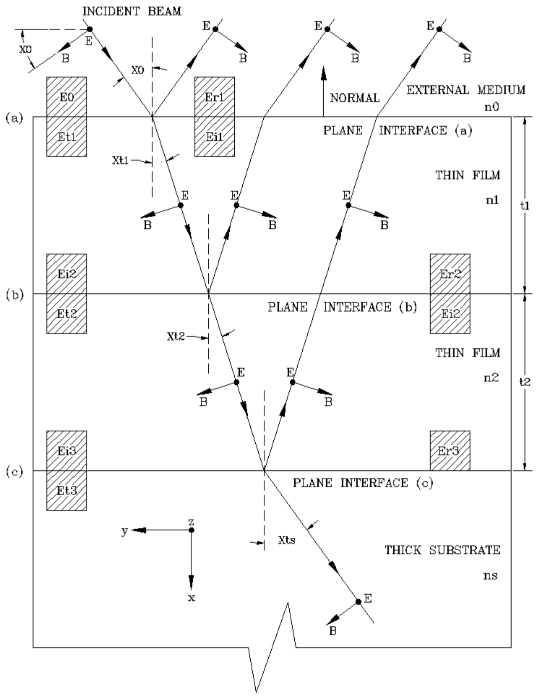

Figure 5.4 Double layer ARC schematic.

The single and double layer anti-reflective coatings were deposited directly on a thick Si substrate. In the case of the single layer thin film anti-reflective coating, the incident radiation beam first encounters plane interface (a) that separates the external medium from the thin film. At plane interface (a), a portion of the incident beam is externally reflected and a portion is refracted and transmitted through the thin film to plane interface (b). Plane interface (b) separates the thin film from the thick substrate. At plane interface (b), a portion of the transmitted beam is internally reflected and a portion is refracted and transmitted into the thick substrate. The internally reflected beam at plane interface (b) is transmitted back through the thin film to plane interface (a) where it is internally reflected, refracted and transmitted to the external medium. A non-normal, incident, radiation beam upon a double layer thin film anti-reflective coating behaves in the same manner as described above with the addition of internal reflection, refraction and transmission at plane interface (c) to account for the second thin film layer.

In Figs. 5.3 and 5.4, E is the electric field vector, B is the magnetic field vector and n_0, n_1 and n_s represent the refractive indices of the external medium, thin film and thick substrate, respectively. The case of normal incidence was assumed for all calculations and results for the total reflectance of a single thin film of SiO_2 and Si_3N_4 are shown in Figs. 5.5 and 5.6 as a function of wavelength for varying film thicknesses.

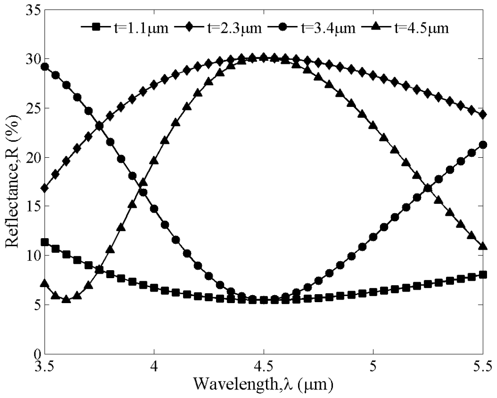

Figure 5.5 Overall, normal, spectral reflectance for a single ARC of SiO_2.

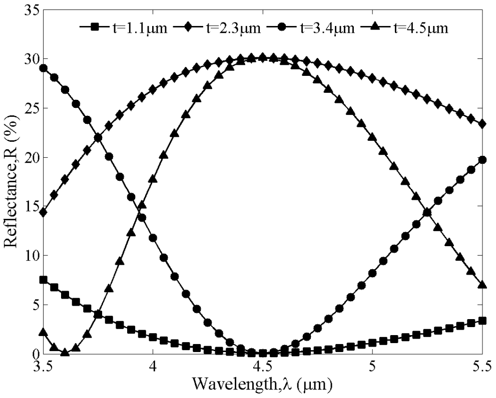

Figure 5.6 Overall, normal, spectral reflectance for a single ARC of Si_3N_4.

Each curve in Figs. 5.5 and 5.6 corresponds to a different thickness of anti-reflective coating. Notice that for both SiO_2 and Si_3N_4, a film thickness of 1.1 μm resulted in the minimum overall reflectance for both detector bandwidths of 3.5-4.1 μm and 4.5-5.1 μm. A single ARC of SiO_2 resulted in an overall reflectance of 7% to 12% in the detector bandwidths, while a single ARC of Si_3N_4 resulted in an overall reflectance of 2% to 8% in the detector bandwidths.

Figure 5.7 illustrates typical reflectance curves from the double layer thin film anti-reflective coating calculations. The single layer ARC results revealed, a film thickness of 1.1 μm minimized overall, normal, spectral reflectance. Therefore, in the double layer ARC calculations one film thickness was held constant at 1.1 μm while the other film thickness was varied.

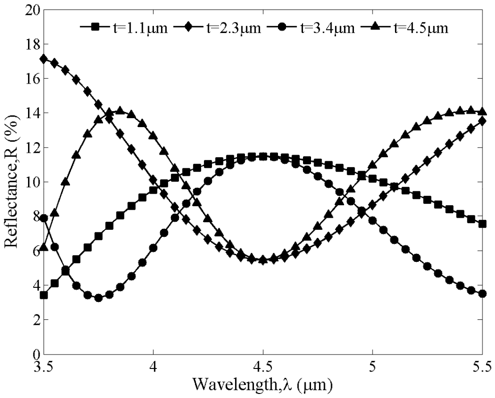

Figure 5.7 Overall, normal, spectral reflectance for a double layer ARC.

The results presented in Fig. 5.7 are for a double layer ARC corresponding to a top layer of SiO_2 fixed at 1.1 μm thick and a bottom layer of Si_3N_4 whose thickness varied from 1.1-4.5 μm. Notice that the overall, normal, spectral reflectance values vary from approximately 3% to 17% in the detector bandwidths. Additional results from the double layer thin film anti-reflective coating calculations are provided in Appendix A. The double layer ARC results indicated there was no unique combination of SiO_2 and Si_3N_4 film thickness that yielded a minimum reflectance, over both detector bandwidths, less than the minimum reflectance calculated for a single thin film. Based on this indication, a single thin film of Si_3N_4 1.1 μm thick was selected as the anti-reflective coating.

6 IRT Imaging Facility

Calibration and experimental data acquisition were achieved through the use of an IRT imaging facility. A schematic of the IRT imaging facility is illustrated in Fig. 6.1. The IRT imaging facility consists of the following components: 1) an IR camera, 2) a microscope objective, 3) a camera stand, 4) a vertical (z-direction) micro-traverse stage (VMTS), 5) a leveling platform, 6) a horizontal (x and y-direction) micro-traverse stage (HMTS), 7) an x-direction stepper motor driver, 8) a y-direction stepper motor driver, 9) an x-direction waveform generator, 10) a y-direction waveform generator, 11) a SCB 68 data acquisition (DAQ) card and 12) a computer with LabVIEW^{TM}.

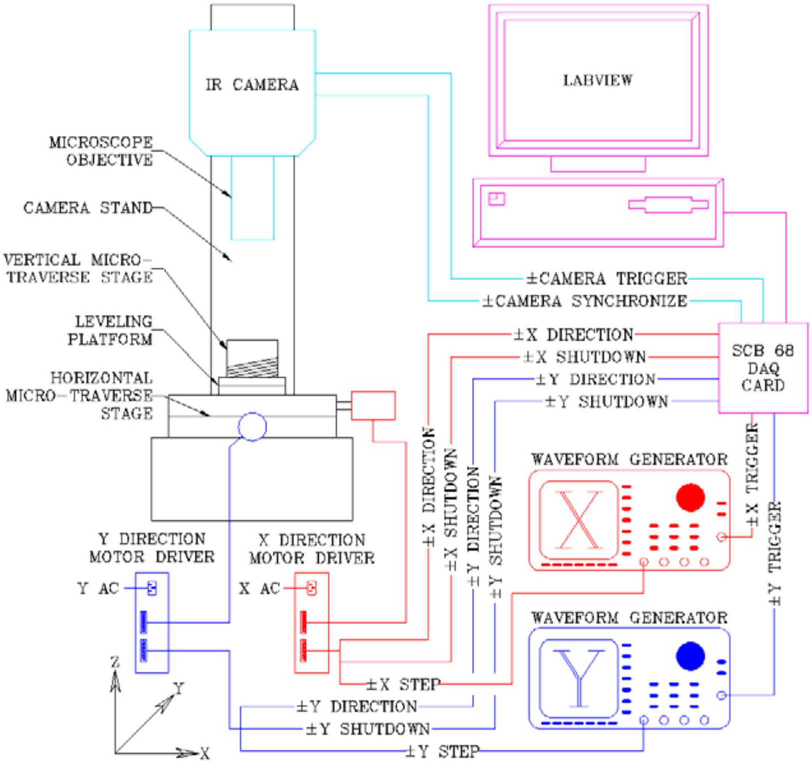

Figure 6.1 IRT imaging facility.

The IR camera (including microscope objective) and the horizontal micro-traverse stage bolted directly to the camera stand. The leveling platform bolted to the horizontal micro-traverse stage. The vertical micro-traverse stage bolted to the leveling platform.

During data acquisition the test section bolted directly to the vertical micro-traverse stage. The IR camera was wired to the SCB 68 DAQ card. The horizontal micro-traverse stage was wired to the x and y direction stepper motor drivers. The x and y direction stepper motor drivers were wired to the x and y direction wave form generators as well as the SCB 68 DAQ card. Detailed wiring connections at the stepper motor drivers, waveform generators, IR camera and the SCB-68 DAQ card are provided in Appendix E.

The IR camera detected radiation in two separate mid-range wavelength bands of 3.5-4.1 μm and 4.5-5.1 μm. The camera consisted of a front illuminated 256 x 256 Indium Antimonide (InSb) focal plane array of photovoltaic-type detectors cryogenically cooled to 77 K to ensure high sensitivity and low noise measurement. The microscope objective with a 30 mm fixed focal distance provided a field of view (FOV) measuring 2.56 mm by 2.36 mm. The 2.56 mm by 2.36 mm FOV translated into a 256 pixel by 236 pixel FOV with a 10 μm/pixel resolution. Radiation intensity distributions could be recorded at a maximum rate of 120 frames/sec. The x and y-direction stepper motor drivers, set to 0.1 μm/step resolution, required a step, direction and motor shutdown signal. The step signal was an externally triggered 1000 Hz, 2.5 V peap-peak square wave generated by two arbitrary waveform generators. The direction signal was a ± 5 V signal and the motor shutdown signal was a boolean on or off. IR camera triggering and synchronization, waveform generator triggering as well as stepper motor driver step, direction and motor shutdown were all controlled by a single LabVIEW^{TM} program through the SCB 68 DAQ card. The make, model and relevant specifications of each component comprising the IRT imaging facility are provided in Appendix E.

7 Calibration

The primary objective of IRT in this study was to obtain surface temperature measurements of the heat sink gold layer/microchannel top wall. This was achieved by utilizing Equation 5.8, where T_{Au} could be determined through knowledge of $E_{det,sens}$. The spatial dependence inherent in the thermal noise components (C), silicon refractive index (n_{Si}), gold layer emissivity (ε_{Au}) and gold layer temperature (T_{Au}) from one location to the next within the heat sink, as well as the difficulties associated with quantifying these factors analytically necessitated careful and accurate calibration of the heat sink over the operating temperature range at known temperatures.

With the heat sink attached to the experimental test section and flow loop (see Sections 8.1 and 8.2 for details), accurate temperature information was unknown except just upstream of the heat sink inlet. The inability to quantify, analytically or experimentally, the gold layer temperature under controlled flow conditions, made an in-situ calibration of the heat sink impossible. This led to the development of a separate calibration test section.

7.1 Calibration Test Section

Heat sink calibration was accomplished through the use of a calibration test section. A schematic of the calibration test section is illustrated in Fig. 7.1. The calibration test section provided a known temperature distribution at 0.063 in (1.59 mm) below the heat sink bottom surface and was used to determine a reference temperature to/against which the radiation intensities recorded by the IR camera were calibrated. The calibration test section consisted of the following components: 1) a copper cylinder, 2) cartridge heaters, 3) rigid cellular glass peripheral insulation, 4) Garolite G7 base insulation, 5) aluminum adaptor legs, 6) T-type thermocouples, 7) a dry interface thermal film, 8) a high conductivity thermal paste and 9) thermal stretch tape. Detailed fabrication drawings of the calibration test section components are provided in Appendix C. The make, model and relevant specifications of each component comprising the calibration test section are also provided in Appendix C.

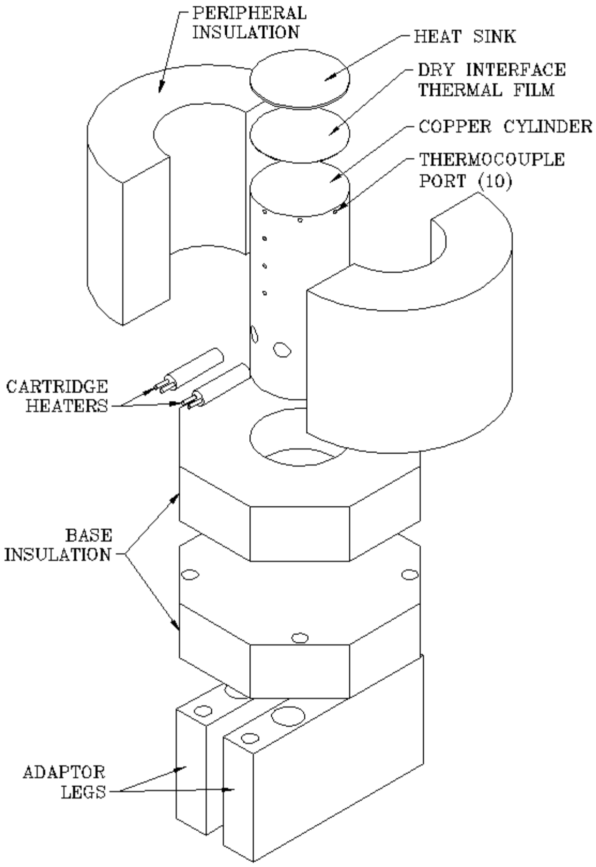

Figure 7.1 Calibration test section.

7.2 Calibration Test Section Assembly and Operation

The cartridge heaters were coated with a thin layer of OmegaTherm® 201 high conductivity thermal paste and press fit into the copper cylinder. The copper cylinder was then press fit into the Garolite G7 base insulation. The ten thermocouple ports were filled with OmegaTherm® 201 high conductivity paste and a 0.010 in (0.25 mm) bead diameter calibrated T-type thermocouple was inserted into each one. The wires of each thermocouple were wrapped around the copper cylinder to mitigate line loses. A layer of thermal stretch tape was applied to the copper cylinder to secure the thermocouple wires and provide a thin layer of insulation. Finally, the rigid cellular glass peripheral insulation was cut to length, placed around the copper cylinder and secured with a high adhesive grey film (aka duct tape).

The embedded cartridge heaters were wired for AC power and controlled using a variac. The heater voltage and current were measured and monitored using handheld Tektronix® DM 250 multimeters. The base and peripheral insulation facilitated one dimensional axial conduction within the copper cylinder. The temperature distribution within the copper cylinder was monitored and recorded, through LabVIEW™, utilizing ten T-type thermocouples. Three axial thermocouples and seven near surface thermocouples were wired directly to a National Instruments SCXI 1300 series cold-junction-compensated, high accuracy temperature module and to a National Instruments PCI-6220 data acquisition board via a SCXI 1000 chassis. Figure 7.2 illustrates a side view of the copper cylinder denoting the axial thermocouple depths and locations for clarity. Figure 7.3 illustrates a top view of the copper cylinder denoting the near surface thermocouple depths and locations for clarity.

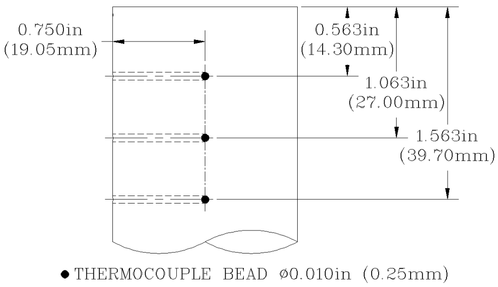

Figure 7.2 Axial TC location.

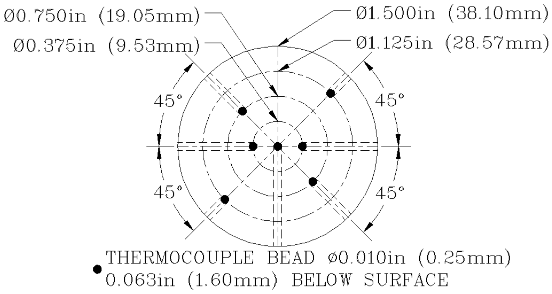

Figure 7.3 Near surface TC location.

The heat sink was placed on the end of the heated copper cylinder and calibrated at nominal temperatures of 25°C, 45°C, 65°C, 85°C, 105°C and 125°C. Micro-Faze® dry interface thermal film was utilized between the heat sink and copper cylinder surface to minimize contact resistance.

7.3 Calibration Data Acquisition Procedure

To acquire calibration data, the calibration test section (see Fig. 7.1) was bolted directly to the vertical micro-traverse stage of the IRT imaging facility (see Fig. 6.1). The camera stand was leveled using sheet metal shims and a bull's eye level. The ten T-type thermocouples embedded in the calibration test section were connected to the SCXI 1300 series cold-junction-compensated, high-accuracy temperature module.

The top surface of the calibration test section copper cylinder was cleaned with a cotton swab and isopropyl alcohol. A circular piece of Micro-Faze® A6 dry interface thermal film measuring approximately Ø1.500 in (38.10 mm), cut to match the copper cylinder and heat sink outer diameters, was applied to the copper cylinder. The heat sink bottom surface was cleaned with a cotton swab and isopropyl alcohol and placed on top of the Micro-Faze® thermal film. Light to moderate finger pressure (~ 5-10 psi, ~ 35-70 kPa) was applied to the heat sink to facilitate adhesion between the copper cylinder, Micro-Faze® thermal film and heat sink.

The calibration test section was leveled using a bull's eye level and the leveling platform of the IRT imaging facility. The heat sink top surface was then cleaned with a cotton swab and isopropyl alcohol. Voltage was applied to the cartridge heaters and the copper cylinder was heated until the near surface thermocouples measured a steady 135°C. The calibration test section was then allowed to cool to room temperature. Heating the calibration test section in this manner allowed total wetting between the copper cylinder, Micro-Faze® thermal film and heat sink thereby, minimizing contact resistance. After cooling to room temperature, voltage was applied to the cartridge heaters and the copper cylinder was heated until the near surface thermocouples measured a steady 25°C. Approximately three hours were required for the calibration test section to reach steady state.

Once steady state was reached, the IR camera and the LabVIEW™ calibration program were configured for data acquisition. The left and top edges of the IR camera field of view were aligned with the Kapton® tape right edge and heat sink circumferential edge, respectively. The IR camera was focused on the desired focal plane, the heat sink gold layer and the LabVIEW™ calibration data acquisition program was started. An outline listing the explicit chronological order and clarifying details of the calibration data acquisition procedure are provided in Appendix I.

Calibration radiation intensity measurements, in the form of IR images, were taken, at 60 frames per second, over the entire heat sink number 4 surface. A 1/2 field of view overlap in both the x and y direction was incorporated to mitigate intensity variations at the image edges due to the camera optics. This resulted in 1,152 individual images necessary to capture the entire heat sink surface. Figure 7.4 illustrates 1,152 IR camera fields of view, measuring 2.56 mm x 2.36 mm each, overlaid on the heat sink surface.

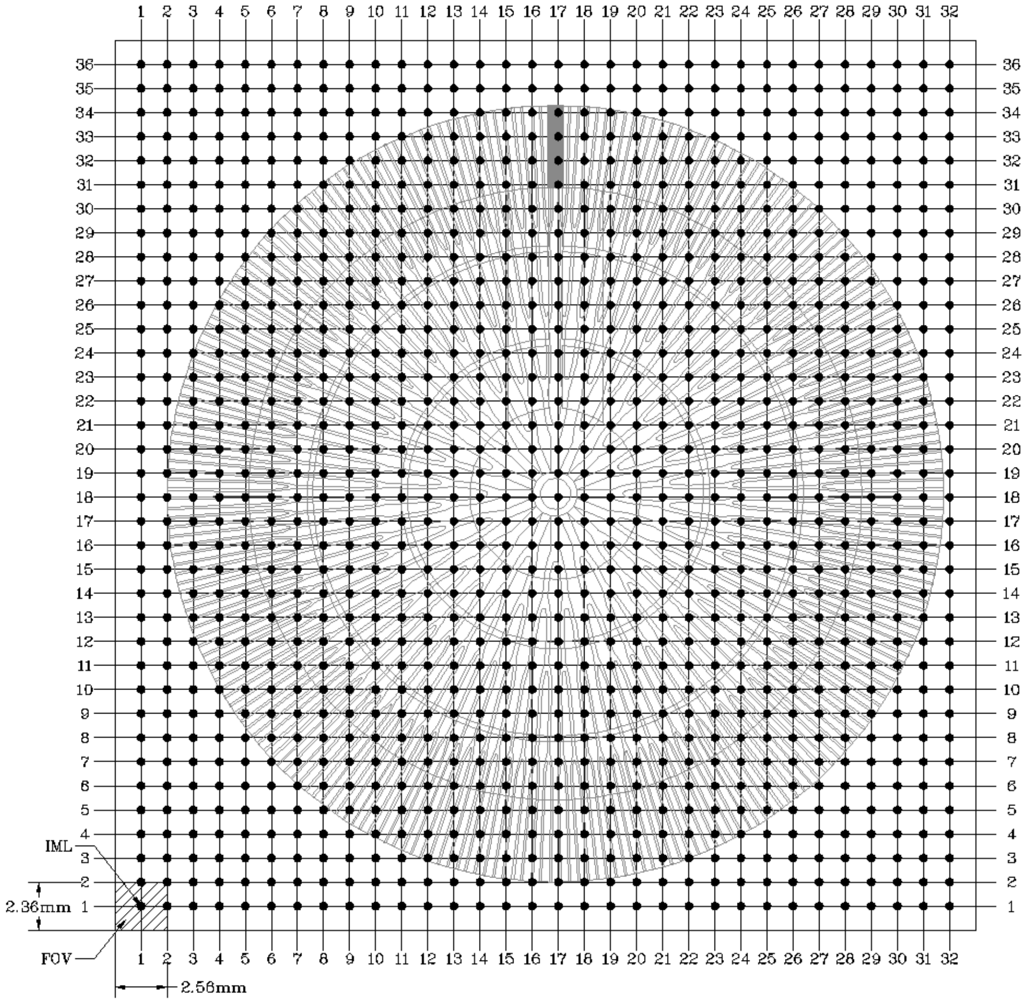

Figure 7.4 1,152 IR camera fields of view overlaid on the heat sink surface.

For clarity a solid circular node was placed in the center of each field of view and represents a physical position in space where calibration data were acquired. Positions where images were acquired are referred to as image locations (IML) and are numbered for data identification purposes. Figure 7.5 illustrates the calibration IML numbering.

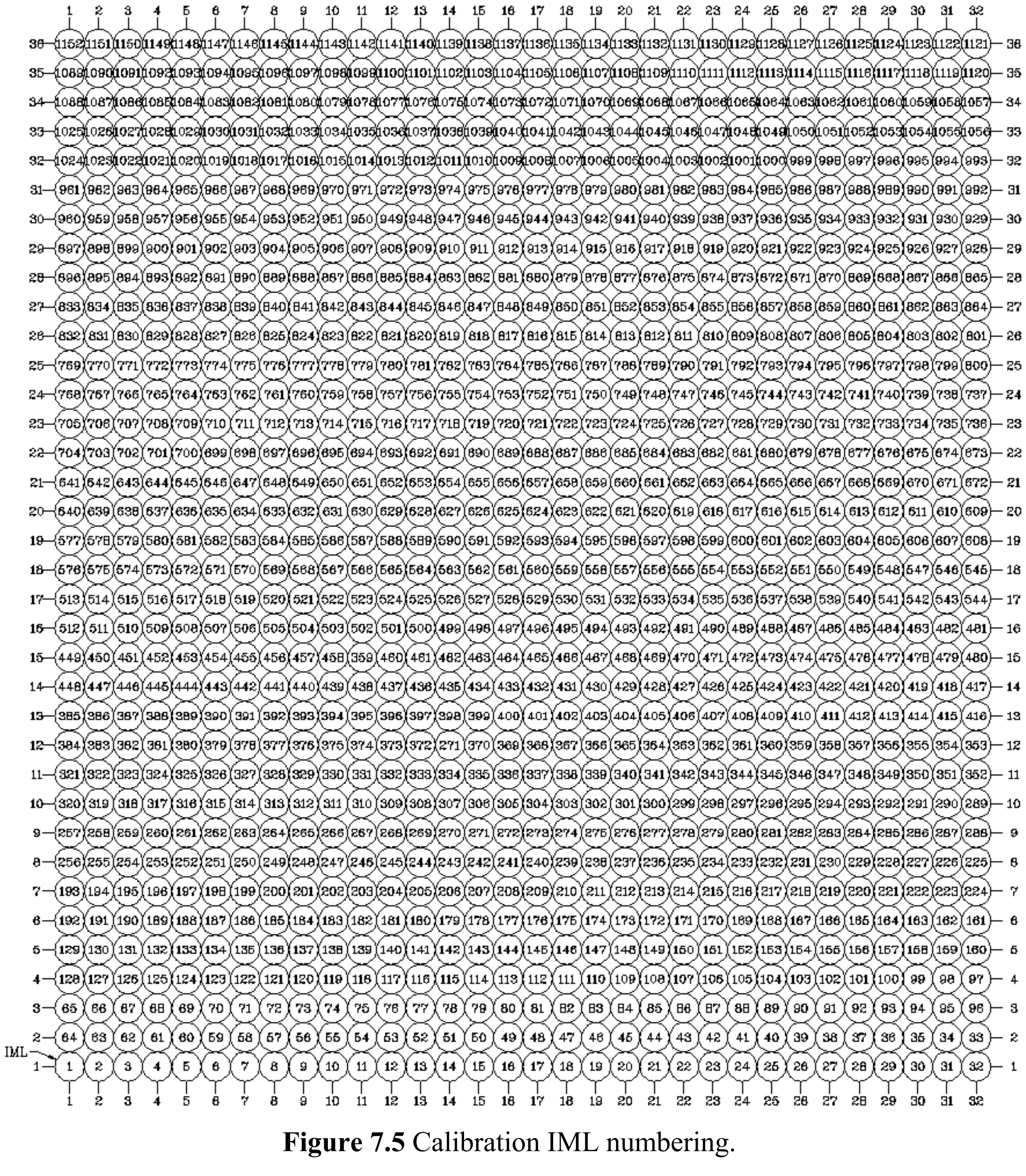

Figure 7.5 Calibration IML numbering.

Each numbered circle in Fig. 7.5 represents a single solid circular node/IML illustrated in Fig. 7.4. To relate a specific numbered IML to an actual physical location on the heat sink, Figs. 7.4 and 7.5 are meant to be used in conjunction. To this end, row and column numbers have been provided around the periphery of each figure.

A single calibration image, at six nominal calibration temperatures of 25°C, 45°C, 65°C, 85°C, 105°C and 125°C, was acquired at each of the 1,152 image locations illustrated in Fig. 7.5. The calibration temperatures were defined as nominal because, despite the fact time was provided for the calibration test section to reach steady state (> 3 hours per calibration temperature), the time required to acquire data (> 8 hours per calibration temperature) made it difficult to maintain a fixed temperature distribution within the calibration test section with negligible temporal and spatial fluctuations. In otherwords, from calibration IML 1 to calibration IML 1,152, the test section temperature would fluctuate about a nominal value during data acquisition. To account for temporal temperature fluctuations of the calibration test section, the temperature distribution within the copper cylinder was also recorded at each of the 1,152 image locations illustrated in Fig. 7.5. One hundred measurements from each of the ten T-type thermocouples at each image location were recorded at a sampling rate of 10 kHz. All calibration data were acquired through the calibration data acquisition LabVIEW^{TM} program (see Appendix K for program details). Figures 7.6-7.11 illustrate typical examples of radiation intensity images taken at each nominal calibration temperature.

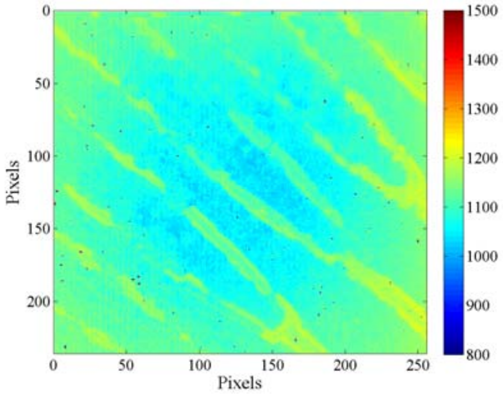

Figure 7.6 25°C calibration radiation intensity image (IML 824).

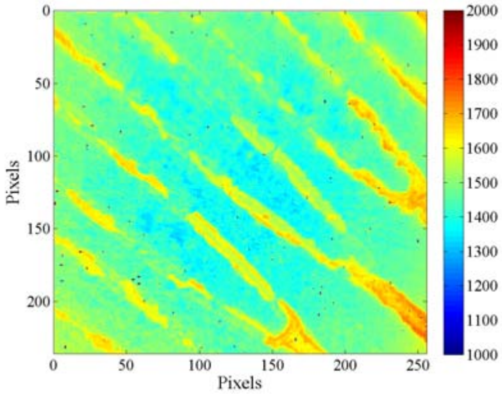

Figure 7.7 45°C calibration radiation intensity image (IML 824).

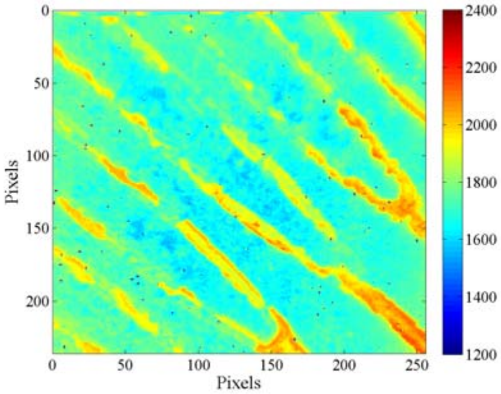

Figure 7.8 65°C calibration radiation intensity image (IML 824).

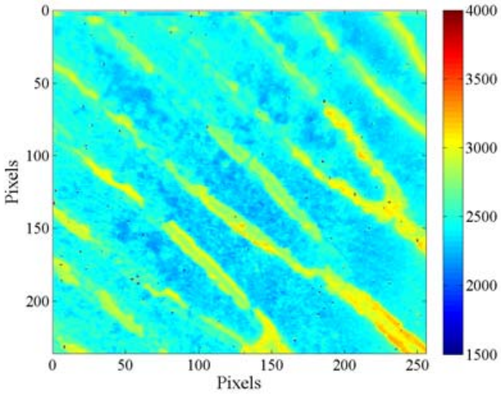

Figure 7.9 85°C calibration radiation intensity image (IML 824).

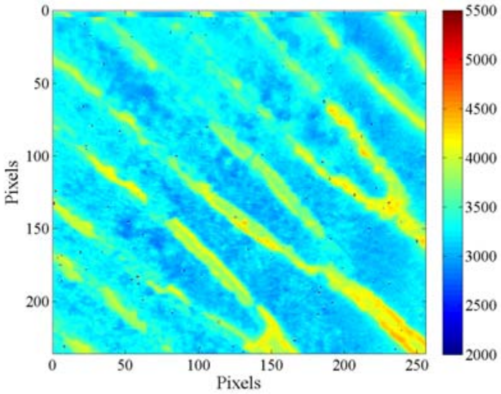

Figure 7.10 105°C calibration radiation intensity image (IML 824).

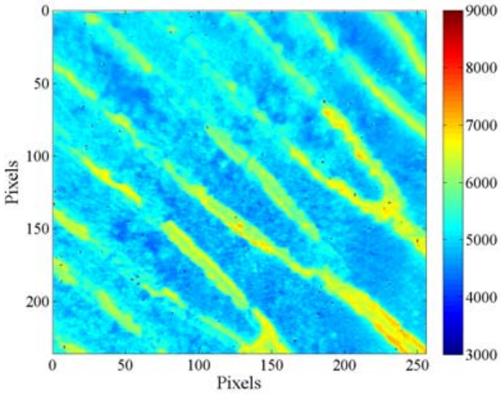

Figure 7.11 125°C calibration radiation intensity image (IML 824).

The calibration radiation intensity images illustrated in Figs. 7.6-7.11 were taken at image location 824, which corresponded to a bifurcation at the k=3 to k=4 branching level located in the upper left quadrant of the heat sink directly above the outer heater ring. Figure 7.12 illustrates the physical location of IML 824.

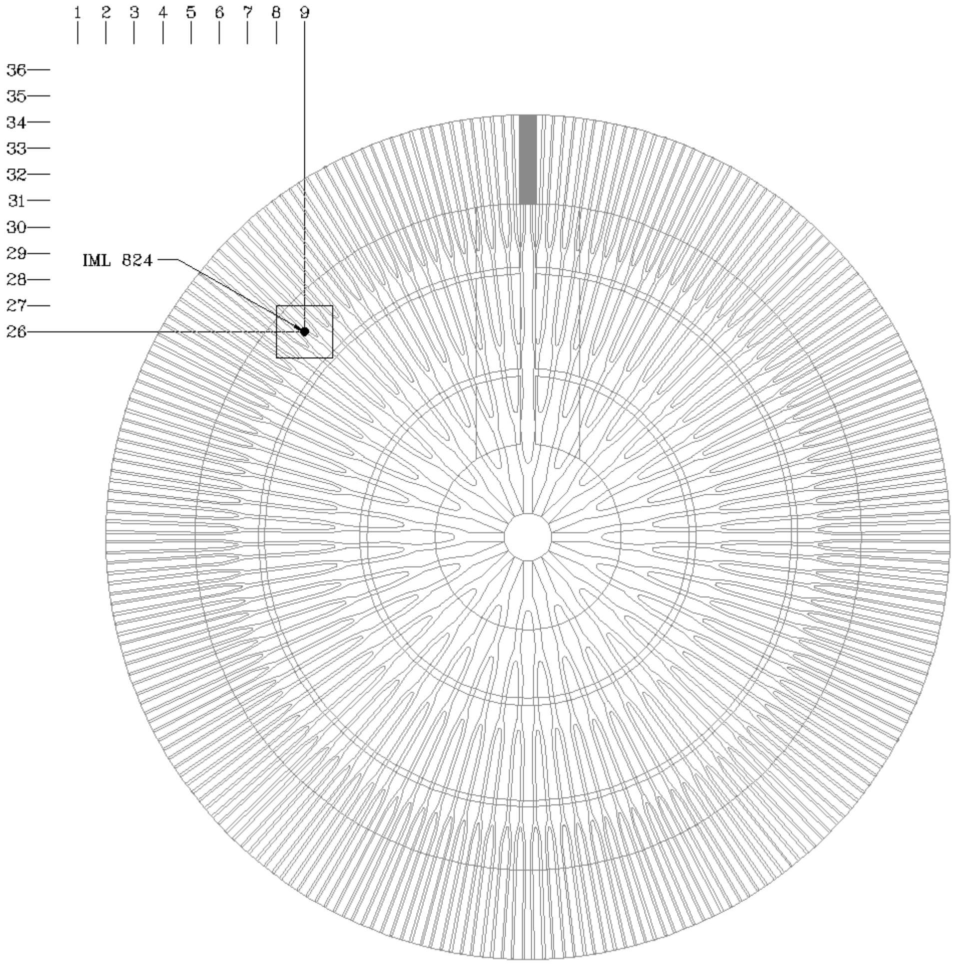

Figure 7.12 Physical location of IML 824.

Each calibration radiation intensity image in Figs. 7.6-7.11 measures 236 x 256 pixels and the contour color is in arbitrary units of the detector proportional to radiation intensity. Typical radiation intensity values range from 800-1500 at 25°C, 1000-2000 at 45°C, 1200-2400 at 65°C, 1500-4000 at 85°C, 2000-5500 at 105°C and 3000-9000 at 125°C. The fractal-like branching microchannel network top wall is clearly visible and represented by pixel coloration varying from green to red. The non-channel silicon substrate of the heat sink is also visible and represented by pixel coloration varying from blue to green.

Ideally, the intensity at all locations for a given calibration temperature would be uniform. However, the observed variations could result from non-uniform gold layer thickness. In addition to this, high intensity regions (indicated by red pixel coloration) within the channel walls are also observed. These high intensity regions exist due to fabrication defects during the gold-silicon eutectic bonding process that resulted in the absence of the gold layer at multiple random locations along the microchannel. The absence of a gold layer allows non-focused radiation from the heater rings and the working fluid to reach the detector array resulting in a localized intensity increase.

7.4 Data Organization and Identification

The quantity of calibration and experimental data expected required the development of an organizational system by which acquired data could be quickly and easily identified. A file naming scheme was developed to provide pertinent at-a-glance information as well as a unique identification number for both calibration and experimental data. Appendix N provides detailed information pertaining to the calibration and experimental data file naming schemes.

7.5 Calibration Data Reduction and Analysis

All intensity images obtained using the IRT imaging setup were output as a binary file with a header unique to the camera manufacturer. In this case, the IR images were binary files with an .iri extension. The manufacturer supplied software capable of processing .iri image files proved to be inadequate in efficiently handling large quantities of images. Software packages like Matlab® provided image processing, computational and analysis options exceeding those available through the manufacturer supplied software. For these reasons, Matlab® was used for all data reduction and analysis. Prior to data reduction and analysis, a file conversion was necessary to convert all raw intensity images from a binary .iri file to a .lvm ASCII text data file. This conversion was accomplished using an Infrared Image Processing LabVIEW™ program [46]. The converted files consisted of a single 236 x 256 numerical array of detector radiation intensity units easily read by Matlab®. The details of the file conversion LabVIEW™ program are provided in Appendix O.

The first step in calibration data reduction and analysis was the calculation of the overlapped average (OLA) intensity for a given image location. The OLA intensity was calculated directly from the converted calibration intensity images.

Incorporating a 1/2 field of view overlap in both the x and y direction during data acquisition resulted in each image sharing partial images with 8 neighboring images. To clarify consider the 9 adjacent images shown in Fig. 7.13. Figure 7.13 illustrates an image at location 824 and its 8 peripheral adjacent images at locations 776, 777, 778, 823, 825, 840, 841, and 842. Each image has been broken up into quadrants to illustrate the 1/2 field of view overlap. The partial image captured in the upper left quadrant of the image at location 824 has been captured in 3 adjacent images namely, the image at location 840, the image at location 841 and the image at location 825. Specifically, the upper left quadrant of IML 824 is spatially identical and common to the upper right quadrant of IML 825, the lower right quadrant of IML 840 and the lower left quadrant of IML 841.

A similar pattern is observed for the remaining quadrants of IML 824. The upper right quadrant of IML 824 is spatially identical and common to the lower right quadrant of IML 841, the lower left quadrant of IML 842 and the upper left quadrant of IML 823. The lower left quadrant of IML 824 is spatially identical and common to the upper left quadrant of IML 777, the upper right quadrant of IML 776 and the lower right quadrant of IML 825. Finally, the lower right quadrant of IML 824 is spatially identical and common to the lower left quadrant of IML 823, the upper left quadrant of IML 778 and the upper right quadrant of IML 777.

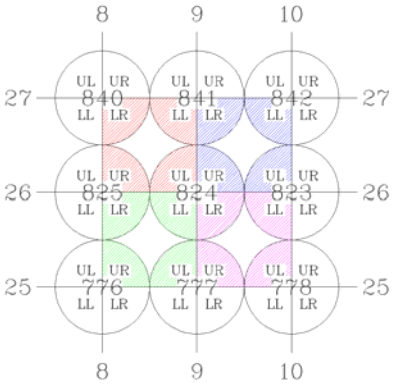

Figure 7.13 Spatially identical and common data for IML 824.

Ultimately, 4 intensity values for each pixel within a given image were acquired. The OLA intensity at a single image location was determined by computing the average of these four intensity values per pixel for each quadrant of the desired image location. OLA intensities were calculated at 255 individual image locations to completely visualize the entire heat sink surface. Figures 7.14 and 7.15 illustrate the locations where the calibration OLA intensities were calculated and the IML numbering.

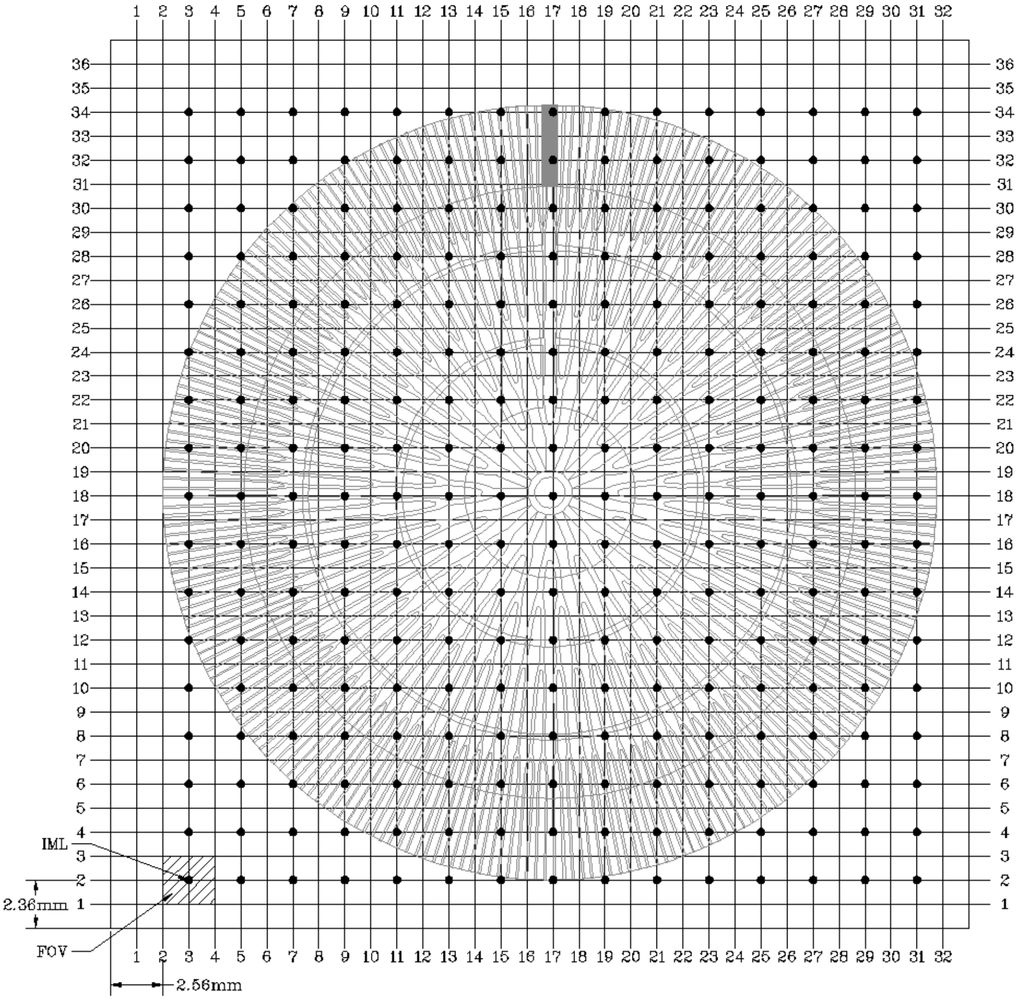

Figure 7.14 Calibration OLA intensity image locations.

The solid circular nodes in Fig. 7.14 indicate locations where overlapped averages were calculated.

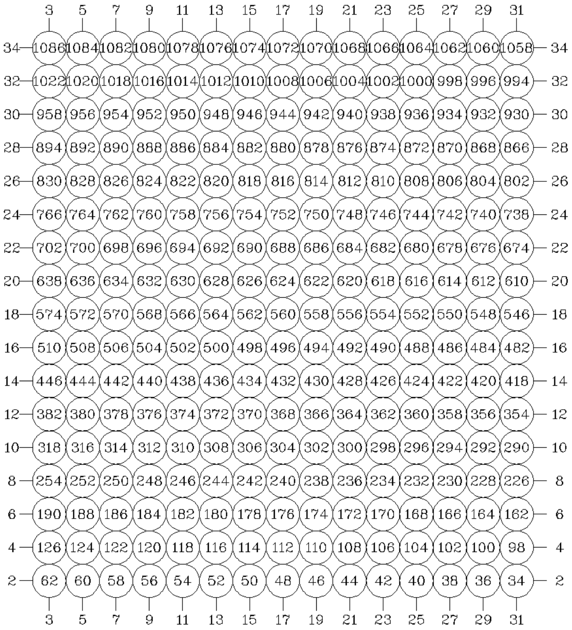

	3	5	7	9	11	13	15	17	19	21	23	25	27	29	31	
34	1086	1084	1082	1080	1078	1076	1074	1072	1070	1068	1066	1064	1062	1060	1058	34
32	1022	1020	1018	1016	1014	1012	1010	1008	1006	1004	1002	1000	998	996	994	32
30	958	956	954	952	950	948	946	944	942	940	938	936	934	932	930	30
28	894	892	890	888	886	884	882	880	878	876	874	872	870	868	866	28
26	830	828	826	824	822	820	818	816	814	812	810	808	806	804	802	26
24	766	764	762	760	758	756	754	752	750	748	746	744	742	740	738	24
22	702	700	698	696	694	692	690	688	686	684	682	680	678	676	674	22
20	638	636	634	632	630	628	626	624	622	620	618	616	614	612	610	20
18	574	572	570	568	566	564	562	560	558	556	554	552	550	548	546	18
16	510	508	506	504	502	500	498	496	494	492	490	488	486	484	482	16
14	446	444	442	440	438	436	434	432	430	428	426	424	422	420	418	14
12	382	380	378	376	374	372	370	368	366	364	362	360	358	356	354	12
10	318	316	314	312	310	308	306	304	302	300	298	296	294	292	290	10
8	254	252	250	248	246	244	242	240	238	236	234	232	230	228	226	8
6	190	188	186	184	182	180	178	176	174	172	170	168	166	164	162	6
4	126	124	122	120	118	116	114	112	110	108	106	104	102	100	98	4
2	62	60	58	56	54	52	50	48	46	44	42	40	38	36	34	2
	3	5	7	9	11	13	15	17	19	21	23	25	27	29	31	

Figure 7.15 Calibration OLA IML numbering.

Figures 7.16-7.21 illustrate examples of OLA calibration intensity images calculated at each nominal calibration temperature for image location 824.

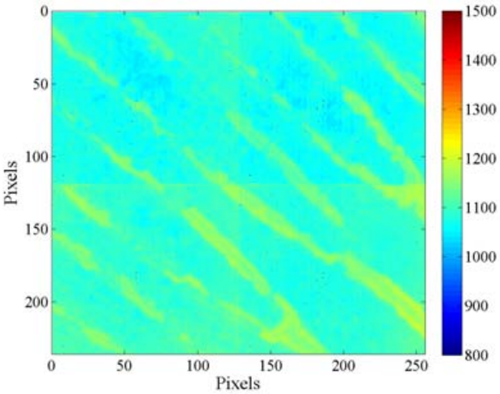

Figure 7.16 25°C OLA intensity (IML 824).

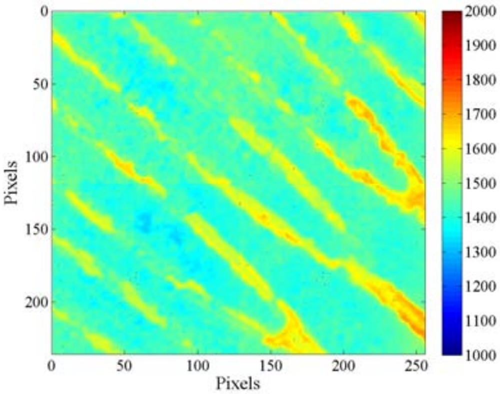

Figure 7.17 45°C OLA intensity (IML 824).

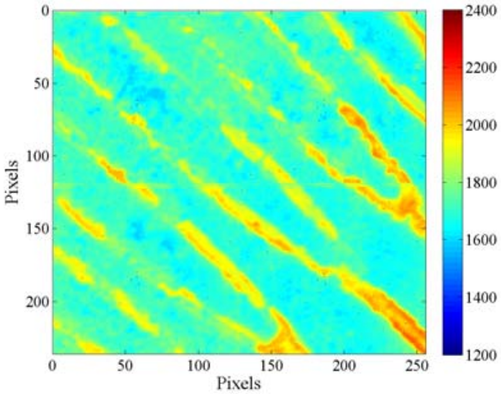

Figure 7.18 65°C OLA intensity (IML 824).

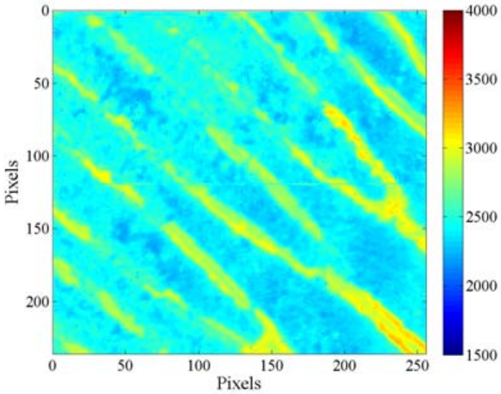

Figure 7.19 85°C OLA intensity (IML 824).

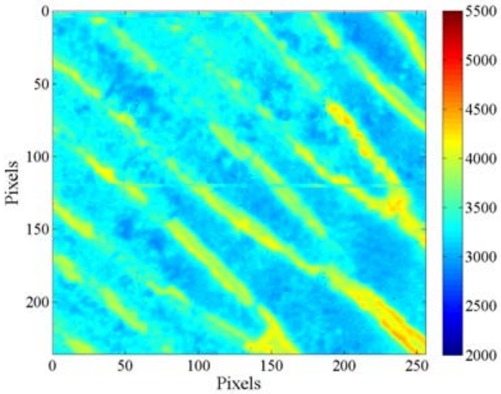

Figure 7.20 105°C OLA intensity (IML 824).

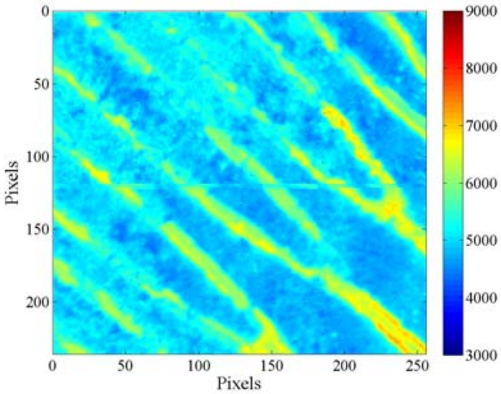

Figure 7.21 125°C OLA intensity (IML 824).

The 255 OLA intensities were pieced together to create a piecewise (PW) average intensity map of the entire heat sink surface. Figures 7.22-7.27 illustrate the PW average intensities of the entire heat sink surface at each nominal calibration temperature

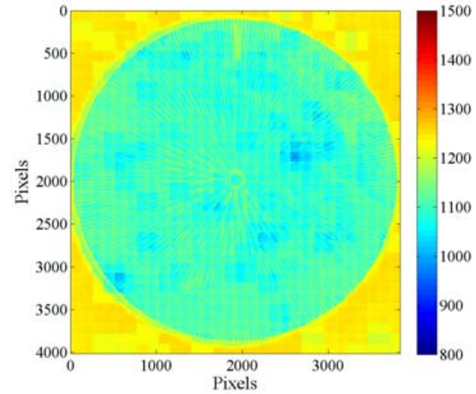

Figure 7.22 25°C PW OLA intensity map.

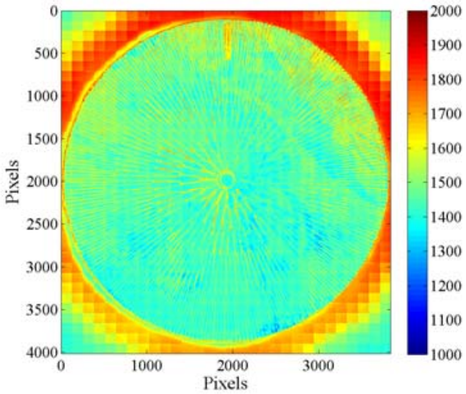

Figure 7.23 45°C PW OLA intensity map.

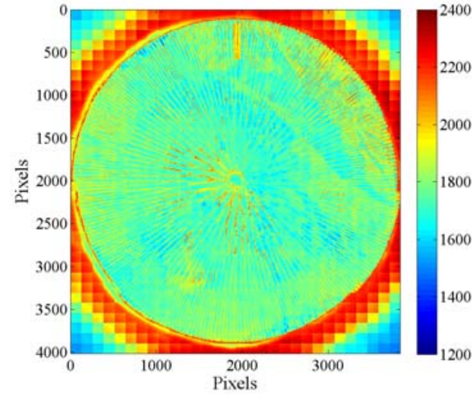

Figure 7.24 65°C PW OLA intensity map.

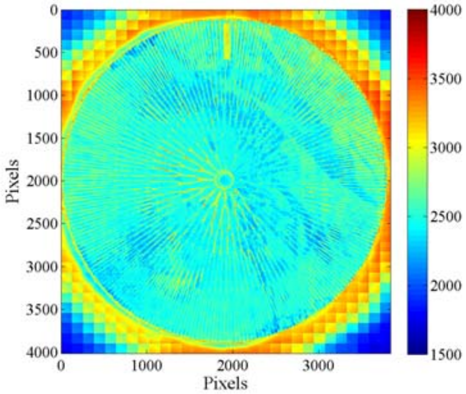

Figure 7.25 85°C PA OLA intensity map.

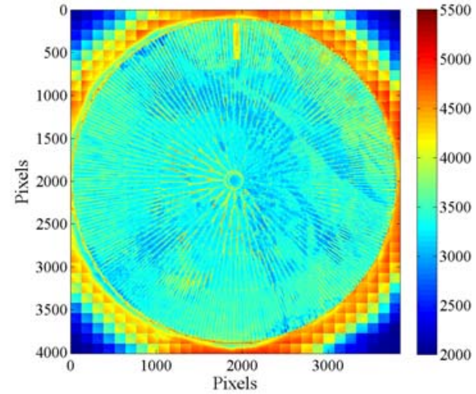

Figure 7.26 105°C PW OLA intensity map.

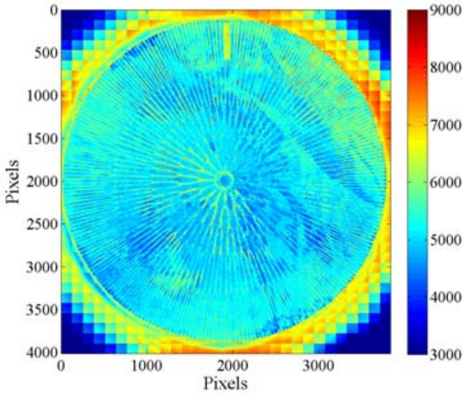

Figure 7.27 125°C PW OLA intensity map.

The calculation of the 255 OLA intensities and the creation of the heat sink surface PW OLA intensity maps was performed for each calibration temperature (25°C, 45°C, 65°C, 85°C, 105°C and 125°C) and accomplished using Matlab®. The details of the OLA intensity Matlab® program are provided in Appendix P. The details of the PW OLA intensity Matlab® program are provided in Appendix Q.

8 Experimental Facility

The experimental facility used to acquire flow data consisted of two main components: 1) the experimental test section and 2) the experimental flow loop.

8.1 Experimental Test Section

The experimental test section consisted of the following components: 1) a vacuum chuck, 2) a liquid reservoir and 3) a liquid reservoir cover. The vacuum chuck secured the heat sink in place during operation. Since flow exited the heat sink directly to atmosphere, a reservoir was required for liquid containment. To minimize vapor contact with the microscope objective during flow boiling, a reservoir cover, incorporating an optical access port, was utilized. The reservoir cover bolted directly to the liquid reservoir during data acquisition. Figure 8.1 illustrates an exploded view of the experimental test section components.

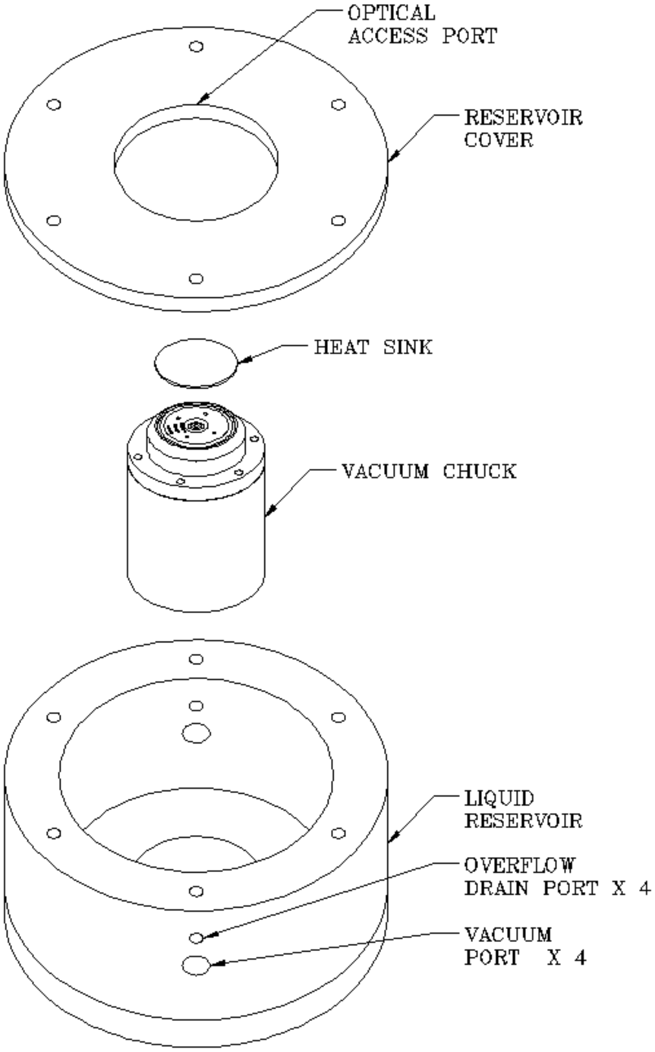

Figure 8.1 Experimental test section.

The vacuum chuck was press fit into the opening at the bottom of the liquid reservoir. The vacuum chuck bottom plane extended past the liquid reservoir bottom plane approximately 1.250 in (31.75 mm) to allow external access to the vacuum, flow inlet, and electrical wiring ports. During data acquisition, the heat sink was placed on top of the vacuum chuck (see Fig. 8.2) and held in place via a vacuum supplied by a pump. Six pogo pins contacted the heater ring contact pads and provided electrical connections to DC power supplies. Flow entered the vacuum chuck through an inlet port at the bottom and two silicone o-rings (inner and outer) provided a liquid seal between the vacuum chuck and the heat sink. The o-rings also guarded against any electrical hazard by preventing the inlet flow from contacting the pogo pins during flow loop operation.

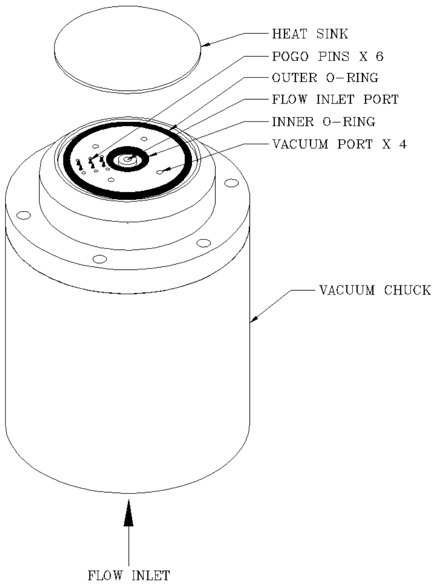

Figure 8.2 Vacuum chuck.

Note the experimental test section and vacuum chuck used in this study were designed and fabricated by Brian Daniels and Rebecca Cullion, both former graduate students at Oregon State University.

8.2 Experimental Flow Loop

The experimental flow loop consisted of the following components: 1) a hot water heater, 2) a pump, 3) an inlet filter, 4) an inlet mass flow meter, 5) a constant temperature oil bath, 6) the experimental test section and 7) an outlet mass flow meter. A schematic of the flow loop is provided in Fig. 8.3.

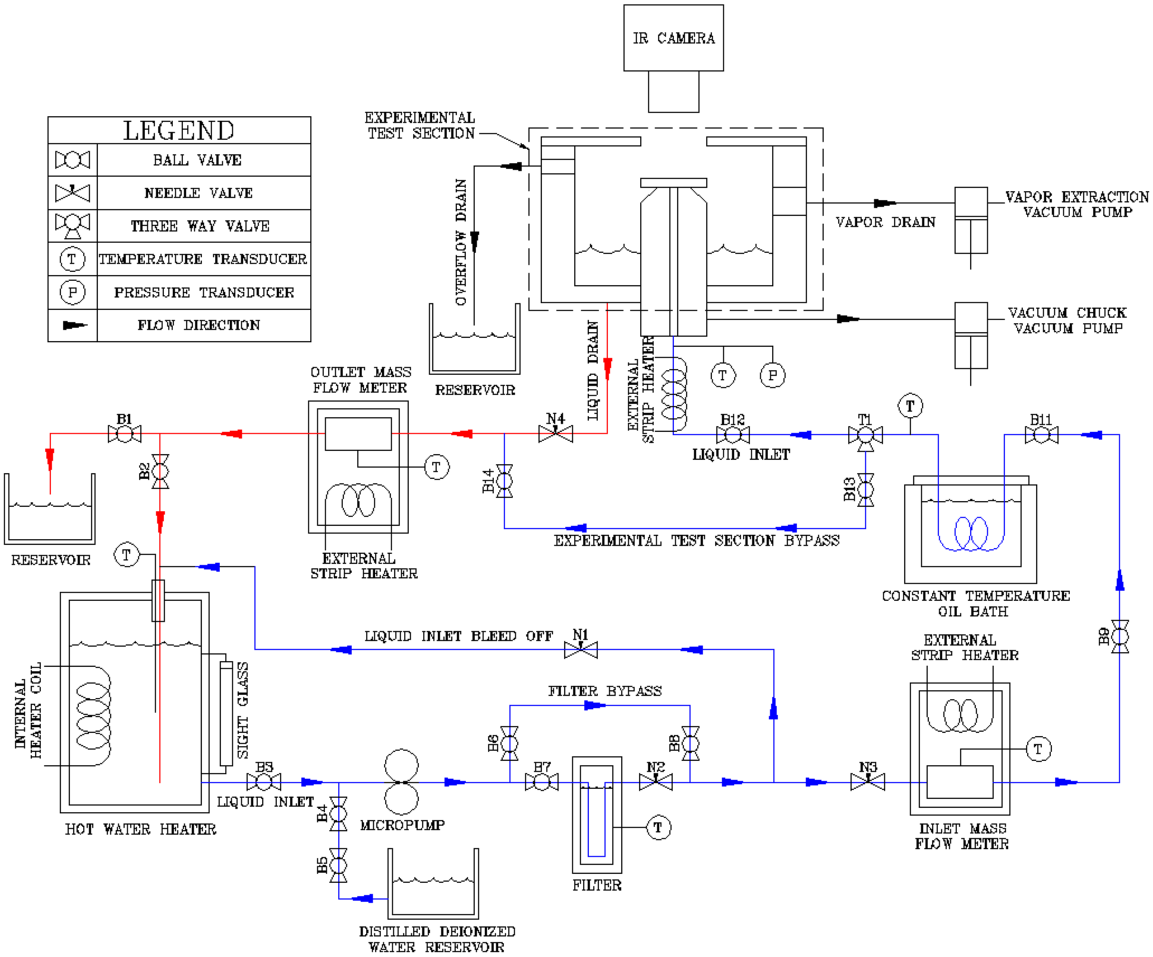

Figure 8.3 Experimental flow loop schematic.

Distilled, deionized, degassed water was preheated to a desired temperature in the hot water heater. The water was pumped from the hot water heater through a filter, inlet mass flow meter and constant temperature hot oil bath prior to reaching the experimental test section. Water flowed through the vacuum chuck and into the heat sink. Water exiting the heat sink collected in the liquid reservoir and drained by gravity from the reservoir through the outlet mass flow meter and back to the hot water heater. Bypass lines around the filter and experimental test section were provided for component isolation and flow loop configuration flexibility. The experimental test section bypass line was used to circulate the working fluid while the system achieved steady state. The liquid inlet bleed off line and needle valves N1, N2 and N3 were used to control the inlet flow rate. Needle valve N4 was used to control the outlet flow rate from the experimental test section liquid reservoir.

Two coriolis mass flow meters were used to measure mass flow rates into and out of the experimental test section. The inlet mass flow meter was positioned downstream of the filter and upstream of the experimental test section, and constant temperature hot oil bath. The outlet mass flow meter was positioned downstream of the experimental test section. Flow temperature was measured at the hot water heater, filter, inlet mass flow meter, outlet mass flow meter, constant temperature hot oil bath and experimental test section inlet. Inlet flow differential gage pressure was measured at the experimental test section inlet. Individual direct current power supplies provided power to the micropump, hot water heater controller, inlet pressure transducer and heat sink heater rings.

The voltage and current supplied to each heater ring was measured and utilized to determine the total electrical energy applied to the heat sink. Flow temperature, pressure, and mass flow rate, as well as heater ring voltage and current were measured and recorded by LabVIEW^{TM} through two SCB 68 DAQ cards. A voltage divider was implemented to limit the heater ring power supply output voltage to protect the DAQ cards. The make, model and specifications of each component comprising the experimental flow loop are provided in Appendix D. Note that the experimental flow loop used in this study was initially designed and assembled by Brian Daniels and Rebecca Cullion, both former graduate students at Oregon State University.

8.3 Experimental Data Acquisition Procedure

To acquire experimental data, the experimental test section (see Fig. 8.1) was bolted directly to the vertical micro-traverse stage of the IRT imaging facility (see Fig. 6.1). The camera stand was leveled using sheet metal shims and a bull's eye level. The liquid inlet, liquid drain and vacuum pump lines of the experimental flow loop were connected to the experimental test section. The constant temperature oil bath was turned on and set to 95°C. The hot water heater was filled with deionized distilled water until the liquid level in the sight glass measured approximately 1.000 in (25.40 mm) from the top. The hot water heater and controller were turned on and the controller was set to 100°C to boil/degas the deionized distilled water. Degassing took place for a minimum of 30 minutes.

After completing the degassing process, the hot water heater controller was programmed to an operating set point of 85°C. At this point the flow loop data acquisition LabVIEW^{TM} program was started. The flow loop data acquisition LabVIEW^{TM} program records 1) the inlet and outlet mass flow rates, 2) the working fluid temperature at the hot water heater, filter, constant temperature oil bath exit and vacuum chuck inlet, 3) the working fluid differential gage pressure at the vacuum chuck inlet and 4) the voltage and current supplied to the heat sink heater rings. The pump was turned on and deionized distilled degassed water was circulated through the flow loop bypassing the experimental test section. The external strip heaters on the inlet and outlet mass flow meters were turned on and fluid was circulated through the flow loop for a minimum of 2 hours to allow the system to reach steady state.

After the flow loop reached steady state, the vacuum chuck pogo pins and the heater ring contact pads were aligned and the heat sink was placed on the vacuum chuck. Power was applied to the vacuum pump to secure the heat sink to the vacuum chuck. The circulating flow was then diverted to the experimental test section and the pump voltage was adjusted to achieve the desired mass flow rate. Power was applied to the external strip heater just down stream of the vacuum chuck until the desired inlet flow temperature was reached. Power was applied to the heater rings and the voltage was increased in 0.5 volt increments until the desired power input was reached. Approximately 2 minutes was allowed between each incremental voltage increase to prevent heat sink fracture as a result of rapid thermal expansion.

The IR camera and standard objective were mounted to a tripod and placed directly over the camera stand and experimental test section. The standard objective allowed the entire heat sink to be captured in one field of view and provided a qualitative means to identify “areas of interest.” Such “areas” were defined as areas within the heat sink where flow boiling phenomena (inferred from gold layer intensity changes) was observed more often than randomly and less often than continuously.

After identifying the “areas of interest” the IR camera and microscope objective were remounted on the IRT imaging facility camera stand and configured for data acquisition. The left and top edges of the IR camera field of view were aligned with the Kapton® tape right edge and heat sink circumferential edge, respectively. The IR camera was focused on the desired focal plane (the heat sink gold layer) and data acquisition at the previously identified “areas of interest” commenced. An outline listing the explicit chronological order and clarifying details of the experimental data acquisition procedure are provided in Appendix L.

Experimental radiation intensity measurements, in the form of IR images, were taken, at 30 frames per second, at 255 individual “areas of interest.” A 1/2 field of view overlap in both the x and y direction was incorporated during data acquisition to mitigate intensity variations at the image edges due to the camera optics. Figure 8.4 illustrates 255 IR camera fields of view overlaid on the heat sink surface. Each field of view measures 2.56 mm x 2.36 mm.

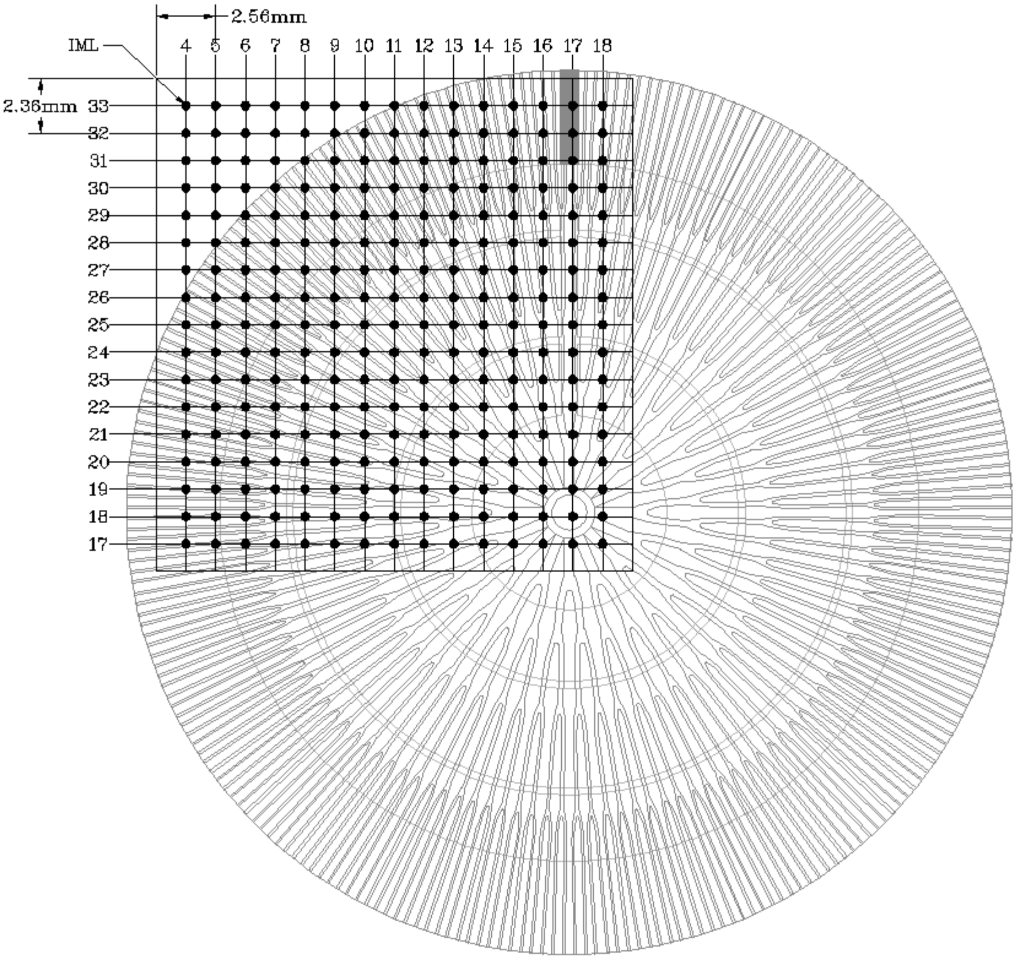

Figure 8.4 255 IR camera fields of view overlaid on the heat sink surface.

For clarity a solid circular node was placed in the center of each field of view and represents a physical position in space where experimental data were acquired. As with the calibration data, positions where images were acquired are referred to as image locations (IML) and are numbered for data identification purposes. Figure 8.5 illustrates the experimental IML numbering.

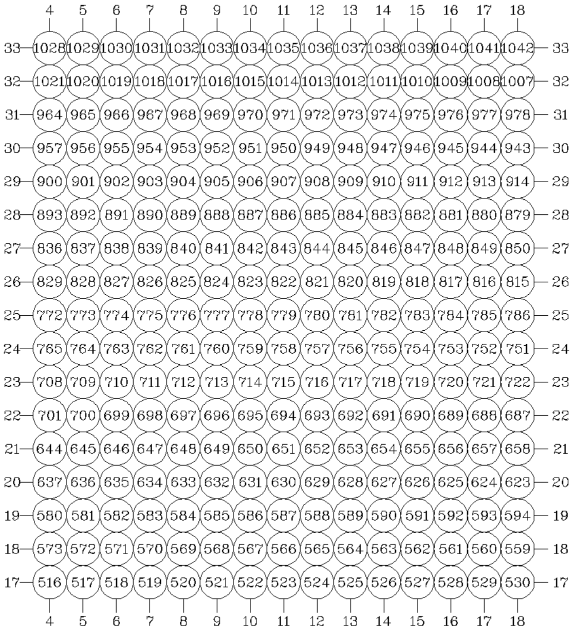

Figure 8.5 Experimental IML numbering.

Each numbered circle in Fig. 8.5 represents a single solid circular node/IML illustrated in Fig. 8.4. To relate a specific numbered IML to an actual physical location on the heat sink, Figs. 8.4 and 8.5 are meant to be used in conjunction. To this end, row and column numbers have been provided around the periphery of each figure.

Experimental data were acquired for an inlet mass flow rate of 15.8 gm/min, an inlet temperature of 88°C, and a total heat sink power input of 30 W. Four thousand experimental images were acquired at 30 frames per second at each of the 255 image locations illustrated in Figs. 8.4 and 8.5. The time required to acquire all experimental data exceeded 13 hours and Figures 8.6-8.8 are provided to illustrate the temporal variations of the inlet mass flow rate, inlet temperature and total heat sink power input during experimental data acquisition.

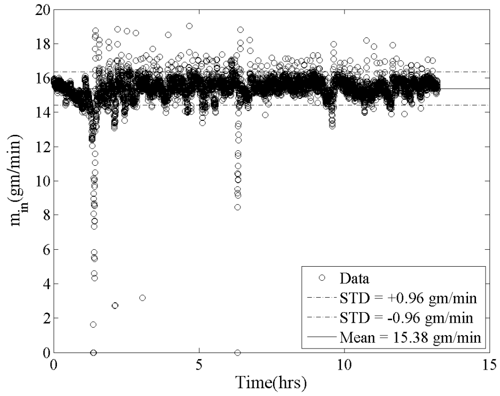

Figure 8.6 Inlet mass flow rate temporal variation.

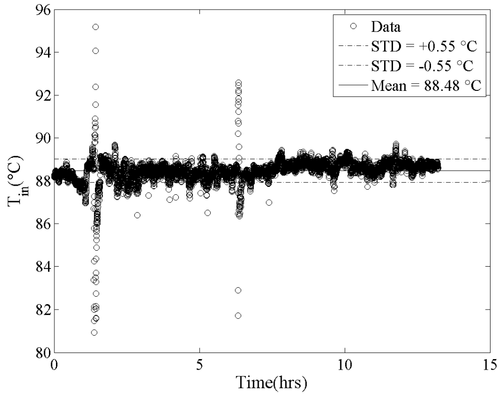

Figure 8.7 Inlet temperature temporal variation.

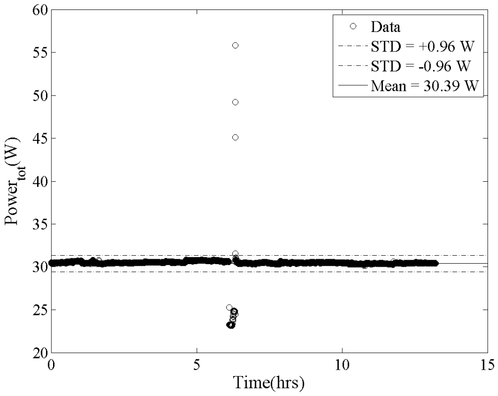

Figure 8.8 Total power input temporal variation.

Notice in Figs. 8.6-8.8 that at approximately 2 and 6 hours into data acquisition the experimental facility experienced both positive and negative spikes in the inlet mass flow rate, inlet temperature and total heat sink power input. The reason for these spikes was unknown and experimental data were not acquired at these times.

Four thousand experimental radiation intensity images per image location were acquired based upon the results of preliminary experimental data. Preliminary experimental data were acquired and a running average temperature was calculated at specific pixel locations within an image. Figure 8.9 illustrates a preliminary experimental temperature image at IML 824. The running average temperature was calculated (over 4,000 images) at three different pixel locations and are illustrated in Figs. 8.10-8.12.

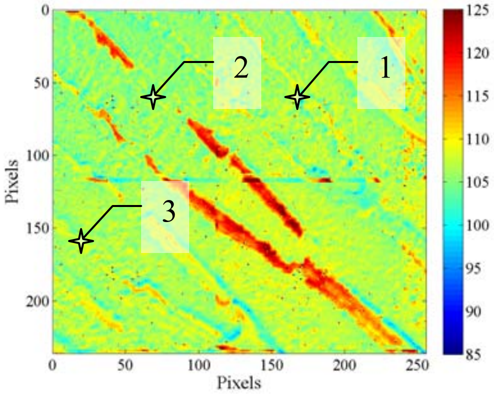

Figure 8.9 Preliminary experimental temperature image (IML 824)

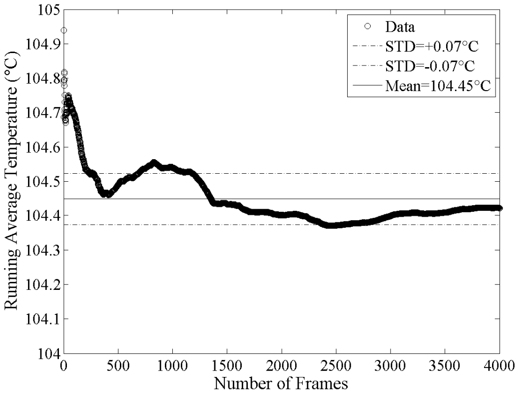

Figure 8.10 Average temperature pixel 1 (IML 824)

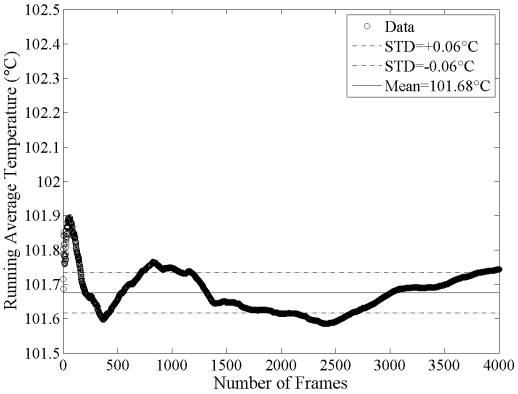

Figure 8.11 Average temperature pixel 2 (IML 824)

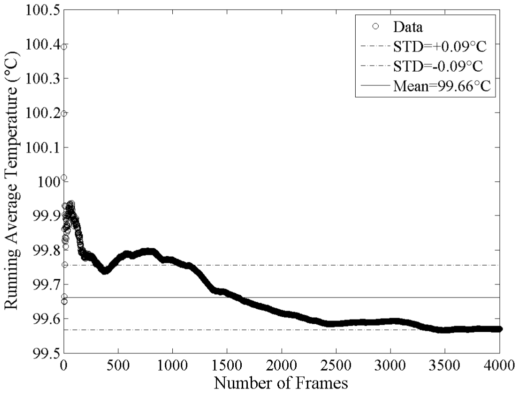

Figure 8.12 Average temperature pixel 3 (IML 824)

Figures 8.10-8.12 illustrate that the average temperature at a particular pixel location varies temporally, but the standard deviation is on the order of 0.06°C -0.0.9°C. The expected standard deviations, with a 4,000 frame sample size, are less than the expected uncertainties. Therefore, 4,000 frames per image location were deemed statistically adequate for experimental data acquisition.

Figure 8.13 illustrates a typical example of a radiation intensity image taken for the experimental flow conditions.

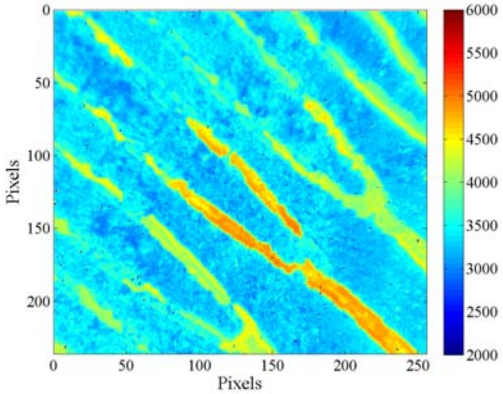

Figure 8.13 Experimental radiation intensity image (IML 824).

The experimental radiation intensity image illustrated in Figure 8.13, was taken at image location 824, which corresponded to a bifurcation at the k=3 to k=4 branching level located in the upper left quadrant of the heat sink directly above the outer heater ring (see Fig. 7.12).

The experimental radiation intensity image measures 236 x 256 pixels and the contour color is in arbitrary detector units proportional to radiation intensity. Typical radiation intensity values range from 2000-6000 at the experimental flow conditions.

8.4 Experimental Data Reduction and Analysis

The first step in experimental data reduction and analysis was the calculation of an average intensity for a given image location. Recall that 4,000 images were taken at each experimental image location. Figure 8.14 illustrates and example of the experimental average intensity for a single image location.

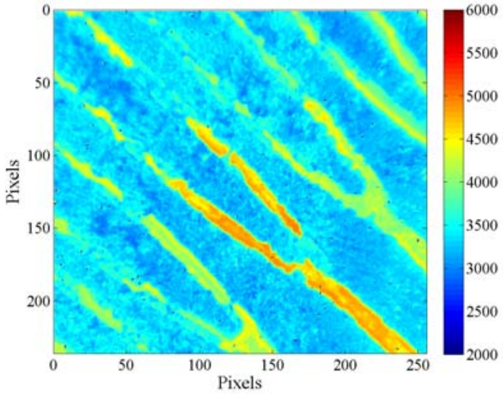

Figure 8.14 Experimental temporally averaged intensity (IML 824).

The second step in the experimental data reduction and analysis was the calculation of the OLA intensity for a given image location. The experimental OLA intensities were calculated directly from the converted experimental intensity images in exactly the same manner the calibration OLA intensities were calculated (see Section 7.5 for reference). Figure 8.15 illustrates an example of the experimental OLA intensity for a single image location.

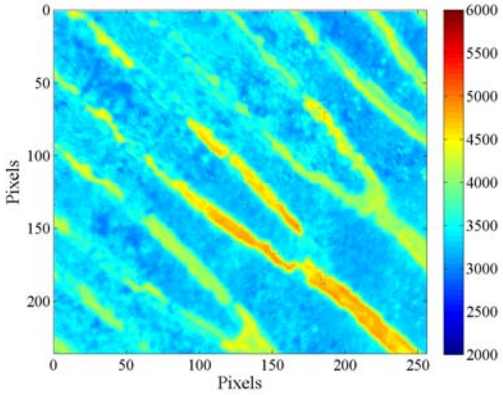

Figure 8.15 Experimental OLA intensity (IML 824).

Experimental OLA intensities were calculated at 56 individual image locations to completely visualize the "area of interest." Figures 8.16 and 8.17 illustrate the locations where the experimental OLA intensities were calculated and the IML numbering.

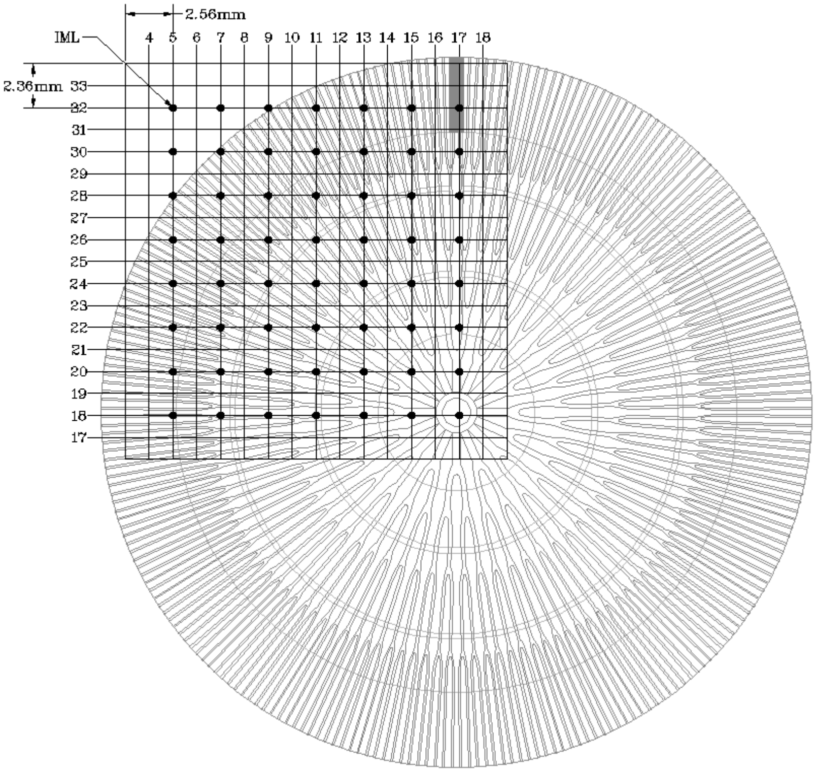

Figure 8.16 Experimental OLA intensity image locations.

The solid circular nodes in Fig. 8.16 indicate locations where overlapped averages were calculated.

	5	7	9	11	13	15	17	
32	1020	1018	1016	1014	1012	1010	1008	32
30	956	954	952	950	948	946	944	30
28	892	890	888	886	884	882	880	28
26	828	826	824	822	820	818	816	26
24	764	762	760	758	756	754	752	24
22	700	698	696	694	692	690	688	22
20	636	634	632	630	628	626	624	20
18	572	570	568	566	564	562	560	18
	5	7	9	11	13	15	17	

Figure 8.17 Experimental OLA IML numbering.

The OLA intensities were then pieced together to create a PW average intensity map of the “area of interest.” The “area of interest” corresponded to approximately 1/4 of the heat sink surface. Figure 8.18 illustrates the experimental PW OLA intensity map of approximately 1/4 of the heat sink surface.

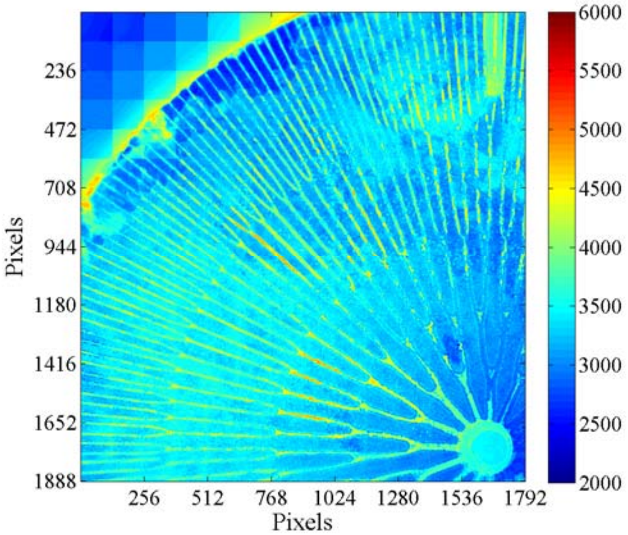

Figure 8.18 Experimental PW OLA intensity map.

The calculation of the 56 OLA intensities and the creation of the PW OLA intensity map was accomplished using Matlab®. The details of the OLA intensity Matlab® program are provided in Appendix P. The details of the PW OLA intensity Matlab® program are provided in Appendix Q.

9 Data Reduction and Analysis

Using the calibration test section, the temperature distribution within the copper cylinder and radiation intensity images of the entire heat sink surface were simultaneously acquired for temperatures of 25°C, 45°C, 65°C, 85°C, 105°C and 125°C. The calibration images and temperature distribution data were used to generate temperature verses intensity calibration curves for each pixel within an image. Using the experimental test section and flow loop, radiation intensity images were acquired at "areas of interest". The calibration curves generated from the calibration images and temperature distribution data were used to convert the experimental images from intensity to temperature. Prior to converting intensity to temperature, however the calibration images required alignment with the experimental images. The processes of image alignment and intensity to temperature conversion are detailed in this chapter.

9.1 Calibration Image Alignment and Shifting

The calibration and experimental data acquired and processed to this point was in arbitrary detector units proportional to radiation intensity. The calibration OLA intensities as well as the calibration test section thermocouple temperature measurements were ultimately used to convert the experimental OLA intensities to temperatures. A reliable conversion from radiation intensity to temperature was possible only if the calibration and experimental OLA intensities were spatially identical, pixel for pixel. Figures 9.1-9.7 illustrate the spatial discrepancies between the calibration and experimental OLA intensities. Notice the spatial discrepancy of the microchannel among the images as indicated by the arrow.

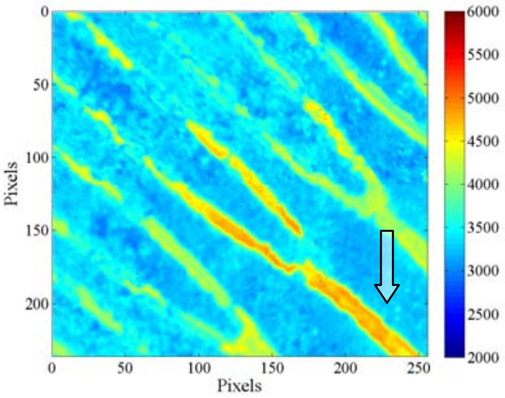

Figure 9.1 Experimental OLA intensity (IML 824).

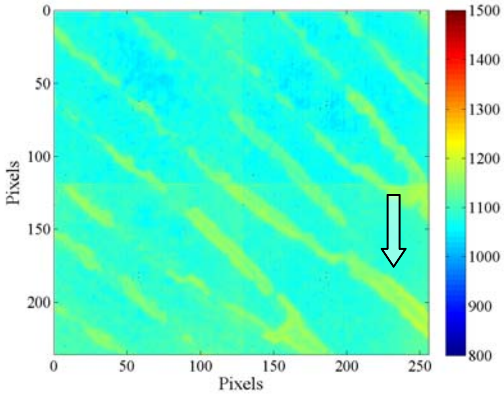

Figure 9.2 25°C OLA intensity (IML 824).

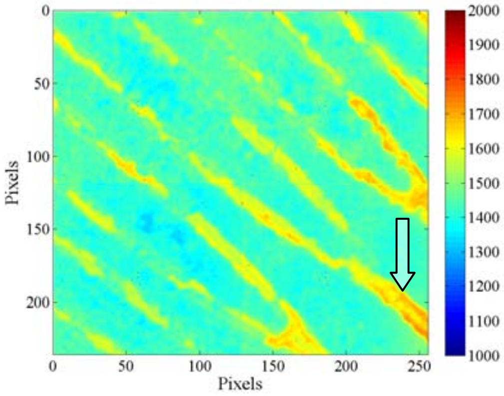

Figure 9.3 45°C OLA intensity (IML 824).

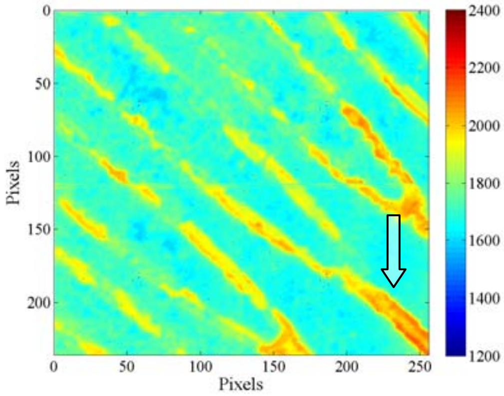

Figure 9.4 65°C OLA intensity (IML 824).

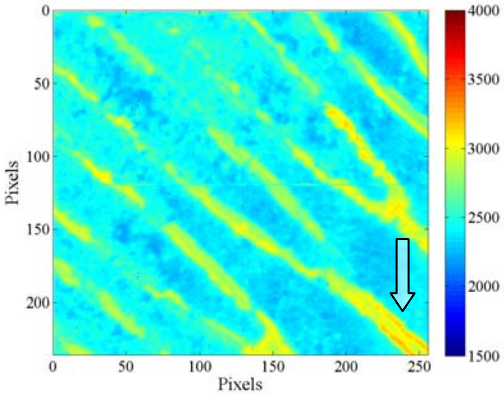

Figure 9.5 85°C OLA intensity (IML 824).

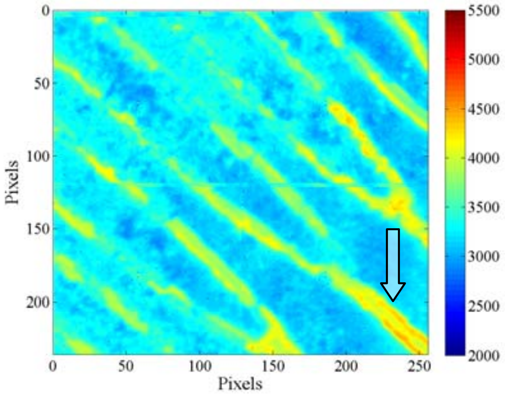

Figure 9.6 105°C OLA intensity (IML 824).

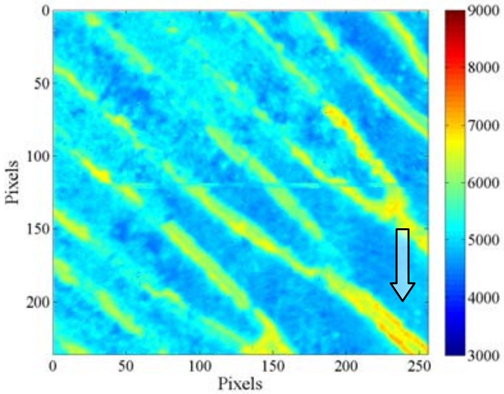

Figure 9.7 125°C OLA intensity (IML 824).

The spatial discrepancies among the acquired data resulted from physically aligning the Kapton® tape reference point with the IR camera field of view during calibration and experimental data acquisition. The Kapton® tape was on the top surface of the heat sink, while the desired focal plane (the gold layer) was 500 μm below the top surface of the heat sink. Focusing the IR camera required vertical movement of the test section rather than vertical movement of the camera. Therefore, once alignment with the reference point was achieved the test section was moved to focus the IR camera on the gold layer. The movement of the test section after alignment with the reference point resulted in the spatial mismatch illustrated in Figs. 9.1-9.7.

To correct the spatial mismatch between the calibration and experimental OLA intensity data, a cross correlation algorithm was developed to calculate the necessary x and y directional shift an image would need to undergo, relative to a base image to result in two separate but spatially identical images. In this instance, the experimental OLA intensities were defined as the base images and the x and y directional shift was calculated for the calibration OLA intensities.

The x and y directional shift information was used to generate a shifted calibration OLA intensity image. The shifted calibration OLA intensity image was generated by simultaneously deleting data from, and adding data to the original calibration OLA intensity image. The added data were obtained from adjacent calibration OLA intensity images. Figure 9.8 illustrates the calibration OLA intensity images required for image shifting.

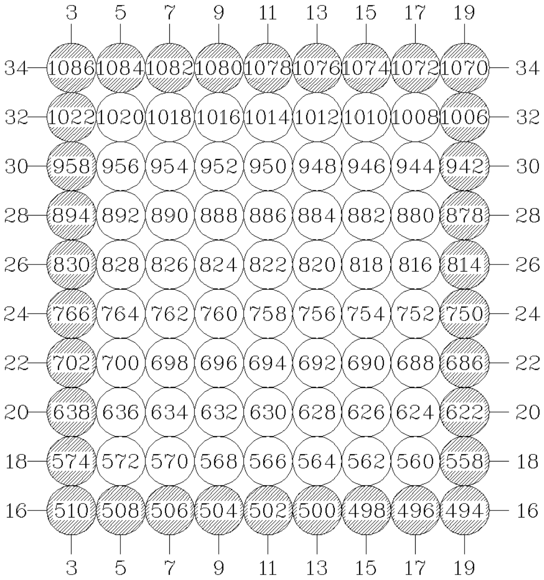

Figure 9.8 Calibration OLA intensity images required for image shifting.

The shaded image locations in Fig. 9.8 indicate the extra calibration data required at each nominal calibration temperature. The extra calibration data ensured each calibration OLA intensity image had exactly 8 peripheral images from which to pull data. The 1/2 field of view overlap incorporated during data acquisition, limited the calibration OLA intensity image shifting to a maximum of 128 pixels in the x direction and 118 pixels in the y direction.

To clarify how new shifted calibration OLA intensity images were generated, consider Fig. 9.3. The calculated x and y directional shift for this calibration temperature and image location was, for example (-25, -4). Since the images were indexed from the upper left hand corner, this calibration OLA intensity image was shifted up 4 pixels (-y) and to the left 25 pixels (-x) to be properly aligned with the experimental OLA intensity image in Fig. 9.1.

The shifted calibration OLA intensity image was generated by deleting data from the left and top edges, while simultaneously adding data to the right and bottom edges of the original calibration OLA intensity image. For this calibration OLA intensity image, the added data comes from adjacent calibration OLA intensity images at locations 822, 758 and 760. Figure 9.9 clarifies where data were deleted from and added to the original calibration OLA intensity image.

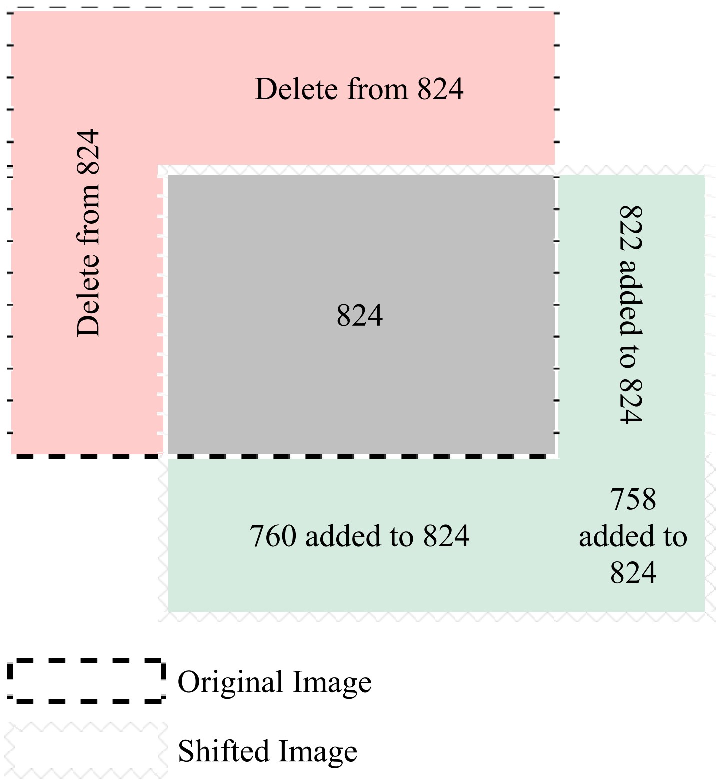

Figure 9.9 Shifted calibration OLA intensity image generation schematic.

Figures 9.10 and 9.11 compare the 45°C shifted calibration OLA intensity image to the experimental OLA intensity image. Notice that the spatial mismatch has been corrected as indicated by the arrow.

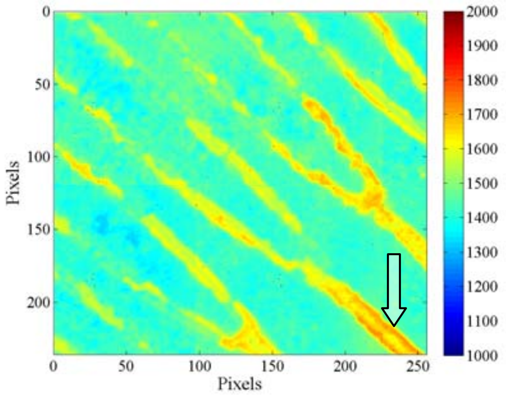

Figure 9.10 45°C shifted calibration OLA intensity (IML 824).

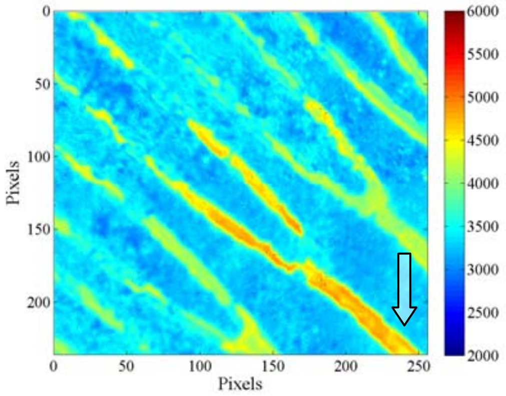

Figure 9.11 Experimental OLA intensity (IML 824).

A shifted calibration OLA intensity image was generated at each of the 56 experimental image locations for each of the six nominal calibration temperatures. This resulted in the generation of 336 shifted calibration OLA intensity images that were utilized in the final step of calibration and experimental data reduction and analysis, which was the conversion of experimental intensities to temperatures. The shifted calibration OLA intensity images were generated using Matlab®. The details of the calibration OLA intensity shifting Matlab® program are provided in Appendix R.

9.2 Conversion of Intensity to Temperature

Conversion of the experimental OLA intensities to temperatures required the determination of intensity vs. temperature calibration curves at each pixel within a given image. Calibration curves were determined utilizing the shifted calibration OLA intensity values as well as the near surface thermocouple temperatures measured during calibration.

A single calibration curve was generated for each pixel within each image. Each image contains 236 x 256 pixels therefore, 60,416 calibration curves were determined for each image. The calibration curves were 4th order polynomials and were generated using Matlab®. The details of the intensity to temperature conversion Matlab® program are provided in Appendix S. Figure 9.12 illustrates an example of a calibration curve at a single pixel location and Fig. 9.13 illustrates an example of an experimental OLA intensity image converted to temperature.

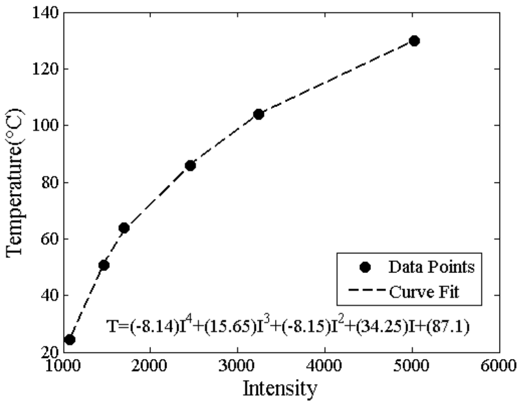

Figure 9.12 Intensity vs. temperature calibration curve.

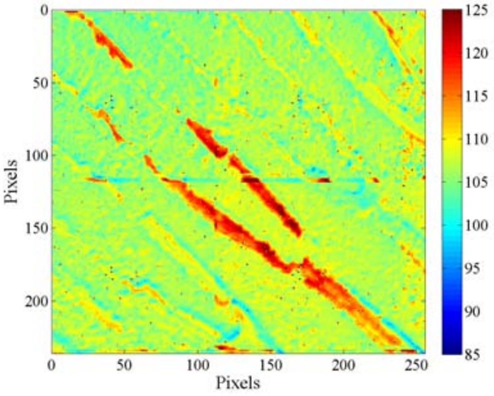

Figure 9.13 Experimental OLA temperature (IML 824).

Once all of the experimental OLA intensity images were converted to temperature, they were pieced together to generate a PW average temperature map of approximately 1/4 of the heat sink surface. Figure 9.14 illustrates the experimental PW OLA temperature of approximately 1/4 of the heat sink surface.

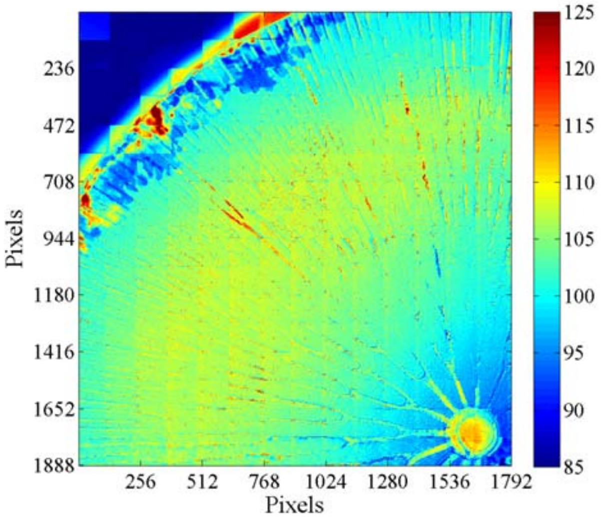

Figure 9.14 Experimental PW OLA temperature map.

10 Uncertainty Analysis

To quantify the error in the measurement technique proposed in this thesis, a rigorous uncertainty analysis was performed and is documented in this section. Uncertainty contributions were classified into two main categories: 1) the calibration test section experimental uncertainty or the temperature uncertainty resulting from calibration test section use and 2) the spatial resolution errors resulting from movement of the horizontal micro-traverse as well as image shifting and alignment.

10.1 Calibration Test Section Experimental Uncertainty.

Uncertainty in the temperature resulted from several sources: 1) uncertainty in the thermocouples used for calibration, 2) a bias error due to a difference between the thermocouple location in the calibration test section and the gold layer of the heat sink channel top wall, 3) IR camera noise and 4) a curve fit error associated with the conversion of intensity to temperature. A 1-D conduction analysis was used to quantify the temperature error due to the physical difference between the calibration test section thermocouple location and heat sink gold layer location. To be conservative, with regard to the 1-D conduction assumption, the error is represented as a bias error and included in the uncertainty analysis rather than correcting for it during data analysis with a potentially inaccurate model.

Ten T-type thermocouples were embedded in the calibration test section and used to monitor and record the temperature distribution within the copper cylinder during calibration data acquisition (see Sections 7.1-7.3 as well as Figs. 7.1-7.3 for clarity). Three of the embedded thermocouples were axial and seven were near surface. The uncertainty in the temperature measured by these thermocouples results from two sources: 1) thermocouple calibration and 2) thermocouple spatial and temporal uncertainty. The thermocouple calibration included a curve fit error, a NIST standard error and a temporal standard deviation of the measured temperature during thermocouple calibration. The thermocouple spatial and temporal uncertainty included a spatial and temporal standard deviation of the measured temperature during calibration data acquisition. Recall the thermocouples were embedded in the calibration test section during calibration data acquisition.

10.1.1 Thermocouple Calibration Uncertainty

Prior to being embedded in the calibration test section, the thermocouples were calibrated against a NIST traceable RTD using a hot oil bath for temperatures ranging from 25°C to 125°C. Calibration was performed for ascending and descending temperatures in 20°C increments. Two thousand temperature measurements were obtained for each thermocouple at each calibration temperature of 25°C, 45°C, 65°C, 85°C, 105°C and 125°C. The temporal standard deviation (S_{time}) at each calibration temperature was calculated for each thermocouple. A linear regression analysis was performed and a curve fit error (CFE) for each thermocouple was determined. The NIST standard error (NISTE) was provided by the RTD manufacturer. The temporal standard deviations, curve fit errors and NIST standard error are documented on Table 10.1.

Table 10.1 S_{time}, CFE and NISTE for thermocouple calibration data.

	Axial			**Near Surface**						
Temp	**TC1**	**TC2**	**TC3**	**TC4**	**TC5**	**TC6**	**TC7**	**TC8**	**TC9**	**TC10**
25°C	0.01	0.01	0.01	0.01	0.01	0.01	0.01	0.01	0.01	0.01
45°C	0.03	0.06	0.03	0.03	0.05	0.06	0.02	0.02	0.03	0.07
65°C	0.16	0.15	0.38	0.32	0.24	0.18	0.52	0.16	0.15	0.36
85°C	0.43	0.50	0.71	0.22	0.49	0.46	0.59	0.43	0.39	0.22
105°C	0.13	0.33	0.11	0.17	0.43	0.34	0.32	0.10	0.20	0.27
125°C	0.48	0.35	0.37	0.30	0.26	0.41	0.36	0.32	0.61	0.17
CFE(°C)	0.41	0.40	0.50	0.54	0.46	0.51	0.59	0.40	0.41	0.61
NISTE(°C)	0.30	0.30	0.30	0.30	0.30	0.30	0.30	0.30	0.30	0.30
▨	Minimum and maximum temporal standard deviations.									

The minimum thermocouple calibration uncertainty ($U_{TC,cal,min}$) was determined by root-sum-squaring the minimum temporal standard deviation ($S_{min,time}$) within the calibration temperature range with the curve fit error and the NIST standard error. The maximum thermocouple calibration uncertainty ($U_{TC,cal,max}$) was determined by root-sum-squaring the maximum temporal standard deviation ($S_{max,time}$) within the calibration temperature range with the curve fit error and the NIST standard error. Table 10.2 documents the minimum and maximum thermocouple calibration uncertainties for each of the ten T-type thermocouples.

Table 10.2 Minimum and maximum thermocouple calibration uncertainties.

	Axial			**Near Surface**						
Uncertainty	**TC1**	**TC2**	**TC3**	**TC4**	**TC5**	**TC6**	**TC7**	**TC8**	**TC9**	**TC10**
$U_{TC,cal,min}$(°C)	0.51	0.50	0.59	0.62	0.55	0.59	0.66	0.50	0.51	0.68
$U_{TC,cal,max}$(°C)	0.70	0.70	0.92	0.69	0.74	0.75	0.88	0.66	0.79	0.77

The average minimum and maximum uncertainties were calculated from the values in Table 10.2 for both the axial and near surface thermocouples. Table 10.3 documents the average minimum and maximum uncertainties.

Table 10.3 Avarage min. and max. thermocouple calibration uncertainties.

	Axial			**Near Surface**						
Uncertainty	**TC1**	**TC2**	**TC3**	**TC4**	**TC5**	**TC6**	**TC7**	**TC8**	**TC9**	**TC10**
$U_{TC,cal,min,avg}$(°C)	0.53			0.59						
$U_{TC,cal,max,avg}$(°C)	0.77			0.75						

The average minimum and maximum thermocouple calibration uncertainties documented in Table 10.3 are considered valid in the temperature range of 25°C to 125°C for all image locations. The axial thermocouple temperature data were not used in converting intensity to temperature and therefore, do not contribute to the total uncertainty. The uncertainty information associated with the axial thermocouples documented in Tables 10.1-10.3 is for completeness purposes only.

10.1.2 Thermocouple Spatial and Temporal Uncertainty

An average of the seven near surface thermocouples was used to determine a reference temperature to/against which the intensity maps were calibrated. At each calibration image location (see Figs. 7.4 and 7.5) 100 temperature measurements from each near surface thermocouple was recorded and averaged both spatially and temporally to determine the reference temperature for that image location. This procedure was repeated for six nominal calibration temperatures of 25°C, 45°C, 65°C, 85°C, 105°C and 125°C.

The calibration temperatures were defined as nominal because, despite the fact time was provided for the calibration test section to reach steady state (> 3 hours per calibration temperature), the time required to acquire data (> 8 hours per calibration temperature) made it difficult to maintain a fixed temperature distribution within the calibration test section with negligible temporal and spatial fluctuations. In essence, from calibration image location 1 to calibration image location 1,152, the reference temperature would fluctuate about a nominal value during calibration data acquisition. These fluctuations did not contribute to the uncertainty since a spatially and temporally averaged reference temperature was determined for each calibration image location. However, spatial and temporal fluctuations exist within an image location that contributes to the uncertainty in temperature.

The temporal and spatial fluctuations within an image location were quantified by calculating the standard deviation and the standard deviation of the means in both space and time. Since 100 temperature measurements, from seven near surface thermocouples, and one IR image were recorded at each calibration image location, the standard deviation of this thermocouple data represents the expected temperature fluctuations between individual IR images. The standard deviation of the means, on the other hand, represents the expected temperature fluctuations between sets of IR images. These temperature fluctuations will vary from image location to image location. Since 1,152 calibration image locations exist, the temperature fluctuations were calculated only for a subset of calibration image locations that correspond directly to experimental image locations. The temporal and spatial standard deviations ($S_{TC,time}$ and $S_{TC,space}$) were calculated at each nominal calibration temperature for several image locations and are documented in Tables 10.4 and 10.5. The temporal and spatial standard deviations of the means ($\sigma_{TC,time}$ and $\sigma_{TC,space}$) were calculated at each nominal calibration temperature for several image locations and are documented in Tables 10.6 and 10.7.

Table 10.4 Thermocouple temporal standard deviation.

$S_{TC,time}$ (°C)	Nominal Calibration Temperature					
IML	**25°C**	**45°C**	**65°C**	**85°C**	**105°C**	**125°C**
562	0.01	0.01	0.01	0.01	0.01	0.01
566	0.01	0.01	0.01	0.01	0.01	0.01
570	0.01	0.01	0.01	0.01	0.01	0.01
690	0.01	0.01	0.01	0.01	0.01	0.01
694	0.01	0.01	0.01	0.01	0.01	0.01
698	0.01	0.01	0.01	0.01	0.01	0.01
818	0.01	0.01	0.01	0.01	0.01	0.01
822	0.01	0.01	0.01	0.01	0.01	0.01
826	0.01	0.01	0.01	0.01	0.01	0.01
946	0.01	0.01	0.01	0.01	0.01	0.01
950	0.01	0.01	0.01	0.01	0.01	0.01
954	0.01	0.01	0.01	0.01	0.01	0.01
▨	Minimum and maximum temporal standard deviations					

Table 10.5 Thermocouple spatial standard deviation.

$S_{TC,space}$ (°C)	Nominal Calibration Temperature					
IML	**25°C**	**45°C**	**65°C**	**85°C**	**105°C**	**125°C**
562	0.37	0.42	0.47	0.55	0.64	0.77
566	0.37	0.42	0.46	0.55	0.64	0.77
570	0.36	0.42	0.47	0.55	0.63	0.77
690	0.37	0.42	0.46	0.55	0.64	0.78
694	0.37	0.42	0.46	0.55	0.65	0.78
698	0.37	0.42	0.47	0.55	0.63	0.78
818	0.37	0.42	0.47	0.55	0.64	0.78
822	0.37	0.42	0.46	0.55	0.64	0.78
826	0.37	0.42	0.46	0.56	0.64	0.79
946	0.36	0.42	0.47	0.56	0.63	0.79
950	0.36	0.42	0.46	0.56	0.64	0.78
954	0.37	0.42	0.46	0.55	0.64	0.79
▨	Minimum and maximum spatial standard deviations					

Table 10.6 Thermocouple temporal standard deviation of mean.

$\sigma_{TC,time}$ (°C)	Nominal Calibration Temperature					
IML	**25°C**	**45°C**	**65°C**	**85°C**	**105°C**	**125°C**
562	0.00	0.00	0.00	0.00	0.00	0.00
566	0.00	0.00	0.00	0.00	0.00	0.00
570	0.00	0.00	0.00	0.00	0.00	0.00
690	0.00	0.00	0.00	0.00	0.00	0.00
694	0.00	0.00	0.00	0.00	0.00	0.00
698	0.00	0.00	0.00	0.00	0.00	0.00
818	0.00	0.00	0.00	0.00	0.00	0.00
822	0.00	0.00	0.00	0.00	0.00	0.00
826	0.00	0.00	0.00	0.00	0.00	0.00
946	0.00	0.00	0.00	0.00	0.00	0.00
950	0.00	0.00	0.00	0.00	0.00	0.00
954	0.00	0.00	0.00	0.00	0.00	0.00
▨	Minimum and maximum temporal standard deviation of the means					

Table 10.7 Thermocouple spatial standard deviation of mean.

$\sigma_{TC,space}$ (°C)	Nominal Calibration Temperature					
IML	**25°C**	**45°C**	**65°C**	**85°C**	**105°C**	**125°C**
562	0.14	0.16	0.18	0.21	0.24	0.29
566	0.14	0.16	0.18	0.21	0.24	0.29
570	0.14	0.16	0.18	0.21	0.24	0.29
690	0.14	0.16	0.18	0.21	0.24	0.30
694	0.14	0.16	0.18	0.21	0.24	0.30
698	0.14	0.16	0.18	0.21	0.24	0.30
818	0.14	0.16	0.18	0.21	0.24	0.30
822	0.14	0.16	0.17	0.21	0.24	0.30
826	0.14	0.16	0.17	0.21	0.24	0.30
946	0.14	0.16	0.18	0.21	0.24	0.30
950	0.14	0.16	0.18	0.21	0.24	0.30
954	0.14	0.16	0.18	0.21	0.24	0.30
▨	Minimum and maximum spatial standard deviation of the means					

The minimum thermocouple spatial and temporal uncertainty, for a single IR image, ($U1_{TCST,min}$) was determined by root-sum-squaring the minimum temporal standard deviation ($S_{TC,time,min}$) within the calibration temperature range with the minimum spatial standard deviation ($S_{TC,space,min}$). The maximum thermocouple spatial and temporal uncertainty, for a single IR image, ($U1_{TCST,max}$) was determined by root-sum-squaring the maximum temporal standard deviation ($S_{TC,time,max}$) within the calibration temperature range with the maximum spatial standard deviation ($S_{TC,space,max}$).

The minimum thermocouple spatial and temporal uncertainty, for a set of IR images, ($U2_{TCST,min}$) was determined by root-sum-squaring the minimum temporal standard deviation of the mean ($\sigma_{TC,time,min}$) within the calibration temperature range with the minimum spatial standard deviation of the mean ($\sigma_{TC,space,min}$). The maximum thermocouple spatial and temporal uncertainty, for a set of IR images, ($U2_{TCST,max}$) was determined by root-sum-squaring the maximum temporal standard deviation of the mean ($\sigma_{TC,time,max}$) within the calibration temperature range with the maximum spatial standard deviation of the mean ($\sigma_{TC,space,max}$). Table 10.8 documents these minimum and maximum thermocouple spatial and temporal uncertainties.

Table 10.8 Min. and max. thermocouple spatial and temporal uncertainties.

IML	**$U1_{TCST,min}$ (°C)**	**$U1_{TCST,max}$ (°C)**	**$U2_{TCST,min}$ (°C)**	**$U2_{TCST,max}$ (°C)**
562	0.37	0.77	0.14	0.29
566	0.37	0.77	0.14	0.29
570	0.36	0.77	0.14	0.29
690	0.37	0.78	0.14	0.30
694	0.37	0.78	0.14	0.30
698	0.37	0.78	0.14	0.30
818	0.37	0.78	0.14	0.30
822	0.37	0.78	0.14	0.30
826	0.37	0.79	0.14	0.30
946	0.36	0.79	0.14	0.30
950	0.36	0.78	0.14	0.30
954	0.37	0.79	0.14	0.30

The uncertainties documented in Table 10.8 are dominated by the spatial fluctuation in temperature. The total contribution to the uncertainty in temperature resulting from the thermocouples used during calibration was determined by root-sum-squaring the average near surface thermocouple calibration uncertainties (see Table 10.3) with the thermocouple spatial and temporal uncertainties (see Table 10.8). The total thermocouple uncertainties are documented in Table 10.9.

Table 10.9 Total thermocouple uncertainty.

IML	$U1_{TC,tot,min}$ (°C)	$U1_{TC,tot,max}$ (°C)	$U2_{TC,tot,min}$ (°C)	$U2_{TC,tot,max}$ (°C)
562	0.69	1.07	0.61	0.80
566	0.69	1.08	0.61	0.80
570	0.69	1.07	0.61	0.80
690	0.69	1.08	0.61	0.81
694	0.70	1.09	0.61	0.81
698	0.69	1.08	0.61	0.81
818	0.69	1.09	0.61	0.81
822	0.70	1.09	0.61	0.81
826	0.69	1.09	0.61	0.81
946	0.69	1.09	0.61	0.81
950	0.69	1.08	0.61	0.81
954	0.69	1.09	0.61	0.81

The axial thermocouple temperature data were not used in converting intensity to temperature and therefore, do not contribute to the uncertainties reported here.

10.1.3 Temperature Bias due to Location Mismatch.

The calibration test section provided temperature measurements at a depth of 0.063 in (1.59 mm) below the heat sink bottom surface. Since the heat sink gold layer temperature was the desired measurand and the calibration test section temperature was known at a location other than the heat sink gold layer, a one-dimensional conduction analysis between the calibration test section known temperature plane and the heat sink gold layer/focal plane was performed in an attempt to quantify the temperature difference between the two locations. To be conservative, with regard to the one-dimensional conduction assumption, the temperature difference calculated was considered a bias error and included in the uncertainty analysis rather than correcting for it during data analysis with a potentially inaccurate model.

The conduction path length through the calibration test section copper cylinder is 0.063 in (1.59 mm). The thermal conductivity of copper was taken to be 393 W/m °C [42]. The thermal resistance of the copper was calculated to be approximately 4.04 x 10^{-6} m^2 °C/W. The Micro-Faze® dry interface thermal film consisted of a 0.002 in (0.05 mm) thick aluminum substrate sandwiched between two 0.002 in (0.05 mm) thick layers of thermal compound. Therefore, the conduction path length through the Micro-Faze® thermal film measured 0.006 in (0.15 mm). The manufacturer reported thermal resistance was given as 0.03 in^2 °C/W (1.94 x 10^{-5} m^2 °C/W) at 55°C and 10 psi. The conduction path length through the bottom silicon wafer of the heat sink was 500 µm. The thermal conductivity of silicon was taken to be 98.9 W/m °C [42]. The thermal resistance of the silicon was calculated to be approximately 5.06 x 10^{-6} m^2 °C/W. Figure 10.1 illustrates the resistance diagram used to calculate the temperature difference.

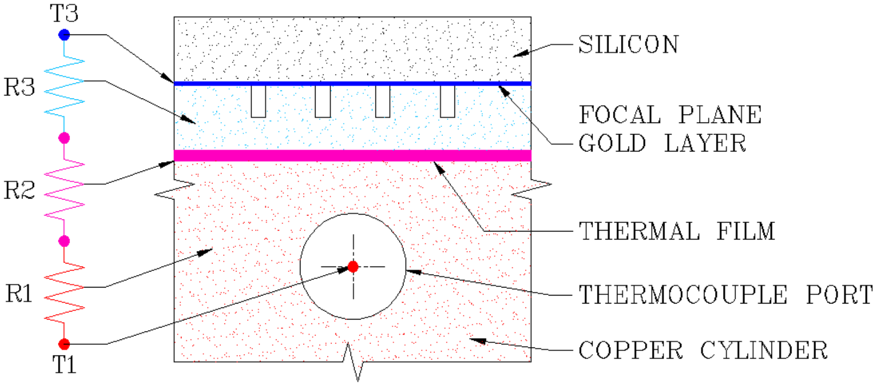

Figure 10.1 Bias error 1D conduction resistance diagram.

The temperature differences or bias errors were calculated for each calibration temperature using the following relationship.

$$T_1 - T_3 = q''(R_1 + R_2 + R_3) \qquad 10.1$$

Where

Nominal Temperature (°C)	Heat Flux Input, q” (W/m^2)	Thermal Resistance, R1 (m^2 °C/W)	Thermal Resistance, R2 (m^2 °C/W)	Thermal Resistance, R3 (m^2 °C/W)
25	0	4.04×10^{-6}	1.94×10^{-5}	5.06×10^{-6}
45	2052			
65	4154			
85	6157			
105	8576			
125	12630			

Table 10.10 documents the temperature difference / bias error calculated, at each calibration temperature, using Equation 11.1.

Table 10.10 Temperature bias due to location mismatch.

Nominal Temperature (°C)	**U_{bias} (°C)**
25	0.00
45	0.06
65	0.12
85	0.17
105	0.24
125	0.36

The temperature difference / bias error documented in Table 10.10 are considered valid for all image locations.

10.1.4 IR Camera Noise

Uncertainty in the temperature measurements arose due to intensity fluctuations during calibration or the presence of noise. To quantify this uncertainty, 100 intensity images were taken at 12 image locations for each of the nominal calibration temperatures. The 12 image locations were selected to be commensurate with experimental OLA image locations identified previously. Intensity data were acquired at the shaded image locations illustrated in Fig. 10.2.

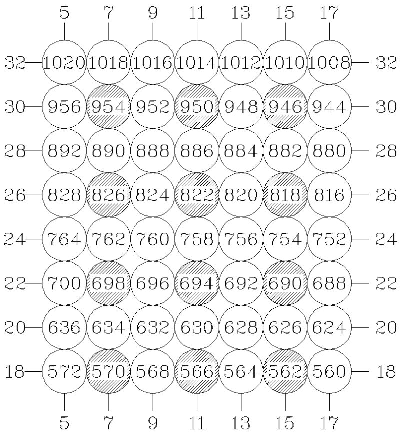

Figure 10.2 Calibration intensity uncertainty image locations.

A total of 7,200 intensity images were acquired using the calibration data acquisition procedure outlined in Section 7.3 The intensity images were converted to temperature and the temporal standard deviation ($S_{N,time}$) was calculated at each pixel within every image for each of the nominal calibration temperatures. The maximum and minimum temporal standard deviation for each image is documented in Table 10.11. The temporal standard deviation of the means ($\sigma_{N,time}$) was also calculated at each pixel within every image location for each of the nominal calibration temperatures. The maximum and minimum temporal standard deviation of the means is documented in Table 10.12.

Table 10.11 IR camera noise temporal standard deviation.

$S_{N,time}$ (°C)	Nominal Calibration Temperature											
	25°C		45°C		65°C		85°C		105°C		125°C	
IML	**Min**	**Max**	**Min**	**Max**	**Min**	**Max**	**Min**	**Max**	**Min**	**Max**	**Min**	**Max**
562	0.09	0.54	0.11	0.74	0.11	0.75	0.12	0.67	0.16	1.15	0.35	1.32
566	0.12	1.05	0.14	1.16	0.13	1.23	0.14	1.27	0.20	1.66	0.40	1.91
570	0.09	0.49	0.12	0.64	0.12	0.69	0.13	0.70	0.20	1.20	0.28	1.38
690	0.10	0.54	0.13	0.82	0.12	0.86	0.14	0.80	0.20	1.45	0.40	1.66
694	0.18	0.85	0.21	0.98	0.21	1.04	0.25	1.16	0.35	1.96	0.47	2.25
698	0.14	0.70	0.19	0.94	0.18	0.87	0.19	0.83	0.25	1.28	0.37	1.48
818	0.08	0.59	0.11	0.78	0.11	0.77	0.12	1.09	0.17	1.84	0.54	2.11
822	0.41	0.83	0.56	1.14	0.54	1.21	0.57	2.37	0.78	2.34	0.80	2.69
826	0.12	0.61	0.15	0.85	0.13	0.79	0.14	0.74	0.22	1.53	0.49	1.75
946	0.14	0.68	0.17	0.82	0.17	0.81	0.16	0.81	0.25	2.00	0.44	2.30
950	0.08	0.65	0.11	0.83	0.11	0.87	0.12	0.88	0.15	1.66	0.34	1.91
954	0.24	1.11	0.31	1.30	0.33	1.37	0.34	1.89	0.42	2.26	0.80	2.48

Table 10.12 IR camera noise temporal standard deviation of the mean.

$\Sigma_{N,time}$ (°C)	Nominal Calibration Temperature											
	25°C		45°C		65°C		85°C		105°C		125°C	
IML	**Min**	**Max**	**Min**	**Max**	**Min**	**Max**	**Min**	**Max**	**Min**	**Max**	**Min**	**Max**
562	0.01	0.05	0.01	0.07	0.01	0.07	0.01	0.07	0.02	0.11	0.04	0.13
566	0.01	0.11	0.01	0.12	0.01	0.12	0.01	0.13	0.02	0.17	0.04	0.19
570	0.01	0.05	0.01	0.06	0.01	0.07	0.01	0.07	0.02	0.12	0.03	0.14
690	0.01	0.05	0.01	0.08	0.01	0.09	0.01	0.08	0.02	0.14	0.04	0.17
694	0.02	0.08	0.02	0.10	0.02	0.10	0.03	0.12	0.04	0.20	0.05	0.23
698	0.01	0.07	0.02	0.09	0.02	0.09	0.02	0.08	0.03	0.13	0.04	0.15
818	0.01	0.06	0.01	0.08	0.01	0.08	0.01	0.11	0.02	0.18	0.05	0.21
822	0.04	0.08	0.06	0.11	0.05	0.12	0.06	0.24	0.08	0.23	0.08	0.27
826	0.01	0.06	0.01	0.08	0.01	0.08	0.01	0.07	0.02	0.15	0.05	0.18
946	0.01	0.07	0.02	0.08	0.02	0.08	0.02	0.08	0.02	0.20	0.04	0.23
950	0.01	0.07	0.01	0.08	0.01	0.09	0.01	0.09	0.02	0.17	0.03	0.19
954	0.02	0.11	0.03	0.13	0.03	0.14	0.03	0.19	0.04	0.23	0.08	0.25

The results presented in Tables 10.11 and 10.12 represent a typical variation in temperature within an image location for a specific nominal calibration temperature as a result of intensity fluctuations during calibration data acquisition. The standard deviations represent the expected temperature fluctuations between individual IR images and the standard deviation of the means represents the expected temperature fluctuations between sets of IR images.

10.1.5 Conversion of Intensity to Temperature Uncertainty

The conversion of intensity to temperature uncertainty resulted from the curve fit error that arose during the 4th order polynomial calibration curve generation (see Section 9.2 for calibration curve generation details). Recall, 60,416 calibration curves were generated for each image to convert from intensity to temperature. A curve fit error is calculated for each of the 60,416 calibration curves. The average curve fit error for a specific image was taken as the curve fit error for that image and was considered valid within the temperature range of 25°C – 125°C. The minimum, maximum and average curve fit errors for a subset of experimental images are documented in Table 10.13 to provide a representative example of the magnitude of the curve fit error.

Table 10.13 Curve fit errors for selected experimental image locations.

IML	Minimum Curve Fit Error (°C)	Maximum Curve Fit Error (°C)	Average Curve Fit Error (°C)
562	0.00	9.14	0.91
566	0.00	8.82	0.71
570	0.00	7.50	0.83
690	0.00	7.29	0.57
694	0.00	6.35	0.60
698	0.00	6.79	0.43
818	0.00	6.86	0.52
822	0.00	6.96	0.44
826	0.00	8.36	0.95
946	0.00	8.93	0.72
950	0.00	7.89	0.67
954	0.00	7.62	0.62

10.2 Total Uncertainty

The total uncertainty in the temperature measurements was calculated by root sum squaring: 1) the total thermocouple uncertainty (Table 10.9), 2) the temperature bias error

(Table 10.10), 3) the temperature uncertainty due to IR camera noise (Table 10.11 and 10.12) and 4) the average curve fit error associated with converting intensity to temperature (Table 10.13). Table 10.14 documents the maximum and minimum total temperature uncertainty between individual IR images ($U1_{tot}$) at each calibration temperature for a set of selected image locations. Table 10.15 documents the maximum and minimum total temperature uncertainty between sets of IR images ($U2_{tot}$) at each calibration temperature for a set of selected image locations.

Table 10.14 Total temperature uncertainty for individual images.

$U1_{tot}$ (°C)	**Nominal Calibration Temperature**											
	25°C		**45°C**		**65°C**		**85°C**		**105°C**		**125°C**	
IML	**Min**	**Max**	**Min**	**Max**	**Min**	**Max**	**Min**	**Max**	**Min**	**Max**	**Min**	**Max**
562	1.15	1.50	1.15	1.59	1.15	1.60	1.16	1.57	1.18	1.83	1.25	1.96
566	1.00	1.67	1.00	1.74	1.01	1.79	1.01	1.82	1.04	2.12	1.13	2.33
570	1.08	1.44	1.09	1.50	1.09	1.52	1.10	1.53	1.12	1.83	1.17	1.97
690	0.90	1.34	0.91	1.47	0.91	1.50	0.92	1.47	0.95	1.91	1.04	2.09
694	0.94	1.51	0.95	1.58	0.95	1.63	0.97	1.71	1.01	2.33	1.10	2.60
698	0.82	1.36	0.84	1.50	0.84	1.46	0.85	1.44	0.88	1.75	0.96	1.92
818	0.87	1.34	0.87	1.44	0.88	1.44	0.89	1.64	0.91	2.21	1.08	2.46
822	0.92	1.44	1.00	1.64	0.99	1.69	1.02	2.65	1.16	2.63	1.21	2.96
826	1.18	1.57	1.19	1.68	1.19	1.65	1.19	1.63	1.22	2.12	1.32	2.30
946	1.01	1.47	1.01	1.54	1.02	1.54	1.02	1.55	1.06	2.40	1.15	2.67
950	0.97	1.43	0.97	1.52	0.98	1.54	0.98	1.56	1.00	2.10	1.08	2.32
954	0.96	1.67	0.98	1.81	0.99	1.86	1.00	2.27	1.05	2.60	1.28	2.80
▨	Maximum and minimum values.											

Table 10.15 Total temperature uncertainty for sets of images.

U2$_{tot}$ (°C)	**Nominal Calibration Temperature**											
	25°C		**45°C**		**65°C**		**85°C**		**105°C**		**125°C**	
IML	**Min**	**Max**	**Min**	**Max**	**Min**	**Max**	**Min**	**Max**	**Min**	**Max**	**Min**	**Max**
562	1.10	1.21	1.10	1.22	1.10	1.22	1.11	1.23	1.12	1.24	1.15	1.27
566	0.94	1.08	0.94	1.08	0.94	1.08	0.95	1.09	0.97	1.11	1.00	1.14
570	1.03	1.15	1.03	1.16	1.04	1.16	1.04	1.17	1.06	1.18	1.09	1.22
690	0.83	0.99	0.84	1.00	0.84	1.00	0.85	1.01	0.87	1.03	0.91	1.07
694	0.86	1.01	0.86	1.01	0.86	1.02	0.87	1.03	0.89	1.06	0.93	1.09
698	0.75	0.92	0.75	0.92	0.76	0.93	0.77	0.94	0.78	0.96	0.83	1.00
818	0.80	0.96	0.80	0.97	0.81	0.97	0.82	0.98	0.84	1.01	0.88	1.05
822	0.75	0.93	0.76	0.93	0.76	0.94	0.77	0.97	0.79	0.98	0.84	1.03
826	1.13	1.25	1.13	1.25	1.14	1.26	1.14	1.26	1.15	1.28	1.19	1.31
946	0.94	1.09	0.95	1.09	0.95	1.09	0.96	1.10	0.97	1.13	1.01	1.16
950	0.91	1.05	0.91	1.06	0.91	1.06	0.92	1.07	0.94	1.09	0.98	1.13
954	0.87	1.03	0.87	1.03	0.88	1.04	0.89	1.05	0.90	1.07	0.94	1.11
▨	Maximum and minimum values.											

The maximum and minimum uncertainty values within the set of image locations at each nominal calibration temperature are highlighted to illustrate the range of uncertainty that exists in these data. The uncertainty in temperature can vary from one image to the next by 0.82°C-1.67°C at 25 °C and 0.96°C-2.80°C at 125°C. The uncertainty in temperature can vary from one image set to the next by 0.75°C-1.25°C at 25°C and 0.83°C-1.31°C at 125°C. It is imperative to note that while many sources of measurement uncertainty have been identified and quantified, any intensity variation from sensor to sensor within the focal plane array has not been included in this uncertainty analysis.

10.3 Spatial Resolution

In addition to the uncertainty in temperature values, it was also important to document spatial resolution errors since this technique claims a 10 μm resolution. To obtain accurate temperature measurements, it was imperative to match, pixel for pixel, the calibration OLA intensity and experimental OLA intensity images. Spatial resolution errors result from two main sources: 1) the uncertainty, in both the x and y directions, of the horizontal micro-traverse and 2) the manual alignment procedure of the Kapton® tape reference point with the IR camera field of view. The spatial resolution error resulting from the manual alignment procedure of the Kapton® tape was corrected using an image shifting algorithm, however the image shifting algorithm itself introduces a spatial resolution error. The uncertainty associated with both the horizontal micro-traverse and the image shifting algorithm is discussed as a part of the spatial resolution of this measurement technique.

10.3.1 Horizontal Micro-Traverse Spatial Uncertainty

The horizontal micro-traverse used for data acquisition, a Parker 406008LN, provided 8.000 in (20.32 cm) of total travel in both the x and y direction. To quantify the spatial uncertainty of the traverse, an optical grid was used. The optical grid, illustrated in Fig. 10.3 consisted of 40 parallel lines spaced 0.25 mm apart. The lines consisted of black paint applied to a thin, clear plastic sheet. The plastic sheet was sandwiched between two black metal frames. The optical grid measured approximately 2.000 in. x 2.000 in. (50.80 mm x 50.80 mm) overall.

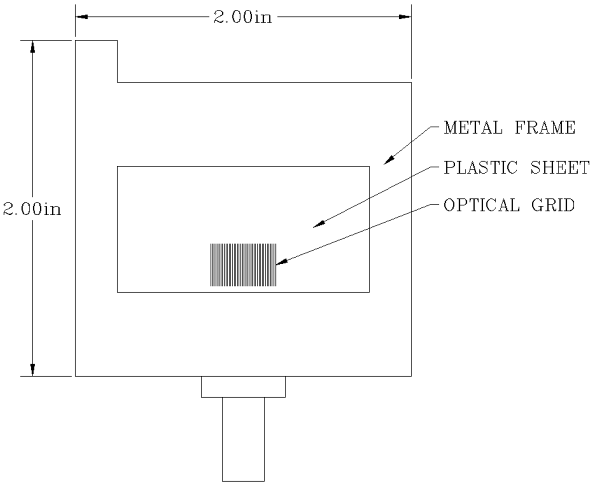

Figure 10.3 Optical grid.

The optical grid was mounted directly to the vertical micro-traverse stage of the IRT imaging facility. A disk heater was placed directly beneath and 2.000 in. (50.80 mm) below the optical grid. A heat source was required to visualize the optical grid with the IR camera. Once mounted to the IRT imaging facility, a bull's eye level was used to level the optical grid and the IR camera in the xy plane. Figure 10.4 illustrates the IRT imaging facility with the optical grid and disk heater for clarification.

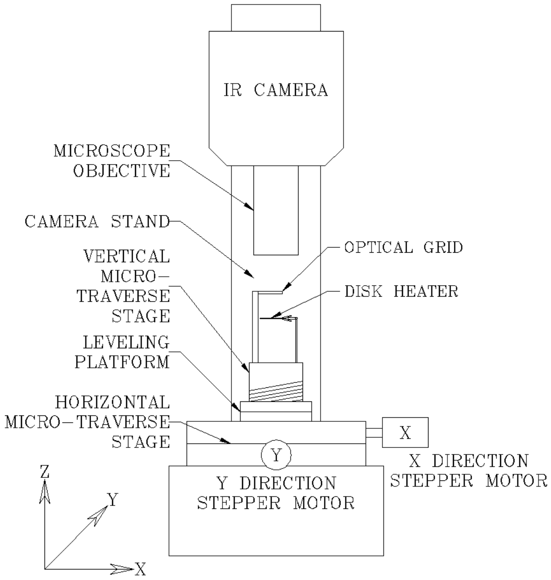

Figure 10.4 IRT imaging facility with optical grid and disk heater.

To quantify the spatial uncertainty in the x direction, the optical grid was aligned such that the grid lines lie in the xy plane oriented parallel to the IRT imaging facility y axis. The parallel lines of the optical grid were aligned with the IR camera field of view left edge (see Fig. 10.5 for clarity).

To quantify the spatial uncertainty in the y direction, the optical grid was aligned such that the grid lines lie in the xy plane oriented parallel to the IRT imaging facility x axis. The parallel lines of the optical grid were aligned with the IR camera field of view top edge (see Fig. 10.6 for clarity).

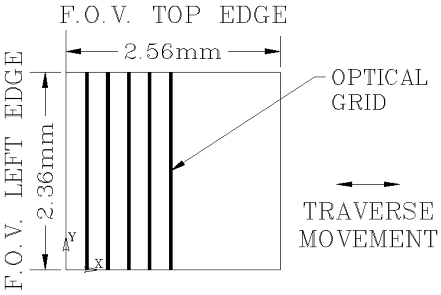

Figure 10.5 X direction F.O.V alignment.

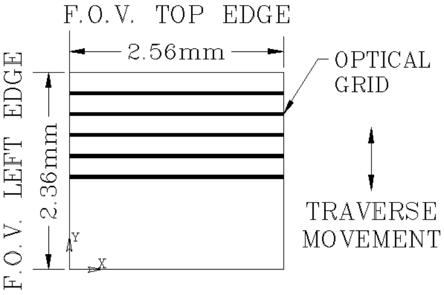

Figure 10.6 Y direction F.O.V alignment.

Once alignment was achieved, the horizontal micro-traverse stage was manipulated to center the first line of the optical grid within the IR camera field of view. A single image was acquired with the optical grid at this location. This position was defined as image location 1 (see Figs. 10.7 and 10.9). Successive images were acquired at 1.00 mm increments until the end of the optical grid was reached. The end of the optical grid was defined as image location 11. At image location 11 the horizontal micro-traverse had translated only 10.00 mm. Since the heat sink measured 38.10 mm in diameter the horizontal micro-traverse was translated an additional 30.00 mm in 1.00 mm increments past the end of the optical grid. Once the horizontal micro-traverse had translated a total of 40.00 mm in 1.00 mm increments, the horizontal micro-traverse was translated 40.00 mm in one continuous motion back to image location 1 where a final image was acquired. This position was defined as image location 12 (see Figs. 10.8 and 10.10).

This procedure resulted in a total of 12 images and was repeated for both the x and y directions. Note that the heat source below the optical grid was placed such that it moved with the grid when the horizontal micro-traverse stage was manipulated. Figures 10.7-10.10 illustrate radiation intensity images of the optical grid in both the x and y directions at image locations 1 and 12.

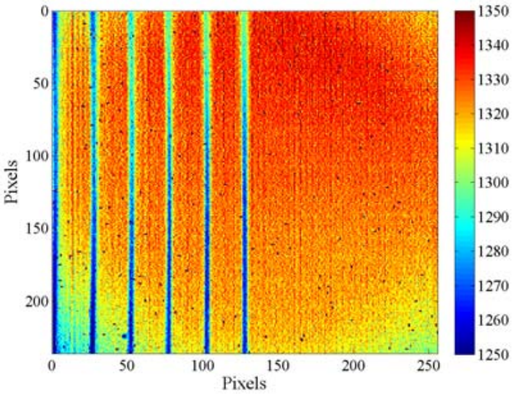

Figure 10.7 Optical grid x-dir. IML 1.

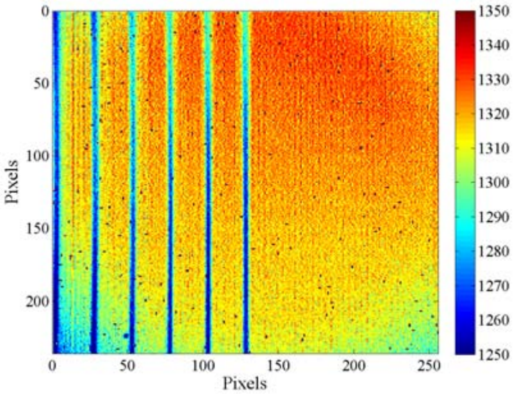

Figure 10.8 Optical grid x-dir. IML 12.

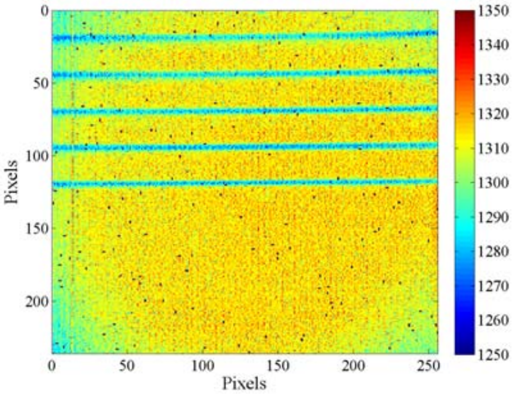

Figure 10.9 Optical grid y-dir. IML 1.

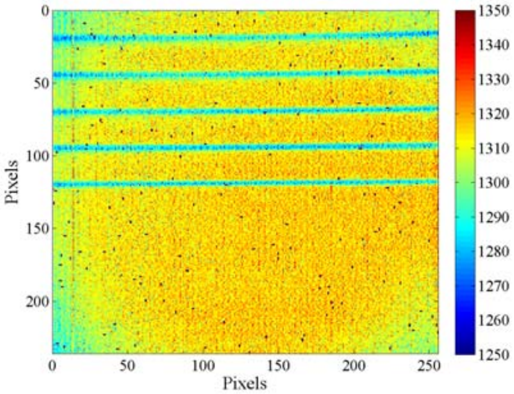

Figure 10.10 Optical grid y-dir. IML 12.

To ultimately quantify the positional accuracy and repeatability of the horizontal micro-traverse, the intensity distributions for Figs. 10.7-10.10 were plotted against their spatial / pixel location. The spatial location of the measured intensity at image location 12 was then compared to the spatial location of the measured intensity at image location 1. Figures 10.11-10.14 illustrate plots of pixel location vs. intensity at image locations 1 and 12.

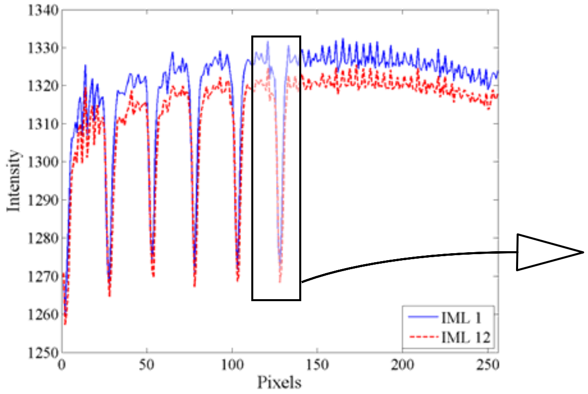

Figure 10.11 Intensity vs. pixels x-dir. IML 1 &12.

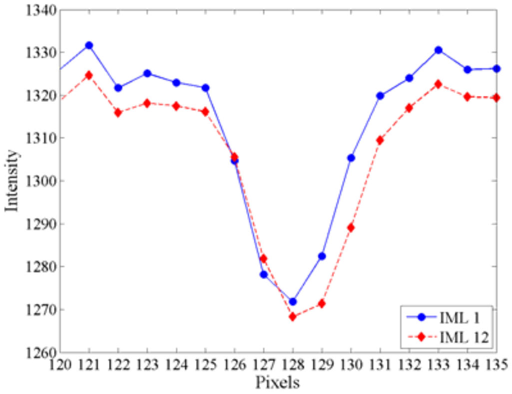

Figure 10.12 Intensity vs. pixels x-dir. IML 1 &12.

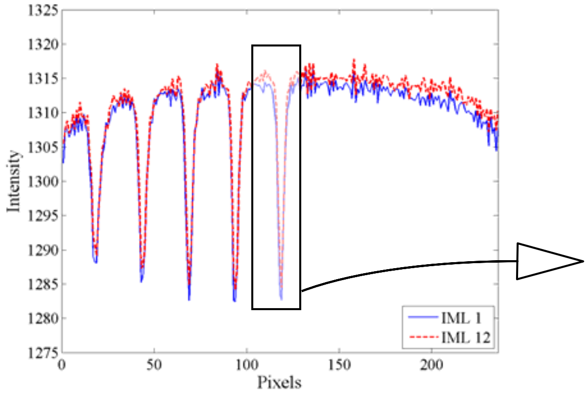

Figure 10.13 Intensity vs. pixels y-dir. IML 1 &12.

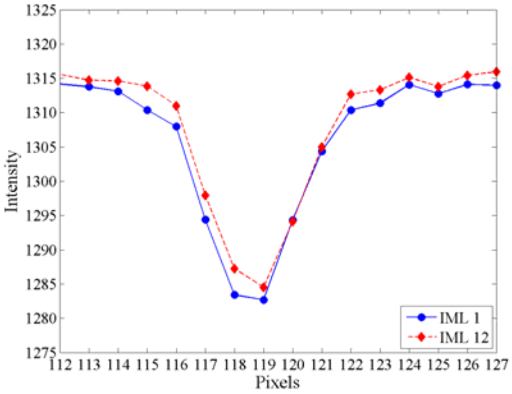

Figure 10.14 Intensity vs. pixels y-dir. IML 1 &12.

Figures 10.11 and 10.13 illustrate plots of pixel location vs. intensity of the optical grid as seen by the entire camera field of view. The sharp, periodic decreases in intensity correspond to actual optical grid lines. A comparison of image location 12 to image location 1 illustrated that incremental movement of the horizontal micro-traverse resulted in directly overlapping grid lines. This indicated that the horizontal micro-traverse was operating in accurate and repeatable increments. A closer examination of overlapping grid lines further quantifies this positional accuracy and repeatability. Figures 10.12 and 10.14 illustrate plots of pixel location vs. intensity for a single overlapping optical grid line at image locations 1 and 12.

Notice in Figs. 10.12 and 10.14 that the intensity values vary within an image location, but the pixel locations of these intensities do not. The varying intensity values from one image location to the next results in an apparent “spatial mismatch.” This is clearly illustrated in Fig. 10.10. The spatial mismatch illustrated in Fig. 10.10 is an illusion. Notice that each data point from image location 1 matches the pixel location exactly of each data point from image location 12. It was suspected that the “spatial mismatch” resulted from temperature changes in the heat source used during data acquisition or non-uniform optical grid line construction. Either of these would affect the measured intensity at a specific pixel location and could ultimately have caused the observed “spatial mismatch.”

With this in mind, it was concluded from these data, that a spatial mismatch does not exist. If a spatial mismatch does exist, it was less than 1 pixel (< 10 μm) and could not be quantified with these data or by utilizing the IR camera. The manufacturer reported positional accuracy and repeatability for the horizontal micro-traverse were ±25 μm and ±5 μm respectively. These manufacturer reported values apply to the entire table travel of 8.000 in (20.32 cm). Since the heat sink measured 38.10 mm in diameter, only 1.500 in of total travel was being used. Therefore, it was not altogether unrealistic to expect a positional accuracy and repeatability of less than 10 μm over 1.500 in (38.10 mm) of table travel. The complete set of horizontal micro-traverse spatial uncertainty data for image locations 2-10 are provided in Appendix T.

Table 10.16 Horizontal micro-traverse spatial uncertainty.

	Horizontal Micro-Traverse Spatial Uncertainty
X Direction	< 10 μm
Y Direction	< 10 μm

10.3.2 Shifted Calibration Image Spatial Uncertainty

The shifted calibration images were generated by comparing the calibration and experimental OLA intensity images. This was accomplished by utilizing Matlab®’s normxcorr2 function to compute the 2D normalized cross-correlation of the experimental and calibration OLA intensities. An x and y offset was determined and indicated the required x and y directional shift necessary for the calibration OLA intensity image to undergo such that the 2D normalized cross correlations of the experimental and calibration OLA intensity images aligned properly.

The 2D normalized cross correlation was calculated utilizing the entire image where applicable. To quantify any spatial discrepancies arising from shifted calibration OLA intensity image generation, each of the 336 images required was generated 10 separate times. The same x and y directional shift was calculated on 10 separate occasions. Therefore, it was concluded that the spatial uncertainty for the shifted calibration image generation was less than 1 pixel (< 10 μm). The x and y directional shift was recorded and tabulated for all 336 images (See Appendix U).

Table 10.17 Shifted calibration image spatial uncertainty.

Shifted Calibration Image Spatial Uncertainty.
< 10 μm

11 Discussion and Conclusions

A direct, non-intrusive measurement technique for quantitative thermal visualization of top surface wall temperatures in a fractal-like branching microchannel heat sink during flow boiling has been demonstrated and thoroughly documented. The processes necessary for quantitative temperature measurement, such as the use of an anti-reflective coating as well as detailed calibration and experimental data acquisition, reduction and analysis procedures have been provided. Significant sources of measurement uncertainty have been identified and rigorously quantified. Results indicate that temperatures can be obtained with a spatial resolution of 10 μm and an uncertainty varying from 0.82°C-1.67°C at 25°C and 0.96°C-2.80°C at 125°C.

It is imperative to note that the data reduction and analysis procedures used to determine the temperatures documented in this thesis provides an over estimate of the microchannel surface temperatures by as much as 4.43°C. Recall that 4,000 experimental radiation intensity images were acquired at each of the 255 experimental image locations (see Figs. 8.4 and 8.5). These 4,000 images were temporally averaged resulting in a single experimental average intensity image for each image location. This average intensity was substituted into the 4th order calibration curve to determine an average temperature (T_{ave1}). To correct this over estimation of the microchannel surface temperatures the 4,000 experimental radiation intensity images should have been converted to temperature first, then averaged to determine an average temperature (T_{ave2}).

Both methodologies for determining the average temperature have been expressed mathematically to illustrate the over estimation in the methodology used in this thesis.

$$T_{ave1} = A + B\frac{\sum_{4000}^{1} I}{4000} + C\left(\frac{\sum_{4000}^{1} I}{4000}\right)^2 + D\left(\frac{\sum_{4000}^{1} I}{4000}\right)^3 + E\left(\frac{\sum_{4000}^{1} I}{4000}\right)^4 \qquad 11.1$$

$$T_{ave2} = A + B\frac{\sum_{4000}^{1} I}{4000} + C\frac{\sum_{4000}^{1} I^2}{4000} + D\frac{\sum_{4000}^{1} I^3}{4000} + E\frac{\sum_{4000}^{1} I^4}{4000} \qquad 11.2$$

Notice that the first two terms on the right hand side of Equations 11.1 and 11.2 are identical. The difference between the two methodologies becomes apparent when comparing the non-linear terms of Equations 11.1 and 11.2. For example, the 3rd term on the right had side of Equation 11.1 is greater than the 3rd term on the right hand side of Equation 11.2. The same is true for both the 4th and 5th terms as well. Even though the methodology used here (T_{ave1}) provides an over estimation of the microchannel surface temperature it was selected to reduce the overall time required for data reduction and analysis. The computational time required to determine T_{ave1} was on the order of hours while than the computational time required to determine T_{ave2} was on the order of years.

Ideally, the surface temperature data acquired would be used to determine local convective heat transfer coefficients, provided the local fluid temperature was known. Unfortunately, during data acquisition, it was observed that each heat sink received from WTC contained two major flaws: 1) channel blockages and 2) gold layer penetrations. These flaws prevented any assertions with regard to convective heat transfer coefficients being made with any certainty. Particularly since these experimental results were originally intended to be compared to computational results. Therefore, the analysis presented in this work was limited to local temperature data only.

11.1 Channel Blockages

During experimental data acquisition, it was observed that liquid failed to exit the heat sink at specific peripheral locations. A magnified examination of the heat sink microchannel exits revealed that some exits did not exist, indicating a k=4 level channel blockage at the very least. Qualitatively, non existent channel exits resulted in a permanent, preexisting flow resistance within the heat sink independent of the resultant boiling flow phenomena. It was expected that the vapor formation within the microchannels due to the boiling phenomena would restrict flow in parts of the heat sink at least temporarily. These flow restrictions were considered naturally occurring and dependent upon the flow conditions, channel geometry, channel material and construction. The permanent flow resistances potentially altered the naturally occurring flow paths through the heat sink under the given flow conditions. The extent of the existing channel blockages was unquantifiable without total destruction of the heat sink. Since total heat sink destruction would render it useless, knowledge of the channel blockages was limited to observable blockages existing at the microchannel exit.

11.2 Gold Layer Penetrations

During experimental data acquisition, high intensity regions (indicated by red pixel coloration) within the channel walls were observed. In these high intensity regions, fluid could be observed flowing through the microchannel. These high intensity regions existed due to fabrication defects during the gold-silicon eutectic bonding process that resulted in the absence of the gold layer at multiple random locations along the microchannel. The absence of a gold layer allows non-focused radiation from the heater rings and the working fluid to reach the detector array resulting in a localized intensity increase. The entire procedure presented in this thesis for obtaining microchannel wall temperature data were predicated upon the idea of a uniform IR-opaque gold surface. Therefore, data acquired at locations where gold layer penetrations exist was considered inaccurate.

12 Recommendations for Future Work

The following recommendations would increase the quality, and efficiency of future work involving wall temperature measurements in fractal-like branching microchannel heat sinks using IRT. The following recommendations are numbered to indicate relative importance.

1) Locate an alternate reputable manufacturer capable of fabricating silicon heat sinks involving the silicon-gold eutectic boding process. Elimination of the quality inspection and testing as well as the modifications and preparation for data acquisition would result in a higher quality of data.
2) Integrate a reference point on the desired focal plane/microchannel top wall during fabrication. The post fabrication reference point application resulted in a misalignment between the calibration images and the experimental images that required correction during data reduction and analysis. The integration of a permanent reference point during fabrication could eliminate the need for image shifting and alignment.
3) Combine the data acquisition and file conversion LabVIEW^{TM} programs. The file conversion is a necessary step to prepare the raw data for reduction and analysis. A combination of these programs would streamline the data acquisition process and allow data reduction and analysis to occur immediately after acquisition.
4) Further development of all LabVIEW^{TM} and Matlab$^{®}$ programs used during data acquisition, reduction and analysis. These processes required significant quantities of time. Data acquisition required time on the order of weeks and data reduction and analysis required time on the order of months. While this is inherent and expected with experimental research an overall streamlining of these programs is necessary to improve processing speed. For example, preallocating memory during data reduction and analysis could reduce the time required to perform these process. In addition to this, all programs could be made more user friendly.

5) Designate a realistic quantity of memory for the storage of raw and processed data. In excess of 1.2 million raw IR images were acquired for this research. The total memory requirement for this research was approximately 1 terabyte. Insufficient storage space was problematic at times.

BIBLIOGRAPHY

[1] Montelpare, S., and Ricci, R., 2004, “An Experimental Method for Evaluating the Heat Transfer Coefficient of Liquid-Cooled Short Pin Fins Using Infrared Thermography,” Experimental Thermal and Fluid Sciences, 28, pp. 815-824.

[2] Han, G., Bird, J.C., Johan, K., Westin, A., Cao, Z., and Breuer, K., 2004, “Infrared Diagnostics for Measuring Fluid and Solid Motion Inside Silicon Microdevices,” Microscale Thermophysical Engineering, 8, pp. 169-182.

[3] Patil, V.A., 2005, “Application of Infrared Thermography for Temperature Measurements in Microscale Internal and External Flows,” M.S. thesis, Oregon State University, Corvallis, OR.

[4] Qu, W., and Mudawar, I., 2004, “Transport Phenomena in Two-Phase Micro-Channel Heat Sinks,” ASME Journal of Electronic Packaging, 126, pp. 213-224.

[5] Lee, P., and Garimella, V., 2008, “Saturated Flow Boiling Heat Transfer and Pressure Drop in Silicon Microchannel Arrays,” International Journal of Heat and Mass Transfer, 51, pp. 789-806.

[6] Hestroni, G., Mosyak, A., Pogrebnyak, E., and Yarin, L.P., 2005, “Heat Transfer in Micro-Channels: Comparision of Experiments with Theory and Numerical Results,” International Journal of Heat and Mass Transfer, 48, pp. 5580-5601.

[7] Kandlikar, S., 2002, “Fundamental Issues Related to Flow Boiling in Minichannels and Microchannels,” Experimental Thermal and Fluid Science, 26, pp. 389-407.

[8] Zhang, L., Koo, J., Jiang, L., Asheghi, M., Goodson, K.E., Santiago, J.G., and Kenny, T.W., 2002, “Measurements and Modeling of Two-Phase Flow in Microchannels With Nearly Constant Heat Flux Boundary Conditions,” Journal of Microelectromechanical Systems, 11, pp. 12-19.

[9] Astarita, T., Cardone, G., Carlomagno, G.M., and Meola, C., 2000, “A Survey on Infrared Thermography for Convective Heat Transfer Measurements,” Optics & Laser Technology, 32, pp. 593-610.

[10] Astarita, T., Cardone, G., and Carlomagno, G.M., 2006, “Infrared Thermography: An Optical Method in Heat Transfer and Fluid Flow Visualisation,” Optics and Lasers in Engineering, 44, pp. 261-281.

[11] Mori, M., Novak, L., and Sekavcnik, M., 2007, “Measurements on Rotating Blades Using IR Thermography,” Experimental Thermal and Fluid Science, 32, pp. 387-396.

[12] Sargent, S.R., Hedlund, C, R., and Ligrani, P.M., 1998, “An Infrared Thermography Imaging System for Convective Heat Transfer Measurements in Complex Flows,” Measurement Science & Technology, 9, pp. 1974-1981.

[13] Carlomagno, G.M., de Luca, L., and Yang, W.J., 1989, “Infrared Thermography in Heat Transfer,” *Handbook of Flow Visualization*, Hemisphere Publishing Company, New York, NY, pp. 531-553, Chap. 32.

[14] Hestroni, G., Rozenblit, R., and Yarin, L.P., 1996, “A Hot-Foil Infrared Technique for Studying the Temperature Field of a Wall,” Measurement Science & Technology, 7, pp. 1418-1427.

[15] Hestroni, G., Mosyak, A., and Segal, Z., 2001, “Non-Uniform Temperature Distribution in Electronic Devices Cooled by Flow in Parallel Channels,” *IEEE Transactions on Components and Packaging Technologies*, Vol. 24 (1), pp. 16-23.

[16] Hestroni, G., Mosyak, A., Segal, Z., and Pogrebnyak, E., 2003, “Two-Phase Flow Patterns in Parallel Micro-Channels,” International Journal of Multiphase Flows, 9, pp. 341-360.

[17] Hollingworth, K.D., 2004, “Liquid Crystal Imaging of Flow Boiling in Minichannels,” Proceedings of the Second International Conference on Microchannels and Minichannels (ICMM 2004), Rochester, NY, ICMM2004-2320, pp. 57-66.

[18] Hapke, I., Hartwig, B., and Schmidt J., 2002, “Flow Boiling of Water and n-Heptane in Microchennels,” Microscale Thermophysical Engineering, 6 (2), pp. 99-115.

[19] Patil, V.A., and Narayanan, V., 2006, "Spatially Resolved Temperature Measurement in Microchannels," Microfluidics and Nanofluidics, 2, pp. 291-300.

[20] Accetta, J.S., Schumaker, D.L., and Zissas, G.J., 1993, "Radiometry," *The Infrared and Electro-Optical Systems Handbook*, SPIE Optical Engineering Press, Bellingham, WA, pp. 317-360, Chap. 4.

[21] Rogalski, A., 2002, "Infrared Detectors: an Overview," Infrared Physics & Technology, 43, pp. 187-210.

[22] Horny, N., 2003, "FPA Camera Standardisation," Infrared Physics & Technology, 44, pp. 109-119.

[23] Hamamatsu Photonics K.K., Solid State Division, 2004, "Characteristics and Use of Infrared Detectors," Technical Information SD-12, pp. 3-43.

[24] Rainieri, S., and Pagliarini, G., 2002, "Data Procssing Technique Applied to the Calibration of a High Performance FPA Infrared Camera," Infrared Physics & Technology, 43, pp. 345-351.

[25] Tuckerman, D.B., and Pease, R.F.W., 1981, "High Performance Heat Sinking for VLSI," IEEE Electron Device Lett., EDI-2 (5), pp. 126-277.

[26] Pence, D.V., Cullion, R.N., and Alharbi, A.Y., 2003, "Fluid Flow Through Microscale Fractal-Like Branching Channel Networks," Journal of Fluids Engineering, 125, pp. 1051-1057.

[27] West, G.B., Brown, J.H., and Enquist, B.J., 1997, "A General Model for the Origin of Allometric Scaling Laws in Biology," Science, 276, pp. 122-126.

[28] Pence, D.V., 2002, "Reduced Pumping Power and Wall Temperature in Microchannel Heat Sinks with Fractal-Like Branching Channel Networks," Microscale Thermophysical Engineering, 6, pp. 319-330.

[29] Pence, D.V., Cullion, R.N., and Alharbi, A.Y., 2004, "Thermal Characteristics of Microscale Fractal-Like Branching Channels," Journal of Fluids Engineering, 126, pp. 744-752.

[30] Mei, Y., Lahiji, G.R., and Najafi, K., 2002, "A Robust Gold-Silicon Eutectic Wafer Bonding Technology for Vacuum Packaging," 0-9640024-4-2, Solid-State Sensor, Actuator and Microsyatems Workshop, Hilton Head Island, SC.

[31] Hordvik, A., and Skolnik, L., 1977, "Photoacoustic Measurements of Surface and Bulk Absorption in HF/DF Laser Window Materials," Applied Optics, 16 (11), pp. 2919-2924.

[32] Patil, V.A., and Narayanan, V., 2005, "Spatially Resolved Heat Transfer Rates in an Impinging Circular Microscale Jet," Nanoscale and Microscale Thermophysical Engineering, 9, pp. 183-197.

[33] Goodson, K.E., and Asheghi, M., 1997, "Near-Field Optical Thermometry," Microscale Thermophysical Engineering, 1, pp. 225-235.

[34] Wu, H.Y., and Cheng, P., 2003, "Visualization and Measurements of Periodic Boiling in Silicon Microchannels," International Journal of Heat and Mass Transfer, 46, pp. 2603-2614.

[35] Qu, W., and Mudawar, I., 2003, "Flow Boiling Heat Transfer in Two-Phase Micro-Channel Heat Sinks-I. Experimental Investigation and Assessment of Correlation Methods," International Journal of Heat and Mass Transfer, 46, pp. 2755-2771.

[36] Qu, W., and Mudawar, I., 2003, "Flow Boiling Heat Transfer in Two-Phase Micro-Channel Heat Sinks-II. Annular Two-Phase Flow Model," International Journal of Heat and Mass Transfer, 46, pp. 2773-2784.

[37] Palm, B., 2001, "Heat Transfer in Microchannels," Microscale Thermophysical Engineering, 5, pp. 155-175.

[38] Thome, J.R., 2004, "Boiling in Microchannels: A Review of Experiment and Theory," International Journal of Heat and Fluid Flow, 25, 128-139.

[39] Kandlikar, S., 2004, "Heat Transfer Mechanisms During Flow Boiling in Microchannels," ASME Journal of Heat Transfer, 126, pp. 8-16.

[40] Kandlikar, S., 2006, “Nucleation Characteristics and Stability Considerations During Flow Boiling in Microchannels,” Experimental Thermal and Fluid Science, 30, 441-447.

[41] Lee, J., and Mudawar, I., 2005, “Two-Phase Flow in High Heat Flux Micro-Channel Heat Sink for Refrigeration Cooling Applications: Part I-Pressure Drop Characteristics,” International Journal of Heat and Mass Transfer, 48, 928-940.

[42] Incropera, F.P., Dewitt, D.P., Bergman, T.L., and Lavine, A.S., 2007, *Fundamentals of Heat and Mass Transfer*, John Wiley & Sons, Hoboken, NJ, pp. 724-878, Chap. 12-13.

[43] Figliola, R.S., and Beasley, D.E., 1995, *Theory and Design for Mechanical Measurements*, John Wiley & Sons, Hoboken, NJ, pp. 125-169, Chap. 4.

[44] Siegel, R., and Howell, J., 2002, *Thermal Radiation Heat Transfer*, Taylor & Francis, New York, NY, pp. 1-31, 71-102, 777-822, Chap. 1,3,18.

[45] Pedrotti, F.L., and Pedrotti, L.S., 1993, *Introduction to Optics*, Prentice Hall, Englewood Cliffs, NJ, pp. 172-185, 200-221, 224-245, 391-405, Chap. 8,10,11,19.

[46] Pearen, K., and Zarins, A., 2005, “Infrared Image Processing,” Oregon State University, Mechanical Engineering Department, ME 552 Instrumentation, Instructor Dr. Vinod Narayanan.

APPENDIX A: Single and double layer anti-reflective coating calculations.

OBJECTIVE:

Formulate the general equations necessary to describe the theory of multilayer thin films and anti-reflective coatings. These equations will be generated using the transfer matrix method as outlined in Pedrotti, [45].

ASSUMPTIONS:

1) The transfer matrix method is more efficient than the ray tracing method. The transfer matrix method considers all transmitted and reflected beams as already summed in corresponding electromagnetic fields that satisfy the general boundary conditions required by Maxwell's equations [45]. The ray tracing method, on the other hand, addresses the multiple reflections emerging from the thin film. The amplitudes of all the individual reflected or transmitted beams are summed to find the resultant reflectance or transmittance [45]. The ray tracing method becomes complex and tedious rather rapidly as multiple beams are considered. As a result of this complexity, a two beam approximation is often used. The two beam approximation considers only the first two beams emerging from the thin film. The remaining emerging beams are considered to be negligible since their amplitudes diminish rapidly [45]. The two beam approximation is valid if the reflectance of the film is small [45]. The transfer matrix method eliminates the two beam approximation used in the ray tracing method.
2) The film thickness is of the order of the wavelength of light incident upon it. The film is considered thin.
3) The substrate thickness is several orders of magnitude greater than the wavelength of light incident upon it. The substrate is considered thick.
4) The thin film is homogeneous.
5) The thin film is isotropic.
6) There is no wave attenuation. All mediums involved are non-absorbing.

NOMENCLATURE:

Table A 1 Multi-layer thin film anti-reflective coating calculation nomenclature.

Nomenclature	**Definition**
E	Electric field vector (EFV)
E_0	EFV magnitude sum of all beams externally incident upon interface (a)
E_{i1}	EFV magnitude sum of all beams internally incident upon interface (a)
E_{i2}	EFV magnitude sum of all beams internally incident upon interface (b)
E_{i3}	EFV magnitude sum of all beams internally incident upon interface (c)
E_{r1}	EFV magnitude sum of all beams reflected at interface (a)
E_{r2}	EFV magnitude sum of all beams reflected at interface (b)
E_{r3}	EFV magnitude sum of all beams reflected at interface (c)
E_{t1}	EFV magnitude sum of all beams transmitted from interface (a)
E_{t2}	EFV magnitude sum of all beams transmitted form interface (b)
E_{t3}	EFV magnitude sum of all beams transmitted form interface (c)
B	Magnetic field vector (MFV)
n_0	External medium refractive index
n_1	First thin film refractive index
n_2	Second thin film refractive index
n_s	Thick substrate refractive index.
t_1	First thin film thickness
t_2	Second thin film thickness
X_0	Angle of incidence
X_{t1}	Angle of transmittance at top surface of the first thin film
X_{t2}	Angle of transmittance at top surface of the second thin film
X_{ts}	Angle of transmittance at top surface of the thick substrate
S	Poynting vector
ε_0	Permittivity of free space
c_0	Wave speed in a vacuum
c	Wave speed in a specific medium
n	Refractive index
μ_0	Permeability of free space
E_a	Total electric field vector at interface (a)
E_b	Total electric field vector at interface (b)
E_c	Total electric field vector at interface (c)
B_a	Total magnetic field vector at interface (a)
B_b	Total magnetic field vector at interface (b)
B_c	Total magnetic field vector at interface (c)
B_0	MFV magnitude sum of all beams externally incident upon interface (a)
B_{i1}	MFV magnitude sum of all beams internally incident upon interface (a)
B_{i2}	MFV magnitude sum of all beams internally incident upon interface (b)
B_{i3}	MFV magnitude sum of all beams internally incident upon interface (c)
B_{r1}	MFV magnitude sum of all beams reflected at interface (a)

Nomenclature	**Definition**
B_{r2}	MFV magnitude sum of all beams reflected at interface (b)
B_{r3}	MFV magnitude sum of all beams reflected at interface (c)
B_{t1}	MFV magnitude sum of all beams transmitted from interface (a)
B_{t2}	MFV magnitude sum of all beams transmitted form interface (b)
B_{t3}	MFV magnitude sum of all beams transmitted form interface (c)
γ_0	Variable defined in this calculation to simplify notation
γ_1	Variable defined in this calculation to simplify notation
γ_2	Variable defined in this calculation to simplify notation
γ_s	Variable defined in this calculation to simplify notation
δ	Phase difference as a result of **two** traversals of the thin film (general)
δ_1	Phase difference as a result of **two** traversals of the first thin film
k	Propagation constant
Δ	Optical path length difference
λ	Wavelength in a specific medium
λ_0	Wavelength in a vacuum
M_1	First thin film transfer matrix
$M_{1(11)}$	First thin film transfer matrix element (1,1)
$M_{1(12)}$	First thin film transfer matrix element (1,2)
$M_{1(21)}$	First thin film transfer matrix element (2,1)
$M_{1(22)}$	First thin film transfer matrix element (2,2)
r	Reflection coefficient
τ	Transmission coefficient
M_T	Multi-layer thin film transfer matrix
$M_{T(11)}$	Multi-layer thin film transfer matrix element (1,1)
$M_{T(12)}$	Multi-layer thin film transfer matrix element (1,2)
$M_{T(21)}$	Multi-layer thin film transfer matrix element (2,1)
$M_{T(22)}$	Multi-layer thin film transfer matrix element (2,2)
R	Total thin film reflectance
R_1	First thin film total reflectance
ν	Wave frequency
$R_{1\ min}$	First thin film minimum total reflectance

CALCULATION:

Consider the reflection of a non-normal incident beam upon a single layer thin film as illustrated in Fig. A1.

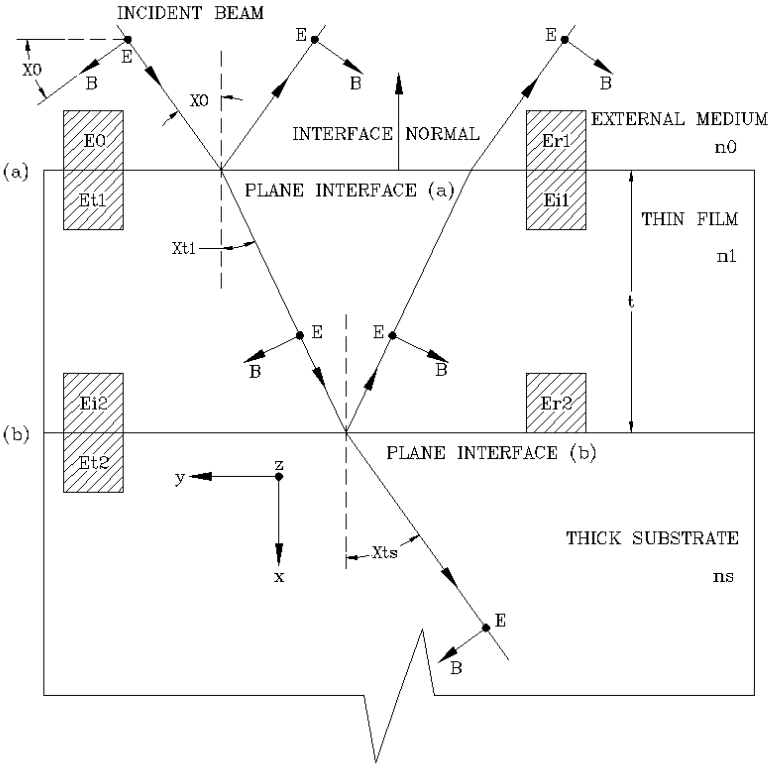

Figure A 1 Single layer anti-reflective coating schematic.

Figure A1 illustrates the reflection of the non-normal incident beam upon a single thin film layer. The incident beam is externally reflected at plane interface (a). Plane interface (a) separates the external medium, from the thin film. Upon external reflection at plane interface (a), a portion of the incident beam is refracted and transmitted through the thin film until it reaches plane interface (b) where it is subsequently internally reflected. Plane interface (b) separates the thin film from the thick substrate. Upon internal reflection at plane interface (b) a portion of the incident beam is again refracted and transmitted into the thick substrate [45]. Along each beam the electric field vector E is defined to be in the direction perpendicular to the plane of incidence, therefore pointing out of the page. This is indicated by the bold dot. The plane of incidence is defined as containing both the normal to the interface and the incident beam direction. Recall that two lines define a plane, therefore the interface normal and the incident beam direction define a plane parallel to this sheet of paper. This plane is the plane of incidence. From electromagnetic theory, it is known that for plane waves the magnetic field vector B propagates perpendicular to the electric field vector E. Notice that the y-component of the magnetic field vector B reverses direction upon reflection [45].

From electromagnetic theory the energy of a plane electromagnetic wave propagates in the direction of the Poynting vector defined as

$$S = \varepsilon_0 c_0^2 E \times B \tag{A1}$$

The magnitudes of the electric and magnetic fields are related by

$$E = cB \tag{A2}$$

The refractive index of a material is defined as

$$n = \frac{c_0}{c} \tag{A3}$$

The wave speed in a vacuum is a constant value defined as

$$c_0 = \frac{1}{\sqrt{\varepsilon_0 \mu_0}} \tag{A4}$$

Rearranging A2 the magnetic field vector magnitude can be expressed as

$$B = \frac{c}{E} \tag{A5}$$

Substituting A3 into A5, the magnetic field vector magnitude can be expressed as

$$B = \frac{En}{c_0} \tag{A6}$$

Substituting A4 into A6, the magnetic field vector magnitude can be expressed as

$$B = En\sqrt{\varepsilon_0\mu_0} \qquad \text{A7}$$

To identify the boundary conditions of the electric and magnetic fields incident upon interfaces (a) and (b) keep the following in mind. The tangential components of the resultant electric and magnetic fields are continuous across the interface. In other words, the magnitudes of E and B on either side of the interface are equal. Since the electric field vector direction has been chosen perpendicular to the plane of incidence, E is everywhere parallel and tangent to the interface planes (a) and (b). The magnetic field vector consists of both a tangential (y-direction) and perpendicular (x-direction) component [45]. The boundary conditions for the electric field at interface (a) and (b) are defined as

$$E_a = E_0 + E_{r1} \qquad \text{A8}$$

$$E_a = E_{t1} + E_{i1} \qquad \text{A9}$$

$$E_b = E_{i2} + E_{r2} \qquad \text{A10}$$

$$E_b = E_{t2} \qquad \text{A11}$$

The boundary conditions for the magnetic field at interface (a) and (b) are defined as

$$B_a = B_0\cos(X_0) - B_{r1}\cos(X_0) \qquad \text{A12}$$

$$B_a = B_{t1}\cos(X_{t1}) - B_{i1}\cos(X_{t1}) \qquad \text{A13}$$

$$B_b = B_{i2}\cos(X_{t1}) - B_{r2}\cos(X_{t1}) \qquad \text{A14}$$

$$B_b = B_{t2}\cos(X_{ts}) \qquad \text{A15}$$

A minus sign is introduced in equations A12, A13 and A14 due to the fact that the magnetic field vector y-component reverses direction upon reflection. Utilizing A7, the magnetic field vector magnitudes can be written in terms of electric field vector magnitudes.

$$B_0 = E_0 n_0 \sqrt{\varepsilon_0 \mu_0} \tag{A16}$$

$$B_{r1} = E_{r1} n_0 \sqrt{\varepsilon_0 \mu_0} \tag{A17}$$

$$B_{t1} = E_{t1} n_1 \sqrt{\varepsilon_0 \mu_0} \tag{A18}$$

$$B_{i1} = E_{i1} n_1 \sqrt{\varepsilon_0 \mu_0} \tag{A19}$$

$$B_{i2} = E_{i2} n_1 \sqrt{\varepsilon_0 \mu_0} \tag{A20}$$

$$B_{r2} = E_{r2} n_1 \sqrt{\varepsilon_0 \mu_0} \tag{A21}$$

$$B_{t2} = E_{t2} n_s \sqrt{\varepsilon_0 \mu_0} \tag{A22}$$

Substituting A16 and A17 into A12, A18 and A19 into A13, A20 and A21 into A14 and A22 into A15 the magnetic field boundary conditions become

$$B_a = \left(n_0 \sqrt{\varepsilon_0 \mu_0} \cos(X_0)\right)\left(E_0 - E_{r1}\right) \tag{A23}$$

$$B_a = \left(n_1 \sqrt{\varepsilon_0 \mu_0} \cos(X_{t1})\right)\left(E_{t1} - E_{i1}\right) \tag{A24}$$

$$B_b = \left(n_1 \sqrt{\varepsilon_0 \mu_0} \cos(X_{t1})\right)\left(E_{i2} - E_{r2}\right) \tag{A25}$$

$$B_b = \left(n_s \sqrt{\varepsilon_0 \mu_0} \cos(X_{ts})\right)\left(E_{t2}\right) \tag{A26}$$

Defining a new variable

$$\gamma_0 = n_0\sqrt{\varepsilon_0\mu_0}\cos(X_0) \tag{A27}$$

$$\gamma_1 = n_1\sqrt{\varepsilon_0\mu_0}\cos(X_{t1}) \tag{A28}$$

$$\gamma_s = n_s\sqrt{\varepsilon_0\mu_0}\cos(X_{ts}) \tag{A29}$$

Substituting A27, A28, and A29 into A23, A24, A25 and A26 the magnetic field boundary conditions become

$$B_a = \gamma_0(E_0 - E_{r1}) \tag{A30}$$

$$B_a = \gamma_1(E_{t1} - E_{i1}) \tag{A31}$$

$$B_b = \gamma_1(E_{i2} - E_{r2}) \tag{A32}$$

$$B_b = \gamma_s(E_{t2}) \tag{A33}$$

The electric field vectors E_{i2} and E_{t1} differ due to a phase difference that develops as a result of **one** traversal of the thin film [45]. The phase difference is defined as

$$\delta = k\Delta \tag{A34}$$

The propagation constant is defined as

$$k = \frac{2\pi}{\lambda} \tag{A35}$$

The optical path length difference is defined as

$$\Delta = 2n_1 t_1 (\cos(X_{t1})) \qquad \text{A36}$$

The derivation of the propagation constant, the optical path length difference and phase difference are provided in Appendix B. Equation B33 defines the phase difference resulting from **two** traversals of the first thin film. If half the phase difference is used and the wavelength is taken to be in a vacuum the phase difference between E_{i2} and E_{t1} due to **one** traversal of the first thin film can be defined as

$$\delta_1 = \frac{2\pi\, n_1 t_1 \cos(X_{t1})}{\lambda_0} \qquad \text{A37}$$

The phase difference between E_{i2} and E_{t1} due to **one** traversal of the thin film can be expressed as

$$E_{i2} = E_{t1} e^{-i\delta_1} \qquad \text{A38}$$

$$E_{t1} = E_{i2} e^{-i\delta_1} \qquad \text{A39}$$

Notice that E_{i1} differs from E_{r2} in the same manner that E_{i2} differs from E_{t1}, therefore

$$E_{i1} = E_{r2} e^{-i\delta_1} \qquad \text{A40}$$

$$E_{r2} = E_{i1} e^{-i\delta_1} \qquad \text{A41}$$

Substituting A38 and A41 into A10 and A32 the terms E_{i2} and E_{r2} can be eliminated from the boundary conditions at plane interface (b).

$$E_b = E_{t1} e^{-i\delta_1} + E_{i1} e^{i\delta_1} \qquad \text{A42}$$

$$B_b = \gamma_1 \left(E_{t1} e^{-i\delta_1} - E_{i1} e^{i\delta_1}\right) \qquad \text{A43}$$

Solving A42 and A43 simultaneously.

$$E_{t1} = \frac{\gamma_1 E_b + B_b}{2\gamma_1} e^{i\delta_1} \qquad \text{A44}$$

$$E_{i1} = \frac{\gamma_1 E_b - B_b}{2\gamma_1} e^{-i\delta_1} \qquad \text{A45}$$

Substituting A44 and A45 into A9 and A31 gives the boundary conditions at plane interface (a) in terms of the boundary conditions at plane interface (b).

$$E_a = E_{t1} + E_{i1} = \frac{\gamma_1 E_b + B_b}{2\gamma_1} e^{i\delta_1} + \frac{\gamma_1 E_b - B_b}{2\gamma_1} e^{-i\delta_1} \qquad \text{A46}$$

$$B_a = \gamma_1 \left(E_{t1} - E_{i1}\right) = \gamma_1 \left(\frac{\gamma_1 E_b + B_b}{2\gamma_1} e^{i\delta_1} - \frac{\gamma_1 E_b - B_b}{2\gamma_1} e^{-i\delta_1} \right) \qquad \text{A47}$$

Expanding, rearranging and simplifying A46 and A47

$$E_a = \frac{E_b}{2}\left(e^{i\delta_1} + e^{-i\delta_1}\right) + \frac{B_b}{2\gamma_1}\left(e^{i\delta_1} - e^{-i\delta_1}\right) \qquad \text{A48}$$

$$B_a = \frac{\gamma_1 E_b}{2}\left(e^{i\delta_1} - e^{-i\delta_1}\right) + \frac{B_b}{2}\left(e^{i\delta_1} + e^{-i\delta_1}\right) \qquad \text{A49}$$

Recall the circular identities.

$$2\cos(\delta_1) = \left(e^{i\delta_1} + e^{-i\delta_1}\right) \qquad \text{A50}$$

$$2i\sin(\delta_1) = \left(e^{i\delta_1} - e^{-i\delta_1}\right) \qquad \text{A51}$$

Substituting A50 and A51 into A48 and A49 and simplifying

$$E_a = E_b(\cos(\delta_1)) + B_b\left(\frac{i\sin(\delta_1)}{\gamma_1}\right) \qquad \text{A52}$$

$$B_a = E_b(i\,\gamma_1\sin(\delta_1)) + B_b(\cos(\delta_1)) \qquad \text{A53}$$

Expressing A52 and A53 in matrix form.

$$\begin{bmatrix} E_a \\ B_a \end{bmatrix} = \begin{bmatrix} \cos(\delta_1) & \dfrac{i\sin(\delta_1)}{\gamma_1} \\ i\,\gamma_1\sin(\delta_1) & \cos(\delta_1) \end{bmatrix} \begin{bmatrix} E_b \\ B_b \end{bmatrix} \qquad \text{A54}$$

Define the 2 x 2 matrix on the right hand side of A54 as the transfer matrix for the first thin film.

$$M_1 = \begin{bmatrix} \cos(\delta_1) & \dfrac{i\sin(\delta_1)}{\gamma_1} \\ i\,\gamma_1\sin(\delta_1) & \cos(\delta_1) \end{bmatrix} = \begin{bmatrix} M_{1(11)} & M_{1(12)} \\ M_{1(21)} & M_{1(22)} \end{bmatrix} \qquad \text{A55}$$

Substituting the A8, A11, A30, A33 and A55 into A54

$$\begin{bmatrix} E_0 + E_{r1} \\ \gamma_0(E_0 - E_{r1}) \end{bmatrix} = \begin{bmatrix} M_{1(11)} & M_{1(12)} \\ M_{1(21)} & M_{1(22)} \end{bmatrix} \begin{bmatrix} E_{t2} \\ \gamma_s E_{t2} \end{bmatrix} \qquad \text{A56}$$

Expressing A56 as two separate equations

$$E_0 + E_{r1} = M_{1(11)}E_{t2} + M_{1(12)}\gamma_s E_{t2} \qquad \text{A57}$$

$$\gamma_0(E_0 - E_{r1}) = M_{1(21)}E_{t2} + M_{1(22)}\gamma_s E_{t2} \qquad \text{A58}$$

Dividing both sides of A57 and A58 by E_0

$$1+\frac{E_{r1}}{E_0}=M_{1(11)}\frac{E_{t2}}{E_0}+M_{1(12)}\gamma_s\frac{E_{t2}}{E_0} \qquad \text{A59}$$

$$\gamma_0\left(1-\frac{E_{r1}}{E_0}\right)=M_{1(21)}\frac{E_{t2}}{E_0}+M_{1(22)}\gamma_s\frac{E_{t2}}{E_0} \qquad \text{A60}$$

Defining the reflection and transmission coefficients respectively

$$r=\frac{E_{r1}}{E_0} \qquad \text{A61}$$

$$\tau=\frac{E_{t2}}{E_0} \qquad \text{A62}$$

Substituting A61 and A62 into A59 and A60

$$1+r=M_{1(11)}\tau+M_{1(12)}\gamma_s\tau \qquad \text{A63}$$

$$\gamma_0(1-r)=M_{1(21)}\tau+M_{1(22)}\gamma_s\tau \qquad \text{A64}$$

Solving A63 and A64 simultaneously

$$r=\frac{\left(\gamma_0M_{1(11)}\right)+\left(\gamma_0\gamma_sM_{1(12)}\right)-\left(M_{1(21)}\right)-\left(\gamma_sM_{1(22)}\right)}{\left(\gamma_0M_{1(11)}\right)+\left(\gamma_0\gamma_sM_{1(12)}\right)+\left(M_{1(21)}\right)+\left(\gamma_sM_{1(22)}\right)} \qquad \text{A65}$$

$$\tau=\frac{\left(2\gamma_0\right)}{\left(\gamma_0M_{1(11)}\right)+\left(\gamma_0\gamma_sM_{1(12)}\right)+\left(M_{1(21)}\right)+\left(\gamma_sM_{1(22)}\right)} \qquad \text{A66}$$

Equations A65 and A66 allow for the evaluation of the reflective and transmissive properties of a single layer thin film represented by the transfer matrix [45]. Substituting A55 into A65 and rearranging

$$r = \frac{\cos(\delta_1)(\gamma_0 - \gamma_s) + i\sin(\delta_1)\left(\frac{\gamma_0\gamma_s}{\gamma_1} - \gamma_1\right)}{\cos(\delta_1)(\gamma_0 + \gamma_s) + i\sin(\delta_1)\left(\frac{\gamma_0\gamma_s}{\gamma_1} + \gamma_1\right)} \qquad \text{A67}$$

Multiplying both the numerator and denominator of A67 by γ_1

$$r = \frac{\cos(\delta_1)\gamma_1(\gamma_0 - \gamma_s) + i\sin(\delta_1)(\gamma_0\gamma_s - \gamma_1^2)}{\cos(\delta_1)\gamma_1(\gamma_0 + \gamma_s) + i\sin(\delta_1)(\gamma_0\gamma_s + \gamma_1^2)} \qquad \text{A68}$$

Substituting A27, A28 and A29 into A68 and simplifying

$$r = \frac{\cos(\delta_1)\, n_1 \cos(X_{t1})\{n_0 \cos(X_0) - n_s \cos(X_{ts})\} + \ldots}{\cos(\delta_1)\, n_1 \cos(X_{t1})\{n_0 \cos(X_0) + n_s \cos(X_{ts})\} + \ldots}$$

$$\frac{\ldots i\sin(\delta_1)\{n_0 \cos(X_0) n_s \cos(X_{ts}) - (n_1 \cos(X_{t1}))^2\}}{\ldots i\sin(\delta_1)\{n_0 \cos(X_0) n_s \cos(X_{ts}) + (n_1 \cos(X_{t1}))^2\}} \qquad \text{A69}$$

For the special case of normally incident light

$$X_0 = X_{t1} = X_{ts} = 0 \qquad \text{A70}$$

$$\cos(X_0) = \cos(X_{t1}) = \cos(X_{ts}) = 1 \qquad \text{A71}$$

Substituting A71 into A69

$$r = \frac{\cos(\delta_1)(n_1)(n_0 - n_s) + i\sin(\delta_1)((n_0 n_s) - (n_1)^2)}{\cos(\delta_1)(n_1)(n_0 + n_s) + i\sin(\delta_1)((n_0 n_s) + (n_1)^2)} \qquad \text{A72}$$

In general the total reflectance is defined as

$$R = r\bar{r} = (|r|)^2 \qquad \text{A73}$$

Equation A73 defines the total reflectance as the product of the reflection coefficient and the complex conjugate of the reflection coefficient. The total reflectance is also equal to the square of the absolute value of the reflection coefficient. Substituting A73 into A72

$$R_1 = \frac{\cos(\delta_1)^2 (n_1)^2 (n_0 - n_s)^2 + \sin(\delta_1)^2 \left((n_0 n_s) - (n_1)^2\right)^2}{\cos(\delta_1)^2 (n_1)^2 (n_0 + n_s)^2 + \sin(\delta_1)^2 \left((n_0 n_s) + (n_1)^2\right)^2} \qquad \text{A74}$$

The wave speed through a specific medium and a vacuum can be related to the wavelength through the frequency by the following relationships.

$$c = \lambda \nu \qquad \text{A75}$$

$$c_0 = \lambda_0 \nu \qquad \text{A76}$$

In equations A75 and A76 the frequency does not change when a wave travels from one material to another material with a different refractive index [44]. When spectral radiation travels from one medium to another the frequency remains constant while the wavelength changes due to the change in propagation velocity [44]. Substituting A75 and A76 into A3 and simplifying, the general expression for the refractive index can be written in terms of a wavelength ratio.

$$n = \frac{\lambda_0}{\lambda} \qquad \text{A77}$$

The refractive index of the first thin film can be expressed as

$$n_1 = \frac{\lambda_0}{\lambda_1} \qquad \text{A78}$$

For the case of quarter wavelength film thickness, the thin film thickness is defined as

$$t_1 = \frac{\lambda_1}{4} \qquad \text{A79}$$

Substituting A78 into A79

$$t_1 = \frac{\lambda_0}{4n_1} \qquad \text{A80}$$

Substituting A71 and A80 into A37 and simplifying

$$\delta_1 = \frac{\pi}{2} \qquad \text{A81}$$

Substituting A81 into A74 and simplifying

$$R_1 = \frac{\left((n_0 n_s) - (n_1)^2\right)^2}{\left((n_0 n_s) + (n_1)^2\right)^2} \qquad \text{A82}$$

The total reflectance is minimized when A82 is zero or when the numerator of A82 is zero. Therefore, the minimum total reflectance corresponds to

$$R_{1\min} = n_1 = \sqrt{n_0 n_s} \qquad \text{A83}$$

These results apply solely to a single layer thin film, but are easily amenable to multi-layer thin films. For example, if the plane interface (b) is the interface of another thin film rather than the thick substrate, equation A54 and A55 are still valid. In this case, the electric and magnetic fields at plane interface (b) would be related to the electric and magnetic fields at plane interface (c) at the back boundary of the second thin film by a second transfer matrix [45]. In general

$$\begin{bmatrix} E_a \\ B_a \end{bmatrix} = M_1 M_2 M_3 \ldots M_N \begin{bmatrix} E_N \\ B_N \end{bmatrix} \qquad \text{A84}$$

Defining the overall transfer matrix

$$M_T = M_1 M_2 M_3 \ldots M_N \qquad \text{A85}$$

The overall transfer matrix represents the product of the individual thin film transfer matrices in the order on which the light encounters them. Substituting A85 into A84

$$\begin{bmatrix} E_a \\ B_a \end{bmatrix} = M_T \begin{bmatrix} E_N \\ B_N \end{bmatrix} \qquad \text{A86}$$

Equation A86 is valid for single and multi-layer thin films. Consider the reflection of a non-normal incident beam upon a double layer thin film as illustrated in Fig. A2.

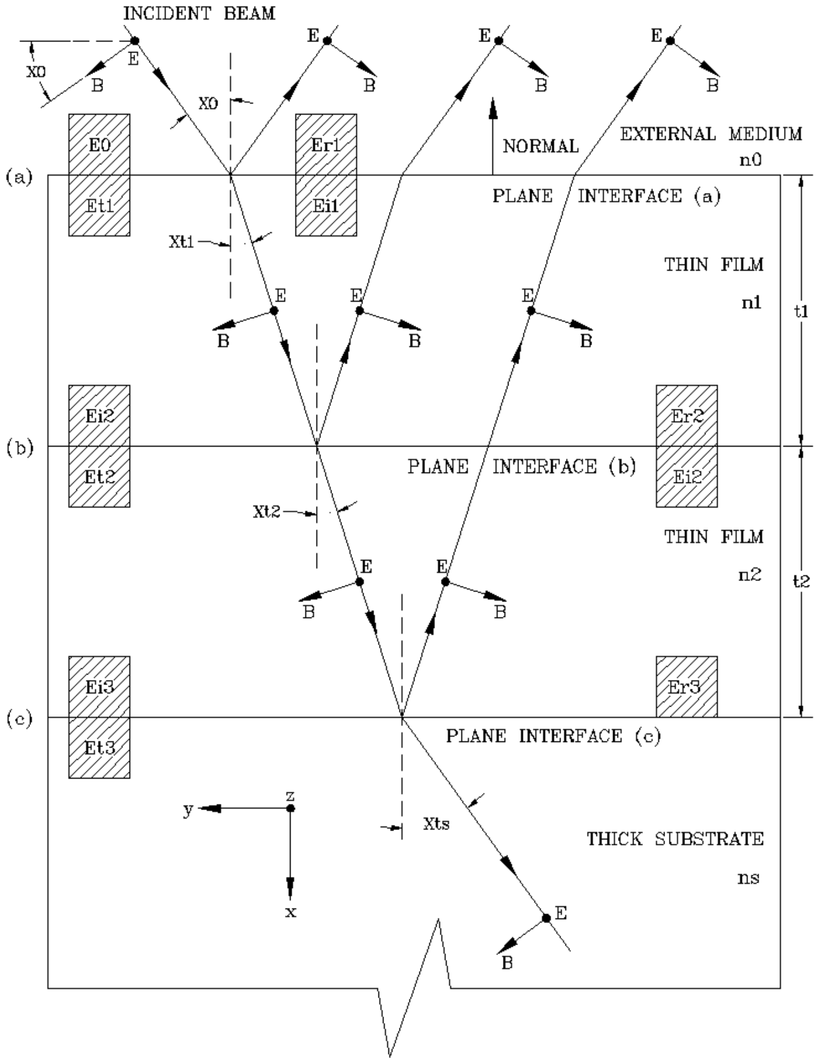

Figure A 2 Double layer anti-reflective coating schematic.

Define the transfer matrix for the second thin film

$$M_2 = \begin{bmatrix} \cos(\delta_2) & \dfrac{i\sin(\delta_2)}{\gamma_2} \\ i\,\gamma_2\sin(\delta_2) & \cos(\delta_2) \end{bmatrix} = \begin{bmatrix} M_{2(11)} & M_{2(12)} \\ M_{2(21)} & M_{2(22)} \end{bmatrix} \qquad \text{A87}$$

Substituting A55 and A87 into A85

$$M_T = \begin{bmatrix} \cos(\delta_1)\cos(\delta_2) - \sin(\delta_1)\sin(\delta_2)\frac{\gamma_2}{\gamma_1} & \frac{i\cos(\delta_1)\sin(\delta_2)}{\gamma_2} + \frac{i\cos(\delta_2)\sin(\delta_1)}{\gamma_1} \\ i\,\gamma_1\cos(\delta_2)\sin(\delta_1) + i\,\gamma_2\cos(\delta_1)\sin(\delta_2) & \cos(\delta_1)\cos(\delta_2) - \sin(\delta_1)\sin(\delta_2)\frac{\gamma_1}{\gamma_2} \end{bmatrix} \qquad \text{A87}$$

$$M_T = \begin{bmatrix} M_{T(11)} & M_{T(12)} \\ M_{T(21)} & M_{T(22)} \end{bmatrix} \qquad \text{A88}$$

For a double layer thin film a new parameter needs to be defined. (See A27, A28 and A29 for reference).

$$\gamma_2 = n_2\sqrt{\varepsilon_0\mu_0}\cos(X_{t2}) \qquad \text{A89}$$

The reflection coefficient for a double layer thin film in terms of the transfer matrix is defined as (see A65 for reference).

$$r_2 = \frac{(\gamma_0 M_{T(11)}) + (\gamma_0\gamma_s M_{T(12)}) - (M_{T(21)}) - (\gamma_s M_{T(22)})}{(\gamma_0 M_{T(11)}) + (\gamma_0\gamma_s M_{T(12)}) + (M_{T(21)}) + (\gamma_s M_{T(22)})} \qquad \text{A90}$$

Substitute A87 into A90

$$r_2 = \frac{\cos(\delta_1)\cos(\delta_2)(\gamma_0 - \gamma_s) - \sin(\delta_1)\sin(\delta_2)\left(\frac{\gamma_0\gamma_2}{\gamma_1} - \frac{\gamma_s\gamma_1}{\gamma_2}\right) + \ldots}{\cos(\delta_1)\cos(\delta_2)(\gamma_0 + \gamma_s) - \sin(\delta_1)\sin(\delta_2)\left(\frac{\gamma_0\gamma_2}{\gamma_1} + \frac{\gamma_s\gamma_1}{\gamma_2}\right) + \ldots}$$

$$\frac{\ldots i\cos(\delta_1)\sin(\delta_2)\left(\frac{\gamma_0\gamma_s}{\gamma_2} - \gamma_2\right) + i\cos(\delta_2)\sin(\delta_1)\left(\frac{\gamma_0\gamma_s}{\gamma_1} - \gamma_1\right)}{\ldots i\cos(\delta_1)\sin(\delta_2)\left(\frac{\gamma_0\gamma_s}{\gamma_2} + \gamma_2\right) + i\cos(\delta_2)\sin(\delta_1)\left(\frac{\gamma_0\gamma_s}{\gamma_1} + \gamma_1\right)} \qquad \text{A91}$$

Substitute A27, A28, A29 and A89 into A91. Multiply the numerator and denominator of A91 by $\gamma_1\gamma_2$ and cancel out the constant $(\varepsilon_0\mu_0)^{1/2}$.

$$r_2 = \frac{\cos(\delta_1)\cos(\delta_2)n_1\cos(X_{t1})n_2\cos(X_{t2})\{n_0\cos(X_0) - n_s\cos(X_{ts})\} - \ldots}{\cos(\delta_1)\cos(\delta_2)n_1\cos(X_{t1})n_2\cos(X_{t2})\{n_0\cos(X_0) + n_s\cos(X_{ts})\} - \ldots}$$
$$\frac{\ldots\sin(\delta_1)\sin(\delta_2)\{n_0\cos(X_0)(n_2\cos(X_{t2}))^2 - n_s\cos(X_{ts})(n_1\cos(X_{t1}))^2\} + \ldots}{\ldots\sin(\delta_1)\sin(\delta_2)\{n_0\cos(X_0)(n_2\cos(X_{t2}))^2 + n_s\cos(X_{ts})(n_1\cos(X_{t1}))^2\} + \ldots}$$
$$\frac{\ldots i\cos(\delta_1)\sin(\delta_2)\{n_0\cos(X_0)n_s\cos(X_{ts})n_1\cos(X_{t1}) - (n_2\cos(X_{t2}))^2 n_1\cos(X_{t1})\} + \ldots}{\ldots i\cos(\delta_1)\sin(\delta_2)\{n_0\cos(X_0)n_s\cos(X_{ts})n_1\cos(X_{t1}) + (n_2\cos(X_{t2}))^2 n_1\cos(X_{t1})\} + \ldots}$$
$$\frac{\ldots i\cos(\delta_2)\sin(\delta_1)\{n_0\cos(X_0)n_s\cos(X_{ts})n_2\cos(X_{t2}) - (n_1\cos(X_{t1}))^2 n_2\cos(X_{t2})\}}{\ldots i\cos(\delta_2)\sin(\delta_1)\{n_0\cos(X_0)n_s\cos(X_{ts})n_2\cos(X_{t2}) + (n_1\cos(X_{t1}))^2 n_2\cos(X_{t2})\}} \quad \text{A92}$$

For the special case of normally incident light

$$X_0 = X_{t1} = X_{t2} = X_{ts} = 0 \quad \text{A93}$$

$$\cos(X_0) = \cos(X_{t1}) = \cos(X_{t2}) = \cos(X_{ts}) = 1 \quad \text{A94}$$

Substituting A94 into A92

$$r_2 = \frac{\cos(\delta_1)\cos(\delta_2)n_1n_2\{n_0 - n_s\} - \sin(\delta_1)\sin(\delta_2)\{n_0(n_2)^2 - n_s(n_1)^2\} + \ldots}{\cos(\delta_1)\cos(\delta_2)n_1n_2\{n_0 + n_s\} - \sin(\delta_1)\sin(\delta_2)\{n_0(n_2)^2 + n_s(n_1)^2\} + \ldots}$$
$$\frac{\ldots i\cos(\delta_1)\sin(\delta_2)\{n_0n_sn_1 - (n_2)^2 n_1\} + i\cos(\delta_2)\sin(\delta_1)\{n_0n_sn_2 - (n_1)^2 n_2\}}{\ldots i\cos(\delta_1)\sin(\delta_2)\{n_0n_sn_1 + (n_2)^2 n_1\} + i\cos(\delta_2)\sin(\delta_1)\{n_0n_sn_2 + (n_1)^2 n_2\}} \quad \text{A95}$$

Substitute A95 into A73

$$\begin{aligned}
R_2 = {} & \frac{\cos(\delta_1)^2\cos(\delta_2)^2(n_1)^2(n_2)^2\{n_0-n_s\}^2-\ldots}{\cos(\delta_1)^2\cos(\delta_2)^2(n_1)^2(n_2)^2\{n_0+n_s\}^2-\ldots} \\
& \frac{\ldots 2\cos(\delta_1)\cos(\delta_2)\sin(\delta_1)\sin(\delta_2)n_1n_2(n_0-n_s)\{n_0(n_2)^2-n_s(n_1)^2\}+\ldots}{\ldots 2\cos(\delta_1)\cos(\delta_2)\sin(\delta_1)\sin(\delta_2)n_1n_2(n_0+n_s)\{n_0(n_2)^2+n_s(n_1)^2\}+\ldots} \\
& \frac{\ldots\sin(\delta_1)^2\sin(\delta_2)^2\{n_0(n_2)^2-n_s(n_1)^2\}^2+\ldots}{\ldots\sin(\delta_1)^2\sin(\delta_2)^2\{n_0(n_2)^2+n_s(n_1)^2\}^2+\ldots} \\
& \frac{\ldots\cos(\delta_1)^2\sin(\delta_2)^2\{n_0n_sn_1-(n_2)^2n_1\}^2+\ldots}{\ldots\cos(\delta_1)^2\sin(\delta_2)^2\{n_0n_sn_1+(n_2)^2n_1\}^2+\ldots} \\
& \frac{\ldots 2\cos(\delta_1)\cos(\delta_2)\sin(\delta_1)\sin(\delta_2)\{n_0n_sn_1-(n_2)^2n_1\}\{n_0n_sn_2-(n_1)^2n_2\}+\ldots}{\ldots 2\cos(\delta_1)\cos(\delta_2)\sin(\delta_1)\sin(\delta_2)\{n_0n_sn_1+(n_2)^2n_1\}\{n_0n_sn_2+(n_1)^2n_2\}+\ldots} \\
& \frac{\ldots\cos(\delta_2)^2\sin(\delta_1)^2\{n_0n_sn_2-(n_1)^2n_2\}^2}{\ldots\cos(\delta_2)^2\sin(\delta_1)^2\{n_0n_sn_2+(n_1)^2n_2\}^2}
\end{aligned} \qquad \text{A96}$$

From A77 the refractive index of the second thin film can be expressed as

$$n_2 = \frac{\lambda_0}{\lambda_2} \qquad \text{A97}$$

For the case of quarter wavelength film thickness, the second thin film thickness is defined as

$$t_2 = \frac{\lambda_2}{4} \qquad \text{A98}$$

The phase difference between E_{i3} and E_{t2} due to **one** traversal of the second thin film can be defined as (see A37 for reference).

$$\delta_2 = \frac{2\pi\, n_2 t_2 \cos(X_{t2})}{\lambda_0} \qquad \text{A99}$$

Substitute A94, A97 and A98 into A99 and simplify

$$\delta_2 = \frac{\pi}{2} \qquad \text{A100}$$

Substitute A81 and A100 into A96 and simplify

$$R_2 = \frac{\left(n_0 (n_2)^2 - n_s (n_1)^2\right)^2}{\left(n_0 (n_2)^2 + n_s (n_1)^2\right)^2} \qquad \text{A101}$$

The total reflectance is minimized when A101 is zero or when the numerator of A101 is zero. Therefore, the minimum total reflectance corresponds to

$$R_{2\,\min} = \frac{n_2}{n_1} = \sqrt{\frac{n_s}{n_0}} \qquad \text{A102}$$

RESULTS:

The preceding calculation derived relationships for single and double layer thin films that minimize the total reflectance. Recall, normal incidence and one quarter wavelength film thickness were assumed. For optimization purposes, it is desirable to quantify total reflectance variations with changing film thickness and material. The IR camera operating wavelength ranges are known to be 3.5-4.1 μm and 4.5-5.1 μm. For the purposes of this calculation the camera operating wavelength ranges are considered continuous and define a single wavelength range at which light is incident upon the thin films.

$$\lambda_1 = 3.5\ \mu\text{m} - 5.1\ \mu\text{m} \qquad \text{A103}$$

$$\lambda_2 = 3.5\ \mu\text{m} - 5.1\ \mu\text{m} \qquad \text{A104}$$

Define the midpoint of the incident wavelength range.

$$\lambda_{1\,\mathrm{mid}} = 4.5\ \mu\mathrm{m} \qquad \text{A105}$$

$$\lambda_{2\,\mathrm{mid}} = 4.5\ \mu\mathrm{m} \qquad \text{A106}$$

Define a thin film thickness multiplier (T) and calculate the thin film thickness.

$$t_1 = \lambda_{1\,\mathrm{mid}} T_1 \qquad \text{A107}$$

$$t_2 = \lambda_{2\,\mathrm{mid}} T_2 \qquad \text{A108}$$

Calculate the phase difference due to **one** traversal of the thin film. Substitute A71 and A78 into A37 as well as A94 and A97 into A99.

$$\delta_1 = \frac{2\pi\, t_1}{\lambda_1} \qquad \text{A109}$$

$$\delta_2 = \frac{2\pi\, t_2}{\lambda_2} \qquad \text{A110}$$

A range of phase differences are calculated over the incident wavelength range for film thicknesses of 1.1 µm, 2.3 µm, 3.4 µm, and 4.5 µm, which correspond to thickness multipliers of 25%, 50% , 75% and 100% respectively. The refractive indices are taken to be

$$n_{SiO_2} = n_1 \text{ or } n_2 = 1.46 \qquad \text{A111}$$

$$n_{Si_3N_4} = n_1 \text{ or } n_2 = 1.90 \qquad \text{A112}$$

$$n_{Air} = n_0 = 1.00 \qquad \text{A113}$$

$$n_{Si} = n_s = 3.43 \qquad \text{A114}$$

Calculations of silicon overall reflectance with a single and double layer thin film anti-reflective coating were performed for varying film thicknesses of SiO_2 and Si_3N_4. SiO_2 and Si_3N_4 were the only materials available to WTC for use as anti-reflective coatings. Calculate the total reflectance by substituting A109 - A114 into A74 and A96.

The case of normal incidence was assumed for all calculations and results for the total reflectance of a single thin film of SiO_2 and Si_3N_4 are shown in Figs. A3 and A4 as a function of wavelength for varying film thicknesses.

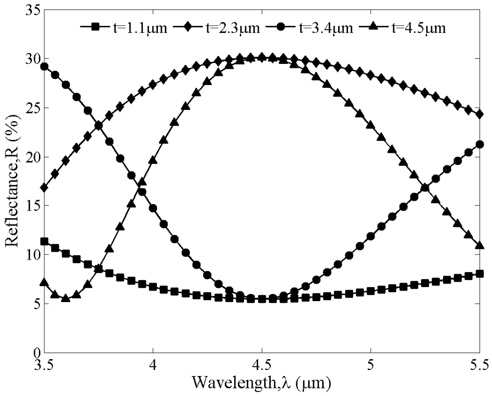

Figure A 3 Overall, normal, spectral reflectance for a single ARC of SiO_2.

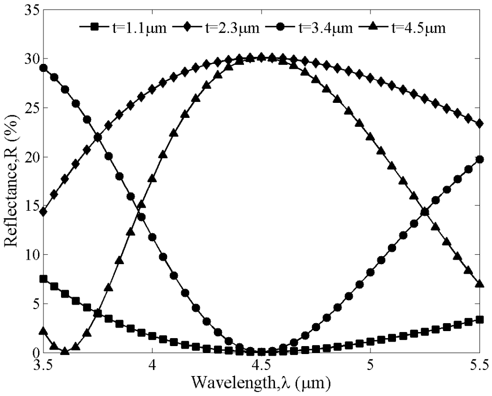

Figure A 4 Overall, normal, spectral reflectance for a single ARC of Si_3N_4.

Each curve in Figs. A3 and A4 corresponds to a different thickness of anti-reflective coating. Notice that for both SiO_2 and Si_3N_4, a film thickness of 1.1 μm resulted in the minimum overall reflectance for both detector bandwidths of 3.5-4.1 μm and 4.5-5.1 μm. A single ARC of SiO_2 resulted in an overall reflectance of 7% to 12% in the detector bandwidths, while a single ARC of Si_3N_4 resulted in an overall reflectance of 2% to 8% in the detector bandwidths.

Figures A5, A6, A7 and A8 illustrate typical reflectance curves from the double layer thin film anti-reflective coating calculations. The single layer ARC results revealed, a film thickness of 1.1 μm minimized overall, normal, spectral reflectance. Therefore, in the double layer ARC calculations one film thickness was held constant at 1.1 μm while the other film thickness was varied.

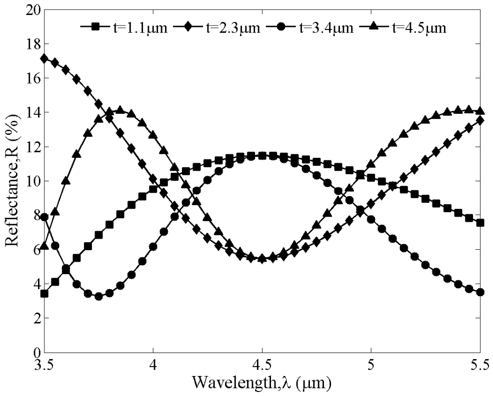

Figure A 5 Overall, normal, spectral reflectance double layer ARC.

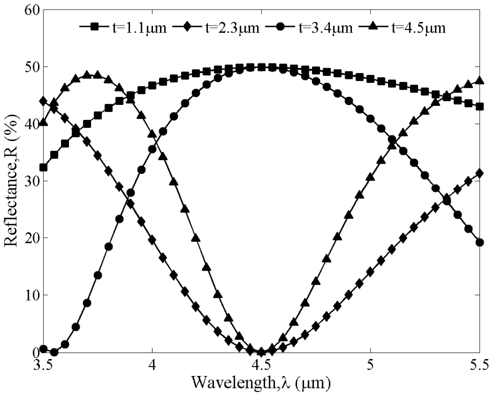

Figure A 6 Overall, normal, spectral reflectance double layer ARC.

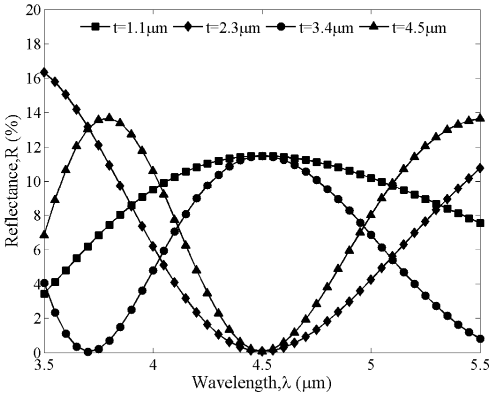

Figure A 7 Overall, normal, spectral reflectance double layer ARC.

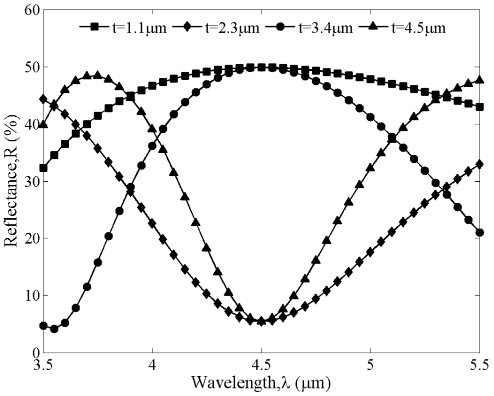

Figure A 8 Overall, normal, spectral reflectance double layer ARC.

The results presented in Fig. A5 are for a double layer ARC corresponding to a top layer of SiO_2 fixed at 1.1 μm thick and a bottom layer of Si_3N_4 whose thickness varied from 1.1-4.5 μm. Notice that the overall, normal, spectral reflectance values vary from approximately 3% to 17% in the detector bandwidths.

The results presented in Fig. A6 are for a double layer ARC corresponding to a top layer of Si_3N_4 fixed at 1.1 μm thick and a bottom layer of SiO_2 whose thickness varied from 1.1-4.5 μm. Notice that the overall, normal, spectral reflectance values vary from approximately 0% to 50% in the detector bandwidths.

The results presented in Fig. A7 are for a double layer ARC corresponding to a top layer of SiO_2 whose thickness varied from 1.1-4.5 μm and a bottom layer of Si_3N_4 fixed at 1.1 μm thick. Notice that the overall, normal, spectral reflectance values vary from approximately 0% to 16% in the detector bandwidths.

The results presented in Fig. A8 are for a double layer ARC corresponding to a top layer of Si_3N_4 whose thickness varied from 1.1-4.5 μm and a bottom layer of SiO_2 fixed at 1.1 μm thick. Notice that the overall, normal, spectral reflectance values vary from approximately 4% to 50% in the detector bandwidths.

The double layer ARC results indicated there was no unique combination of SiO_2 and Si_3N_4 film thickness that yielded a minimum reflectance, over both detector bandwidths, less than the minimum reflectance calculated for a single thin film. Based on this indication, a single thin film of Si_3N_4 1.1 μm thick was selected as the anti-reflective coating.

APPENDIX B: Propagation constant and optical path length difference derivation.

OBJECTIVE:

Formulate the equations describing the propagation constant and optical path length difference

ASSUMPTIONS:

1) The film thickness is of the order of the wavelength of light incident upon it. The film is considered thin.
2) The substrate thickness is several orders of magnitude greater than the wavelength of light incident upon it. The substrate is considered thick.
3) The thin film is homogeneous.
4) The thin film is isotropic.
5) There is no wave attenuation. All mediums involved are non-absorbing.

NOMENCLATURE:

Table B 1 Propagation constant and optical path length calculation nomenclature.

Nomenclature	**Definition**
n_0	External medium refractive index
n_1	Thin film refractive index
t_1	Thin film thickness
X_0	Angle of incidence
X_{t1}	Angle of trasmittance at interface (a)
δ	Phase difference as a result of **two** traversals of the thin film
k	Propagation constant
Δ	Thin film optical path length difference
λ	Wavelength in a specific medium
AD_{opt}	Optical path length between points A and D
ABC_{opt}	Optical path length from point A to point B to point C
AD	Physical path length between points A and D
AB	Physical path length between points A and B
BC	Physical path length between points B and C
AE	Physical path length between points A and E
EB	Physical path length between points E and B
BF	Physical path length between points B and F
FC	Physical path length between points F and C
AG	Physical path length between points A and G
AC	Physical path length between points A and C

Nomenclature	Definition
GC	Physical path length between points G and C
BG	Physical path length between points B and G
c	Harmonic wave speed
s	Harmonic wave probation time
A	Harmonic wave amplitude

CALCULATION:

A thin film is considered, therefore wave interference must be accounted for in the derivation of the propagation constant and the optical path length difference. Consider the reflection of an incident beam upon a single layer thin film as illustrated in Figure B1.

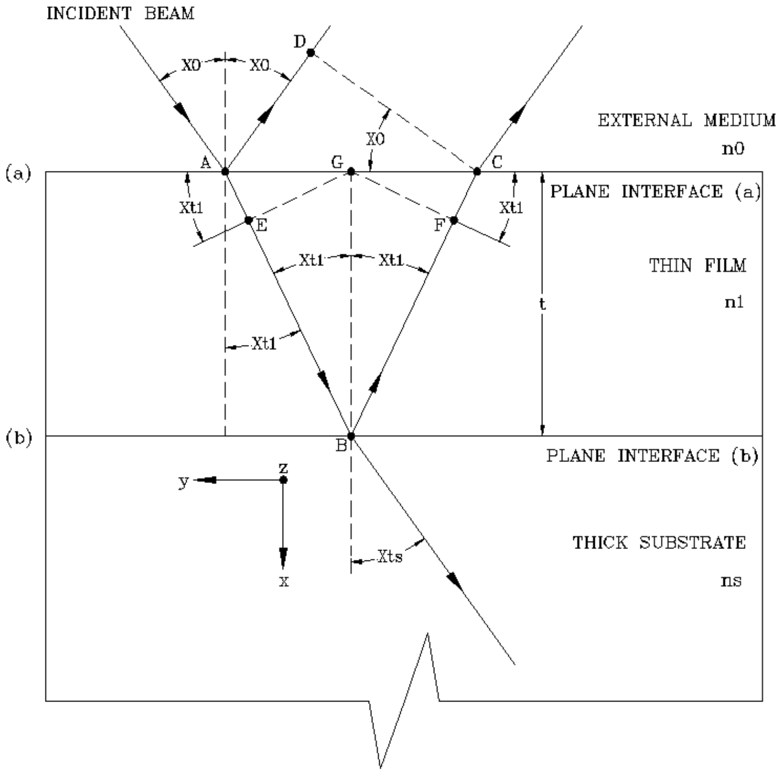

Figure B 1 Reflection of a non-normal incident beam upon a single thin film.

Figure B1 illustrates the reflection of a non-normal incident beam upon a single thin film layer. The incident beam is externally reflected at point A on plane interface (a). Plane interface (a) separates the external medium, from the thin film. Upon external reflection at plane interface (a), a portion of the incident beam is refracted and transmitted through the thin film until it reaches point B on plane interface (b). Plane interface (b) separates the thin film from the thick substrate. At point B the beam is internally reflected back through the thin film to point C on plane interface (a). Also at point B, a portion of the beam is refracted and transmitted into the thick substrate. The beam exits the thin film at point C in the same direction as the beam reflected at point A. The beam will experience multiple internal reflections within the thin film until its intensity is diminished. At this point the two beam approximation is invoked. The two beam approximation considers only the first two beams emerging from the thin film. The remaining emerging beams are considered negligible since their amplitudes diminish rapidly. Therefore, the two beams emerging from the thin film superpose and interfere with each other. Since the two beams travel along different paths from point A onward, a relative phase difference develops that can produce constructive or destructive interference [45]. The phase difference at points C and D between the emerging beams results from the optical path difference between paths AD and ABC. After points C and D are reached, the respective beams are parallel and in the same medium, therefore no additional phase differences exist once the beams emerge from the thin film [45].

Important geometric qualities pertaining to Fig. B1 include but are not limited to the following

1) Triangle ABC is an isosceles triangle. The angle of incidence equals the angle of reflection.
2) Point G lies on the midpoint of line AC. The altitude BG bisects angle ABC.
3) Lines GE and GF are perpendicular to beam paths AB and BC respectively.

As a result of these geometric qualities the following are true

$$AB = BC \tag{B1}$$

$$AG = GC \tag{B2}$$

$$AG = \frac{AC}{2} \tag{B3}$$

$$AB = AE + EB \tag{B4}$$

$$BC = BF + FC \tag{B5}$$

$$\sin(X_0) = \frac{AD}{AC} \tag{B6}$$

$$\sin(X_{t1}) = \frac{AE}{AG} \tag{B7}$$

$$\sin(X_{t1}) = \frac{FC}{GC} \tag{B8}$$

$$\cos(X_{t1}) = \frac{EB}{BG} \tag{B9}$$

$$\cos(X_{t1}) = \frac{BF}{BG} \tag{B10}$$

$$BG = t_1 \tag{B11}$$

Define the optical path lengths

$$AD_{opt} = n_0 AD \tag{B12}$$

$$ABC_{opt} = n_1 (AB + BC) \tag{B13}$$

Define the optical path length difference

$$\Delta = n_1 (AB + BC) - n_0 AD \tag{B14}$$

Substitute B4 and B5 into B14 and rearranging

$$\Delta = n_1(EB + BF) + n_1(AE + FC) - n_0AD \qquad B15$$

Equating B7 and B8, substituting B2 and simplifying

$$AE = FC \qquad B16$$

Equating B9 and B10 and simplifying

$$EB = BF \qquad B17$$

Substitute B3 into B7 and rearranging

$$AC = \frac{2AE}{\sin(X_{t1})} \qquad B18$$

Substituting B18 into B6 and rearranging

$$2AE = AD\frac{\sin(X_{t1})}{\sin(X_0)} \qquad B19$$

From Snell's law relating the angle of incidence to the angle of refraction

$$\frac{\sin(X_{t1})}{\sin(X_0)} = \frac{n_0}{n_1} \qquad B20$$

Substituting B20 into B19 and rearranging.

$$2n_1AE = AD\,n_0 \qquad B21$$

Equation B16 can be rewritten in the following manner

$$2AE = AE + FC \qquad B22$$

Substituting B22 into B21

$$n_1(AE + FC) = AD\, n_0 \qquad B23$$

Substituting B23 into B15 and simplifying

$$\Delta = n_1(EB + BF) \qquad B24$$

Equation B17 can be rewritten in the following manner

$$2EB = EB + BF \qquad B25$$

Substituting B25 into B24

$$\Delta = 2n_1 EB \qquad B25$$

Substituting B11 into B9 and rearranging

$$EB = t_1 \cos(X_{t1}) \qquad B26$$

Substituting B26 into B25

$$\Delta = 2n_1 t_1 \cos(X_{t1}) \qquad B27$$

Equation B27 defines the optical path length difference as a result of **two** traversals of the thin film. The optical path difference gives a physical length by which the beam baths AD and ABC differ. Since this problem deals with harmonic plane waves involving sine and cosine functions, oscillatory in nature, the optical path length difference does not accurately describe the difference between the two emerging beams. The difference is best described through the use of a phase difference. The optical path length difference is related to the phase difference through the use of a propagation constant. The propagation constant is derived from the general equation for a harmonic wave.

$$y = A\sin\left(k(x + cs) + 2\pi\right) \qquad \text{B28}$$

A graphical representation of equation B28 is provided in Fig. B2

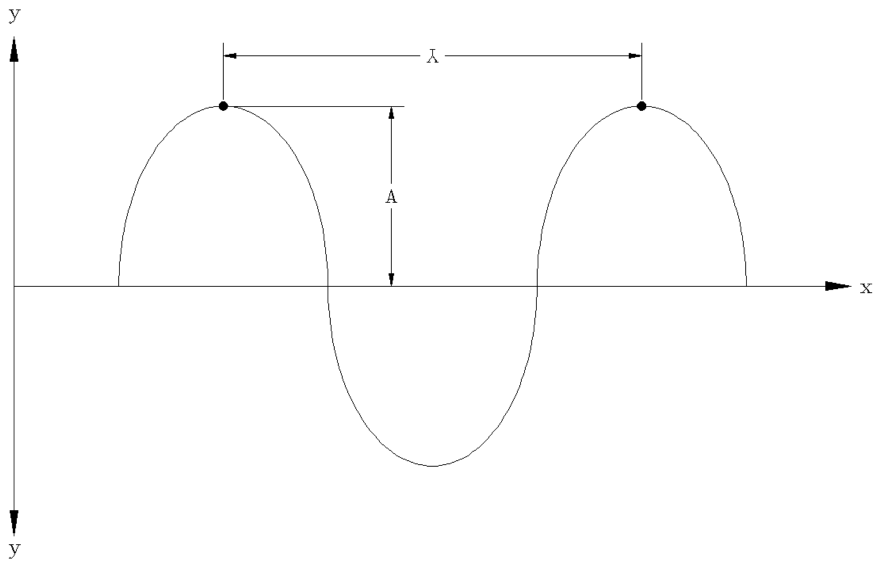

Figure B 2 Illustration of a typical harmonic wave.

In Fig. C2 the repetitive spatial unit of the wave, the wavelength, is designated by λ. If all the x values are increased by λ, the wave will be reproduced. This illustrates the inherent periodicity associated with harmonic waves involving sine and cosine functions. Mathematically, this periodicity can be represented in the following manner [45].

$$y = A\sin\left(k\left((x + \lambda) + cs\right)\right) \qquad \text{B29}$$

Equating B28 and B29

$$\mathrm{A}\sin\left(\mathrm{kx}+\mathrm{k}\lambda+\mathrm{kcs}\right)=\mathrm{A}\sin\left(\mathrm{kx}+\mathrm{kcs}+2\pi\right) \qquad \text{B30}$$

The only way B30 is true is if

$$\mathrm{k}=\frac{2\pi}{\lambda} \qquad \text{B31}$$

Equation B31 defines the propagation constant. The phase difference is defined by both the optical path length difference and the propagation constant.

$$\delta=\mathrm{k}\Delta \qquad \text{B32}$$

Substituting B27 and B31 into B32

$$\delta_1=\frac{4\pi\ \mathrm{n}_1\mathrm{t}_1\cos(\mathrm{X}_{\mathrm{t}1})}{\lambda} \qquad \text{B33}$$

Equation B33 defines the phase difference resulting from **two** traversals of the first thin film.

APPENDIX C: Calibration test section component information.

The calibration test section consists of the following components: 1) a copper cylinder, 2) cartridge heaters, 3) peripheral insulation, 4) base insulation, 5) adaptor legs, 6) T-type thermocouples, 7) a dry interface thermal film, 8) a high conductivity thermal paste and 9) thermal stretch tape. Table C1 documents the calibration test section components make, model and specifications.

Table C 1 Calibration test section component make, model and specifications.

Component	Mfg.	Model	Specifications
Copper cylinder	McMaster Carr	8965K221	• Alloy 101 Extreme Temperature Electronic Grade Copper. • 99.99% pure. • Ø1.500 in x 3.375 in (Ø38.10 mm x 85.73 mm)
Cartridge heaters	Watlow	Firerod E1A52	• 120 v maximum voltage. • 100 W maximum power. • Ø0.250 in x 1.000 in (Ø6.35 mm x 25.40 mm)
Peripheral insulation	McMaster Carr	6140K14	• Ultra Rigid Cellular Glass Pipe Insulation with Self Sealing Jacket. • Ø1.625 in ID x 1.000 in (Ø41.28 mm ID x 25.40 mm) thick.
Base insulation	McMaster Carr	7017K81	• Grade G-7 Garolite. • 3.625 in x 3.625 in x 1.000 in (92.08 mm x 92.08 mm x 25.40 mm) thick.
Adaptor legs	OSU Machine Shop	--	• Aluminum scrap from OSU machine shop.
T-type thermocouples	Omega	5SC-TT-T-30-36	• 30 gauge wire. • 36 in long. • 0.010 in (0.25 mm) bead diameter. • PFA insulation.
Micro-Faze® dry interface thermal film	AOS Thermal Compounds	Micro-Faze® A6	• 0.002 in (50.8 µm) thick aluminum substrate. • 0.002 in (50.8 µm) thick thermal compound layer on each side of the aluminum substrate. • 0.006 in (152.4 µm) total thickness. • 0.02 °C in2/W thermal resistance.

Component	Mfg.	Model	Specifications
High conductivity thermal paste	Omega	OmegaTherm® 201	• Silicone based paste. • Continuous use temperature range of -40°C-200°C.
Thermal stretch tape	Minco	#20 stretch tape	• High temperature self-fusing silicon rubber tape.

Detailed fabrication drawings of the copper cylinder, Garolite base insulation and adaptor legs are provided in Figs C1 – C5.

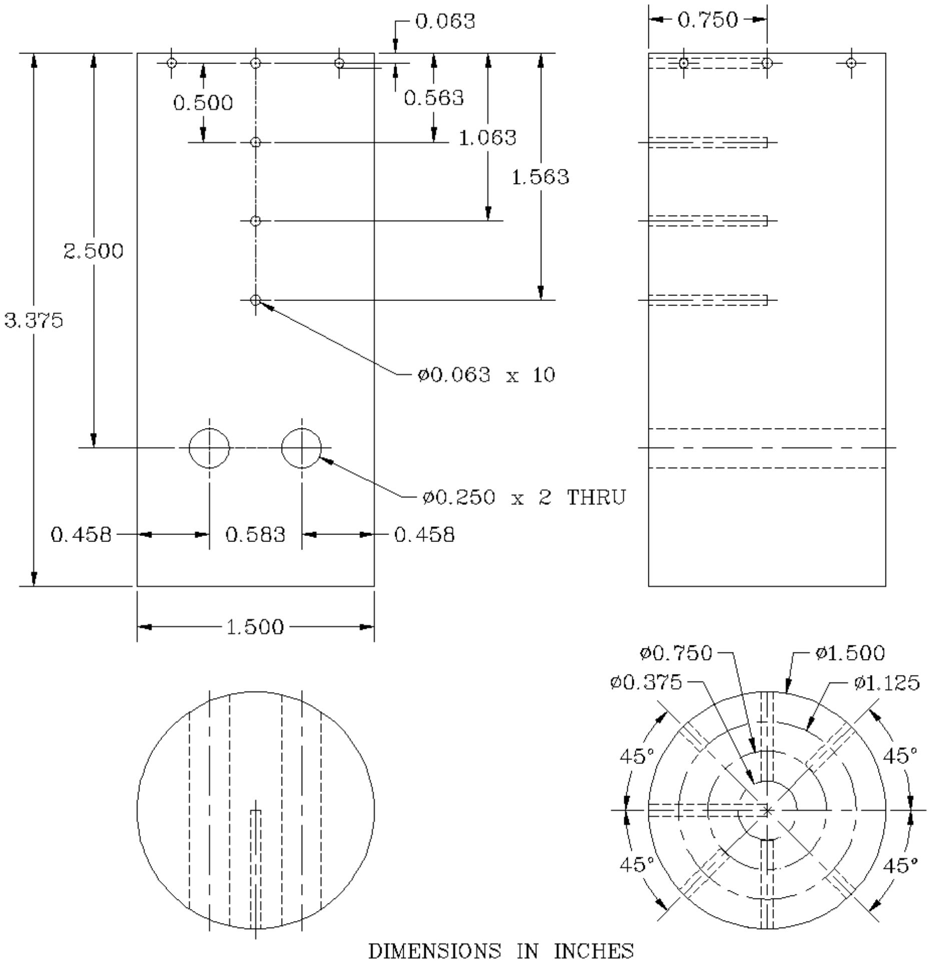

Figure C 1 Copper cylinder fabrication drawing.

The copper cylinder, measuring Ø1.500 in x 3.375 in (Ø38.10 mm x 85.73 mm), was fabricated from alloy 101 extreme temperature electronic grade 99.99% pure copper.

Two holes, Ø0.250 in (Ø6.35 mm), were bored through the copper cylinder to receive the cartridge heaters. Four cylindrical pockets measuring Ø0.063 in x 0.750 in (Ø1.59 mm x 19.05 mm) deep were machined along the copper cylinder's vertical axis to receive the axial thermocouples. Six cylindrical pockets were machined around the copper cylinder's periphery, 0.063 in (1.59 mm) away from the copper cylinder's top surface, to receive the near surface thermocouples. Two of the six near surface thermocouple pockets measure Ø0.063 in x 0.563 in (Ø1.59 mm x 14.29 mm) deep, two pockets measure Ø0.063 in x 0.375 in (Ø1.59 mm x 9.53 mm) deep and two pockets measure Ø0.063 in. x 0.188 in (Ø1.59 mm x 4.76 mm) deep. Figures C2 and C3 illustrate the thermocouple locations for clarity.

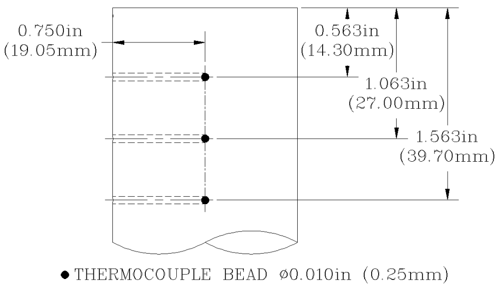

Figure C 2 Axial TC location.

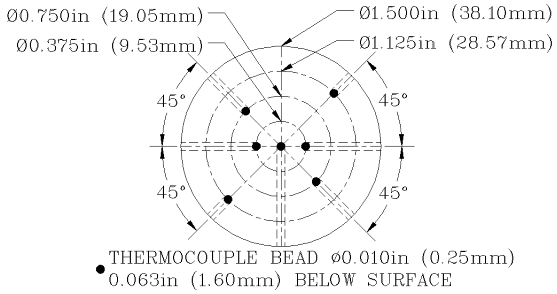

Figure C 3 Near surface TC location.

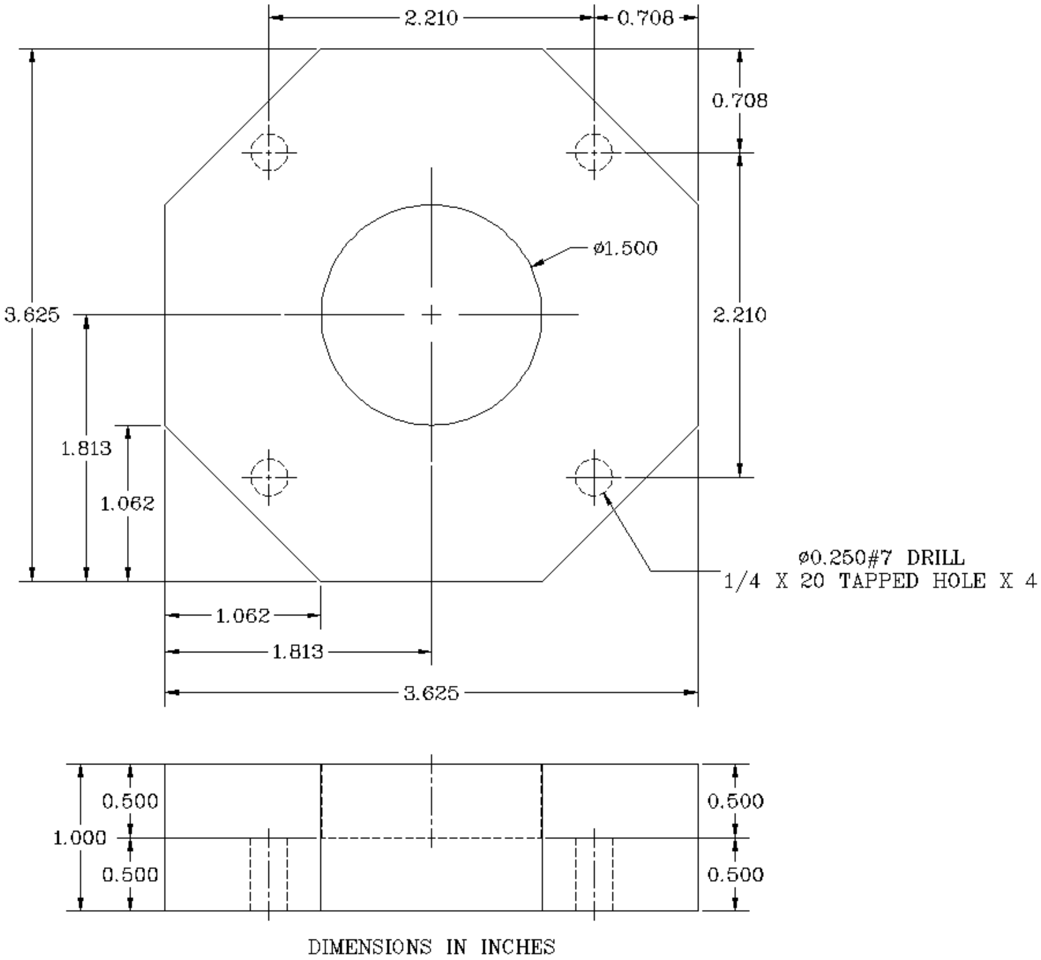

Figure C 4 Garolite base insulation (top plate) fabrication drawing.

A cylindrical pocket measuring Ø1.500 in x 0.500 in (Ø38.10 mm x 12.70 mm) deep was machined into the center of the Garolite base insulation to receive the copper cylinder.

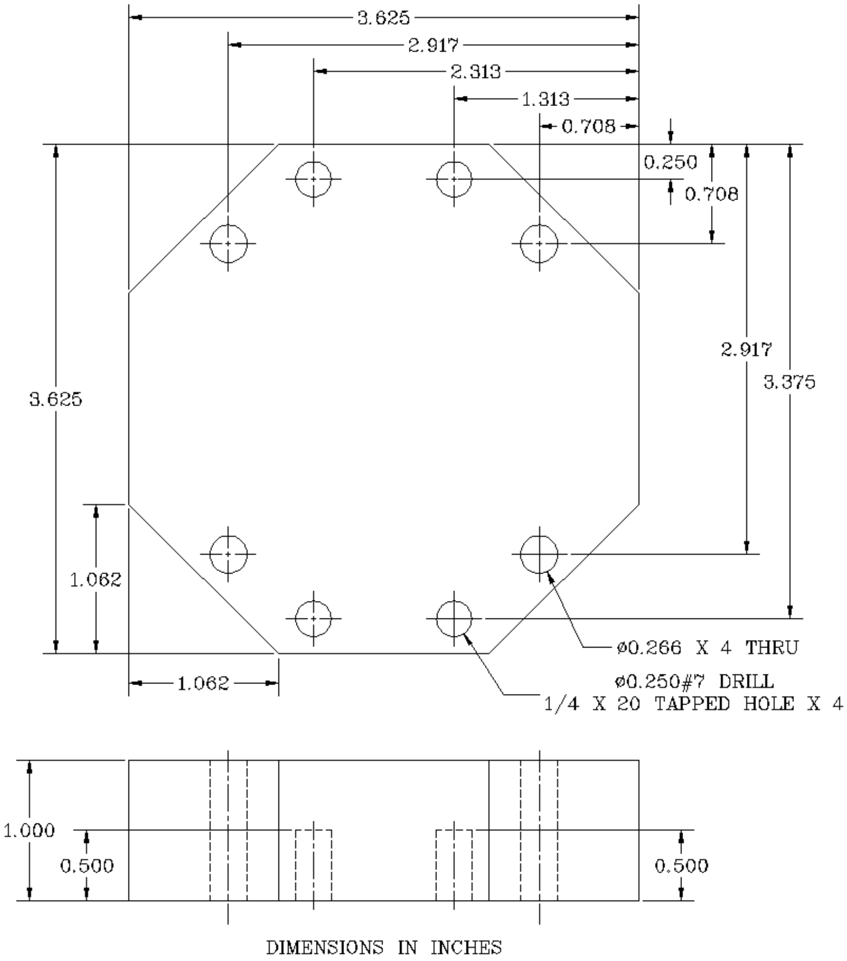

Figure C 5 Garolite base insulation (bottom plate) fabrication drawing.

The bottom plate of the Garolite base insulation bolted directly to the top plate of the Garolite base insulation. The maximum, commercially available thickness of the Garolite G-7 base insulating material was 1.000 in (25.40 mm). Two plates bolted together were necessary to achieve the desired thickness for proper insulation of the copper cylinder.

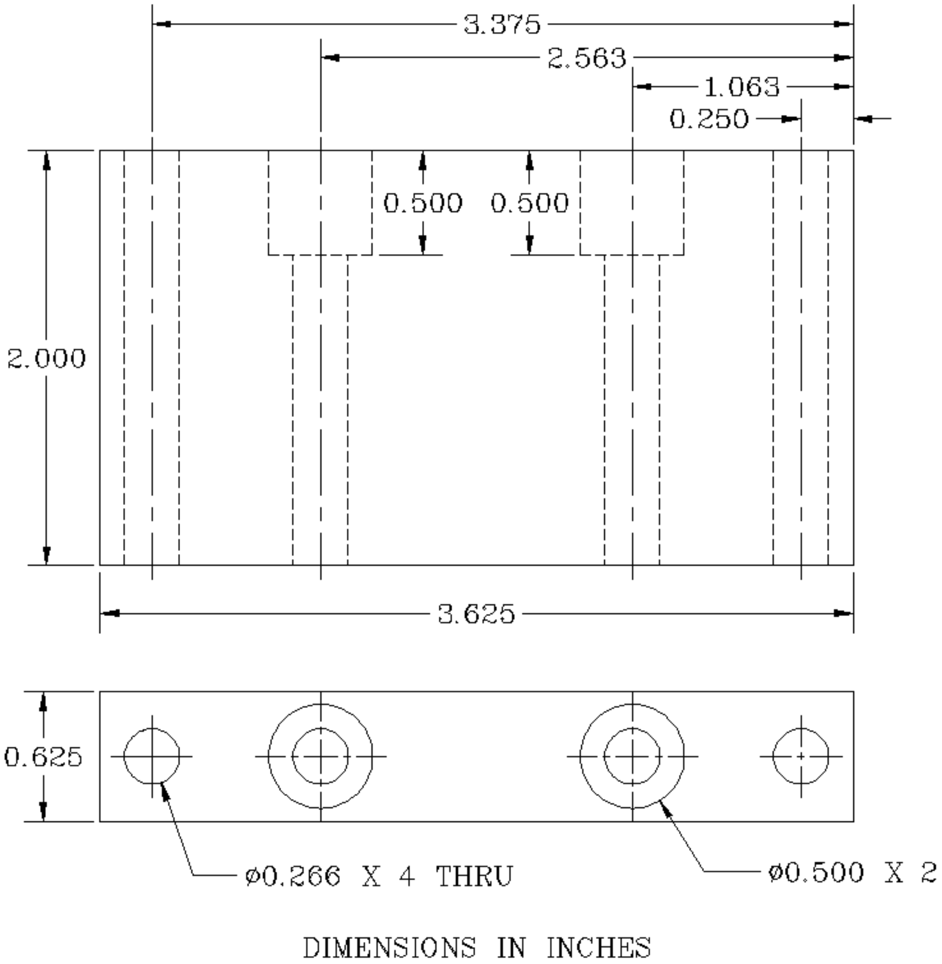

Figure C 6 Adaptor legs fabrication drawing.

The adaptor legs attach the calibration test section to the IRT imaging facility by bolt directly to the Garolite base insulation and the vertical micro-traverse stage.

APPENDIX D: Experimental flow loop component information.

The make, model and specifications for each component of the experimental flow loop are documented on Table D1.

Table D 1 Experimental flow loop component make, model and specifications.

Component	Mfg.	Model	Specifications
Hot Water Heater	Vanguard	1PZ81	• 6 gallon capacity. • 120 VAC. • 2000 W maximum.
Hot Water Heater Controller	Omega	CNi-3244-DC	• 12-36 V. • 3 W maximum. • Manufacturer accuracy of ±0.5°C, 0.03% of reading.
DAQ Card	National Instrument	SCB-68	• Shielded I/O connector block with 86 pin connectors.
Pump Drive	Micropump	Series 180 O/C DC306A	• 500-4000 RPM.
Pump Head	Cole Parmer	74011-01	• 0-150 gm/min.
Filter Housing	Shelco Filters	FOSBN-786DUB	• Pressure rating of 250 psig at 275°F.
Filter Cartridge	Shelco Filters	MS10	• 10 µm pore size.
Voltage Divider	OSU	--	• Designed and fabricated by Younghoon Kwak.
Mass Flow Meter	Micromotion	CMF010N32 3NABUEZZZ	• 0-1370 gm/min • Manufacturer accuracy of 0.10% of the flow rate.
Constant Temperature Oil Bath	Neslab	EX-511	• 41.5 liter capacity. • 3°C-150°C. • 800 W maximum. • Manufacturer stability of ±0.01°C.
RTD	Therm-X	D-SP-4TT-A18-6-36ST	• 0-250°C. • Manufacturer accuracy of ±0.7°C.
Thermocouple	Omega	T-type	• -250°C-350°C. • Manufacturer accuracy of ±1.0°C or 0.75% of reading
Data Logger	Fluke	Hydra	• Portable data acquisition unit.

Component	**Mfg.**	**Model**	**Specifications**
Pressure Transducer	Cole Parmer	EW-68074-08	• 0-25 psig output. • 0.1-5.1 VDC output. • Manufacturer accuracy of ±0.228 kpa.
Vacuum Pump	Barnant	Air Cadet	• 20 in Hg maximum vacuum.
DC Power Supply1	Tektronix®	PS280	• One fixed 5V, 3A output. • Two variable 0-30V, 0-2A outputs.
DC Power Supply2	Agilent	E3617A	• One variable 0-60V, 0-1A output.
DC Power Supply3	Tektronix®	PS2521G	• One variable 0-6V, 0-3A output. • Two variable 0-36V, 0-1.5A outputs.

APPENDIX E: IRT imaging facility component information and wiring details.

The make, model and specifications for each component of the IRT imaging facility are documented on Table E1. Electrical wiring termination points for the stepper motor drivers, waveform generators, IR Camera and the SCB-68 DAQ card are documented on Table E2.

Table E 1 IRT imaging facility component make, model and specifications.

Component	Mfg.	Model	Specifications
IR camera	Nippon Avionics	TVS 8500	• Detector bandwidths of 3.5-4.1 μm and 4.5-5.1 μm. • 256 x 256 InSb photovoltaic focal plane array. • 120 frames/sec maximum data acquisition rate.
Microscope objective	Nippon Avionics	TVS 8500	• 30 mm fixed focal distance. • 2.56 mm x 2.36 mm field of view. • 256 pixel x 236 pixel field of view. • 10 μm/pixel resolution
Camera stand	--	--	• 8 in vertical travel.
Vertical micro-traverse stage	Thorlabs	LJ750	• 25.40 mm total vertical travel. • 10 μm resolution. • 360° rotational capability.
Leveling platform	Newport	37 Series	• ±4° tilt. • ±4° rotation. • 2 μm resolution.
Horizontal micro-traverse stage	Parker	406008LN	• 8 in travel in the x and y direction. • ±25 μm positional accuracy. • ±5 μm positional repeatability. • 5 threads per inch on x and y drive screws.
X-direction stepper motor driver	Compumotor	S6	• 50,800 steps/revolution. • 0.1 μm/step.
Y-direction stepper motor driver	Compumotor	S6	• 50,800 steps/revolution. • 0.1 μm/step.
X-direction wave form generator	Tektronix®	AFG 2020	• Programmable wave form generator.

Component	Mfg.	Model	Specifications
Y-direction wave form generator	Tektronix®	AWG 2021	- Programmable wave form generator.
SCB 68 DAQ card	National Instrument	SCB-68	- Shielded I/O connector block with 68 pin connector.
Computer w/LabVIEW™	Dell	Optiplex GX400	- Standard issue OSU lab computer.

Table E 2 IRT imaging facility component wiring termination points.

Wire	Termination Points			
Description	**From**	**Pin/IO#**	**To**	**Pin/IO#**
+ X Direction	X Motor Driver	Pin 2	SCB 68 DAQ	IO 22 DAC0
- X Direction	X Motor Driver	Pin 15	SCB 68 DAQ	IO 55 A0GND
+ X Shutdown	X Motor Driver	Pin 16	SCB 68 DAQ	IO 17 DIO1
- X Shutdown	X Motor Driver	Pin 17	SCB 68 DAQ	IO 50 DGND
+ X Step	X Motor Driver	Pin 1	X Wave Gen.	CH 1 Output
- X Step	X Motor Driver	Pin 14	X Wave Gen.	CH 1 Output
+ X Trigger	X Wave Gen.	Trigger Input	SCB 68 DAQ	IO 52 DIO0
- X Trigger	X Wave Gen.	Trigger Input	SCB 68 DAQ	IO 18 DGND
+ Y Direction	Y Motor Driver	Pin 2	SCB 68 DAQ	IO 21 DAC1
- Y Direction	Y Motor Driver	Pin 15	SCB 68 DAQ	IO 54 DGND
+ Y Shutdown	Y Motor Driver	Pin 16	SCB 68 DAQ	IO 49 DIO2
- Y Shutdown	Y Motor Driver	Pin 17	SCB 68 DAQ	IO 15 DGND
+ Y Step	Y Motor Driver	Pin 1	Y Wave Gen.	CH 1 Output
- Y Step	Y Motor Driver	Pin 14	Y Wave Gen.	CH 1 Output
+ Y Trigger	Y Wave Gen.	Trigger Input	SCB 68 DAQ	IO 47 DIO3
- Y Trigger	Y Wave Gen.	Trigger Input	SCB 68 DAQ	IO 13 DGND
+ Camera Trig.	IR Camera	Terminal 1	SCB 68 DAQ	IO 2 CTR0
- Camera Trig.	IR Camera	Terminal 2	SCB 68 DAQ	IO 35 DGND
+ Camera Sync.	IR Camera	Terminal 3	SCB 68 DAQ	IO 40 CTR1
- Camera Sync.	IR Camera	Terminal 4	SCB 68 DAQ	IO 7 DGND

APPENDIX F: Heat sink quality inspection and testing details and results.

Details and results of the visual inspection, air flow and heater ring resistance tests performed on each heat sink are provided here.

VISUAL INSPECTION

Each heat sink was subjected to a thorough visual inspection utilizing the naked eye and a Leica Zoom 2000 desktop microscope with a magnification range of 10.5 to 45. The visual inspection was used to determine if the heater rings and the anti-reflective coatings existed on the provided heat sinks. When viewed at an angle, the anti-reflective coating has a green tint to it, therefore its existence could be determined visually. The results of the visual inspection are documented in Table F1.

Table F 1 Visual inspection results.

Heat Sink Number	Heater Rings	Anti-Reflective Coating
1	Yes	Yes
2	Yes	Yes
3	Yes	Yes
4	Yes	Yes
5	Yes	Yes
6	Yes	Yes
7	Yes	No
8	Yes	No
9	No	No
10	No	No
11	No	No
12	No	No

Visual inspection results reveal heat sinks 7, 8, 9, 10, 11, and 12 could not be used for flow data acquisition. In addition to this, magnified visual inspection of the heat sinks revealed pitting on both the top and bottom surfaces. In some instances the pitting actually penetrated the entire depth of the bottom silicon wafer providing a path for fluid to exit the heat sink at a location other than at the periphery. Fluid discharge, through the bottom silicon wafer, upstream of the designed microchannel exit presents an electrical hazard with regard to the vacuum chuck. To verify the potential for this hazard, an air flow test was conducted for each heat sink.

AIR FLOW TEST

A 500 ml Pyrex beaker was filled with enough deionized and distilled water to completely submerge the heat sink. The heat sink was placed in the beaker with the bottom silicon wafer facing upward. A rubber tipped syringe was utilized to force air into the heat sink. Air bubbles were visually observed exiting the heat sink. If the observed bubbles exited the heat sink through the microchannel exit, the heat sink was considered to have passed the air flow test. If the observed bubbles observed exited the heat sink upstream of the microchannel exit, the heat sink was considered to have failed the air flow test. The results of the air flow test are documented in Table F2.

Table F 2 Air flow test results.

Heat Sink Number	Air Flow Test Results
1	Fail
2	Pass
3	Pass
4	Pass
5	Fail
6	Fail
7	Pass
8	Fail
9	Fail
10	Fail
11	Fail
12	Fail

Air flow test results reveal heat sinks 1, 5, 6, 8, 9, 10, 11, and 12 could not be used for flow data acquisition.

HEATER RING RESISTANCE TEST

The resistance for each heater ring, as well as the resistance between adjacent heater rings was measured to verify proper application of the SiO_2 isolative coating. The heater ring contact pads were numbered 1 through 6 and the resistance of every possible path was measured. Resistance measurements were obtained using a handheld multimeter. Figure F1 illustrates the heater ring contact pad numbering scheme.

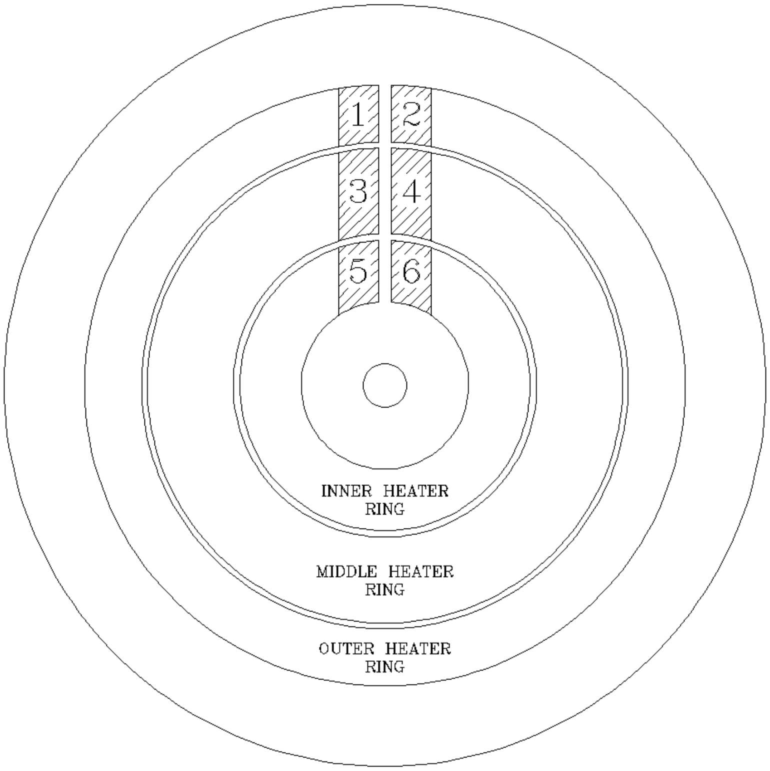

Figure F 1 Contact pad numbering.

In Fig. F1 the heater ring contact pads are numbered 1 through 6, arbitrarily for convenience. The resistance path 1↔2 indicates the resistance between contact pad 1 and contact pad 2, etc. The results for the heater ring resistance test are documented in Table F3.

Table F 3 Heater ring resistance test results (Ω).

	Heat Sink Number											
Resistance Path	**1**	**2**	**3**	**4**	**5**	**6**	**7**	**8**	**9**	**10**	**11**	**12**
1↔2	28	410	8628	565	406	38	27	28	0	0	0	0
1↔3	∞	∞	∞	∞	∞	∞	∞	∞	0	0	0	0
1↔4	∞	∞	∞	∞	∞	∞	∞	∞	0	0	0	0
1↔5	∞	∞	∞	∞	∞	∞	∞	∞	0	0	0	0
1↔6	∞	∞	∞	∞	∞	∞	∞	∞	0	0	0	0
2↔3	∞	∞	∞	∞	∞	∞	∞	∞	0	0	0	0
2↔4	∞	∞	∞	∞	∞	∞	∞	∞	0	0	0	0
2↔5	∞	∞	∞	∞	∞	∞	∞	∞	0	0	0	0

	Heat Sink Number											
Resistance Path	**1**	**2**	**3**	**4**	**5**	**6**	**7**	**8**	**9**	**10**	**11**	**12**
2↔6	∞	∞	∞	∞	∞	∞	∞	∞	0	0	0	0
3↔4	28	673	159	712	412	14	13	13	0	0	0	0
3↔5	∞	∞	∞	∞	∞	∞	∞	∞	0	0	0	0
3↔6	∞	∞	∞	∞	∞	∞	∞	∞	0	0	0	0
4↔5	∞	∞	∞	∞	∞	∞	∞	∞	0	0	0	0
4↔6	∞	∞	∞	∞	∞	∞	∞	∞	0	0	0	0
5↔6	15	579	1043	710	1055	12	12	12	0	0	0	0

Heater ring resistance test results reveal heat sinks 9, 10, 11, and 12 could not be used for flow data acquisition. A measured resistance value of zero indicated that heater rings were non-existent. The resistance values measured between adjacent heater rings approached infinity and indicated that the heater rings were in fact electrically isolated from each other and the heat sink.

SUMMARY OF QUALITY INSPECTION AND TEST RESULTS

A summary of the results from the visual inspection, air flow and the heater ring resistance tests is documented in Table F4.

Table F 4 Summary of quality inspection and testing results.

Heat Sink Number	**Heater Rings**	**ARC**	**Air Flow Test**	**Resistance 1↔2 (Ω)**	**Resistance 3↔4 (Ω)**	**Resistance 5↔6 (Ω)**
1	Yes	Yes	Fail	28	28	15
2	Yes	Yes	Pass	410	673	579
3	Yes	Yes	Pass	8628	159	1043
4	Yes	Yes	Pass	565	712	710
5	Yes	Yes	Fail	406	412	1055
6	Yes	Yes	Fail	38	14	12
7	Yes	No	Pass	27	13	12
8	Yes	No	Fail	28	13	12
9	No	No	Fail	0	0	0
10	No	No	Fail	0	0	0
11	No	No	Fail	0	0	0
12	No	No	Fail	0	0	0

The quality inspection and testing revealed that out of 12 possible heat sinks only 3 proved to be viable candidates for use in flow data acquisition. During preliminary flow data acquisition heat sinks number 2 and 3 proved to be inadequate. Suspected internal microchannel blockages created increased inlet pressures. An increase in inlet pressure resulted in an increase in power supplied to the pump for a desired flow rate. The increased pump power exceeded the acceptable power limits of the pump and resulted in the inability to achieve the desired flow rates. In addition to this, the increased pump power resulted in adequate inlet plenum sealing creating an electrical hazard with the vacuum chuck. Heat sink number 4 was ultimately selected and utilized for flow data acquisition.

APPENDIX G: Heat sink heater ring resistance calculation.

OBJECTIVE:

Calculate the heat sink nichrome heater ring resistance.

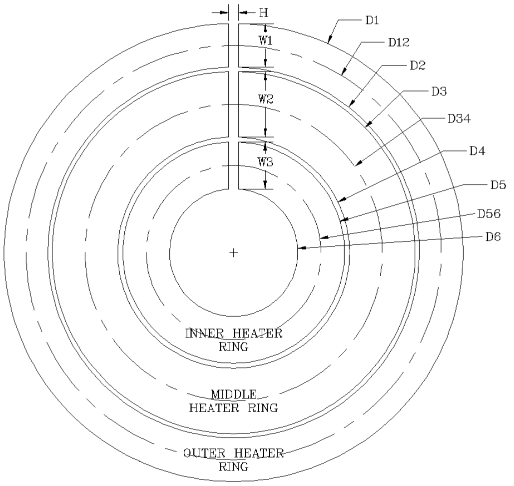

Figure G 1 Heater ring configuration.

NOMENCLATURE:

Table G 1 Heater ring resistance calculation nomenclature.

Nomenclature	Definition	Value
A	Heater ring cross-sectional area	--
D_1	Outer heater ring outer diameter	30.07 (mm)
D_{12}	Outer heater ring middle diameter	27.20 (mm)
D_2	Outer heater ring inner diameter	24.33 (mm)
D_3	Middle heater ring outer diameter	23.77 (mm)
D_{34}	Middle heater ring middle diameter	19.48 (mm)
D_4	Middle heater ring inner diameter	15.19 (mm)
D_5	Inner heater ring outer diameter	14.53 (mm)
D_{56}	Inner heater ring middle diameter	11.45 (mm)
D_6	Inner heater ring inner diameter	8.38 (mm)
H	Heater ring gap width	0.66 (mm)
L	Heater ring length	--
ρ	Nichrome resistivity at 20°C	0.0011 (Ω mm)

Nomenclature	Definition	Value
R_{inner}	Inner heater ring resistance	--
R_{middle}	Middle heater ring resistance	--
R_{outer}	Outer heater ring resistance	--
T	Heater ring thickness	0.5 (µm)
W_1	Outer heater ring width	2.87 (mm)
W_2	Middle heater ring width	4.30 (mm)
W_3	Inner heater ring width	3.08 (mm)
ρ	Nichrome resistivity at 20°C	0.0011 (Ω mm)

CALCULATION:

The electrical resistance of a material is defined as

$$R = \frac{\rho L}{A} \tag{G1}$$

The heater ring length is defined as

$$L = \pi D - H \tag{G2}$$

Where D is the heater ring middle diameter D_{12}, D_{34} or D_{56}. The heater ring cross-sectional area is defined as

$$A = TW \tag{G3}$$

Where W is the heater ring width W_1, W_2 or W_3 Substituting G2 and G3 into G1 and calculating the individual heater ring resistance.

$$R_{outer} = \frac{\rho((\pi D_{12}) - H)}{TW_1} = 64.9796\,\Omega \tag{G4}$$

$$R_{middle} = \frac{\rho((\pi D_{34}) - H)}{TW_2} = 31.0094\,\Omega \tag{G5}$$

$$R_{inner} = \frac{\rho\left(\left(\pi D_{56}\right) - H\right)}{TW_3} = 25.2398\,\Omega \qquad \text{G6}$$

APPENDIX H: Contact pad painting process details.

Physical handling of the heat sink during the contact pad painting process was carried out utilizing latex gloves. Prior to silver conductive paint application, the heat sink was cleaned with isopropyl alcohol and allowed to air dry. Once dry, the electrically isolated areas between and surrounding the contact pads were masked off using painters blue, low adhesive tape. A razor blade and metal straightedge were used to cut the masking tape to the desired thickness. The silver conductive paint was applied to the unmasked areas with a model CW2200MTP Circuit Works, Micro Tip, Conductive Pen. After application, the paint was allowed to dry for 24 hours. After 24 hours drying time, the masking tape was removed and the heat sink was ready for use. Figure H1 illustrates the heat sink masked and unmasked areas.

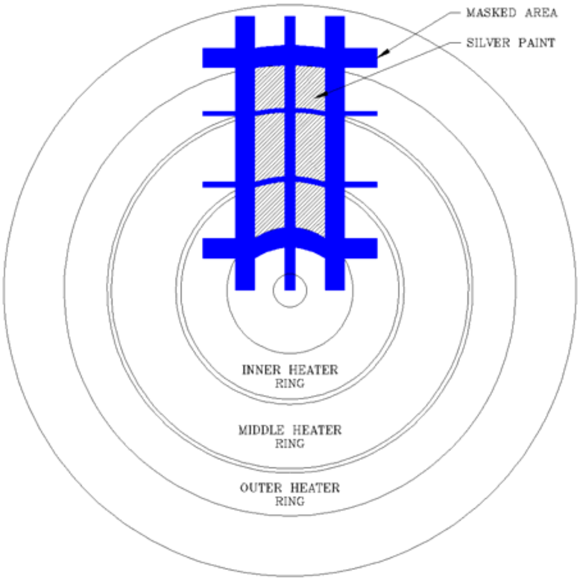

Figure H 1 Contact pad masking.

APPENDIX I: Calibration data acquisition procedure.

The calibration data were obtained using the procedure outlined below. Note that steps indicated by * were performed with latex gloves donned.

1) Bolt the assembled calibration test section directly to the vertical micro-traverse stage of the IRT imaging facility via the two adaptor legs.
2) Level the camera stand in the xy plane using a circular bull's eye level and sheet metal shims. The xy plane is indicated in the schematic of the IRT imaging facility (see Fig. 6.1).
3) Level the camera in the xy plane using a circular bull's eye level.
    a) The camera rotates, in the xz plane, slightly in its mount on the camera stand. The application of slight pressure to the camera sides allow it to be leveled in the xy plane. The xy and xz planes are indicated in the schematic of the IRT imaging facility (see Fig. 6.1).
4) Plug in the ten T-type thermocouples embedded in the calibration test section to the SCXI 1300 temperature module.
    a) The calibration test section axial and near surface temperature distribution is monitored and recorded using these thermocouples.
5) Cut a circular piece of Micro-Faze® A6 dry interface thermal film measuring approximately Ø1.500 in (38.10 mm) to match the copper cylinder and heat sink outer diameters.
    a) A cardboard template and scissors are used to cut the circular piece of Micro-Faze® A6 dry interface thermal film from a 12 in x 12 in sheet.
6) *Clean the copper cylinder top surface using a cotton swab and isopropyl alcohol.
7) *Remove the protective plastic sheet from the bottom surface of the Micro-Faze® thermal film using a straight teasing needle and forceps. This ensures the manufacturer applied thermal compound is not disturbed or removed.
8) *Apply the bottom surface of the Micro-Faze® thermal film to the copper cylinder top surface.

   a) Apply light to moderate finger pressure (5 to 10 psi) to the Micro-Faze$^{®}$ top surface to facilitate adhesion between the copper cylinder and the Micro-Faze$^{®}$ thermal film.
   b) The Micro-Faze$^{®}$ thermal film is naturally tacky. Adhesion achievement is not difficult.

9) *Clean the heat sink bottom surface using a cotton swab and isopropyl alcohol.
10) *Remove the protective plastic sheet from the top surface of the Micro-Faze$^{®}$ thermal film using a straight teasing needle and forceps. This ensures the manufacturer applied thermal compound is not disturbed or removed.
11) *Apply the bottom surface of the heat sink to the top surface of the Micro-Faze$^{®}$ thermal film.
    a) Apply light to moderate finger pressure (5 to 10 psi) to the heat sink top surface to facilitate adhesion between the heat sink and the Micro-Faze$^{®}$ thermal film.
    b) Extreme care must be taken to ensure the heat sink does not fracture.
    c) The Micro-Faze$^{®}$ thermal film is naturally tacky. Adhesion achievement is not difficult.
12) *Level the heat sink in the xy plane. The xy plane is indicated in the schematic of the IRT imaging facility (see Fig. 6.1).
    a) Place a circular bull’s eye level on the top surface of the heat sink.
    b) Adjust the leveling platform to level the heat sink in the xy plane.
13) *Clean the heat sink top surface using a cotton swab and isopropyl alcohol.
    a) The heat sink top surface cleaning should only occur at room temperature. Isopropyl alcohol applied to a heated heat sink surface produces, smudges and smears.
14) Apply voltage to the cartridge heaters to heat the calibration test section copper cylinder.

a) Prior to calibration data acquisition, the copper cylinder was heated until the near surface thermocouples measured a steady 135°C and then allowed to cool to room temperature.

b) Heating the copper cylinder allows total wetting between the copper cylinder, Micro-Faze® thermal film and heat sink therefore, minimizing contact resistance.

15) Apply voltage to the cartridge heater to heat the copper cylinder to 25°C. Three hours were allowed for the calibration test section to reach steady state.

16) Turn on the camera and configure it for data acquisition. See Appendix J for IR camera configuration details.

17) Open the LabVIEW™ calibration program and configure it for data acquisition. See Appendix K for the calibration data acquisition LabVIEW™ program details.

18) Focus the camera on the heat sink top surface and locate the rectangular Kapton® tape strip.

19) Align the Kapton® tape strip right edge with the camera field of view left edge. See Fig. I1 for clarity.

20) Align the heat sink circumferential edge with the camera field of view top edge. See Fig. I1 for clarity.

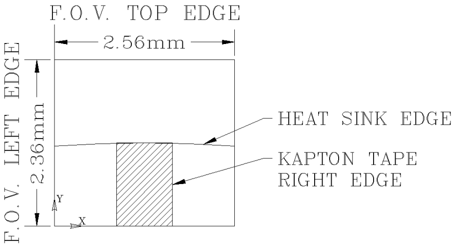

Figure I 1 Kapton® tape alignment with camera field of view.

21) Focus the camera on the desired focal plane, the heat sink gold layer. See Fig. I2 for focal plane identification and clarity.

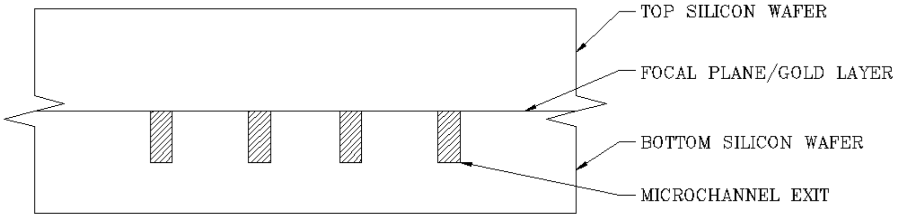

Figure I 2 Heat sink focal plane.

22) Electronically manipulate the horizontal micro-traverse stage such that the heat sink inlet plenum is centered within the camera field of view.
    a) Centering of the inlet plenum in the camera field of view was confirmed by operator visual inspection.
23) After visual confirmation of the inlet plenum centering, the horizontal micro-traverse stage was electronically manipulated to move the heat sink to image location number one (IML1). See Figs. 7.4 and 7.5.
24) Start the calibration data acquisition LabVIEW^{TM} program.

Steps 15-24 were repeated for each of the six nominal calibration temperatures of 25°C, 45°C, 65°C, 85°C, 105°C and 125°C. Table I1 documents the voltage and current requirements for each nominal calibration temperature.

Table I 1 Calibration temperature voltage and current requirements.

Temperature	**25°C**	**45°C**	**65°C**	**85°C**	**105°C**	**125°C**
Voltage (V)	0	13.0	18.5	22.5	26.5	32.0
Current(A)	0	0.180	0.256	0.312	0.369	0.450

APPENDIX J: IR camera data acquisition configuration details.

To configure the camera for data acquisition the following steps were performed.

1) Turn on the camera.
2) Set the camera temperature range to 20°C - 150°C.
    a) Position the cursor on AVIO.
    b) Depress EXE on the camera remote.
    c) Position the cursor on MEASURE.
    d) Depress EXE on the camera remote.
    e) Position the cursor on RANGE.
    f) Depress EXE on the camera remote.
    g) Position the cursor on 20°C - 150°C.
    h) Depress EXE on the camera remote.
3) Enable the camera trigger and synchronize capabilities.
    a) Position the cursor on REC.
    b) Depress EXE on the camera remote.
    c) Position the cursor on RT.
    d) Depress EXE on the camera remote.
    e) Position the cursor on CFG.
    f) Depress EXE on the camera remote.
4) Under the RECORD RT tab.
    a) Set SPEED to 60 frames per second.
    b) Set START to 1.
    c) Set END to 1023.
    d) Set MODE to NORMAL.
    e) Set TRIG to START/EXTTRG.
    f) Set EXTSYNC to ON.
5) Under the RECORD CF tab.
    a) Set HOUR to 0.
    b) Set MIN to 0.
    c) Set SEC to 5.

   d) Set COUNT to 1.
   e) Set TRIG to START/EXTTRG.
   f) Set EXTSYNC to ON.
6) Position the cursor on OK.
7) Depress EXE on camera remote.
8) Position the cursor on EXE.
9) Depress EXE on camera remote.
   a) TRIG? & SYNC? is displayed on the camera monitor.
   b) The camera is waiting for a trigger and synchronization signal from the LabVIEW^{TM} data acquisition program.

APPENDIX K: Calibration data acquisition LabVIEW^{TM} program details.

The calibration data acquisition program is a comprehensive program that controls both x and y direction stepper motors as well as the IR camera trigger and synchronization. The program inputs incorporate a 1/2 field of view overlap in both the x and y direction dictating the stepper motors move the horizontal micro-traverse stage in a manner necessary for data acquisition and analysis. Figure K1 is a flow diagram illustrating the basic structure of the calibration data acquisition program.

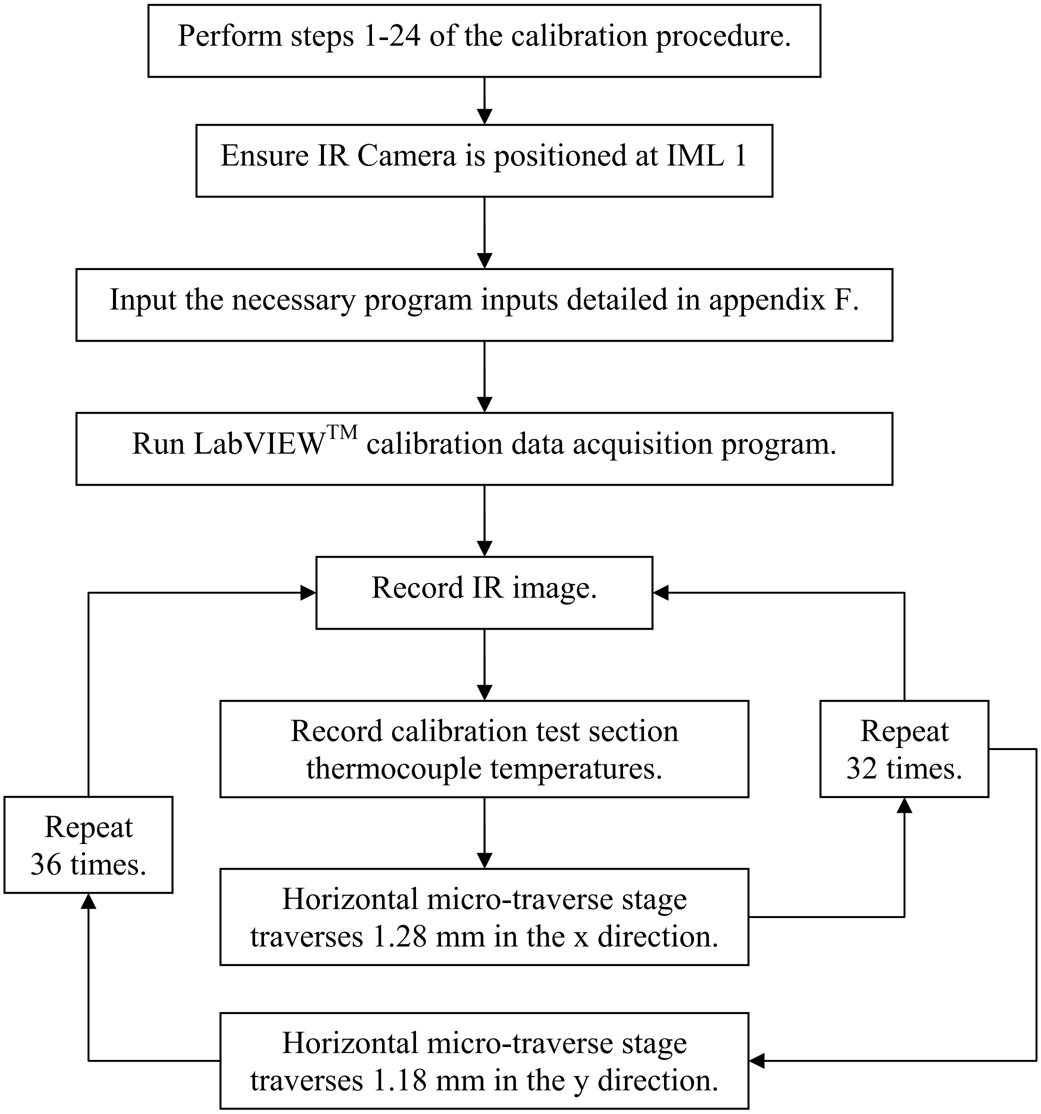

Figure K 1 Calibration data acquisition LabVIEW^{TM} program structure.

The inputs for the calibration data acquisition LabVIEW^{TM} program are outlined below.

1) Set milliseconds to wait M1 to 12,864.
    a) 12,864 milliseconds is the time required to move 1.28 mm in the x direction.
    b) 12,864 milliseconds corresponds to a ½ field of view overlap.
2) Set milliseconds to wait M2 to 11,859.
    a) 11,859 milliseconds is the time required to move 1.18 mm in the y direction.
    b) 11,859 milliseconds corresponds to a ½ field of view overlap.
3) Set ½ total number of columns to 15.
4) Set total number of columns in + x direction to 32.
5) Set total number of columns in – x direction to 32.
6) Set total number of temp. data sets per location in + x direction to 1.
7) Set total number of temp. data sets per location in – x direction to 1.

Using the external triggering and synchronization capabilities of the camera forces any data acquired to be saved to the cameras internal memory. The camera can store a maximum of 1023 images in its internal memory. Therefore, the acquisition of 1,152 calibration images is broken up into two phases. The input settings outlined in steps 1-7 result in a total of 960 calibration images. The input settings outlined in steps 8-14 result in the acquisition of the remaining 192 calibration images.

8) Set milliseconds to wait M1 to 12,864.
9) Set milliseconds to wait M2 to 11,859.
10) Set ½ total number of columns to 3.
11) Set total number of columns in + x direction to 32.
12) Set total number of columns in – x direction to 32.
13) Set total number of temp. data sets per location in + x direction to 1.
14) Set total number of temp. data sets per location in – x direction to 1.

APPENDIX L: Experimental data acquisition procedure.

The experimental images were obtained using the procedure outlined below. Note that steps indicated by * were performed with latex gloves donned. Recall the experimental flow loop schematic illustrated in Fig. L1.

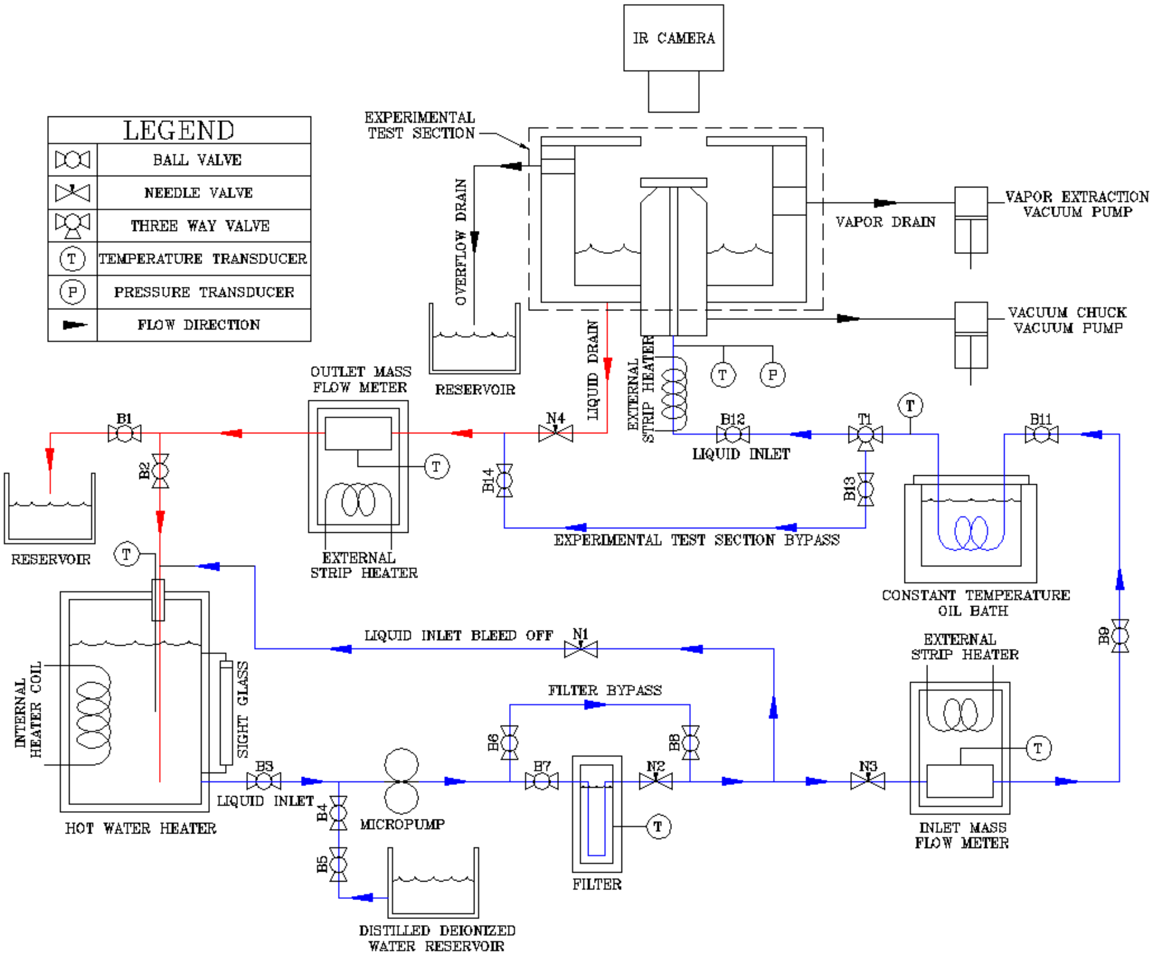

Figure L 1 Experimental flow loop schematic.

1) Bolt the assembled experimental test section directly to the vertical micro-traverse stage of the IRT imaging setup. Note the heat sink is not secured to the vacuum chuck and the camera is not mounted to the camera stand at this point.
2) Connect the liquid inlet, liquid drain, and vacuum pump lines to the experimental test section. Do not connect the heater ring electrical leads at this point.

3) Fill the hot water heater with deionized, distilled water. Deionized, distilled water was gravity fed into the hot water heater from a deionized, distilled water reservoir.
    a) Open valves B3, B4 and B5.
    b) Close valves B6 and B7.

   The hot water heater was filled until the liquid level in the sight glass measured approximately 1.00 in (25.40 mm) from the top. After filling the hot water heater, valves B4 and B5 were closed.
4) Turn on power to the hot water heater controller. The power supply must be set to channel 1 with an output of 0.4 A and 12.0 V. To send power to the hot water heater controller depress the output on/off button.
5) Plug in the hot water heater. Ensure the light switch near the hot water heater controller is in the off position.
6) Set the hot water heater controller set point to 100°C.
    a) See Appendix M for hot water heater controller configuration details.
7) Boil/degas the deionized distilled water for a minimum of 30 minutes. The onset of vapor escaping the opening at the top of the hot water heater signified the beginning of the degassing process.
8) Turn on the constant temperature oil bath.
9) Set the constant temperature oil bath set point to 95°C. The constant temperature oil bath was allowed to warm up during the degassing process.
10) After completing the degassing process, set the hot water heater controller set point to 85°C. 85°C is the hot water heater controller operating set point.
11) Turn on the Fluke data logger. The data logger records the temperature measured by the RTDs located at the constant temperature oil bath exit and the experimental vacuum chuck inlet. The display will read ERROR 6. This indicates no configuration has been set.
12) Configure channels 1 and 3 of the Fluke data logger.
    a) See Appendix M for Fluke data logger configuration details.

13) Start the LabVIEW^{TM} flow loop data acquisition program. The data logger should start to click in a repetitive pattern when the LabVIEW^{TM} program is running.
14) Turn on the pump.
15) Circulate deionized, distilled, degassed water through the flow loop.
    a) Open valves B3, B6, B8, N3, B9, B11, B13, B14 and B2.
    b) Close valves B7, N2, N1, B10, B12, N4, and B1.
    c) Applying 22 VDC to the pump. Notice that 23 VDC is the maximum allowable for the pump.

Notice that the filter, and experimental test section are all bypassed during circulation. Water is allowed to circulate through the flow loop for a minimum of 2 hours to allow the system to reach steady state.

16) Turn on the external strip heaters wrapped around the inlet and outlet mass flow meters. The external strip heaters decrease the time required for the flow loop to reach steady state.
17) Connect three multimeters to the heater ring electrical leads. One multi-meter each for the inner, middle and outer heater ring. The multi-meters should be configured to measure resistance.
18) *Place the heat sink on the vacuum chuck. Ensure that the six pogo pins make contact with the six heater ring contact pads. Successful contact is verified using the resistance values measured by the multimeters.
19) Once successful contact has been achieved, turn on the vacuum chuck vacuum pump. The vacuum pump is activated by a foot pedal.
20) Record the measured heater ring resistances.
21) Verify the voltage divider can accommodate the measured heater ring resistances. Verification is done through the use of an excel spreadsheet program.
22) Determine the voltage necessary for each heater ring to achieve the desired total power input. Voltage and current determination is done through the use of an excel spreadsheet program.

23) Disconnect the three multi-meters from the heater ring electrical leads.
24) Connect the heater ring electrical leads to their respective power supplies. Do not turn on the heater ring power supplies at this point.
25) After the flow loop has reached steady state, divert the flow to the experimental test section.
    a) Open valves B7, N2, B12 and N4.
    b) Close valves B6, B8, B13 and B14
26) Adjust the pump voltage and valves N1, N3 and N4 to achieve the desired mass flow rates.
27) Set the experimental test section inlet temperature to 88°C by using an external strip heater wrapped around a length of pipe just upstream from the vacuum chuck inlet.
    a) Apply 40-50 VAC to this external strip heater.
    b) Use the LabVIEW^{TM} flow loop data acquisition program to monitor the inlet temperature.
28) Place the reservoir cover on the liquid reservoir to minimize vapor interaction with the IR camera.
29) Turn on the heater ring power supplies.
30) Apply the previously determined voltages to the respective heater ring. Incrementally increase the voltage to each heater ring by approximately 0.5 volts until the desired voltage is reached. Allow approximately 2 minutes for voltage and thermal stabilization between each incremental increase.
31) Position the tripod directly above the experimental test section.
32) Mount the IR camera and standard objective on the tripod and position it directly above the experimental test section.
33) Turn on the IR camera and set the temperature range to 20°C - 150°C.
    a) See Appendix J for IR camera configuration details.
34) Focus the IR camera on the heat sink top surface. Ensure the entire heat sink is visible within the camera field of view.

35) Record experimental images at 30 and 120 frames per second. Images recorded at 30 frames per second can be done with the IR camera provided software, TVS viewer. Images recorded at 120 frames per second must be done using the IR camera's internal buffer memory or a removable memory card.
36) Determine "areas of interest" on the heat sink surface. "areas of interest" are defined as positions within the heat sink where the apparent flow boiling phenomenon was observed more often than randomly and less often than continuously.
37) Turn off the IR camera and remove it from the tripod.
38) Remount the IR camera and microscope objective on the IRT imaging facility camera stand.
39) Turn on the camera.
40) Turn on the IR camera and set the temperature range to 20°C - 150°C.
    a) See Appendix J for IR camera configuration details.
41) Focus the camera on the heat sink top surface and locate the rectangular Kapton® tape strip.
42) Align the Kapton® tape strip right edge with the camera field of view left edge.
43) Align the heat sink circumferential edge with the camera field of view top edge.
44) Focus the camera on the desired focal plane, the heat sink gold layer.
45) Electronicallly manipulate the horizontal micro-traverse stage such that the heat sink inlet plenum is centered within the IR camera field of view.
    a) Centering of the inlet plenum in the camera field of view is confirmed by operator visual inspection.
46) After inlet plenum centering visual confirmation, the horizontal micro-traverse stage was electronically manipulated to move the heat sink to a starting image location commensurate with the previously determined "areas of interest". Once at the desired image location experimental image data acquisition can begin.

4,000 experimental images, for a mass flow rate of 15.8 gm/min, an inlet temperature of 88°C, and a total heat sink power input of 30 W, were acquired, at 30 frames per second, at 255 previously determined "locations of interest."

APPENDIX M: Water heater controller and Fluke data logger config. details.

The hot water heater controller configuration details are outlined below.

1) Depress circle arrow until the display reads SP1.
2) Depress enter.
3) Depress the ▲ and ▼ to set the desired temperature.
4) Depress enter.
5) Depress circle arrow until the display reads RUN.
6) Flip the light switch to the on position to send power to the hot water heater.

The Fluke data logger configuration details are outlined below.

1) Turn on the Fluke data logger.
    a) The display will read ERROR 6.
    b) This indicates no configuration has been set.
2) Depress ▲ to set the channel to channel 1.
3) Depress function.
4) Depress ▲ to set the function to Ω.
5) Depress enter. The display will read AUTO.
6) Depress ▲ until the display reads 300.00 Ω.
7) Depress enter.
8) Depress ▲ until the display reads 4T.
9) Depress enter.
    a) Channel 1 has been configured properly.
10) Repeat steps 2-9 for channel 3.

APPENDIX N: Calibration and experimental data identification.

CALIBRATION DATA IDENTIFICATION

Two sets of data were acquired during heat sink calibration. The calibration intensity images and the calibration test section thermocouple temperatures. Figures N1 and N2 illustrate the calibration intensity image file naming scheme and calibration test section thermocouple temperature file naming scheme, respectively.

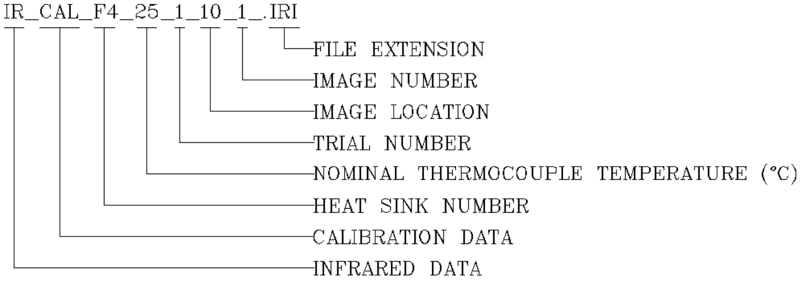

Figure N 1 Calibration intensity image file naming scheme.

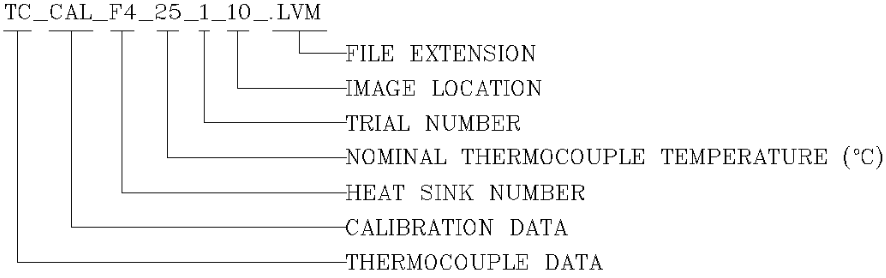

Figure N 2 Calibration thermocouple temperature file naming scheme.

EXPERIMENTAL DATA IDENDIFICATION

Figure N3 illustrates the experimental intensity image file naming scheme.

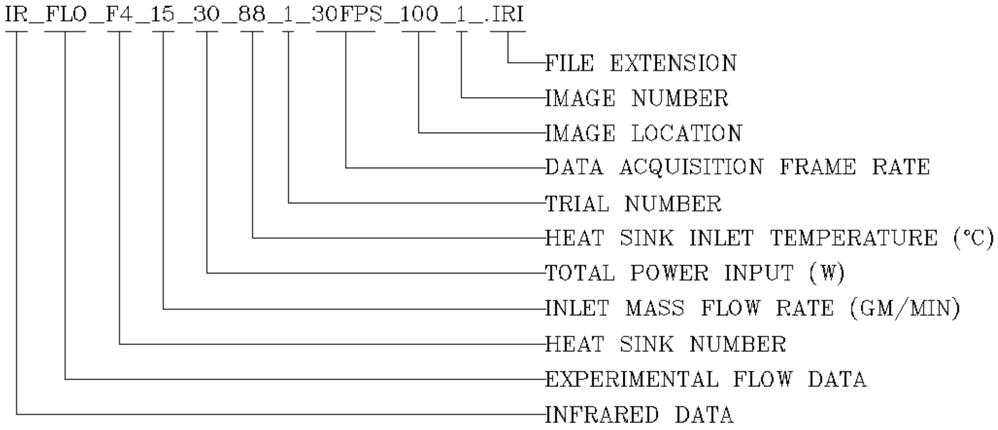

Figure N 3 Experimental intensity image file naming scheme.

APPENDIX O: File conversion LabVIEW^{TM} program details.

The file conversion LabVIEW^{TM} program opens an existing infrared image which is a 16-bit binary .iri file and converts it to an ASCII data string. The ASCII data string is converted to a one dimensional temperature array using a conversion formula extracted from the .iri file. The conversion formula contains coefficients stored as a 64-bit floating point binary number that are converted to decimal format. The ASCII data array is then resized to a 256 x 236 two-dimensional temperature array representing the actual temperature of each pixel in the image [46].

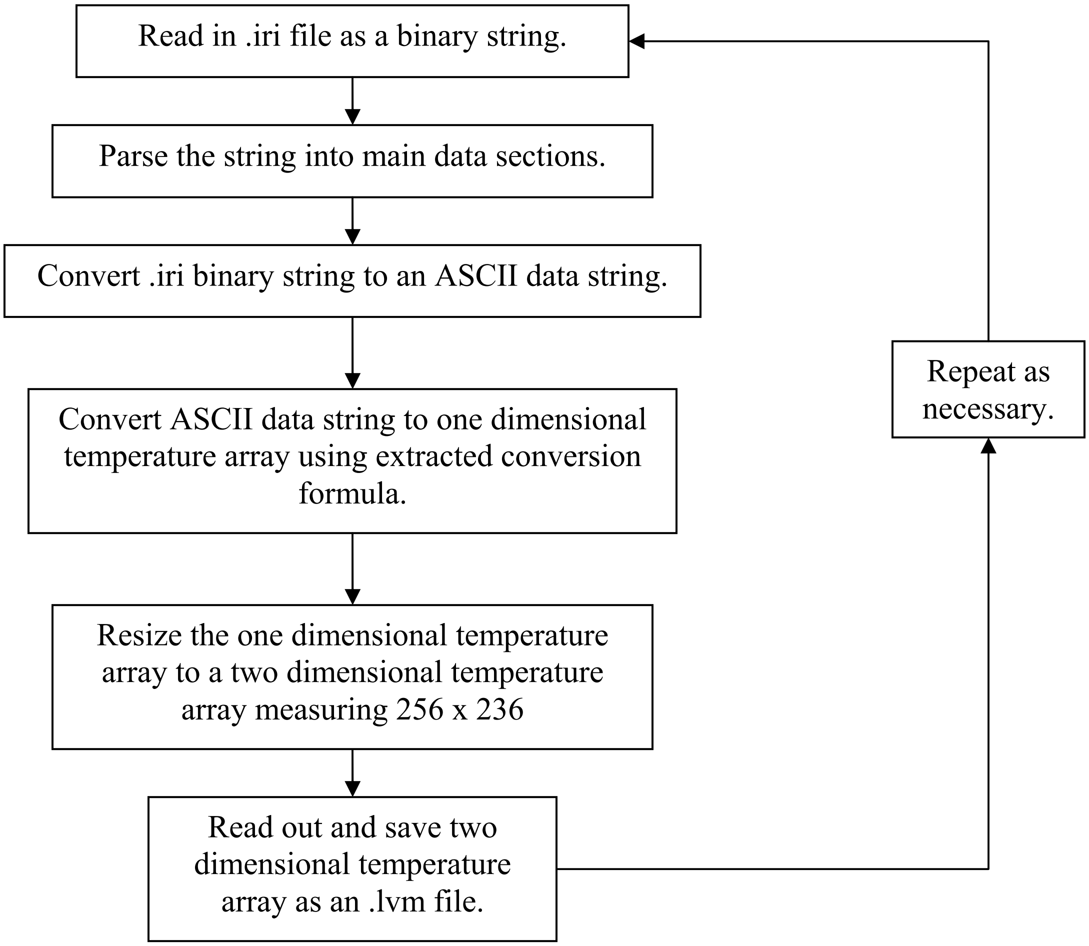

Figure O 1 File conversion LabVIEW^{TM} program structure.

APPENDIX P: OLA intensity Matlab® program details.

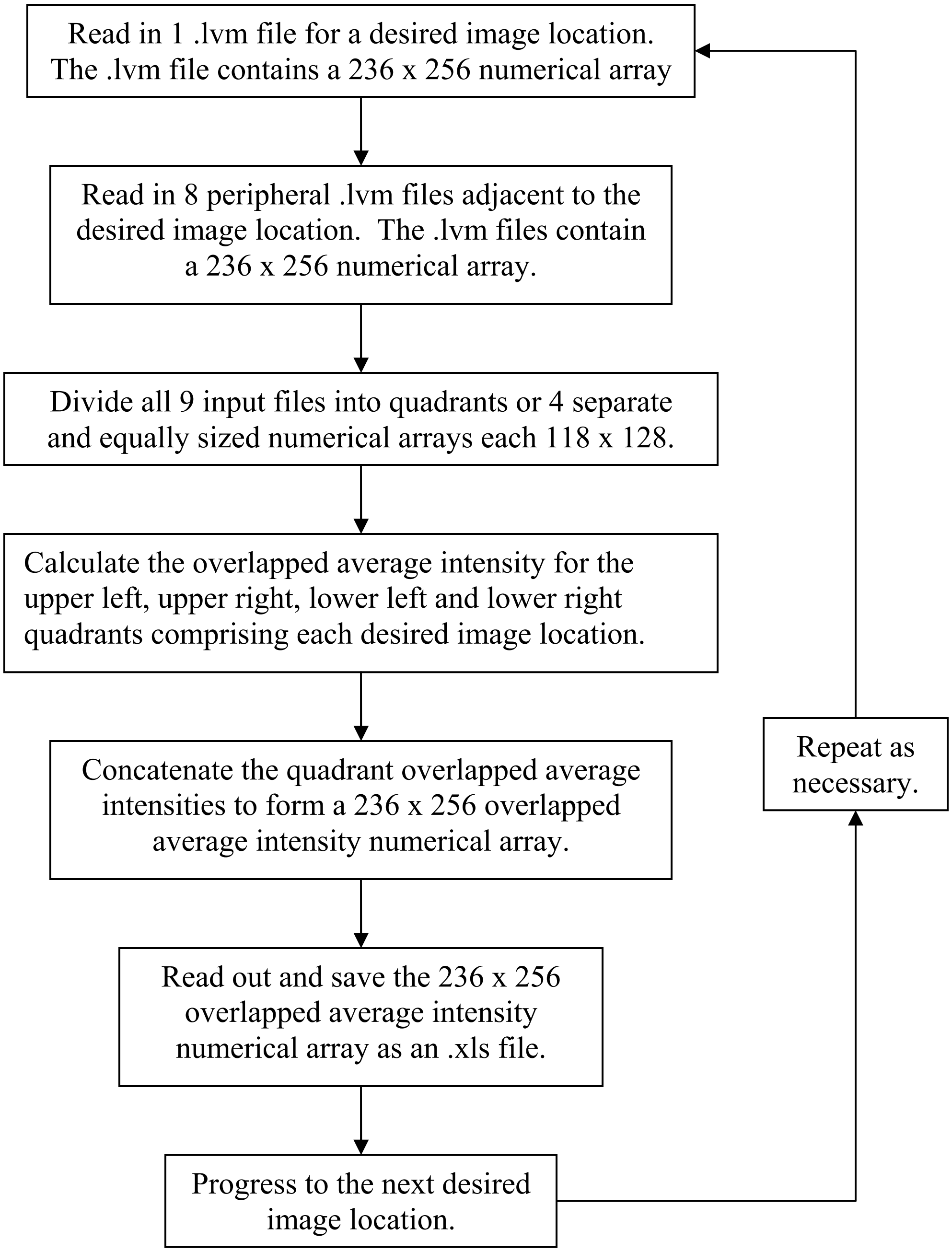

Figure P 1 OLA intensity Matlab$^{\circledR}$program structure.

The actual code for the OLA intensity program is provided below.

```
clear;
clc;

%This loop starts with a folder that contains 1000+ specific image location
%average files in .xls format.  The fractal images are taken with 1/2 field
%of view overlap between successive images in both the x and y direction.
%For a specific image location, data is contained in a total of 9 images.
%One central image and 8 peripheral images.  The 9 images used in
%calculating the average are located in the following orientation.
% 9 8 7
% 4 5 6
% 3 2 1
%For a given set of 9 images
% 94 95 96
% 35 34 33
% 30 31 32
%The above 3 x 3 matrix is interpreted as
%file_in1=32
%file_in2=31
%file_in3=30
%file_in4=35
%file_in5=34
%file_in6=33
%file_in7=96
%file_in8=95
%file_in9=94
%Where information from images 30, 31, 32, 33, 35, 94, 95 and 96 are
%averaged and compiled at image location 34.

%Global variable Initialization

i=34; %Initialize i, the image position to start the data processing
m=62; %The first image location in the last column of interest
p=2; %Initialize p, numerical difference between n and file_in1 location
q=62; %Difference between n and file_in7 location
k=1058; %the first image location in the last row of interest

%The inner for loop starts at image location i and reads in the 9
%necessary .lvm files (one central and 8 peripheral).  The images are
%flipped up and down.  The IR camera generates an image that is 256 pixels
%in x by 236 pixels in y.  The .iri to .lvm software conversion program
%developed in labview converts the .iri file to a .lvm file that is 256
```

```
%pixels in x by 236 pixels in y, but oriented upside down relative to the
%original image. Flipping the .lvm file up and down is necessary to obtain
%the orientation the original image was taken in.  However, flipping the
%image up and down as it is read in caused a double image effect when
%generating a piecewise fractal intensity map.  Therefore, the images are
%not flipped on input, and processed upside down.  This maintains a logical
%approach with regard to matrix/array indexing and concatenation.
%Once each image is read in it is decomposed into 4 quadrant matrices.
%Note that images are indexed at the lower left hand corner whilc matrices
%are indexed from the upper left hand corner.  When the data is decomposed
%into quadrant matrices, the matrix index in the upper left hand corner
%must be used.  For example,UL1 corresponds to the matrix upper left and
%original image upper left (remember the .lvm file is the inverse of the
%original image).  After image decomposition,
%The quadrant matrices are averaged and concatenated to form a
%matrix that is 256 pixels in x by 236 pixels in y that represents the
%average radiation intensity at that location.  The next image to be
%processed is 64 image locations away or the next image in the column.
%Once all the images in the column are processed the inner for loop kicks
%out to the outer for loop where the values of p, q and k are incremented
%and the whole process is repeated for the next column 2 image locations
%away.

for j=i:2:m

    for n=j:64:k

        file_in1=['IR_CAL_F4_25_2_' num2str(n-(p)) '.lvm'];  %Input filename
        rd1=(dlmread(file_in1));  %Assign data file to rd1

        UL1=rd1((1:118),(1:128));  %Matrix upper left
        UR1=rd1((1:118),(129:256));  %Matrix upper right
        LL1=rd1((119:236),(1:128));  %Matrix lower left
        LR1=rd1((119:236),(129:256));  %Matrix lower right

        file_in2=['IR_CAL_F4_25_2_' num2str(n-(p+1)) '.lvm'];  %Input filename
        rd2=(dlmread(file_in2));  %Assign data file to rd2

        UL2=rd2((1:118),(1:128));  %Matrix upper left
        UR2=rd2((1:118),(129:256));  %Matrix upper right
        LL2=rd2((119:236),(1:128));  %Matrix lower left
        LR2=rd2((119:236),(129:256));  %Matrix lower right

        file_in3=['IR_CAL_F4_25_2_' num2str(n-(p+2)) '.lvm'];  %Input filename
```

```
rd3=(dlmread(file_in3)); %Assign data file to rd3

UL3=rd3((1:118),(1:128));  %Matrix upper left
UR3=rd3((1:118),(129:256));  %Matrix upper right
LL3=rd3((119:236),(1:128));  %Matrix lower left
LR3=rd3((119:236),(129:256));  %Matrix lower right

file_in4=['IR_CAL_F4_25_2_' num2str(n+1) '.lvm'];  %Input filename
rd4=(dlmread(file_in4));  %Assign data file to rd4

UL4=rd4((1:118),(1:128));  %Matrix upper left
UR4=rd4((1:118),(129:256));  %Matrix upper right
LL4=rd4((119:236),(1:128));  %Matrix lower left
LR4=rd4((119:236),(129:256));  %Matrix lower right

file_in5=['IR_CAL_F4_25_2_' num2str(n) '.lvm'];  %Input filename
rd5=(dlmread(file_in5));  %Assign data file to rd5

UL5=rd5((1:118),(1:128));  %Matrix upper left
UR5=rd5((1:118),(129:256));  %Matrix upper right
LL5=rd5((119:236),(1:128)); %Matrix lower left
LR5=rd5((119:236),(129:256));  %Matrix lower right

file_in6=['IR_CAL_F4_25_2_' num2str(n-1) '.lvm'];  %Input filename
rd6=(dlmread(file_in6));  %Assign data file to rd6

UL6=rd6((1:118),(1:128));  %Matrix upper left
UR6=rd6((1:118),(129:256));  %Matrix upper right
LL6=rd6((119:236),(1:128));  %Matrix lower left
LR6=rd6((119:236),(129:256));  %Matrix lower right

file_in7=['IR_CAL_F4_25_2_' num2str(n+(q)) '.lvm'];  %Input filename
rd7=(dlmread(file_in7));  %Assign data file to rd7

UL7=rd7((1:118),(1:128));  %Matrix upper left
UR7=rd7((1:118),(129:256));  %Matrix upper right
LL7=rd7((119:236),(1:128));  %Matrix lower left
LR7=rd7((119:236),(129:256));  %Matrix lower right

file_in8=['IR_CAL_F4_25_2_' num2str(n+(q-1)) '.lvm'];  %Input filename
rd8=(dlmread(file_in8));  %Assign data file to rd8

UL8=rd8((1:118),(1:128));  %Matrix upper left
UR8=rd8((1:118),(129:256));  %Matrix upper right
```

```
        LL8=rd8((119:236),(1:128));  %Matrix lower left
        LR8=rd8((119:236),(129:256));  %Matrix lower right

        file_in9=['IR_CAL_F4_25_2_' num2str(n+(q-2)) '.lvm'];  %Input filename
        rd9=(dlmread(file_in9));  %Assign data file to rd9

        UL9=rd9((1:118),(1:128));  %Matrix upper left
        UR9=rd9((1:118),(129:256));  %Matrix upper right
        LL9=rd9((119:236),(1:128));  %Matrix lower left
        LR9=rd9((119:236),(129:256));  %Matrix lower right

        UL=cat(3,UR4,UL5,LL8,LR9);  %Form the 3D array UL
        ULA=mean(UL(:,:,:),3);  %Calculate the average of UL

        UR=cat(3,UR5,UL6,LL7,LR8);  %Form the 3D array UR
        URA=mean(UR(:,:,:),3);  %Calculate the average of UR

        LL=cat(3,UR3,UL2,LL5,LR4); %Form the 3D array LL
        LLA=mean(LL(:,:,:),3);  %Calculate the average of LL

        LR=cat(3,UR2,UL1,LL6,LR5);  %Form the 3D array LR
        LRA=mean(LR(:,:,:),3);  %Calculate the average of LR

        ULA_URA=cat(2,ULA,URA);  %Concatenate horizontally

        LLA_LRA=cat(2,LLA,LRA);  %Concatenate horizontally

        OLA=cat(1,ULA_URA,LLA_LRA);  %Concatenate vertically

        file_out=['OLA_CAL_F4_25_2_' num2str(n) '.xls'];  %Generate an output filename
        disp(file_out)  %Display the output filename for verification.
        xlswrite(file_out,OLA);  %Save/write out the calculated average as a data file.

    end

    p=p+4;  %Increment p by 4
    q=q-4;  %Decrement q by 4
    k=k+2;  %Increment p by 2

end
```

APPENDIX Q: PW OLA intensity Matlab® program details.

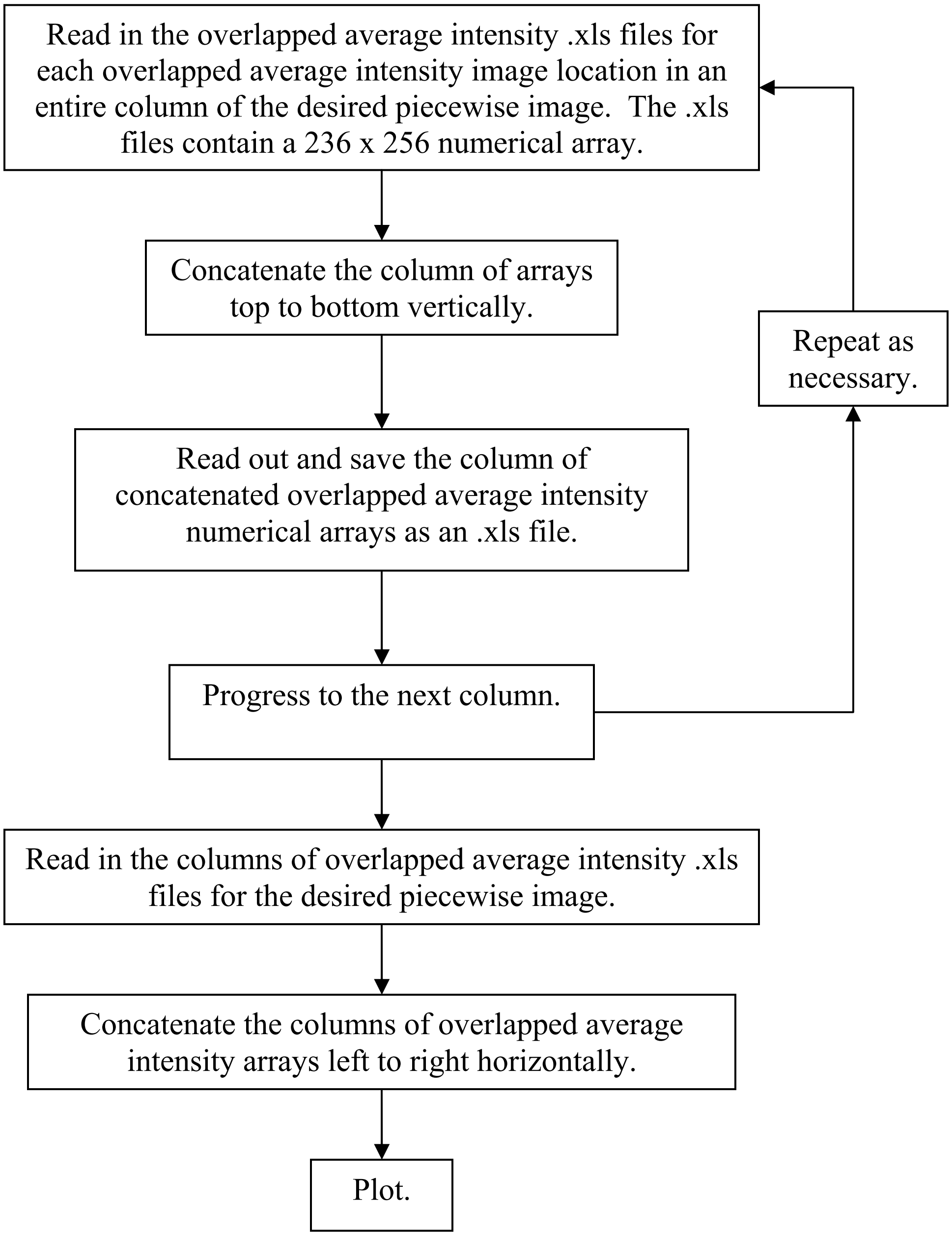

Figure Q 1 PW OLA intensity Matlab® program structure.

The actual code for the PW OLA intensity image generation program is provided below.

```
%VERTICAL CONCATENATION LOOP

%This loop starts with a folder that contains 200+ overlapped average .xls
%files that were generated from the previous data processing loop.

clear;
clc;

%Global variable Initialization

i=34; %Initialize i, the image position to start the data processing
m=62; %The first image location in the last column of interest
p=2; %Initialize p, numerical difference between n and file_in1 location
q=62; %Difference between n and file_in7 location
k=1058; %the first image location in the last row of interest
OLAC=[]; %Define the variable OLAC and make it an empty matrix

%The inner for loop reads in all the overlapped average data files in a
%column and concatenates them.  Once an entire column of overlapped data
%files is concatenated the inner loop kicks out to the outer loop
%where the values of p, q and k are incremented and the whole process is
%repeated for the next column 2 image locations away.

for j=i:2:m

  for n=j:64:k

     file_in=['OLA_CAL_F4_25_2_' num2str(n) '.xls'];  %Generate an input filename
     OLA=(xlsread(file_in));  %Assign data file to OLA
     OLAC=cat(1,OLA,OLAC);  %Concatenate/grow array OLAC vertically

  end

  file_out=['OLAC_CAL_F4_25_2_' num2str(n) '.xls'];  %Generate an output filename
  disp(file_out)  %Display the output filename for verification.
  xlswrite(file_out,OLAC);  %Save/write out the calculated average as a data file.

  OLAC=[];  %Reset the array OLAC to empty

  p=p+4;  %Increment p by 4
  q=q-4;  %Decrement q by 4
```

```
   k=k+2;  %increment k by 2

end

%HORIZONTAL CONCATENATION LOOP

%This loop starts with a folder that contains 17+ concatenated overlapped
%average column .xls files that were generated from the previous data
%processing loop.

clear;
clc;

%Global variable Initialization

m=1086; %The last image location in the last column of interest
k=1058; %the last image location in the first column of interest
OLAT=[]; %Define the variable OLAT and make it an empty matrix

%This for loop reads in the concatenated overlapped average column .xls
%file that were generated from the previous data processing loop and
%concatenates them horizontally.  The result is aa piecewise overlapped
%average fractal in its entirety.

for j=k:2:m

   file_in=['OLAC_CAL_F4_25_2_' num2str(j) '.xls'];  %Generate an input filename
   OLAC=(xlsread(file_in));  %Assign data file to OLA
   OLAT=cat(2,OLAC,OLAT);  %Concatenate/grow array OLAT horizontally

end

%PLOT

%A contour plot is generated here.

imagesc(OLAT)
```

APPENDIX R: Calibration OLA intensity shifting Matlab®program details.

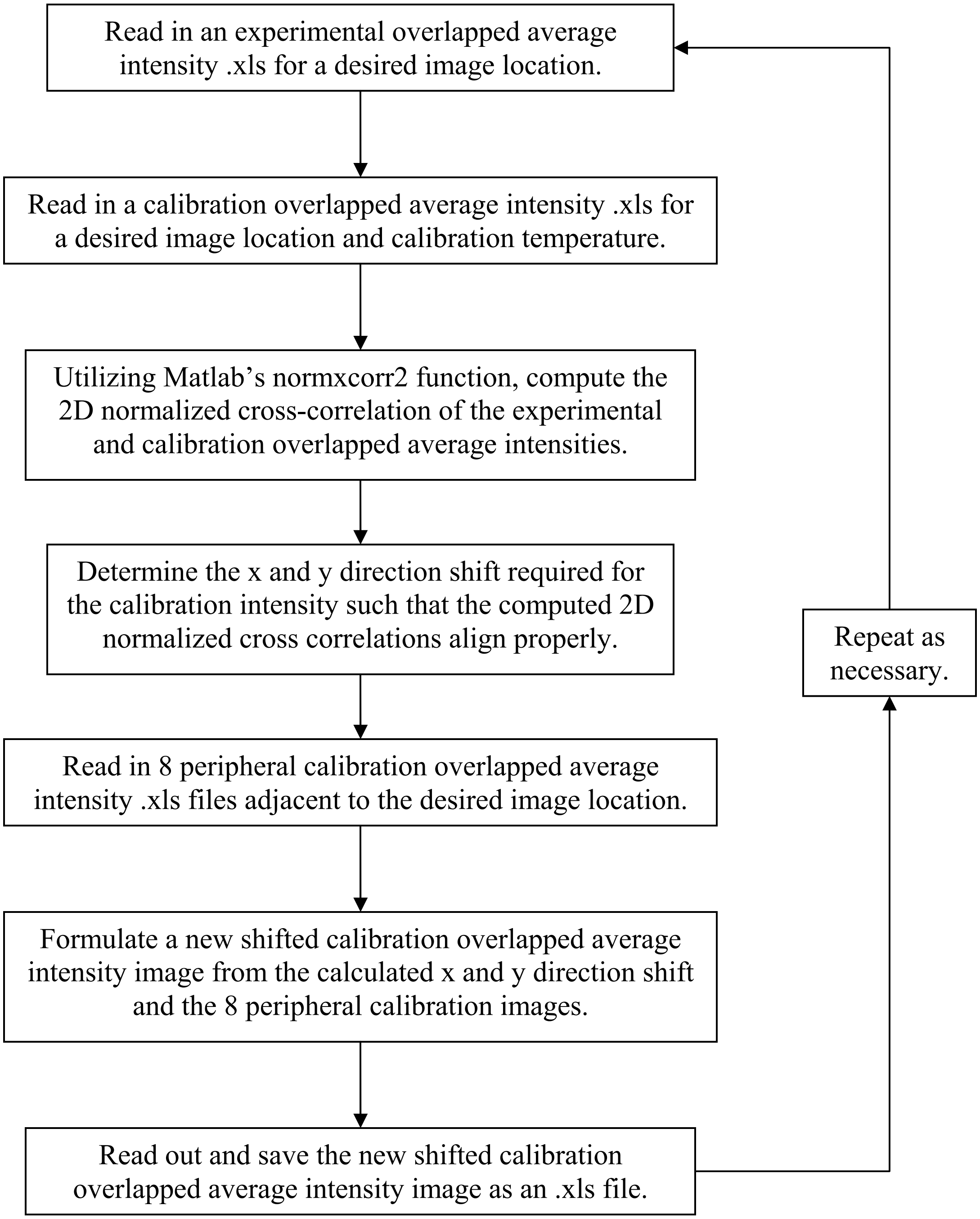

Figure R 1 Calibration OLA intensity shifting Matlab® program structure.

The actual code for the calibration OLA intensity shifting program is provided below.

```
clear
clc
close all

for IML=[(560:2:572),(624:2:636),(688:2:700),(752:2:764),(816:2:828),(880:2:892),…
        …(944:2:954),(1008:2:1016)]; %Enter the image location of intererst

   TEMP=125; %Enter the calibration temperature of interest

   %Generate the flow image location matrix

   IMLMatrix=flipud(fliplr([(494:2:510);(558:2:574);(622:2:638);...
          (686:2:702);(750:2:766);(814:2:830);(878:2:894);...
          (942:2:958);(1006:2:1022);(1070:2:1086)]));

   %Locate the row and column indices within IMLMatrix corresponding to the
   %image location of interest.

   [RIML,CIML]=find(IMLMatrix==IML);

   %Locate the 8 peripheral images adjacent to the image location of interest

   IML1=IMLMatrix((RIML+1),(CIML+1));
   IML2=IMLMatrix((RIML+1),(CIML));
   IML3=IMLMatrix((RIML+1),(CIML-1));
   IML4=IMLMatrix((RIML),(CIML-1));
   IML5=IMLMatrix((RIML),(CIML));
   IML6=IMLMatrix((RIML),(CIML+1));
   IML7=IMLMatrix((RIML-1),(CIML+1));
   IML8=IMLMatrix((RIML-1),(CIML));
   IML9=IMLMatrix((RIML-1),(CIML-1));

   %Generate filenames for the 8 peripheral images adjacent to the image
   %location of interest

   file_in_IML1=['OLAF_CAL_F4_' num2str(TEMP) '_2_' num2str(IML1) '.xls'];
   file_in_IML2=['OLAF_CAL_F4_' num2str(TEMP) '_2_' num2str(IML2) '.xls'];
   file_in_IML3=['OLAF_CAL_F4_' num2str(TEMP) '_2_' num2str(IML3) '.xls'];
   file_in_IML4=['OLAF_CAL_F4_' num2str(TEMP) '_2_' num2str(IML4) '.xls'];
   file_in_IML5=['OLAF_CAL_F4_' num2str(TEMP) '_2_' num2str(IML5) '.xls'];
   file_in_IML6=['OLAF_CAL_F4_' num2str(TEMP) '_2_' num2str(IML6) '.xls'];
```

```
   file_in_IML7=['OLAF_CAL_F4_' num2str(TEMP) '_2_' num2str(IML7) '.xls'];
   file_in_IML8=['OLAF_CAL_F4_' num2str(TEMP) '_2_' num2str(IML8) '.xls'];
   file_in_IML9=['OLAF_CAL_F4_' num2str(TEMP) '_2_' num2str(IML9) '.xls'];

   %Calculate the offset required to allign the images

   base=xlsread(['OLA_FLO_F4_15_30_88_1_30FPS_' num2str(IML) '.xls']);
   a=xlsread(['OLAF_CAL_F4_' num2str(TEMP) '_2_' num2str(IML) '.xls']); %filtered
data

   FLOW=base;

   base=uint8(255/(max(base(:)-min(base(:)))).*(base-min(base(:))));
   a=uint8(255/(max(a(:))-min(a(:))).*(a-min(a(:))));

   a_o=a;

   [H1 W1]=size(base);

   figure('Position',[400 700 W1 H1]),imshow(base)
   title('Base Image(Flow)')
   daspect([1 1 1])

   [H2 W2]=size(a);

   rect=[1 1 255 235];
   a=imcrop(a,rect);
   figure('Position',[850 700 W2 H2]),imshow(a)
   title('Image to shift relative to base image(Calibration)')
   daspect([1 1 1])

   disp('Press any key to correlate these two images')

   pause

   close all

   rect=round(rect);

   c = normxcorr2(a,base);
   [max_c, imax] = max(abs(c(:)));
   [ypeak, xpeak] = ind2sub(size(c),imax(1));
   corr_offset = [(xpeak-size(a,2)) (ypeak-size(a,1))];
```

```
    pad1(:,:,1)=uint8(zeros([436 456]));
    pad1(:,:,2)=uint8(zeros([436 456]));
    pad1(:,:,3)=uint8(zeros([436 456]));

    pad1(101:336,101:356,1)=base; %puts base image in center

    yshift=corr_offset(2)-rect(2); %rows
    xshift=corr_offset(1)-rect(1); %columns

    pad1(101+(yshift):336+(yshift),101+(xshift):356+(xshift),2)=a_o; %shifts image
relative to center

    figure('Position',[850 700 456 436]),imshow(pad1)
    Titletext=['IML=' num2str(IML) ', Red=Base(Flow), Green=Shifted(' num2str(TEMP)
'°C Calibration), X shift=' num2str(xshift) ' Columns, Y shift=' num2str(yshift) ' Rows'];
    title(Titletext)
    daspect([1 1 1])

    disp('Press any key to accept displayed image shift')

    pause

    close all

    %Create a new image based upon the calculated x and y shift

    if ((xshift<0)&&(yshift>0))

        fd5=xlsread(file_in_IML5);
        disp(file_in_IML5)
        fd6=xlsread(file_in_IML6);
        disp(file_in_IML6)
        fd7=xlsread(file_in_IML7);
        disp(file_in_IML7)
        fd8=xlsread(file_in_IML8);
        disp(file_in_IML8)

        FDtop=cat(2,fd8,fd7);
        FDbot=cat(2,fd5,fd6);
        FD=cat(1,FDtop,FDbot);

        SD=FD((237-yshift:472-yshift),(1-xshift:256-xshift));

    elseif ((xshift<0)&&(yshift<0))
```

```
    fd1=xlsread(file_in_IML1);
    disp(file_in_IML1)
    fd2=xlsread(file_in_IML2);
    disp(file_in_IML2)
    fd5=xlsread(file_in_IML5);
    disp(file_in_IML5)
    fd6=xlsread(file_in_IML6);
    disp(file_in_IML6)

    FDtop=cat(2,fd5,fd6);
    FDbot=cat(2,fd2,fd1);
    FD=cat(1,FDtop,FDbot);

    SD=FD((1-yshift:236-yshift),(1-xshift:256-xshift));

elseif ((xshift>0)&&(yshift>0))

    fd4=xlsread(file_in_IML4);
    disp(file_in_IML4)
    fd5=xlsread(file_in_IML5);
    disp(file_in_IML5)
    fd8=xlsread(file_in_IML8);
    disp(file_in_IML8)
    fd9=xlsread(file_in_IML9);
    disp(file_in_IML9)

    FDtop=cat(2,fd9,fd8);
    FDbot=cat(2,fd4,fd5);
    FD=cat(1,FDtop,FDbot);

    SD=FD((237-yshift:472-yshift),(257-xshift:512-xshift));

elseif ((xshift>0)&&(yshift<0))

    fd2=xlsread(file_in_IML2);
    disp(file_in_IML2)
    fd3=xlsread(file_in_IML3);
    disp(file_in_IML3)
    fd4=xlsread(file_in_IML4);
    disp(file_in_IML4)
    fd5=xlsread(file_in_IML5);
    disp(file_in_IML5)

    FDtop=cat(2,fd4,fd5);
```

```
    FDbot=cat(2,fd3,fd2);
    FD=cat(1,FDtop,FDbot);

    SD=FD((1-yshift:236-yshift),(257-xshift:512-xshift));

elseif ((xshift<0)&&(yshift==0))

    fd5=xlsread(file_in_IML5);
    disp(file_in_IML5)
    fd6=xlsread(file_in_IML6);
    disp(file_in_IML6)

    FD=cat(2,fd5,fd6);

    SD=FD((1:236),(1-xshift:256-xshift));

elseif ((xshift>0)&&(yshift==0))

    fd4=xlsread(file_in_IML4);
    disp(file_in_IML4)
    fd5=xlsread(file_in_IML5);
    disp(file_in_IML5)

    FD=cat(2,fd4,fd5);

    SD=FD((1:236),(257-xshift:512-xshift));

elseif ((xshift==0)&&(yshift<0))

    fd2=xlsread(file_in_IML2);
    disp(file_in_IML2)
    fd5=xlsread(file_in_IML5);
    disp(file_in_IML5)

    FD=cat(1,fd5,fd2);

    SD=FD((1-yshift:236-yshift),(1:256));

elseif ((xshift==0)&&(yshift>0))

    fd5=xlsread(file_in_IML5);
    disp(file_in_IML5)
    fd8=xlsread(file_in_IML8);
    disp(file_in_IML8)
```

```
        FD=cat(1,fd8,fd5);

        SD=FD((237-yshift:472-yshift),(1:256));

    elseif ((xshift==0)&&(yshift==0))

        fd5=xlsread(file_in_IML5);
        disp(file_in_IML5)

        FD=fd5;

        SD=FD;

    end

%Plot the flow image and the newly shifted calibration image side by side

[H4 W4]=size(FLOW);

figure('Position',[300 600 2*W4 2*H4]),imagesc(FLOW)
Titletext=['IML=' num2str(IML) ', Base Flow Image'];
title(Titletext)
daspect([1 1 1])

[H5 W5]=size(SD);

figure('Position',[850 600 2*W5 2*H5]),imagesc(SD)
Titletext=['IML=' num2str(IML) ', Shifted Image(' num2str(TEMP) '°C Calibration), X
shift=' num2str(xshift) ' Columns, Y shift=' num2str(yshift) ' Rows'];
title(Titletext)
daspect([1 1 1])

%Pad size for a single image location to overlap the base flow image
%and the newly shifted calibration image

pad2(:,:,1)=uint8(zeros([236 256]));
pad2(:,:,2)=uint8(zeros([236 256]));
pad2(:,:,3)=uint8(zeros([236 256]));

SD1=uint8(255/(max(SD(:))-min(SD(:))).*(SD-min(SD(:))));

pad2(:,:,1)=base;
pad2(:,:,2)=SD1;
```

```
[H6 W6]=size(SD1);

figure('Position',[700 200 W6 H6]),imshow(pad2)
Titletext=['IML=' num2str(IML) ', Red=Base(Flow), Green=Shifted(' num2str(TEMP)
'°C Calibration)'];
title(Titletext)
daspect([1 1 1])

disp('Press any key to export shifted image as a .xls file')

pause

file_out=['OLASWI_CAL_F4_' num2str(TEMP) '_2_' num2str(IML) '.xls'];
disp(file_out)
xlswrite(file_out,SD);

close all

end
```

APPENDIX S: Intensity to temperature conversion Matlab$^{®}$ program details.

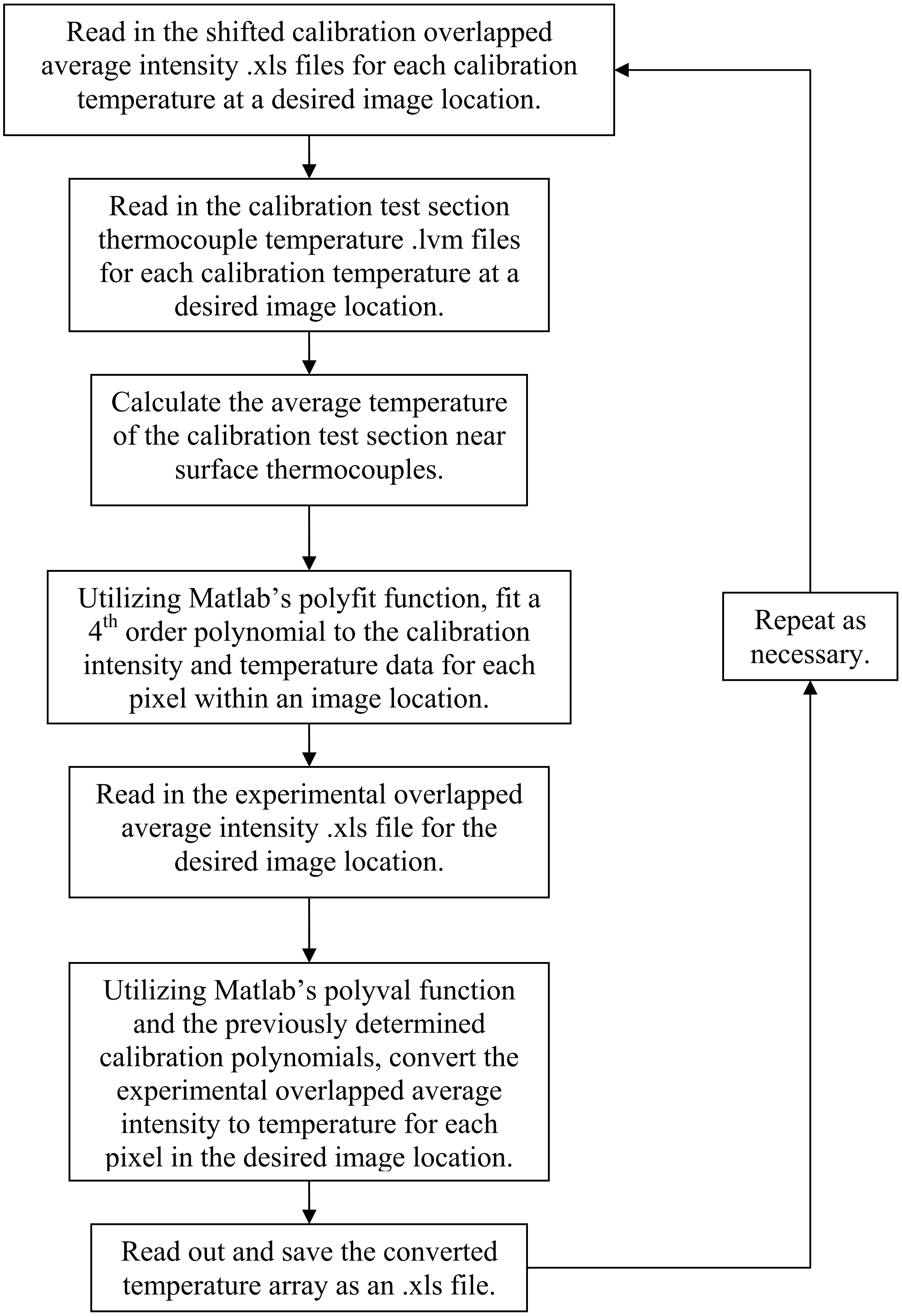

Figure S 1 Intensity to temperature conversion Matlab® program structure.

The actual code for the intensity to temperature conversion program is provided below.

```
clear;
clc;

%Global variable Initialization

i=560; %Initialize i, the image position to start the data processing
m=572; %The first image location in the last column of interest
k=1008; %The last image location in the first row of interest
CoefficientMatrix=[]; %Define CoefficientMatrix and make it empty
CurveFitErrorMatrix=[]; %Define CurveFitErrorMatrix and make it empty

for j=i:2:m

  for n=j:64:k

    file_in_OLAS1=['OLAS_CAL_F4_25_2_' num2str(n) '.xls'];  %Input filename
    disp(file_in_OLAS1) %Display filename
    OLAS1=(xlsread(file_in_OLAS1));  %Assign data file to OLAS1

    file_in_OLAS2=['OLAS_CAL_F4_45_2_' num2str(n) '.xls'];  %Input filename
    disp(file_in_OLAS2) %Display filename
    OLAS2=(xlsread(file_in_OLAS2));  %Assign data file to OLAS2

    file_in_OLAS3=['OLAS_CAL_F4_65_2_' num2str(n) '.xls'];  %Input filename
    disp(file_in_OLAS3) %Display filename
    OLAS3=(xlsread(file_in_OLAS3));  %Assign data file to OLAS3

    file_in_OLAS4=['OLAS_CAL_F4_85_2_' num2str(n) '.xls'];  %Input filename
    disp(file_in_OLAS4) %Display filename
    OLAS4=(xlsread(file_in_OLAS4));  %Assign data file to OLAS4

    file_in_OLAS5=['OLAS_CAL_F4_105_2_' num2str(n) '.xls'];  %Input filename
    disp(file_in_OLAS5) %Display filename
    OLAS5=(xlsread(file_in_OLAS5));  %Assign data file to OLAS5

    file_in_OLAS6=['OLAS_CAL_F4_125_2_' num2str(n) '.xls'];  %Input filename
    disp(file_in_OLAS6) %Display filename
    OLAS6=(xlsread(file_in_OLAS6));  %Assign data file to OLAS6

    file_in_TC1=['TC_CAL_F4_25_2_' num2str(n) '.lvm']; %Input filename
    disp(file_in_TC1) %Display filename
```

```
  TC1=dlmread(file_in_TC1); %Assign data file to TC1
  TC1A=mean(mean(TC1(:,(4:10)))); %Calculate near surface average temperatuture

  file_in_TC2=['TC_CAL_F4_45_2_' num2str(n) '.lvm']; %Input filename
  disp(file_in_TC2) %Display filename
  TC2=dlmread(file_in_TC2); %Assign data file to TC2
  TC2A=mean(mean(TC2(:,(4:10)))); %Calculate near surface average temperatuture

  file_in_TC3=['TC_CAL_F4_65_2_' num2str(n) '.lvm']; %Input filename
  disp(file_in_TC3) %Display filename
  TC3=dlmread(file_in_TC3); %Assign data file to TC3
  TC3A=mean(mean(TC3(:,(4:10)))); %Calculate near surface average temperatuture

  file_in_TC4=[TC_CAL_F4_85_2_' num2str(n) '.lvm']; %Input filename
  disp(file_in_TC4) %Display filename
  TC4=dlmread(file_in_TC4); %Assign data file to TC4
  TC4A=mean(mean(TC4(:,(4:10)))); %Calculate near surface average temperatuture

  file_in_TC5=['TC_CAL_F4_105_2_' num2str(n) '.lvm']; %Input filename
  disp(file_in_TC5) %Display filename
  TC5=dlmread(file_in_TC5); %Assign data file to TC5
  TC5A=mean(mean(TC5(:,(4:10)))); %Calculate near surface average temperatuture

  file_in_TC6=['TC_CAL_F4_125_2_' num2str(n) '.lvm']; %Input filename
  disp(file_in_TC6) %Display filename
  TC6=dlmread(file_in_TC6); %Assign data file to TC6
  TC6A=mean(mean(TC6(:,(4:10)))); %Calculate near surface average temperatuture

  TCA=[TC1A,TC2A,TC3A,TC4A,TC5A,TC6A]; %Generate array TCA

  file_in_IR1=['OLA_FLO_F4_15_30_88_1_30FPS_' num2str(n) '.xls']; %Input
filename
  disp(file_in_IR1) %Display dilename
  IR1=(xlsread(file_in_IR1)); %Assign data file to IR1

    for c=1:256; %Define number of columns in an image
      disp(c) %Display column number

      for r=1:236;
        OLA=[(OLAS1(r,c)),(OLAS2(r,c)),(OLAS3(r,c)),(OLAS4(r,c)),…
       (OLAS5(r,c)),(OLAS6(r,c))]; %Generate array OLA
        [Coefficients,S,mu]=polyfit(OLA,TCA,4); %Fit 4th order polynomial

        FlowIntensity=[(IR1(r,c))]; %Define FlowIntensity
```

```
                    FlowTemp=polyval((Coefficients),(FlowIntensity),[],mu); %Calculate
actual flow temperature
                    FlowTempMatrix(r,c)=FlowTemp; %Generate array of flow temperatures

                    TempCalc=polyval((Coefficients),(OLA),[],mu); %Back calculate
calibration temperatures from calibration curves
                    Table=[(TCA-TempCalc)]; %Generate a table to show the difference
between the measured average thermocouple temperature and the back calculated
temperature from the calibration curves.
                    CurveFitError=sqrt((sum((Table).^2))/1); %Calculate the curve fit error
                    CurveFitErrorMatrix=cat(1,CurveFitErrorMatrix,CurveFitError);
%Assemble all curve fit errors in an array

                end

            end

            file_out=['TEMPFS_FLO_F4_15_30_88_1_30FPS_' num2str(n) '.xls'];
%Output file name
            disp(file_out) %display filename
            xlswrite(file_out,FlowTempMatrix); %Save converted temperature file

            FlowTempMatrix=[]; %Reset FlowTempMatrix to empty

   end

   k=k+2;  %increment k by 2

end
```

APPENDIX T: Horizontal micro-traverse spatial uncertainty data.

X DIRECTION SPATIAL UNCERTAINTY DATA.

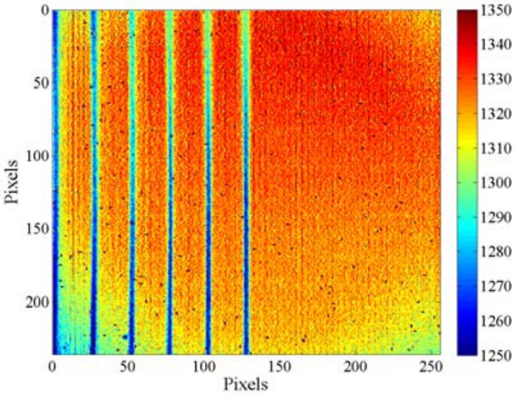

Figure T 1 Optical grid x-dir. IML 1.

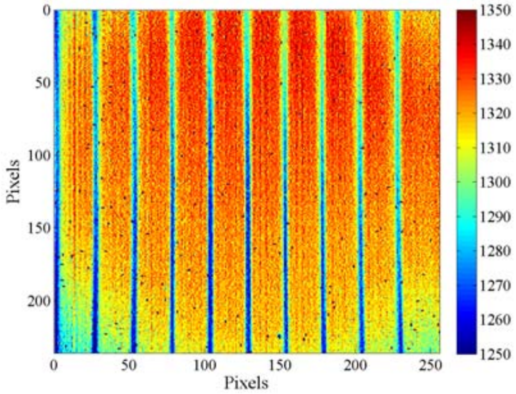

Figure T 2 Optical grid x-dir. IML 2.

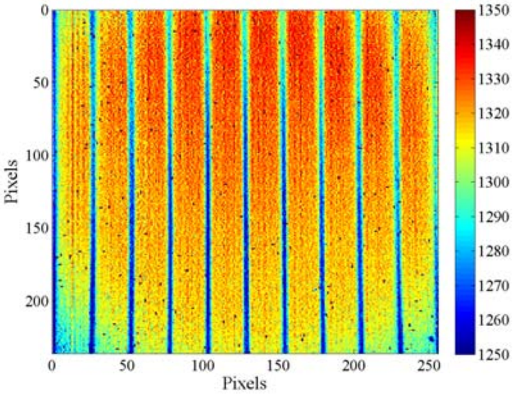

Figure T 3 Optical grid x-dir. IML 3.

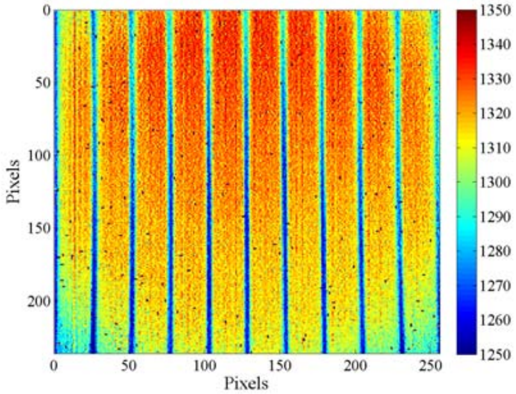

Figure T 4 Optical grid x-dir. IML 4.

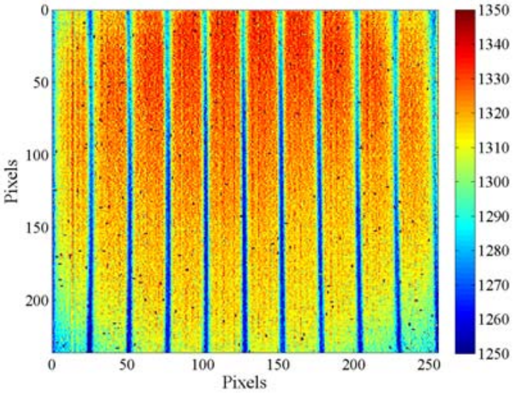

Figure T 5 Optical grid x-dir. IML 5.

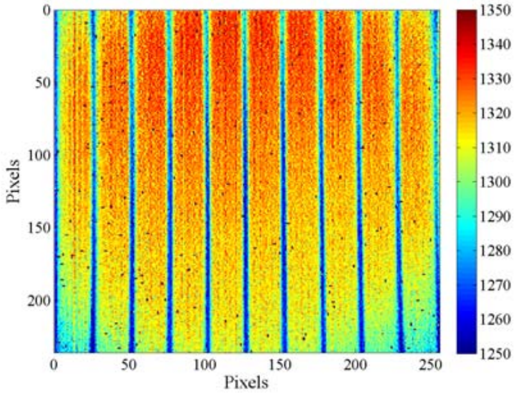

Figure T 6 Optical grid x-dir. IML 6.

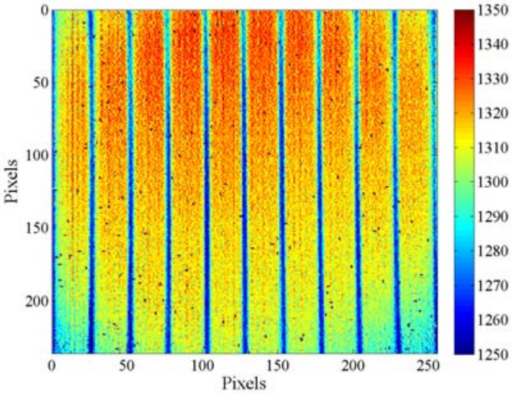

Figure T 7 Optical grid x-dir. IML 7.

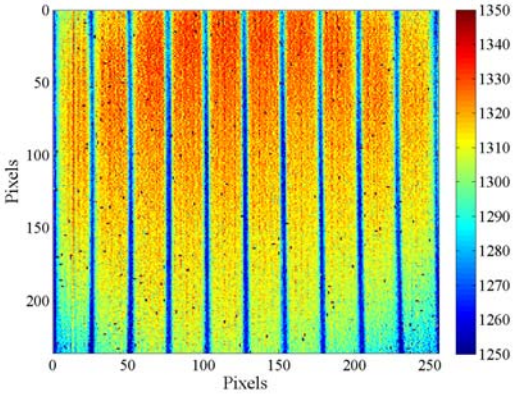

Figure T 8 Optical grid x-dir. IML 8.

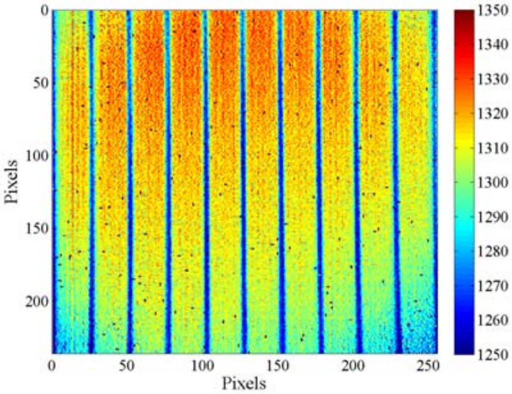

Figure T 9 Optical grid x-dir. IML 9.

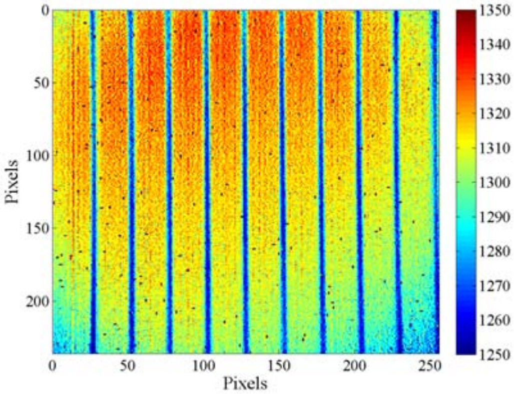

Figure T 10 Optical grid x-dir. IML 10.

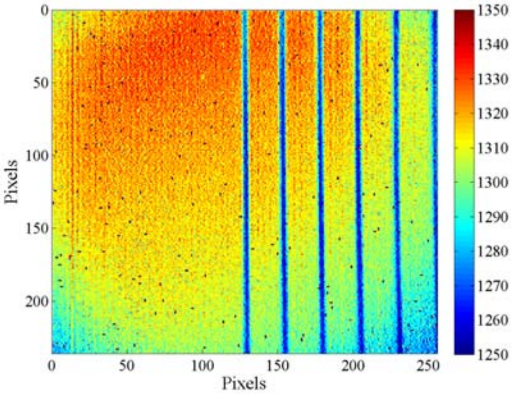

Figure T 11 Optical grid x-dir. IML 11.

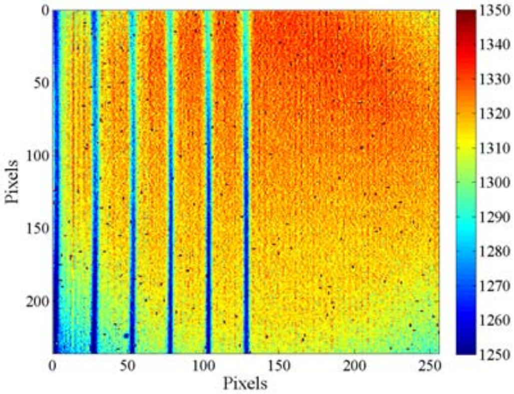

Figure T 12 Optical grid x-dir. IML 12.

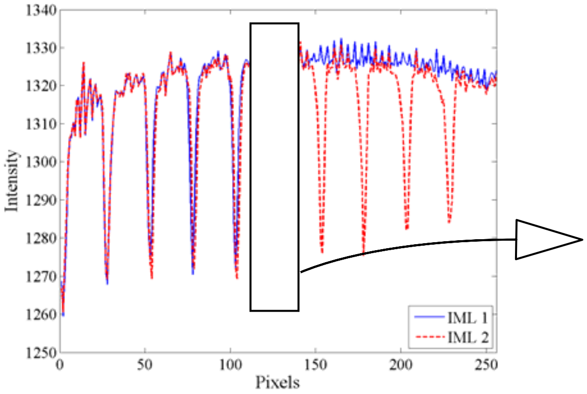

Figure T 13 Intensity vs. pixels x-dir. IML 1 & 2.

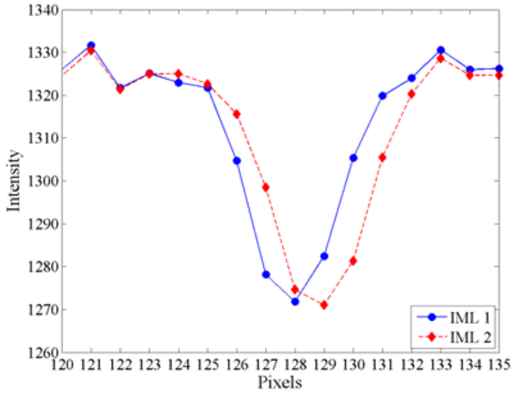

Figure T 14 Intensity vs. pixels x-dir. IML 1 & 2.

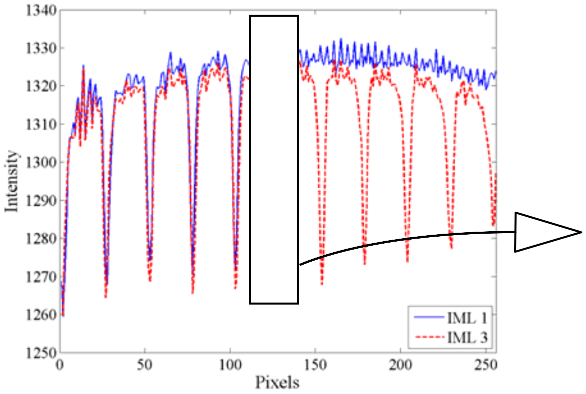

Figure T 15 Intensity vs. pixels x-dir. IML 1 & 3.

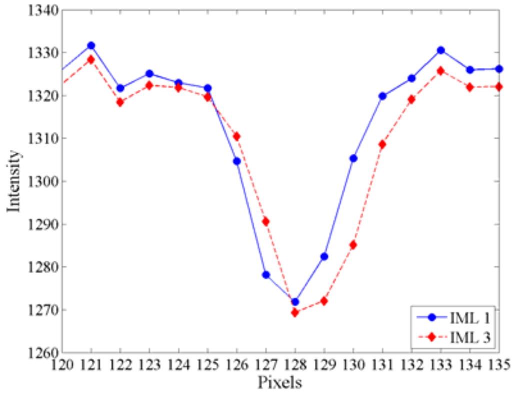

Figure T 16 Intensity vs. pixels x-dir. IML 1 & 3.

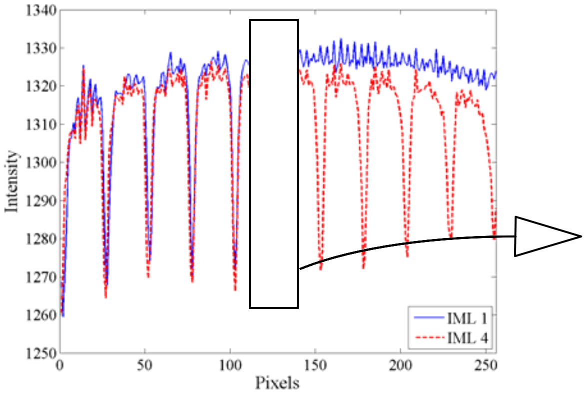

Figure T 17 Intensity vs. pixels x-dir. IML 1 & 4.

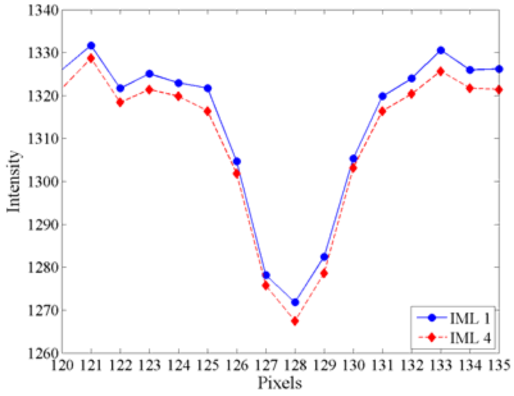

Figure T 18 Intensity vs. pixels x-dir. IML 1 & 4.

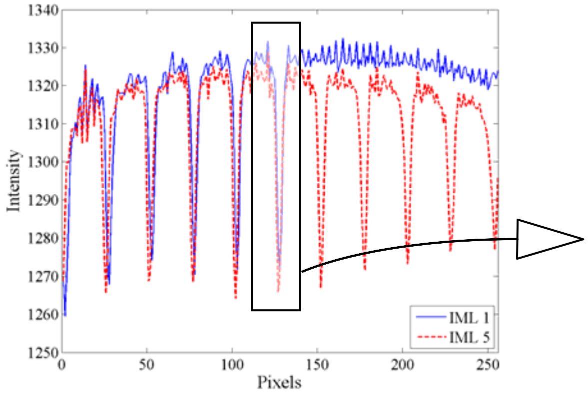

Figure T 19 Intensity vs. pixels x-dir. IML 1 & 5.

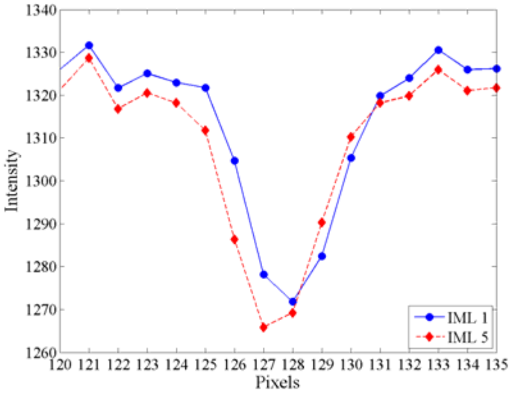

Figure T 20 Intensity vs. pixels x-dir. IML 1 & 5.

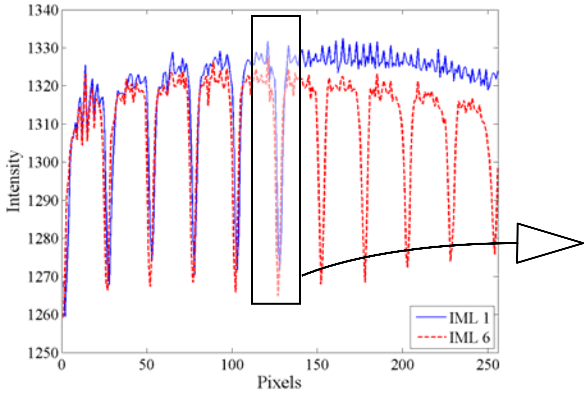

Figure T 21 Intensity vs. pixels x-dir. IML 1 & 6.

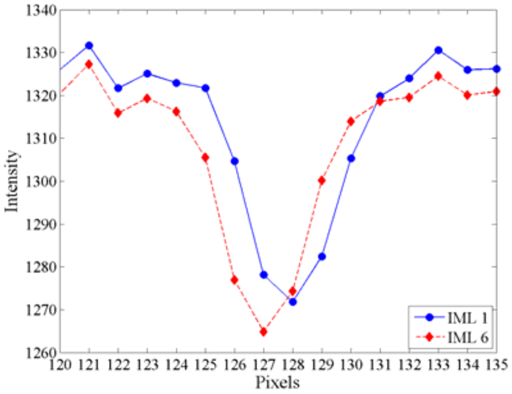

Figure T 22 Intensity vs. pixels x-dir. IML 1 & 6.

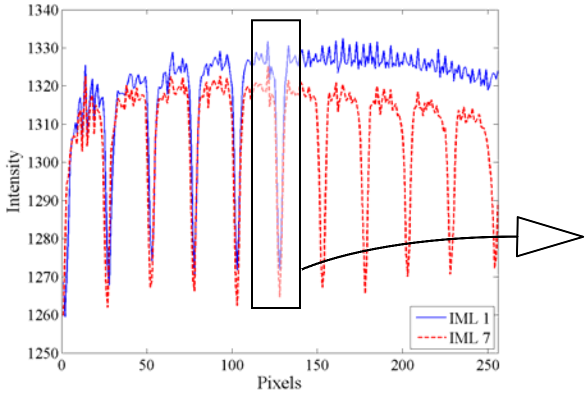

Figure T 23 Intensity vs. pixels x-dir. IML 1 & 7.

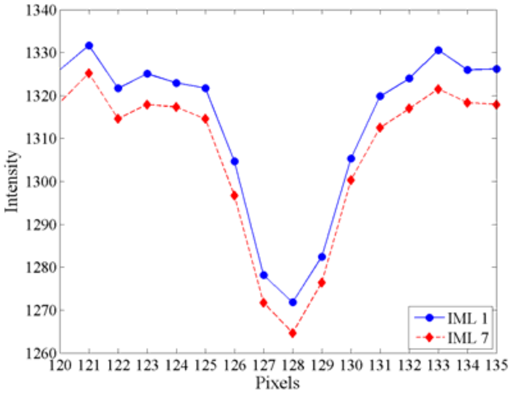

Figure T 24 Intensity vs. pixels x-dir. IML 1 & 7.

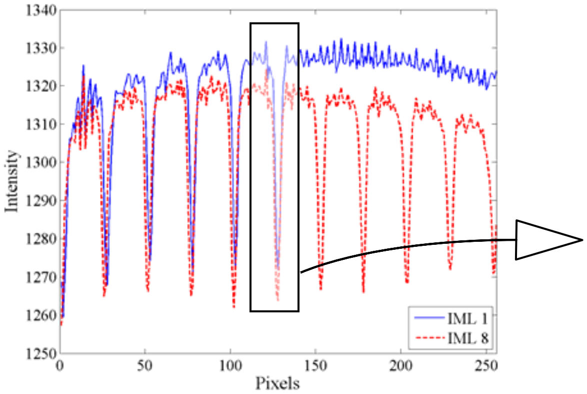

Figure T 25 Intensity vs. pixels x-dir. IML 1 & 8.

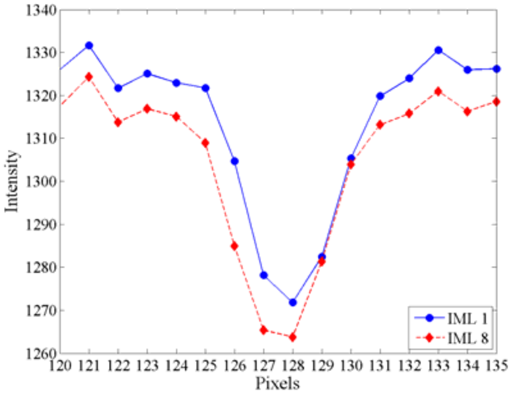

Figure T 26 Intensity vs. pixels x-dir. IML 1 & 8.

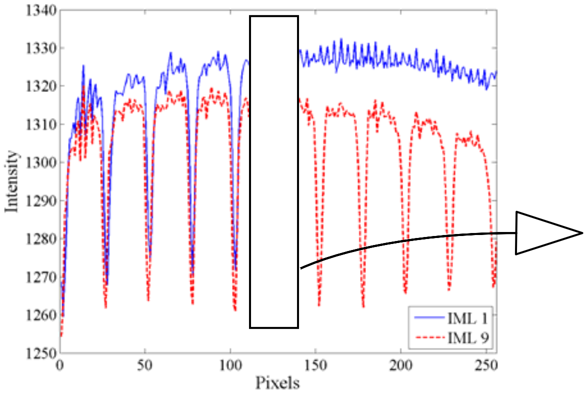

Figure T 27 Intensity vs. pixels x-dir. IML 1 & 9.

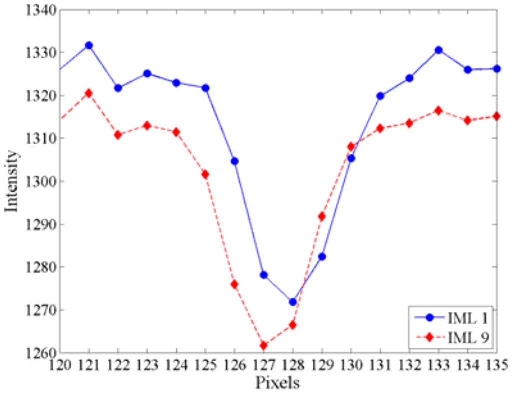

Figure T 28 Intensity vs. pixels x-dir. IML 1 & 9.

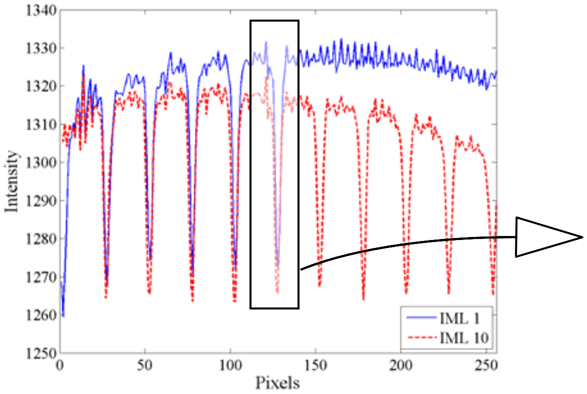

Figure T 29 Intensity vs. pixels x-dir. IML 1 & 10.

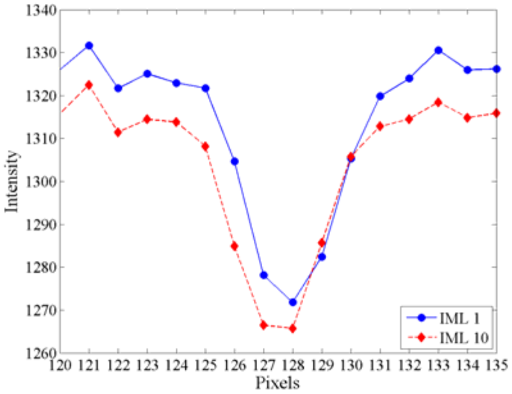

Figure T 30 Intensity vs. pixels x-dir. IML 1 & 10.

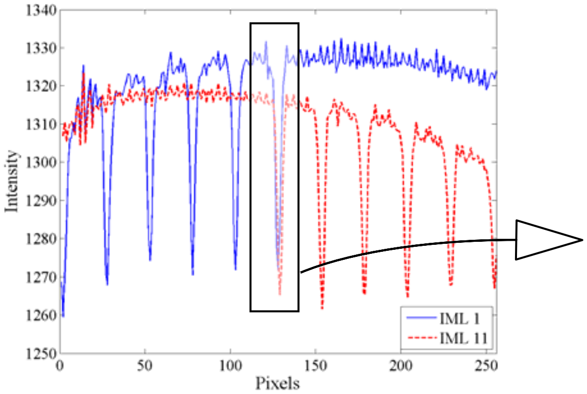

Figure T 31 Intensity vs. pixels x-dir. IML 1 & 11.

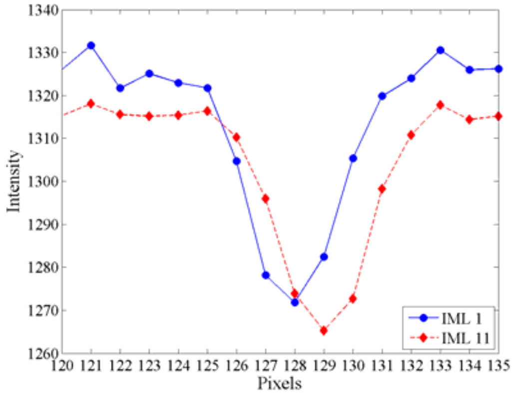

Figure T 32 Intensity vs. pixels x-dir. IML 1 & 11.

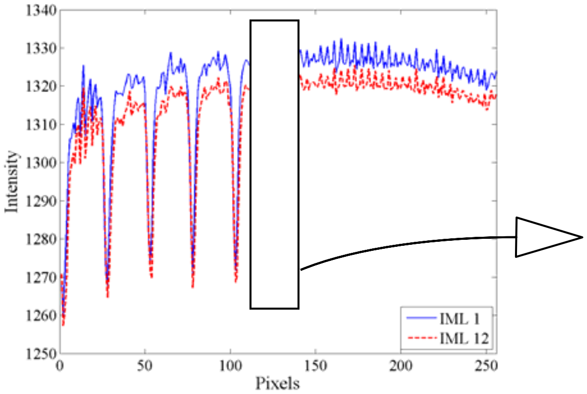

Figure T 33 Intensity vs. pixels x-dir. IML 1 & 12.

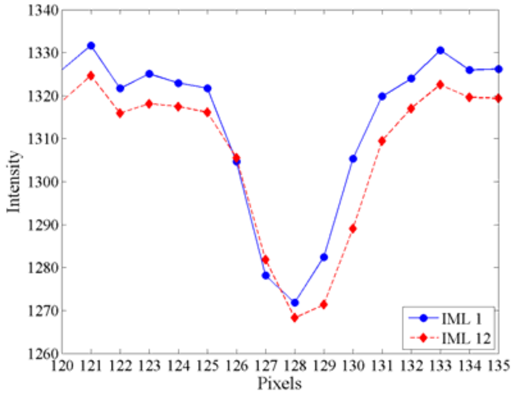

Figure T 34 Intensity vs. pixels x-dir. IML 1 & 12.

Y DIRECTION SPATIAL UNCERTAINTY DATA.

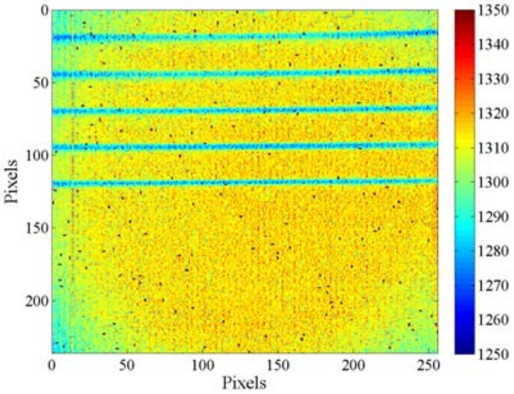

Figure T 35 Optical grid y-dir. IML 1.

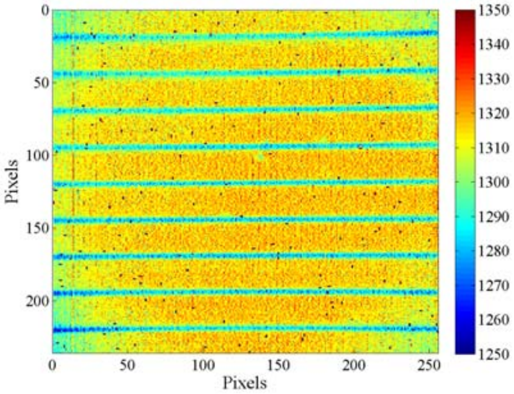

Figure T 36 Optical grid y-dir. IML 2.

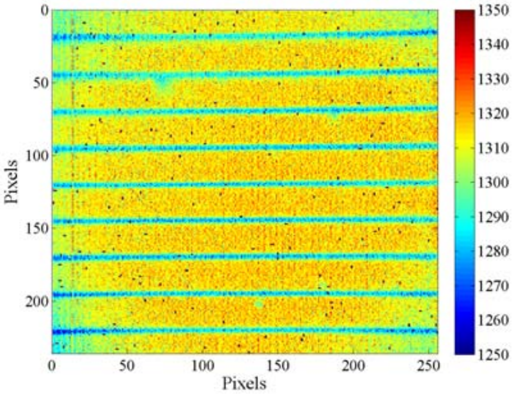

Figure T 37 Optical grid y-dir. IML 3.

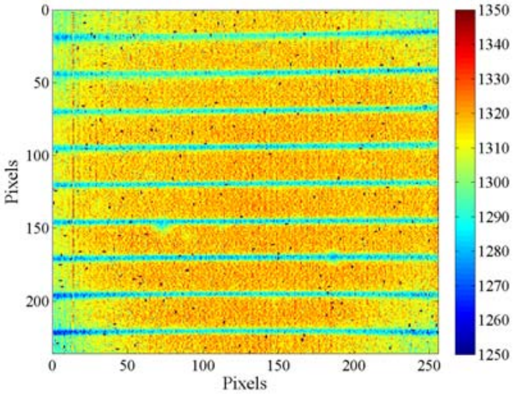

Figure T 38 Optical grid y-dir. IML 4.

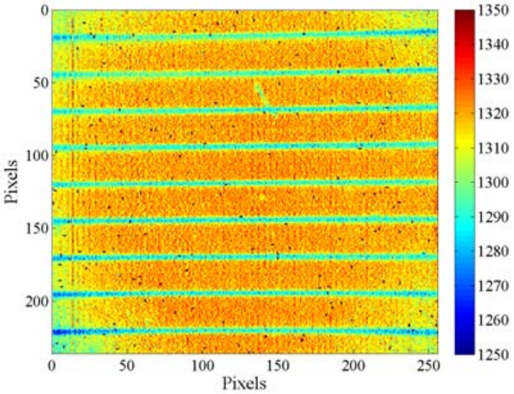

Figure T 39 Optical grid y-dir. IML 5.

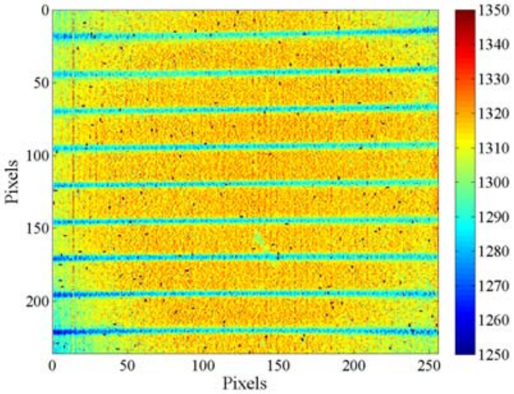

Figure T 40 Optical grid y-dir. IML 6.

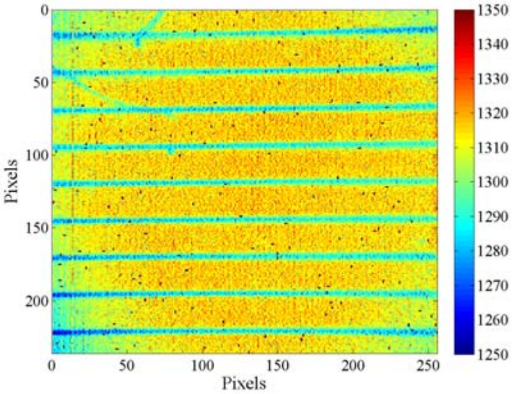

Figure T 41 Optical grid y-dir. IML 7.

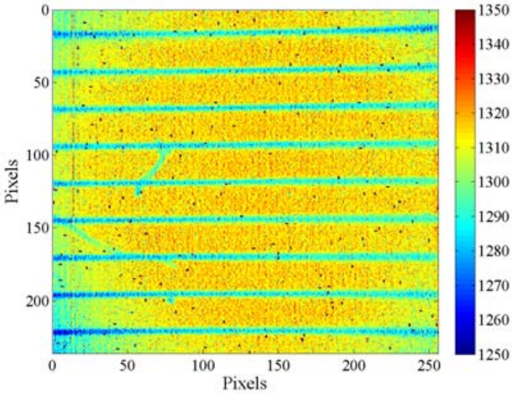

Figure T 42 Optical grid y-dir. IML 8.

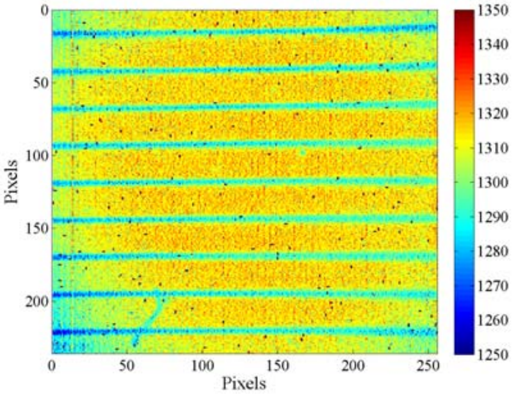

Figure T 43 Optical grid y-dir. IML 9.

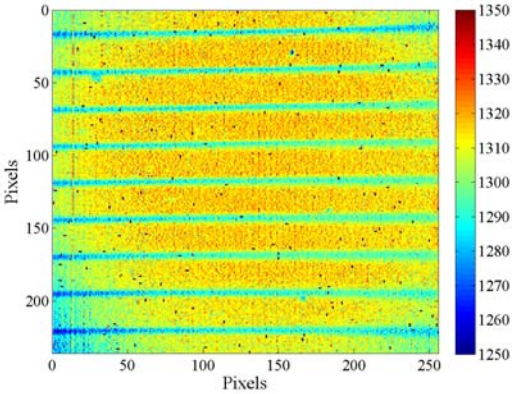

Figure T 44 Optical grid y-dir. IML 10.

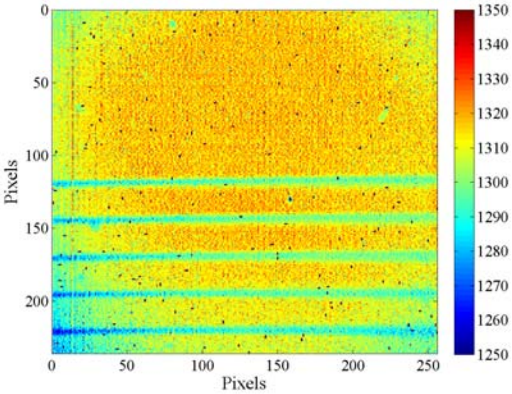

Figure T 45 Optical grid y-dir. IML 11.

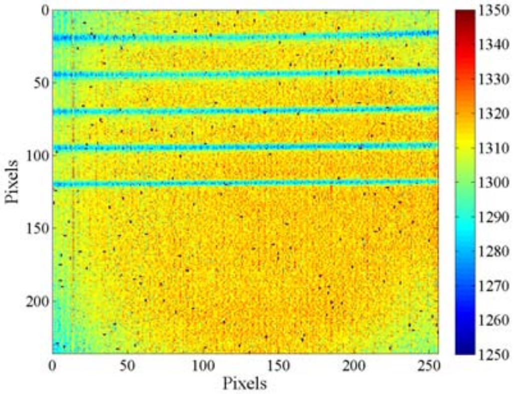

Figure T 46 Optical grid y-dir. IML 12.

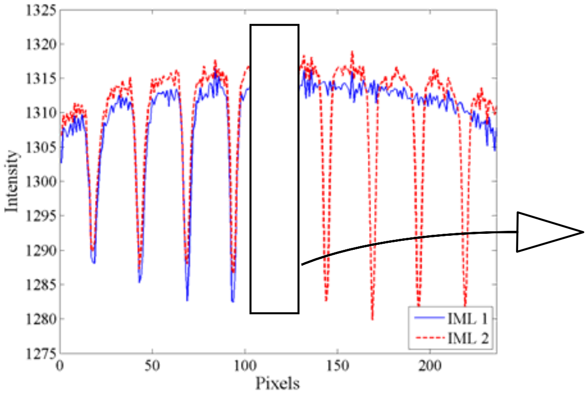

Figure T 47 Intensity vs. pixels y-dir. IML 1 & 2.

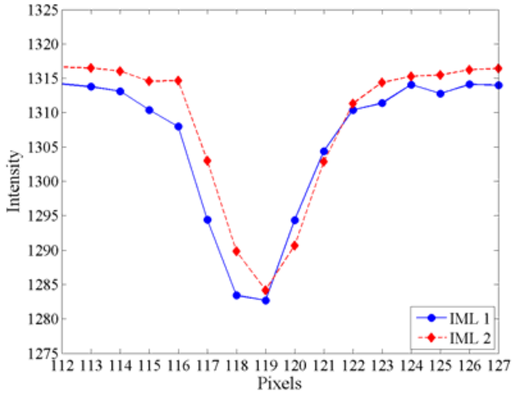

Figure T 48 Intensity vs. pixels y-dir. IML 1 & 2.

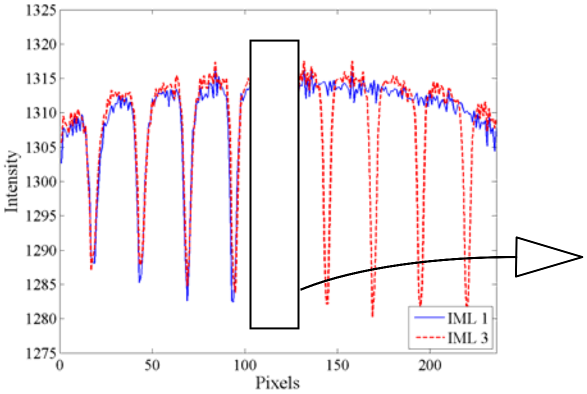

Figure T 49 Intensity vs. pixels y-dir. IML 1 & 3.

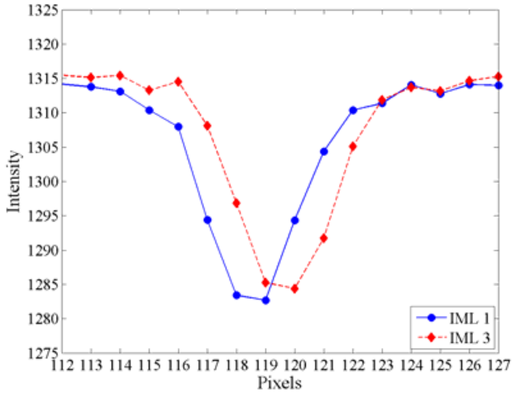

Figure T 50 Intensity vs. pixels y-dir. IML 1 & 3.

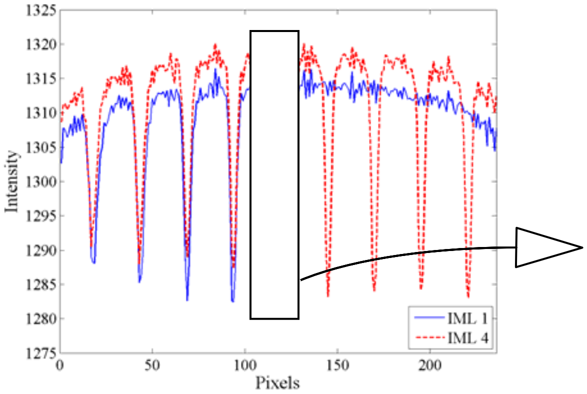

Figure T 51 Intensity vs. pixels y-dir. IML 1 & 4.

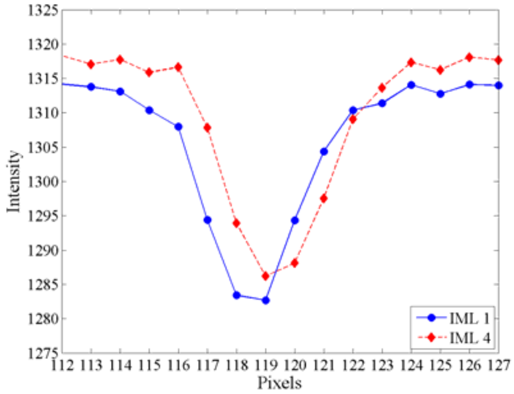

Figure T 52 Intensity vs. pixels y-dir. IML 1 & 4.

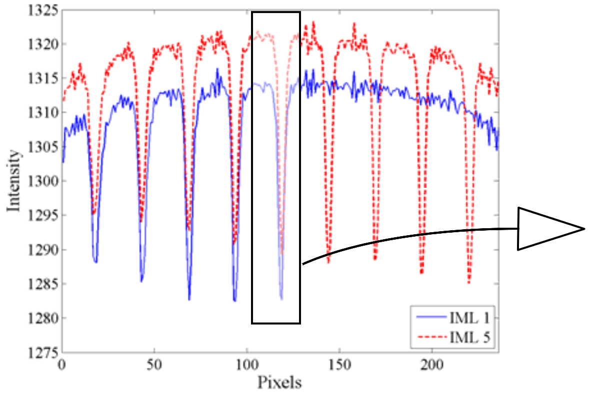

Figure T 53 Intensity vs. pixels y-dir. IML 1 & 5.

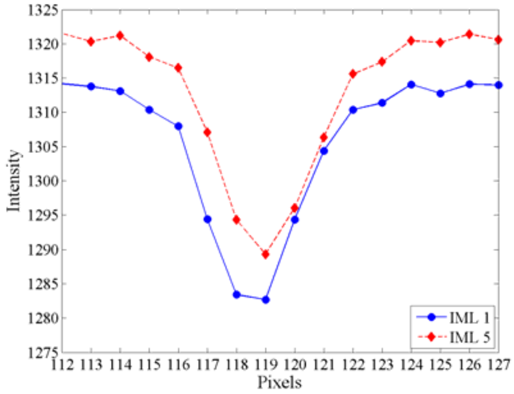

Figure T 54 Intensity vs. pixels y-dir. IML 1 & 5.

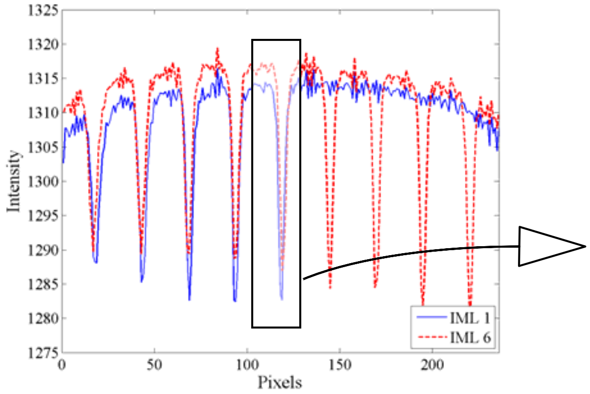

Figure T 55 Intensity vs. pixels y-dir. IML 1 & 6.

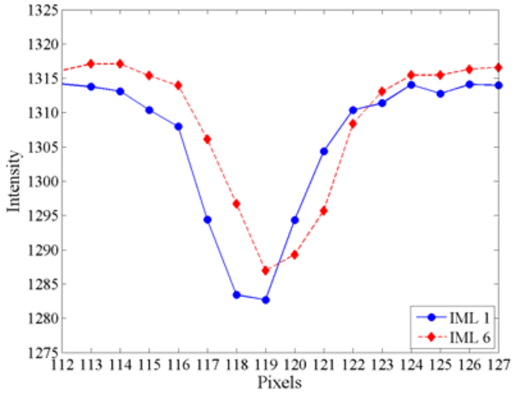

Figure T 56 Intensity vs. pixels y-dir. IML 1 & 6.

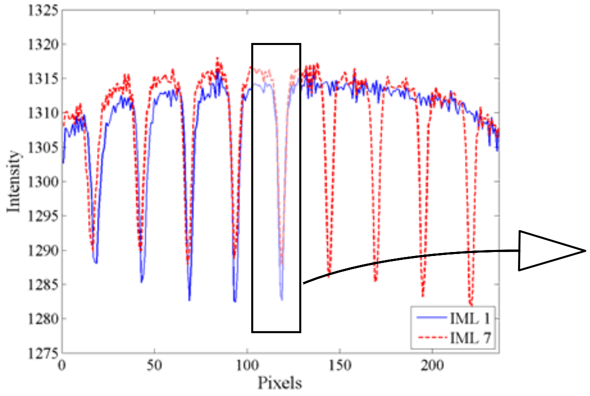

Figure T 57 Intensity vs. pixels y-dir. IML 1 & 7.

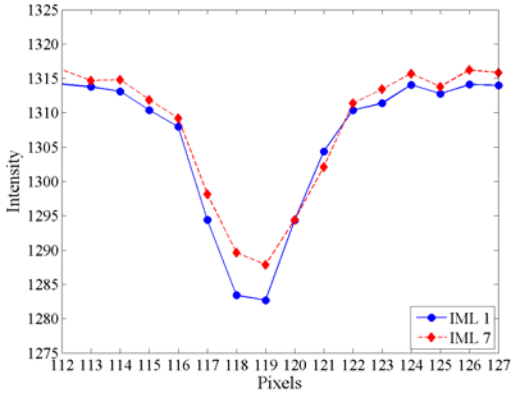

Figure T 58 Intensity vs. pixels y-dir. IML 1 & 7.

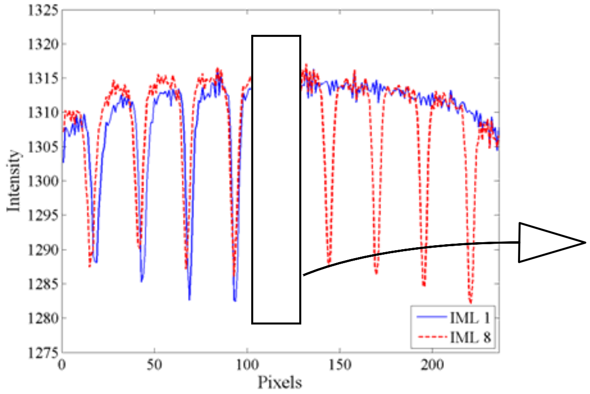

Figure T 59 Intensity vs. pixels y-dir. IML 1 & 8.

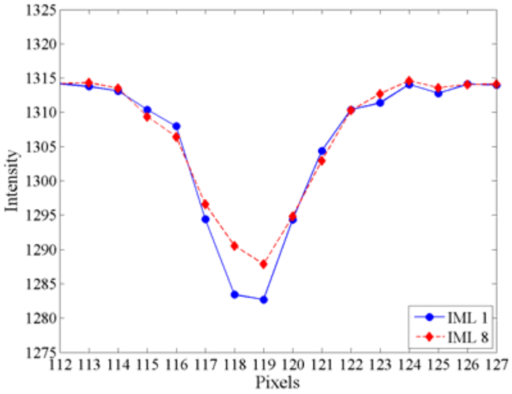

Figure T 60 Intensity vs. pixels y-dir. IML 1 & 8.

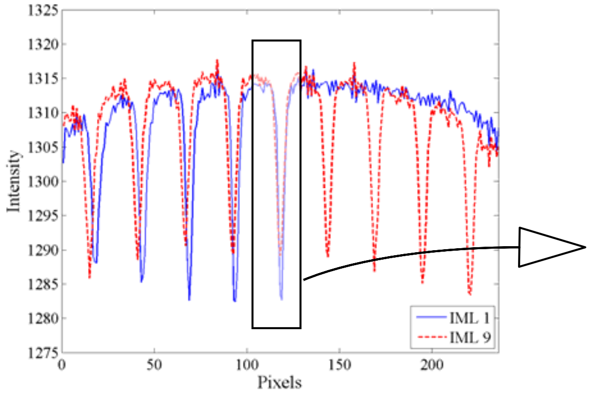

Figure T 61 Intensity vs. pixels y-dir. IML 1 & 9.

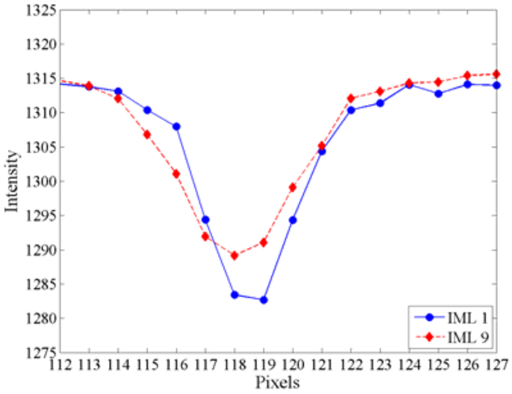

Figure T 62 Intensity vs. pixels y-dir. IML 1 & 9.

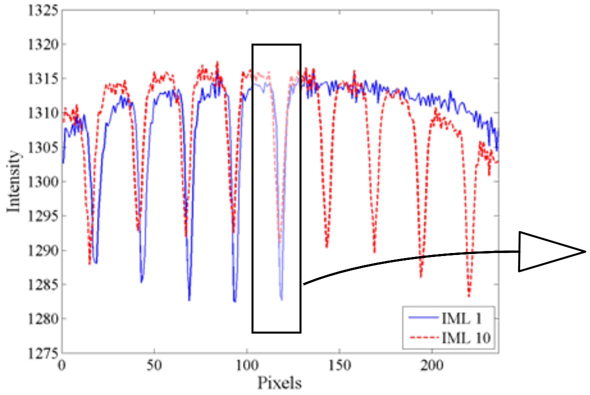

Figure T 63 Intensity vs. pixels y-dir. IML 1 & 10.

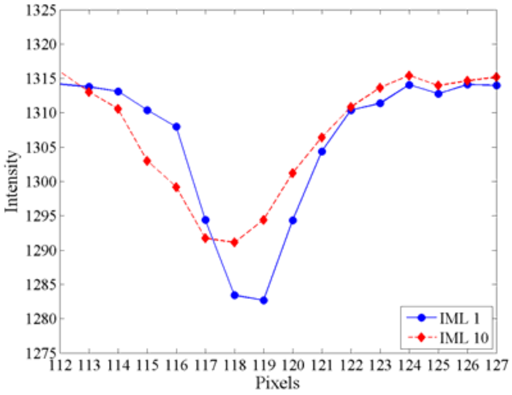

Figure T 64 Intensity vs. pixels y-dir. IML 1 & 10.

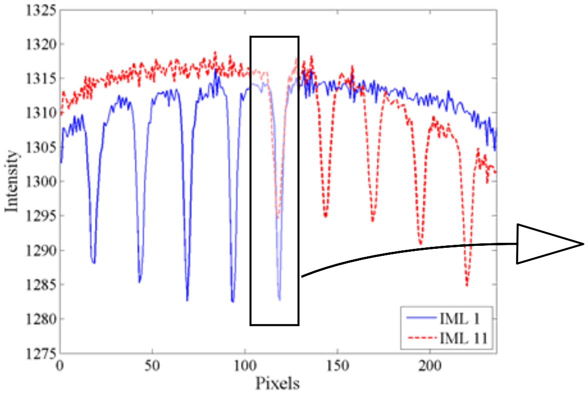

Figure T 65 Intensity vs. pixels y-dir. IML 1 & 11.

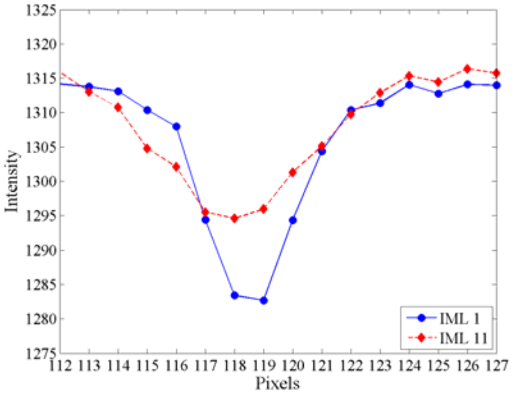

Figure T 66 Intensity vs. pixels y-dir. IML 1 & 11.

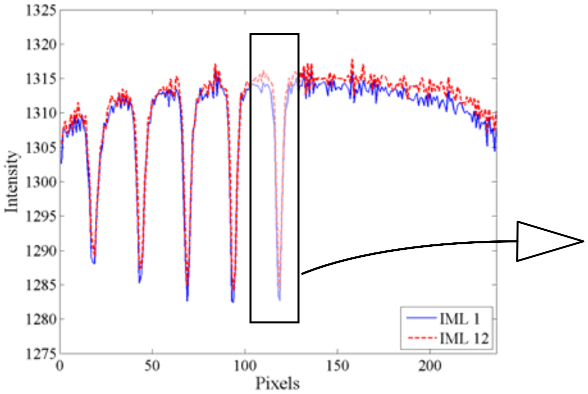

Figure T 67 Intensity vs. pixels y-dir. IML 1 & 12.

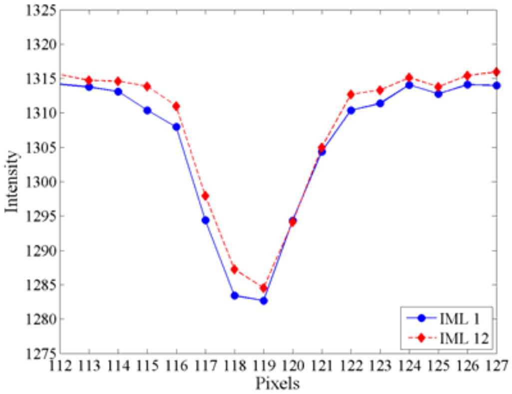

Figure T 68 Intensity vs. pixels y-dir. IML 1 & 12.

APPENDIX U: Calculated x and y calibration image shift.

Table U 1 Calculated x and y directional shift for calibration image shifting.

	25°C		**45°C**		**65°C**		**85°C**		**105°C**		**125°C**	
IML	**X**	**Y**	**X**	**Y**	**X**	**Y**	**X**	**Y**	**X**	**Y**	**X**	**Y**
(#)	**(c)**	**(r)**	**(c)**	**(r)**	**(c)**	**(r)**	**(c)**	**(r)**	**(c)**	**(r)**	**(c)**	**(r)**
560	-31	9	-35	5	-27	-1	-16	-1	-19	1	-15	-1
562	-31	8	-35	4	-26	-1	-16	-2	-18	0	-15	-1
564	-32	7	-36	3	-27	-2	-17	-3	-19	-1	-16	-2
566	-32	7	-36	4	-27	-2	-17	-3	-20	-1	-16	-2
568	-33	7	-37	3	-28	-2	-18	-3	-20	-1	-17	-3
570	-32	6	-36	3	-28	-3	-18	-4	-20	-1	-17	-3
572	-33	6	-36	2	-28	-3	-18	-4	-20	-2	-17	-4
624	-30	9	-34	4	-26	-1	-16	-2	-18	-1	-15	-1
626	-30	8	-35	4	-26	-1	-16	-2	-18	0	-15	-1
628	-31	7	-35	4	-27	-2	-17	-3	-19	-1	-15	-2
630	-31	7	-35	3	-27	-2	-17	-3	-19	-1	-16	-3
632	-32	7	-36	3	-28	-3	-1	-1	-19	-1	-16	-3
634	-31	7	-36	3	-27	-3	-17	-4	-19	-2	-16	-3
636	-32	6	-36	2	-27	-3	-17	-4	-20	-2	-16	-4
688	-29	8	-32	4	-25	-1	-15	-2	-17	0	-14	-2
690	-30	7	-32	4	-25	-1	-15	-2	-18	-1	-14	-2
692	-31	7	-33	3	-26	-2	-16	-3	-18	-1	-15	-2
694	-31	6	-33	3	-26	-2	-16	-4	-18	-1	-15	-3
696	-32	6	-33	3	-27	-3	-17	-4	-18	-1	-15	-3
698	-31	6	-33	2	-26	-3	-16	-4	-18	-2	-15	-4
700	-31	6	-33	2	-26	-3	-17	-5	-19	-2	-16	-4
752	-29	7	-31	3	-24	-2	-14	-3	-16	-1	-13	-2
754	-29	7	-31	3	-25	-2	-15	-3	-17	-1	-14	-3
756	-30	6	-32	2	-25	-3	-15	-4	-17	-1	-14	-3
758	-30	6	-32	2	-25	-3	-15	-4	-17	-1	-13	-3
760	-30	6	-32	2	-26	-3	-15	-4	-18	-2	-15	-4
762	-30	5	-32	1	-26	-4	-15	-5	-17	-2	-14	-4
764	-31	5	-33	1	-26	-4	-16	-5	-18	-2	-15	-5
816	-28	7	-30	3	-24	-2	-14	-3	-16	-1	-13	-3
818	-28	6	-30	3	-24	-3	-14	-4	-16	-1	-13	-3
820	-29	5	-31	2	-24	-3	-14	-4	-17	-2	-13	-4
822	-29	5	-31	1	-24	-3	-14	-4	-16	-2	-13	-4
824	-29	5	-31	1	-25	-4	-15	-5	-17	-3	-13	-4
826	-30	4	-31	1	-25	-5	-14	-5	-17	-3	-13	-5
828	-30	5	-32	1	-25	-5	-16	-5	-17	-4	-14	-5
880	-26	6	-28	2	-22	-3	-12	-4	-14	-2	-11	-4
882	-26	5	-28	1	-22	-4	-12	-5	-14	-2	-11	-4
884	-27	4	-29	1	-23	-4	-12	-5	-15	-3	-11	-5

	25°C		**45°C**		**65°C**		**85°C**		**105°C**		**125°C**	
IML	**X**	**Y**	**X**	**Y**	**X**	**Y**	**X**	**Y**	**X**	**Y**	**X**	**Y**
(#)	**(c)**	**(r)**	**(c)**	**(r)**	**(c)**	**(r)**	**(c)**	**(r)**	**(c)**	**(r)**	**(c)**	**(r)**
886	-27	4	-29	0	-22	-4	-12	-5	-15	-3	-11	-5
888	-28	4	-30	0	-23	-5	-13	-6	-15	-3	-12	-6
890	-28	3	-29	0	-23	-5	-13	-6	-15	-4	-12	-6
892	-30	2	-32	-2	-26	-7	-15	-8	-17	-6	-12	-7
944	-26	5	-25	1	-21	-3	-11	-4	-14	-1	-10	-3
946	-26	5	-26	1	-22	-4	-12	-5	-14	-2	-10	-4
948	-29	-1	-26	1	-22	-4	-12	-5	-14	-2	-11	-4
950	-27	4	-26	0	-22	-4	-12	-5	-14	-2	-11	-5
952	-28	4	-27	0	-23	-5	-13	-6	-15	-3	-11	-5
954	-28	3	-27	-2	-24	-7	-14	-8	-16	-5	-13	-9
956	ND	ND	ND	ND	ND	ND	ND	ND	ND	ND	ND	ND
1008	-25	-1	-24	0	-21	-2	-11	-1	-13	-1	-10	-1
1010	-25	4	-24	0	-21	-4	-11	-5	-13	-3	-10	-5
1012	-26	3	-25	0	-21	-4	-11	-5	-13	-2	-10	-5
1014	-26	2	-25	-1	-21	-4	-10	-3	-12	-1	-8	-1
1016	-27	4	-24	0	-23	-7	-13	-8	-15	-5	-12	-6
1018	ND	ND	ND	ND	ND	ND	ND	ND	ND	ND	ND	ND
1020	ND	ND	ND	ND	ND	ND	ND	ND	ND	ND	ND	ND